Modeling of concrete dehydration and multiphase transfer in nuclear containment concrete wall during loss of cooling accident

Jin Wang

Université de Toulouse

THÈSE

En vue de l'obtention du

DOCTORAT DE L'UNIVERSITÉ DE TOULOUSE

Délivré par : *l'Université Toulouse 3 Paul Sabatier (UT3 Paul Sabatier)*

Présentée et soutenue le *08/06/2016* **par :**

Jin WANG

Modeling of Concrete Dehydration and Multhiphase Transfer in Nuclear Containment Concrete Wall during Loss of Cooling Accident

JURY

Abdelkarim Aït-Mokhtar	Rapporteur
Benoît BARY	Rapporteur
Alain SELLIER	Membre du Jury
Laurie BUFFO-LACARRIÈRE	Membre du Jury

École doctorale et spécialité :
Mécanique, Energétique, Génie civil, & Procédés (ED-MEGeP)
Unité de Recherche :
Laboratoire Matériaux et Durabilité des Constructions
Directeur(s) de Thèse :
Alain SELLIER et *Laurie BUFFO-LACARRIÈRE*
Rapporteurs :
Dr HDR Benoît BARY et *Pr Abdelkarim Aït-Mokhtar*

Acknowledgment

First of all, I would like to express my sincere gratitude to my advisor Professor Alain Sellier and Maître de conférence Laurie Buffo-Lacarrière, who gave me continuous support on my thesis. Without their patience, knowledge, motivation and inspiration, I couldn't have managed to get here today to finish my thesis.

My gratitude to the two reviewers of my defense, Ingénieur de Recherche Benoît Bary and Prof. A. Aït-Mokhtar, who kindly accepted being members of jury of my defense. They carefully reviewed my thesis and gave very inspiring comments on it, which will be interesting for my future work on similar projects.

Many thanks also go to my dear colleague in the lab, who helped me with experiments and discussed some problems with me, which was of great help.

Also, I would like to thank friends in my life, who accompanied me and made me feel warm during my stay here in Toulouse.

I would like to thank my parents, as well as my girlfriend Yingying, who gave me great moral support during the several difficult periods of time. They are the greatest treasure in my life.

At last, to my puppy doudou, who passed away in an unfortunate accident. She was a very gentle and loyal friend to me, and comforted me a lot when my spirits were low. May her R.I.P.

Contents

Notations

For the notations, all the symbols in literature review are either explained or kept as the same as that in the literature.

Latin symbols

A	Calibration constant in hydration model
A_λ	Constant to calculate thermal conductivity[K^{-1}]
a_c	Constant for calculation of capillary pressure(MPa)
a^{AFm}, b^{AFm}	Fitting parameters in dehydration model of monosulfate
a^{CSH}, b^{CSH}	Fitting parameters in dehydration model of C-S-H
a_k	Coefficient to calculate intrinsic permeability of liquid water
b_c	Constant for calculation of capillary pressure(-)
c	Heat capacity of the concrete ($J{\cdot}m^{-3}{\cdot}K^{-1}$)
C_{pl} C_{pv}	Specific heat of fluid($J{\cdot}m^{-3}{\cdot}K^{-1}$)
C_{bw}	Specific heat of boundd water($J{\cdot}m^{-3}{\cdot}K^{-1}$)
C_{ds}	Specific heat of dry material($J{\cdot}m^{-3}{\cdot}K^{-1}$)
$C_{p0clinker}$	Initial volumetric concentration of clinker
E_a^i	The activation energy of the hydrate i for dehydration ($J{\cdot}mol^{-1}$)
$\vec{F}$	Flux of fluid ($kg{\cdot}\ m^{-2}{\cdot}\ s^{-1}$)
g	Chemical activation term in hydration model

$\hat{h}$	Specific enthalpy of the volume(J/kg)
h	Thermal activation in hydration model
h_{eq}	Equivalent heat exchange coefficient on the exterior boundary(W·m^{-2}·K^{-1})
k_{ml} k_{mv}	Effective permeability of liquid water and water vapor(m^2)
k^0_{ml}	Intrinsic permeability of liquid water and water vapor(m^2)
k^0_{mv}	Initial Intrinsic permeability of water vapor(m^2)
k_{rl} k_{rv}	Relative permeability of liquid water and water vapor (-)
$L_{i\to j}$	Heat of phase transition from phase i to phase j (J·mol^{-1})
$L_{s\to l}$	Heat of dehydration (J·kg^{-1})
$m^{sample}(T)$	mass of the sample at temperature T during TGA test
m_w	The mass of water per 1 m^3 of the cement paste (kg/m^3)
m^i	The mass of the hydrate i per 1m^3 of the cement paste (mol/m^3)
$m^{sample}_{initial}$	mass of the sample before TGA test (kg)
m^{sample}_{final}	mass of the sample after the TGA test (kg)
m	Mass of fluid per volume(kg· m^{-3})
m_0	Mass of fluid per volume at dry state(kg· m^{-3})
m_{sat}	Mass of fluid at saturated state(kg· m^{-3})
m_{cp}	Mass of cement paste per 1 m^3 of concrete (kg/m^3)
m^{aggr}	Mass of aggregates per 1 m^3 of concrete (kg/m^3)
M_w	Molar mass of water (kg· mol^{-1})
M^i	The mole mass of the hydrate i (g/mol)
n_{CSH}	The amount of C-S-H per 1m^3 of the cement paste (mol/m^3)

n_{CH}	The amount of CH per 1m^3 of the cement paste (mol/m^3)
n_{AFm}	The amount of AFm per 1m^3 of the cement paste (mol/m^3)
n_{AFt}	The amount of AFt per 1m^3 of the cement paste (mol/m^3)
$n_{C_3AH_6}$	The amount of C_3AH_6 per 1m^3 of the cement paste (mol/m^3)
n_i	The amount of the hydrate i per 1 m^3 of the cement paste
t	Time (s)
n, r_k	Calibration parameters in hydration model
n_{SiO_2}	The amount of $\mathrm{SiO_2}$ per 1m^3 of the cement paste (mol/m^3)
n_{SO_3}	The amount of $\mathrm{SO_3}$ per 1m^3 of the cement paste (mol/m^3)
$n_{Al_2O_3}$	The amount of $\mathrm{Al_2O_3}$ per 1m^3 of the cement paste (mol/m^3)
n_{CaO}	The amount of CaO per 1m^3 of the cement paste (mol/m^3)
Q_{ex}	Heat exchange on the exterior boundary(W·m^{-2})
$\vec{q}$	Heat due to thermal conduction(J·m^{-3}s^{-1})
$\dot{q}$	Heat source due to the phase change and the dehydration of hydrates per 1m^3 of the cement paste (J·m^{-3}·s^{-1})
p_c	Capillary pressure (Pa)
p_{vs}	Saturated vapor pressure (Pa)
p	Constant for calculation of relative permeability of water vapor
R	Ideal gas constant (J·K^{-1} ·mol^{-1})
$\bar{r}_m$	Current thickness of hydrate layers around anhydrous grain (m)
S	Effect of admixture in hydration model
$S_l \quad S_v$	Saturation degree of liquid water and water vapor(-)

T^i_{onset}	The onset temperature of the hydrate i during dehydration i (g/mol)
T_{cr}	Critical temperature of water(K)
T_λ	Reference temperature to calculate thermal conductivity of concrete(K)
T_∞	Temperature at infinite distance(K)
T_{ex}	Temperature on the exterior boundary(K)
$\hat{u}$	Specific internal energy of the volume(J/kg)
$\vec{u}$	Velocity of the flow(m/s)
$\mathbf{v}_l$	Velocity of the liquid phase to the matrix ($m \cdot s^{-1}$)
$\mathbf{v}_g$	Velocity of the gaseous phase to the matrix ($m \cdot s^{-1}$)
$\dot{w_{dehydr}}$	The mass change of the water due to dehydration per $1m^3$ of the cement paste ($kg \cdot m^{-3} s^{-1}$)
w^i	Released water of the hydrate i per $1m^3$ of the cement paste (kg/m^3)
w	Mass of water in hydrates per $1m^3$ of the cement paste (kg/m^3)
w^i_{max}	Total mass of water in hydrate i per $1m^3$ of the cement paste (kg/m^3)
w_{eq}	The mass loss due to the dehydration when equilibrium is reached (kg/m^3)
$\dot{w}_{in}$	The internal source of mass per volume ($kg \cdot m^{-3} \cdot s^{-1}$)
w_l	The mass of liquid water per 1 m^3 of the cement paste (kg/m^3)
w_g	The mass of vapor per 1 m^3 of the cement paste (kg/m^3)
$w^{concrete}_{dehydr}$	Water released in the porosity due to dehydration (kg/m^3)

$\dot{w_{in}}$	The mass change of the water due to phase transition and dehydration per 1m^3 of the cement paste (kg·m^{-3}s^{-1})
$\dot{w_{phase}}$	The mass change of the water due to phase transition per 1m^3 of the cement paste (kg·m^{-3}s^{-1})
W_{ps}	The volumetric concentration of water at saturated state
W_p	The volumetric concentration of water

Greek symbols

$\dot{\alpha}, \alpha$	The rate of hydration (s^{-1}) and hydration degree
β	Klinkenberg constant(bar)
ϵ	Time step control constant
$\eta_l \quad \eta_v$	Dynamic viscosity of liquid water and vapor(kg·m^{-1}s^{-1})
λ	Thermal conductivity (W·m^{-1}·K^{-1})
$\lambda_d(T)$	Thermal conductivity of dry concrete(W·m^{-1}·K^{-1})
$\mu_{l\to v}$	Rate of evaporation(kg·m^{-3}s^{-1})
ξ^i	Degree of dehydration of the hydrate i (-)
ξ^i_{eq}	Equilibrium degree of dehydration of the hydrate i (-)
$\dot{\xi}^i$	Rate of dehydration of the hydrate i (-)
π	Water accessibility to anhydrous phase in hydration model
ρ_s	The density of the matrix (kg·m^{-3})
ρ_l	The density of the liquid water (kg·m^{-3})
ρ_g	The density of the gaseous phase (kg·m^{-3})
$\sigma(T)$	Surface tension(N·m^{-1})

τ^i	The characteristic time of hydrate i for dehydration (s)
ϕ	Porosity of concrete (-)

General Introduction

Nuclear power production has been raised to 2620 billion kW in 2010, with its sharing 13.5% of the world's electricity generation. And two tragic accidents happened in Fukushima and Chernobyl sounded alarm bell to people all over the world about how to utilize the nuclear energy safely. In Chemobyl accident, more than 190,000 km^2 of European territory received levels of ^{137}Cs[1] above 37kBqm^{-2}(Izrael *et al.*, 1996). The contaminant in the nuclear accident always spread widely. In Fukushima Daiichi Nuclear Power Plant(FDNPP) accident, the radiocaesium released to atmosphere was deposited on the surface of the land and ocean(Chino *et al.*, 2011). The area contaminated with radiocaesium at activities larger than 1MBqm^{-2} extended up to 45km from the plant(MEXT, 2011). Even in Greece(Manolopoulou *et al.*, 2012) and France, there were reports about the increase of the radioactive(Perrot *et al.*, 2012).
The tragic accidents happened in Fukushima and Chemobyl showed the whole world the importance of the safety problem of the nuclear engineering, and some flaws in the design of the nuclear power plants in Japan and East Europe have been exposed. Hence, a better comprehension to the nuclear power plant design is required to prevent such accident from happening again. To prevent the leak of the radioactive matter, the transfer properties of reinforced concrete, which are used as the barrier in nuclear power plant and the storage of the nuclear waste are of great importance. Those properties are not so easy to assess because of the complex environment during the accident, but the main problem, which may affect the transfer properties of concrete in the accident, is that the pressure and the temperature of the environment would rise to relatively high level and last for weeks during the accident. Meanwhile, this kind of severe condition lead remarkable changes in the transfer properties of the concrete, and high pressure gas and vapor containing radioactive particles may leak from the containment structure.

When the concrete is exposed to a high temperature environment, the hydrates in the cement paste will decompose and release some water. Some models have been proposed to describe this process. However, the existing models requires repetitive experiments to fit the parameters in the model for difference cement pastes. One of the objectives in this thesis is to propose a model that is able to predict the released water due to dehydration in the cement paste, and this model can be reused for different cement pastes without refitting the parameters. In this model, the released water of each hydrate was calculated independently, and the results of them are summed to get the released water of cement paste due to dehydration. Hence, once the amount of hydrates is given, the released water due to dehydration can be calculated with this model. Furthermore, the amount of hydrates can be calculated with existing model with given composition of cement and curing age.
Another objective in this thesis is to implement the dehydration model in the heat and water transfer model in concrete to predict the temperature and pressure evolution in the containment structure exposed to high temperature up to 200°C. The simulation result is compared with the experimental result in literature without considering the mechanical aspect.
The last objective in this thesis is to investigate the influence of some parameters on the temperature and pressure distribution in the structure with the transfer model, and the model was also adopted to investigate the temperature and pressure distribution in the structure with different sizes and under different thermal loadings.
Hence, this thesis includes two parts:
In the first part, existing dehydration models were compared and a new dehydration model including kinetics and equilibrium of dehydration process was proposed. The dehydration was compared with thermal analysis results both in literature and that performed in LMDC Toulouse.

Chapter1 reviews the literature on characteristic of hardened cement paste at ambient temperature, effect of temperature, and the existing models describing the cement paste dehydration.

Chapter2 proposes the dehydration model for each hydrate and then that for cement paste.

Chapter3 presents the validation of the model with experiments in literature and performed in LMDC Toulouse.

In the second part, the dehydration model was implemented in the thermo-hygral model based on the existing models. The simulation was made with finite element software to validate the model and investigate the influence of some parameters in the model. The model was applied to structures under thermal loadings, and structures with different size to investigate the evolution of temperature and gas pressure.

Chapter1 reviews the literature on heat and water transfer models for concrete and the effect of temperature.

Chapter2 proposed the model describing the water and heat transfer in concrete up to 200°C, and compares the simulation results with MAQ-BETH mock-up.

Chapter3 investigates the influence of latent heat of dehydration, initial intrinsic permeability to vapor and coefficient to calculate intrinsic permeability to liquid water. The model is also applied to structures under thermal loadings up to 200°C with different heating rate(0.05-0.2K/min), and structures with different thicknesses(0.2-0.6m) .

Part I

DEHYDRATION OF CEMENT PASTE

Introduction

To study the dehydration of cement paste, one possible method is to consider the cement paste as a whole during the dehydration, which means the contributions from different hydrates in the cement paste would not be considered independently. With this method, to obtain the mass evolution during dehydration for a cement paste with different composition, experiments will be needed either to get the mass evolution directly or to get fitting parameters in existing models for the present cement paste.
To avoid the repetitive efforts caused by the various compositions of cement pastes, this part develops a method that calculates the dehydration process of hardened cement paste by summing the calculation results of each hydrate. In other words, to consider the dehydration of the hardened cement paste as summation of dehydration of each hydrate that is present in the paste.
Chapter.1 introduced the existing researches on concerning topics, Chapter.2 proposed the dehydration models for each hydrate, and Chapter.3 validated the dehydration model for cement paste by comparison with experimental results in literature and experiments performed in LMDC Toulouse under different heating rates.

Chapter 1

Literature review

1.1 Characteristic of hardened cement paste at ambient temperature

1.1.1 Hydration reactions

The cement paste contains different hydrates, which have different characteristics during dehydration. To study the process of cement paste dehydration, the first thing is to determine the composition of the cement paste and the amount of water in each hydrate.
Hydration means the total changes that occur when anhydrous cement (or one of its constituent phases) mixed with water(Taylor, 1990). The hydration reactions for Portland cement are illustrated below(Tazawa *et al.*, 1995) :

Equation 1.1 and equation1.2 described the hydration processes of the C_3S and C_2S, which produce the porous C-S-H gel. In (Tazawa *et al.*, 1995), the C-S-H gel was expressed as $C_3S_2H_3$. However, C/S ratio and H/S ratio varies with different factors. For example, in (Richardson, 1999), it was reported that C/S ratio varies from 0.7 to 2.3, and in (Jennings, 2000), it was reported that the H/S ratio varies with relative humidity. Hence, the C/S ratio and H/S ratio in C-S-H gel are noted m and n, respectively.

$$C_3S + (3 + n - m)H \rightarrow C_mSH_n + (3 - m)CH \tag{1.1}$$

$$C_2S + (2 + n - m)H \rightarrow C_mSH_n + (2 - m)CH \tag{1.2}$$

The primary initial reaction for C_3A is equation1.3, which produces ettringite. As long as the sulfate is used up before the complete hydration of C_3A, the reaction of equation1.4 which represents the generation of the monosulfate takes place. Once all the ettringite is reacted, C_3A will react following equation1.5.

$$C_3A + 3C\bar{S}H_2 + 26H \rightarrow C_6A\bar{S}_3H_{32} \tag{1.3}$$

$$C_6A\bar{S}_3H_{32} + 2C_3A + 4H \rightarrow 3C_4A\bar{S}H_{12} \tag{1.4}$$

$$C_3A + 6H \rightarrow C_3AH_6 \tag{1.5}$$

The C_4AF shares the similar reacting conditions with C_3A following the equation1.6, 1.7, 1.8.

$$C_4AF + 3C\bar{S}H_2 + 27H \rightarrow C_6(A,F)\bar{S}_3H_{32} + CH \tag{1.6}$$

$$2C_4AF + C_6(A,F)\bar{S}_3H_{32} + 6H \rightarrow 3C_4(A,F)\bar{S}H_{12} + 2CH \tag{1.7}$$

$$C_4AF + 10H + 2CH \rightarrow C_3AH_6 - C_3FH_6(\text{solid} \quad \text{solution}) \tag{1.8}$$

Because the main hydrates of cement pastes are C-S-H, CH, monosulfate and C_3AH_6 in most of the experiments mentioned in this study, only those four hydrates will be be discussed in the development of models. Some other hydrates could exist in pastes produced from more complex binders, so the present study is limited to OPC based binders. According to (Adenot, 1992), the hydration of Portland cement paste produces either ettringite or calcium aluminate hexahydrate. For completely dehydrated ordinary Portland cement, the molar balance equations for hydration are shown in equation.1.9

$$\begin{cases} n_{CH} + mn_{CSH} + 4n_{AFm} + 6n_{AFt}(\text{or } 3n_{C_3AH_6}) = n_{CaO} \\ n_{CSH} = n_{SiO_2} \\ 2n_{AFt}(\text{or } 2n_{C_3AH_6}) + 2n_{AFm} = 2n_{Al_2O_3} \\ 3n_{AFt}(\text{or } 0n_{C_3AH_6}) + n_{AFm} = n_{SO_3} \end{cases} \tag{1.9}$$

The structure of the hydrates, especially the type of water(chemically combined, inter layer,...), and the stoichiometries of hydrates affect the mass change due to dehydration. The following section will introduce the different structures and stoichiometries of hydrates concerning the dehydration.

1.1.2 Structure and stoichiometry of hydrates

The structures of the hydrates influence the mechanism of the dehydration. For example, the crystallized CH has a smaller temperature range for the dehydration process(see fig.5.2 in (Taylor, 1990)) comparing to C-S-H gel which dehydrates almost throughout the whole temperature range when the sample was heated from room temperature to up to 1000°C(see experiments in (Zhang and Ye, 2012).

- Portlandite(CH)
  CH has a layer structure with octahedral calcium atoms and tetrahedral oxygen atoms, which is shown in fig.1.1(Taylor, 1990). Small, full circles represent calcium atoms, large open or shaded circles oxygen atoms; a hydrogen atom, not shown, completes the tetrahedral coordination of each oxygen atom. The structure of CH indicates that during dehydration, each hydroxy stands the same priority, which could be an explanation to the small range of dehydration. In ordinary Portland cement pastes, a content of CH between 15-25% was found by thermal analysis or QXDA.
  Some reported that portlandite in cement paste dehydrates in the temperature range around 400–500°C(Sha *et al.*, 1999)(Zhang and Ye, 2012)(Stepkowska *et al.*, 2004)(Vedalakshmi *et al.*, 2003). Zelić(Jelica Zelic and Jozic, 2007) reported that pure $Ca(OH)_2$ dehydrates at lower temperature to 340°C than that in the concrete.

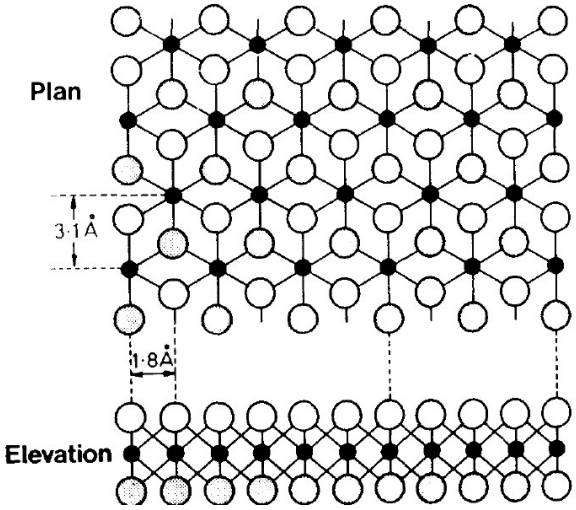

Figure 1.1: Structure of a single layer of CH.(Taylor, 1990)

- Hydrated calcium aluminate(C_3AH_6)
  C_3AH_6 is the only stable ternary phase in the CaO-Al_2O_3-H_2O system at ordinary temperatures(Taylor, 1990), and the SEM of crystals of C_3AH_6(Barnes and Bensted, 2002) was shown in fig.1.2.

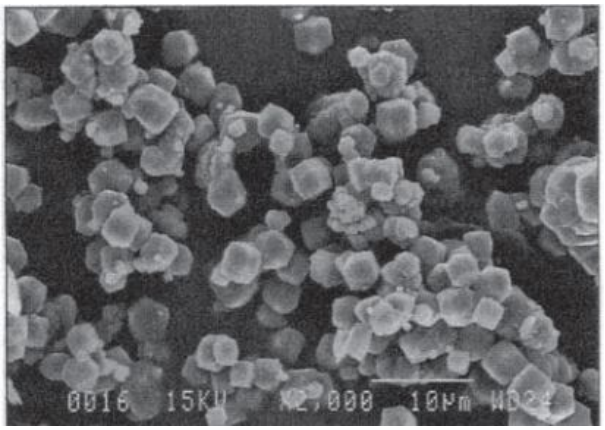

(a)

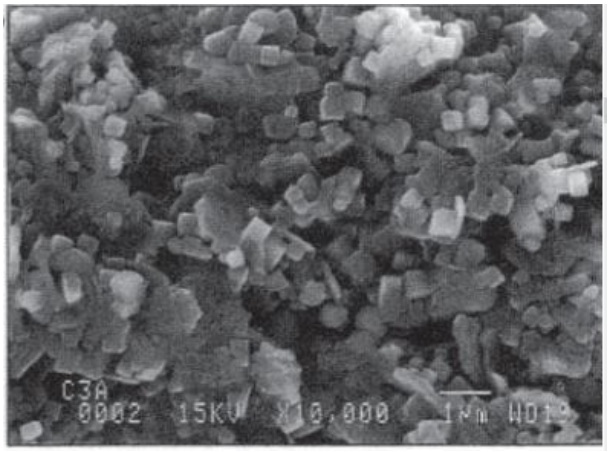

(b)

Figure 1.2: SEM of cubic crystals of C_3AH_6 at magnifications of (a)2000 (b)10,000, respectively(Photographs supplied by Lafarge Alunimates)(Barnes and Bensted, 2002)

Some researches showed that it is thermodynamically stable in the temperature range 20°C–250°C(Dilnesa cited (Matschei *et al.*, 2007b)(Peppler and Wells, 1954)(Wells *et al.*, 1943)(Lothenbach *et al.*, 2012)in (Dilnesa *et al.*, 2014)). The TG test results performed by Dilnesa(Dilnesa *et al.*, 2014) under a heating rate of 20K/min was shown in fig.1.3.

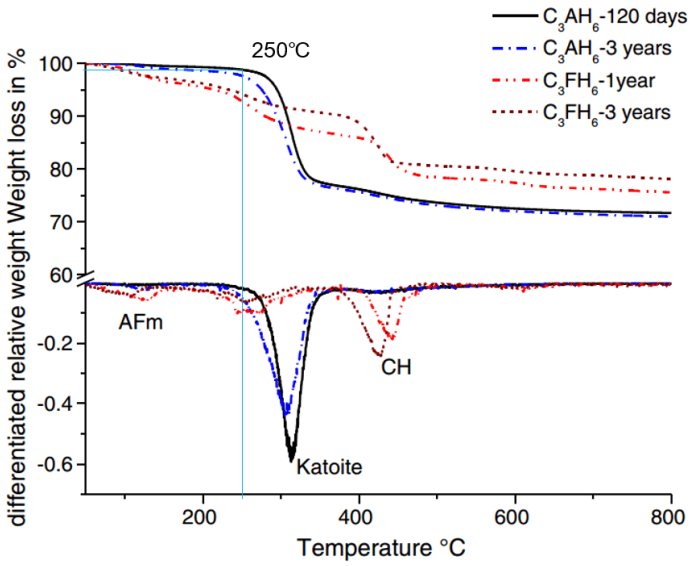

Figure 1.3: Thermal analysis(TGA and DTG) of C_3AH_6 and C_3AH_6 synthesized at 20°C and sampled after different equilibration times(Dilnesa *et al.*, 2014)

When temperature was elevated to 250°C, the mass loss was only around 2%, and the peak of DTG test appeared when then temperatrure was slightly over 300°C. However, in the TG test results from Rivas-Mercury(Rivas-Mercury *et al.*, 2008)(see fig.1.4), in which the heating rate was 2K/min, the peak of the DTG test appeared at 261°C. The difference between the two tests is probably due to the effect of heating rate on the result of TGA test. The effect will be discussed in section.1.2.1.

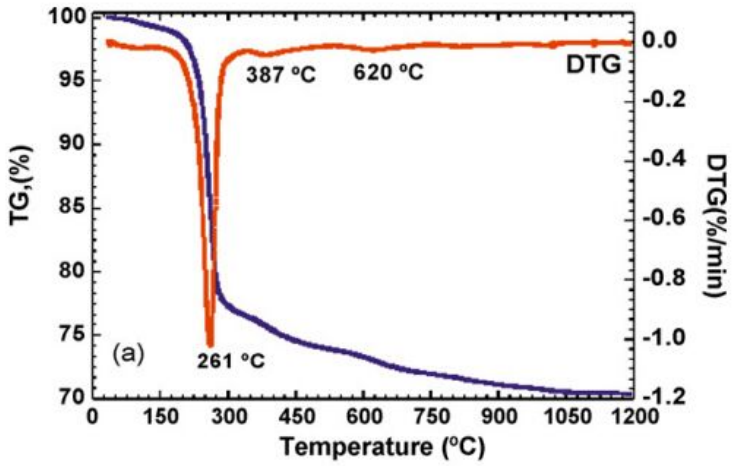

Figure 1.4: TG/DTG experiment by Mercury(Rivas-Mercury *et al.*, 2008)

- Monosulfate($C_4A\bar{S}H_{12}$)
  Monosulfates have lamellar structures, in which there are main layers $[Ca_2Al(OH)_6]^+$ and interlayers $[X\cdot nH_2O]^-$(Ahmed and Taylor, 1967)(Allmann, 1977), where X equals an exchangeable singly charged (e.g. chloride) or half of a doubly charged anion (e.g. sulfate, carbonate and aluminosilicate(Mesbah *et al.*, 2012))(Matschei *et al.*, 2007a). The SEM investigation shows the typical platy, hexagonal shape of the monosulfate $3CaO \cdot Al_2O_3 \cdot CaSO_4 \cdot 12H_2O$(See fig.1.5)(Leisinger *et al.*, 2012), of which the shape of the crystal is similar to other lamellar phases in the whole group.
  It was reported that in the TGA test, the mass loss before 260°C was due to the loss of the interlayer water, and the mainlayer will not dehydrate until the temperature reaches around 290°C(Dilnesa *et al.*, 2012)(Pan Guoyao, 1997)(Leisinger *et al.*, 2012).

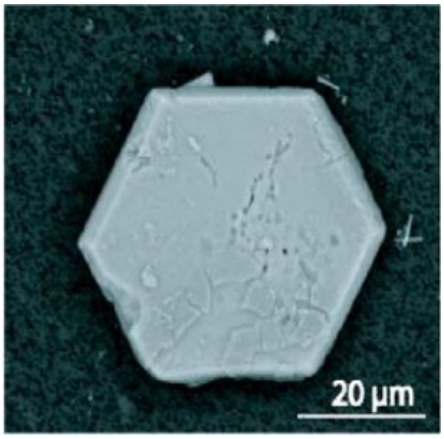

Figure 1.5: The structure of $3CaO{\cdot}Al_2O_3{\cdot}CaSO_4{\cdot}12H_2O$ by SEM(Leisinger *et al.*, 2012)

- Calcium silicate hydrate(C-S-H)
  C-S-H is a generic name for amorphous and/or poorly crystalized calcium silicate hydrates(Taylor, 1990). In the beginning of the study on the structure of C-S-H, some models containing the monomeric units were taken into account.(Bernal, 1952)(Shpynova *et al.*, 1967). However, there is a common defect of this kind of model, which is that they are not consistent with the experimental observations(Richardson, 2004). Since the structure of the dreierkette-based model has a great deal of similarity to some mineral crystals, some of them are used as references for the

description of the structure of C-S-H, of which the 1.4nm Tobermorite and Jennite were mostly used(Richardson, 2004)(Taylor, 1993)(Chen *et al.*, 2004)(Nonat, 2004) (Richardson, 2008)(Richardson and Groves, 1993b)(Jennings, 2008).

The stoichiometry of C-S-H was difficult to determine because of its structural complexity. Usually it was expressed as C_mSH_n, where m is the Ca/Si ratio and n is the H/S ratio.

- **Ca/Si ratio**

  Taylor and Howison(Taylor and Howison, 1956) suggested that $m > 0.83$, which is the value of Ca/Si of Tobermorite with an infinite chain length(Megaw and Kelsey, 1956). Kurczyk(Kurczyk, 1962) suggested m was between 1.8-1.92, which was close to recent experimental results(Young and Hansen, 1986)(Taylor, 1990). However, the interpretation to the structure was not compatible with the experimental observation.

  Richardson and Grove proposed a generalized model including formations that could represent the two structural viewpoints they proposed, which are tobermorite/calcium dioxide (T/CH) and tobermorite/jennite (T/J).(Richardson and Groves, 1993a)(Richardson and Groves, 1992)(Richardson, 2004) (Richardson, 2008).

  The basic assumption of their model is that the structure of C-S-H consists of isolated silicate chains of varying length and with a variable number of silanols, together with $Ca(OH)_2$ in the solid solution. And based on the experimentally observed chain length $(3n-1)$, the formulation is written as

$$Ca_xH_{(6n-2x)}Si_{3n-1}O_{(9n-2)} \cdot Ca(OH)_2 \cdot mH_2O \tag{1.10}$$

  or an alternative formula

$$\left\{Ca_{2n}H_wSi_{3n-1}O_{(9n-2)}\right\} \cdot (OH)_{w+n(y-2)} \cdot Ca_{n-y/2} \cdot mH_2O \tag{1.11}$$

  Where w is the number of silanol groups, and w/n represents the degree of the protonation of the silicate chains. The values of the variables in formula1.11 are required to maintain the layer structure and charge balance. Hence, the limits for them are:

$$\begin{cases} 0 \leq y \leq 2 & n(2-y) \leq w \leq 2n \\ 2 \leq y \leq 4 & 0 \leq w \leq 2n \\ 4 \leq y \leq 6 & 0 \leq w \leq n(6-y) \end{cases} \tag{1.12}$$

And the Ca/Si ratio of the C-S-H follows:

$$\mathrm{Ca/Si} = \frac{n(4+y)}{2(3n-1)} \tag{1.13}$$

From the T/CH point of view, the Ca in the braces $\{\mathrm{Ca}_{2n}\mathrm{H}_w\mathrm{Si}_{3n-1}\mathrm{O}_{(9n-2)}\}$ are the Ca^{2+} in the main layers and $(n-w/2)$ of the $n \cdot y/2$Ca outside the braces are Ca^{2+} in interlayers required for the charge balance, and the rest of the Ca^{2+} of the $n \cdot y/2$Ca outside the braces occur in the layers of CH sandwiched between silicate chains. And in the T/J viewpoint, the rest of the Ca^{2+} is the part of the structural unit in the form of Si-O-Ca-OH.

In the previous models, one obvious defect of some of them is the prediction of the Ca/Si ratio, which is not consistent to the experimental observation. And Richardson(Richardson, 2004) suggested 4 reasons for the fluctuation of the Ca/Si ratio of the C-S-H:

(1) The omission of the tetrahedral, which leads to the change of the chain length of C-S-H, could increase the Ca/Si to 1.25.

(2) Increased content of Ca^{2+} ions balanced by a reduction in silanol groups, which could increase the Ca/Si ratio to 1.5.

(3) Decreased content of Ca^{2+} ions balanced by an increase in silanol groups, which could reduce the Ca/Si ratio.

(4) Incorporation of additional Ca^{2+} ions balanced by additional $(OH)^-$ ions, which could increase the Ca/Si ratio to 2.5 theoretically.

Those four points illustrated the capability of Richadson's model in explaining the experimentally observed Ca/Si, which ranges from 0.7 to 2.3(Richardson, 1999) with an average of 1.75(Richardson, 1999)(Clayden *et al.*, 1984)(SUEUR, 1984)(Taylor and Newbury, 1984)(Richardson and Groves, 1993b)(Richardson, 2000).

Cong and kirkpartirk developed a model based on the tobermorite-like structural unit, which introduced 'defects' into their model. But

their model is not essentially different from Richardson's model and could be written in the form of Richardson's formula for C-S-H stoichiometrically(Richardson, 2004).
Besides, some models from other researchers, like Nonat(Nonat and Lecoq, 1998) and chen et al.(Chen *et al.*, 2004) could also be interpreted by the model of Richardson's.
In Nonat's model(Nonat and Lecoq, 1998) ,two hypothesis were made: 1) the basic tobermorite unit is the same with the unit structure in Richardson's model($y = 2, w/n = 0$); 2) OH^- and Ca^{2+} are in the interlayers of the C-S-H. And in Chen's model(Chen *et al.*, 2004), the unit structure is the same with Nonat's and Richardson's model($y = 2, w/n = 0$).
From previous discussion, the flexibility of Richardson's model is obvious. Besides, according to some other researches, it showed that:

(1) Only in very fine scale(about 100nm), compositional heterogeneous could be shown in C-S-H(Richardson and Groves, 1993b)(Richardson, 2000).

(2) The C-S-H will become more homogeneous compositionally with aging and mean Ca/Si ratio does not vary with age(Richardson, 2000).

Hence, for hardened cements after a relatively long aging, in a scale of more than 100nm, could be compositionally considered as homogenous and the mean Ca/Si ratio 1.75 could be adopted in the presence of CH.

– **H/S ratio**

In Richardson's study(Richardson, 2004), a H/S ratio 1.4 from P.Yu et al.(Yu and Kirkpatrick, 1999) was adopted. In(Buffo-Lacarrière *et al.*, 2012)(Sellier *et al.*, 2011), L. Buffo-Lacarrière and A. Sellier adopted the value concluded by Brouwer(Brouwers, 2004) for Portland cement and modified the formula to be adapted to the slag blended cements. Brouwer proposed that the H/S ratio is related to the Ca/Si. In that model, he proposed that based on the assumption that there is always a difference of 2H between the C-S-

H under P-dried state and the saturated state, the formula of C-S-H should be written as $C_xSH_{x+1.5-y}$, where x is the Ca/Si ratio and $-2 \leq y \leq 0$ depending on the degree of saturation(e.g. when $RH = 80\%, y = -0.7$). Taking $x = 1.75$, C-S-H could be written as $C_{1.75}SH_{3.25}$ when saturated. It is consistent with the results found by Fuji and Kondo(Fujii and Kondo, 1981)(Fujii and Kondo, 1983) and Taylor(Taylor, 1984), and followed the trend discovered by Lu et al(Lu *et al.*, 1993).
Jennings(Jennings, 2000) proposed a structural model for C-S-H and listed the different water content in C-S-H under different relative humidities. Further details will be shown in section 1.1.3.

1.1.3 Water in hardened cement paste

The dehydration process of the cement paste only considers the structural water in the paste that cannot evaporate. Mehta classified the water in hydrated cement paste according to the degree of difficulty to be removed. Besides the water vapor in the pores, there are four types of water(Mehta, 1986):

- **Capillary water.** It is the water that exists in the pores larger than about 5 nm. Capillary water is not affected by the attractive force exerted by the solid surface. He also proposed two subcategories of capillary water according to pore diameter r_ϕ. Water in larger pores (r_ϕ >50nm) is called free water because the removal of which will not significantly change the volume of the paste; water in the smaller pores(5nm>r_ϕ >50nm) is held by capillary tension, and the removal will cause shrinkage of the paste.

- **Adsorbed water**. It is the water that is adsorbed on the solid surface, which is influenced by attractive forces. A major portion of the adsorbed water can be lost when the relative humidity is less than 30%.

- **Interlayer water.** It is the water existing in the C-S-H structure. The interlayer water will lost when the relative humidity is less than 11%.

- **Chemically combined water** It is the water that is an integral part of the microstructure of hydrates. This kind of water cannot be removed by decreasing the relative humidity of the environment alone. It can be removed when the hydrates are heated and dehydration processes are

triggered. All the water in TCA and CH are considered as chemically combined water because of their good crystallinity.

The capillary water, adsorbed water and interlayer water are also called evaporable water, which cannot retain after D-drying(Powers, 1962). The non-evaporable water included the chemically bound water in the hydrates, excluding the interlayer water in C-S-H and monosulfate(Taylor, 1990).

Water in calcium silicate hydrate

Jennings(Jennings, 2004) proposed two different C-S-H by the densities of them: low density(LD) and high density(HD). LD C-S-H has surface pores which are accessible to both water and nitrogen for adsorption and inner pores which are not accessible to nitrogen while accessible to water; HD has only fewer inner pores not accessible to nitrogen. In the refined model CM-II(Jennings, 2008), Jennings refined the structure of the LD mostly. Both the LD and the HD C-S-H consist of the basic unit globule which contains the intra globular pores (IGP). Between globules there are small gel pores (SGP)(See fig.1.6),and between the globule flocs, there are large globule pores (LGP). (See fig.1.7)

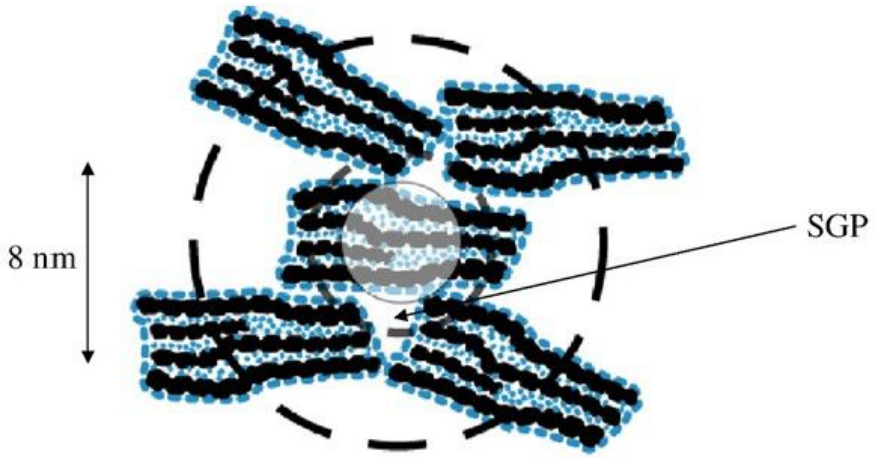

Figure 1.6: Packing of globules showing small gel pores(SPG)(Jennings, 2008).

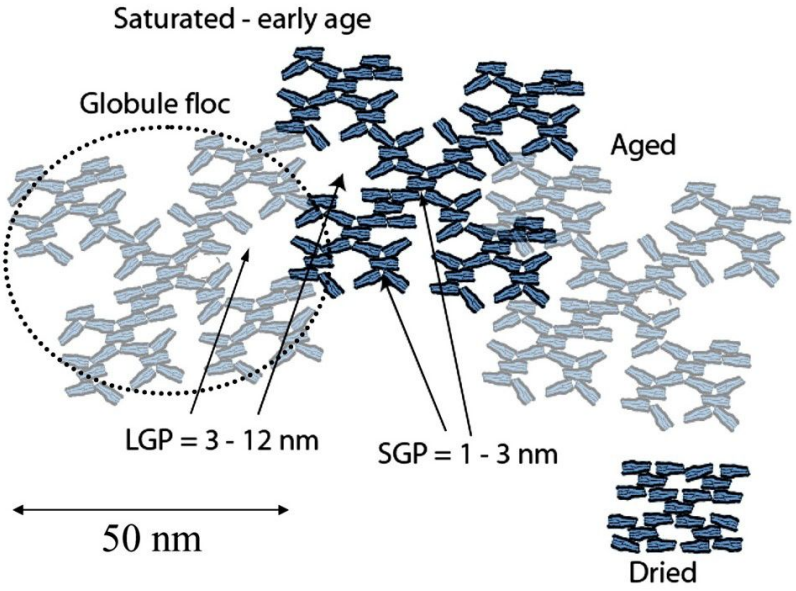

Figure 1.7: Packing of globules showing the large gel pores (LGP) and the aging process(Jennings, 2008).

The positions of water in the globule were defined as three different parts:

(1) adsorbed on the outer surface as a monolayer

(2) adsorbed within the particle, in LGP

(3) in the interlayer space

The amount of water in C-S-H varies with the relative humidity at 20°C and atmospheric pressure(Jennings, 2000):

(1) Saturated, 2.6H_2O is added to the C-S-H, which becomes $C_{1.7}SH_4$.

(2) RH=40%, 0.95H_2O is added to C-S-H, which becomes $C_{1.7}SH_{2.35}$

(3) RH=11%, 0.7H_2O is added to the C-S-H, which becomes $C_{1.7}SH_{2.1}$

(4) D-drying ,which means keeping the sample equilibrated with ice at -79°C by evacuation through a trap cooled in mixed solid CO_2 and ethanol, and the partial pressure of water is 5×10^{-4} [Torr]. the stoichiometry of the C-S-H is $C_{1.7}SH_{1.3-1.5}$

Hence, the amount of water that is affected by dehydration has a average H/S ratio of 1.4, while other water will be considered as free water and modeled with the water retention curve.

Water in monosulfate

The water in the monosulfate was usually considered as two types, which are the interlayer water and the bound water.(Dilnesa *et al.*, 2012)(Leisinger *et al.*, 2012)(Pan Guoyao, 1997). In $Ca_4Al_2(OH)_{12}SO_4 \cdot xH_2O$ $(0 \leq x \leq 6)$, x represents the amount of the interlayer water, and those two types of water have different dehydration mechanism(Leisinger *et al.*, 2012).
If the monosulfate is written as $C_4A\bar{S}H_n$, at room temperature, the water content n of the monosulfate changes with the drying condition as well. As indicated in Table1.1, the amount of interlayer water varies with drying conditions. In(Taylor, 1990), Taylor proposed that the H_2O/Ca ratio should be between 3.5-2.0 with different drying conditions. Hence, the n should be in the range of 14-8 under the drying conditions mentioned.

Table 1.1: The water content of the monosulfate

Drying condition	n		
	(Taylor, 1990)	(Leisinger *et al.*, 2012)	(Berman and Newman, 1963)
Saturated	14		
12% RH			11.83
11% RH	12		
5% RH			10.6
Silica gel		10	
CaO			8.7
D-Drying	8		

1.2 Effect of temperature on hardened cement paste properties

Under elevated temperatures, cement paste will undergo a decomposition process, most of which is the dehydration. For example, the CH will decompose, and produce CaO and H_2O when being heated to around 400°C(Sha *et al.*,

1999)(Stepkowska *et al.*, 2004), and C-S-H will lose the interlayer water and hydroxyl during the temperature arising. The dehydration will change the local pressure and the degree of saturation in the cement paste as well as the structure of the material. As explained below, these phenomena occurs during experimental characterization, such as DTG analysis or others, so the local change of pressure and RH induced by the dehydration changes the thermodynamic condition and cause a delay in the transformation which should be considered in the interpretation of tests and in the models. Now, the main experimental methods to characterize the dehydration will be presented

1.2.1 Experimental techniques

Calorimetry is the measurement of the amount of heat change which takes place in the particular thermal process(Haines, 2002)(i.e. the phase change, decomposition); The thermal analysis consists in a series of techniques, which are applied in a temperature program, for studying some properties of the sample. The common thermal and calorimetric methods are listed below in the table.1.2:

TG/TGA

As can be seen from table.1.2, the TG (or TGA) measured the mass change of the specimen during the fixed process, which is recorded as a series set of data containing the mass of the specimen, the heating time and the Temperature. It is suitable for the test of the decomposition, oxidation or the reaction and changes which are accompanied by mass change while temperature varies. Besides, some other thermal analysis techniques and combining thermal analysis methods are applied for the experiments.

DSC/DTA

Different from the TG/TGA, DSC and DTA are designed to collect the thermal information during the heating/cooling processes. DTA measures the difference of temperature between the reference and the sample, and is able to run the experiments above 1600°C; DSC is able to measure the heat change in

Table 1.2: Thermal analysis methods(Haines, 2002)

Technique	Abbreviation	property	Uses
Thermogravimetry or	TG	Mass	Decompositions
(Thermalgravimetry analysis)	TGA		Oxidations
Differential Thermal analysis	DTA	Temperature difference	Phase changes, reactions
Differential scanning calorimetry	DSC	Power difference or heat flow	Heat capacity, phase changes, reactions
Thermal mechanical analysis	TMA	Deformations	Mechanical changes
Dynamic mechanical analysis	DMA	Dimensional change Moduli	Expansion, Phase changes, glass transitions, polymer cure
Dielectric thermal analysis	DETA	Electrical	as DMA
Evolved gas analysis	EGA	Gases evolved or reacted	Decompositions
Thermoporometry		Optical	Phase changes, Surface reactions, color changes

the experiment quantitatively, and run the experiment from -150°C to 1600°C. Those techniques play an important role in the mineral and clay materials, and by DSC, measurements like heat capacity, enthalpies of transitions and transformations, purity. Chemical kinetics, vapor pressure and thermal conductivity can be done, and with HPDSC, the high pressure (about 7MPa) environment is able to be obtained.

TG-DTA& TG-DSC

TG-DTA and TG-DSC are both called the Simultaneous Thermal Analysis (STA). They run the TG and DTA/DSC experiments at the same time in the same chamber of the equipment. As mentioned above, TG is able to quantitatively measure the mass change in the process and DTA/DSC, which will not be quantitative if the process includes the mass change, is able to measure the heat flux during the process. Combining those two complementary characteristics, those two STA greatly extend the application of the thermal analysis techniques. Table.1.3 shows the processes that appreciate them. Since not all the reactions or the changes take place with change in mass, which is the limit for the TGA and DTG, DSC and DTA are always used as complements.

Effect of testing process

In order to get more reliable results from tests, some factors that could affect the results of the experiments should be paid attention to:

(1) **The size of the sample.** Sometimes the samples of relatively large size would split and little pieces from the sample may jump out of the crucible. And an unexpected temperature gradient may occur during heating/cooling the sample, which may trigger the reaction on the surface earlier than the inner part. If the sample is a complex material like concrete, fine particles may not be able to represent the whole specimen. Usually, a grinding and mix pre-process is recommended, but the grinding has a chance to change the crystalline structure.

(2) **The gas atmosphere.** Some reactions may generate gases themselves which may cause a gas pressure or a gas atmosphere other than the ambient near the surface of the sample; Different purged gas may lead to

Table 1.3: Process amenable to study by TG and DTA/DSC(Haines, 2002)

	TG effect		DTA/DSC effect	
Process	Gain	Loss	Exotherm	Endotherm
Adsorption	✓		✓	
Desorption		✓		✓
Dehydration/desolvation		✓		✓
Sublimation		✓		✓
Vaporization		✓		✓
Decomposition		✓	✓	✓
Solid-solid transition			✓	✓
Solid-gas reaction	✓	✓	✓	✓
Solid-solid reaction	Maybe	Maybe	✓	✓
Crystallization			✓	
Melting				✓
Polymerization		Maybe	✓	
Catalytic reactions	Maybe	Maybe	✓	

different result because of the reactions that may occur between the sample (or the product of former reactions) and the purge gas.

(3) **Heating rate.** At high heating rate, the recorded temperature moves to higher value while the reaction is taking place slowly. This makes the reaction temperature being overestimated for a slow reaction.
The research by Zhang Q. and Ye. G.(Zhang and Ye, 2012) indicated that the faster heating rate (up to 30K/min)led to higher reaction temperature in TG curves, the difference could be up to 100k (comparing the results between the tests with the heating rate 1k/min and 30k/min). In fig.1.8 ,the plots of normalized mass loss vs. temperatures under different heating rate can be observed, in which different differences of the mass loss among the varied heating rates could be found. In the range of below 200°C, the difference between different heating rate were smaller than in the range of 400°C -500°C, which was considered to be the range when the dehydration of the $Ca(OH)_2$ occurs. When it came to 800°C, the differences between varied heating rates declined rapidly to nearly zero, which may be attributed to the decrease of the reactant.

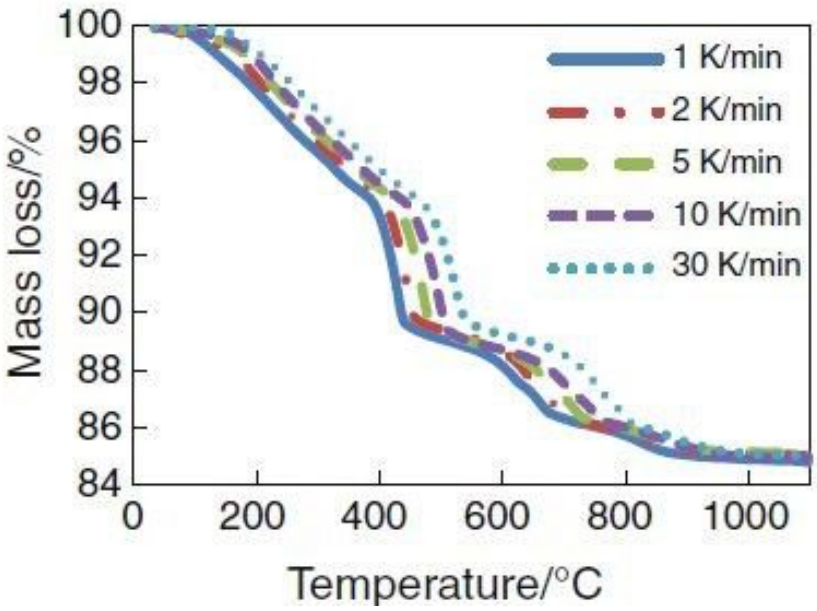

Figure 1.8: TG curves under different heating rate of OPC by Zhang(Zhang and Ye, 2012)

(4) **The redeposit.** If after the sublimation there is a cooling process(or a slight temperature drop while the system stabilizing the temperature),

the sublimation may take place and some of the deposit may be out of the crucible, which will be the cause of the miscalculation.

(5) **The techniques used for the removal of free water.** In order to analyze the dehydration of the cement pastes bulk, free water is always removed before the thermal analysis. Knapen(Knapen *et al.*, 2009) compared several methods commonly applied for the sake of it. Being dried in oven at 105°C accelerated the hydration process if the hydration is still in process, and some of the hydrates could suffer from the dehydration even in lower temperatures. Besides, carbonation can be observed during the drying process. Solvent exchange with ethanol, ether and methanol results in a strong adsorption. Interactions between the strongly absorbed solvent, which produce carbonate-like structure, take place while heating the specimen. Incomplete removal of the residual solvent should be a problem to be taken into account as well. According to his research, vacuum drying is considered the most reliable method for free water removal. The experiment performed by him(Knapen *et al.*, 2009) a vacuum of 25×10^{-2} mbar, and the extracted water was continuously collected in an ice condenser at a temperature of -62°C, corresponding to a water vapor pressure of 8×10^{-3} mbar. The content of $\mathrm{Ca(OH)_2}$ after the drying was almost the same as before, which could be an evidence for no carbonation having occurred. Plus, the result is similar to the frequently used P-drying(The sample being dried with magnesium perchlorate in a sealed system with regular evacuation, and the partial water vapor pressure is around 8×10^{-3}[Torr] in the system at room temperature)(Copeland and Bragg, 1954) and D-drying techniques.(Copeland and Hayes, 1953)

Analysis of the results

The thermal analyses of the reactions for solid phases always take up a period of temperature/time in the graph. This is because the reaction in the solid state is relatively slower than gas/liquid phase, and it takes time for the heat to transfer into the central part of the specimen as well. For this reason, some characteristic temperatures for the decomposition of the specimen have been discussed(Haines, 2002).
There are several different characteristic temperatures in the TG curve, like in fig.1.9, T_p is the peak temperature, whose position depends on the sample

size packing and heat flow properties; T_i and T_f are the initial and final temperatures of the reaction which are difficult to be determined because of the sensitivity of the balance, and the background noise generated during the experiment; T_e, which is defined as the intersection of the tangents of the initial baseline and the steepest point of the curve, is considered as a better representative for the onset of the reaction; some temperatures in the curve represent the progress of the reaction, such as $T_{0.05}$ and$T_{0.5}$, which mean the temperatures at which degrees of reactions are 0.05 and 0.5, separately.
Since the T_i is easily to be affected by impurity of the specimen and the accuracy of the instrument, T_e is always used as a substitute when the rate of the reaction is quite high in the beginning of the reaction. And for a reaction starting slowly, T_i and T_e may be quite different, so $T_{0.05}$ is usually recommended as an indicator of the onset temperature. The situation is the same with the end of the reaction.

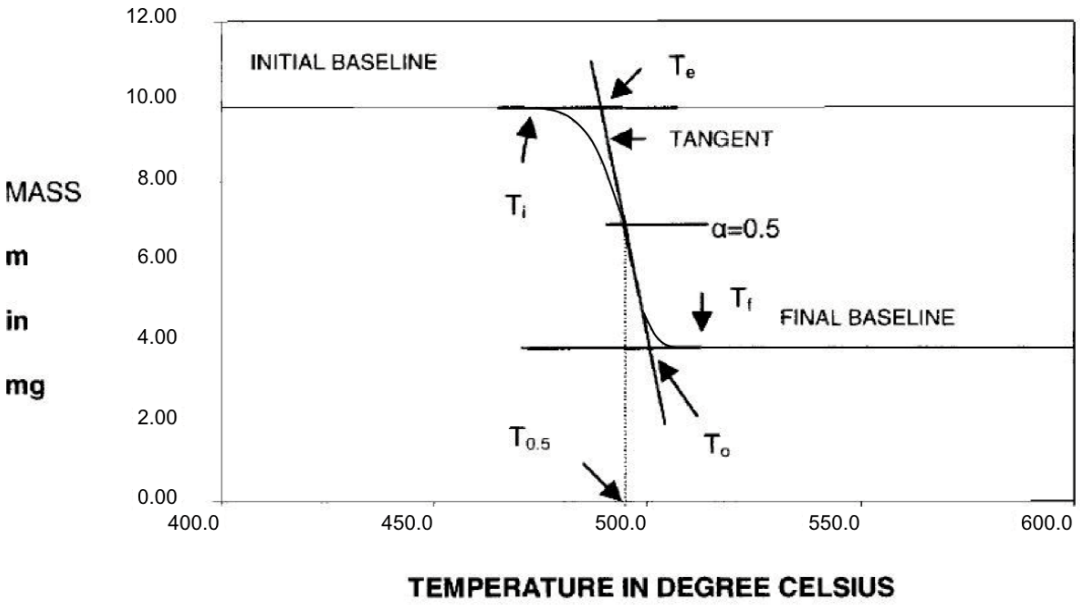

Figure 1.9: Definition of the decomposition temperature on a TG curve(Haines, 2002)

Differences between the characteristic temperatures of the beginning and the end could be calculated as the range of the reaction temperature and the difference of the ordinate axis could be calculated as the mass loss of the reaction. Then, the different pairs of data represents the mass evolution with

temperature.

1.2.2 General features concerning cement paste dehydration

One of the most efficient methods to study dehydration is the thermal analysis, and different sections of the curve reflect dehydrations of different hydrates in cement pastes. Opinions on the dehydration temperature of different hydrates have been given based on results of thermal analysis.(See. table.1.4)

Based on the assumption that the mass loss of dehydration is affected by free water, all of the models above suggested that the dehydration of cement paste without free water starts at around 100°C.

For the crystalline CH, the dehydration limited to a temperature range of 400-550°C relating to different experimental factors like heating rate and the factors illustrated above. This is because there is only one possibility of the site for the hydroxyl. Plus, In different atmosphere, different decomposition temperatures were observed, which ranged 425-500°C(Taylor, 1990), and it also reported that the crystallinity influenced the peaks in DTA test as well.(Sato *et al.*, 2007).

The dehydration of other crystalline hydrates during heating cement pastes have not been reported as much as CH. In the studies above, only R.Vedalakshimi suggested that the calcium aluminate hydrates dehydrates in the temperature range of 295-350°C(Vedalakshmi *et al.*, 2003).

For the temperature range of the dehydration of C-S-H, all the researches mentioned before suggested a onset temperature of 100°C, whilst the range of the reaction temperature varies a lot.

A decomposition of carbonate at around 700°C has been reported in(Sha *et al.*, 1999)(Vedalakshmi *et al.*, 2003)(Bhatty, 1991), together with the report by E.T. Stepkowska(Stepkowska *et al.*, 2004) which suggested a formation temperature of carbonate. It will not introduce more water into the matrix, but ought to be taken into consideration if the pore pressure is considered as variable because the amount of the CO_2 it release brings enough fluctuation to the pore pressure.

Sha considered that only in the narrow range of 40K, the C-S-H dehydrates, which is much different from other reports. YE proposed that through the whole heating process (25-800°C), C-S-H dehydrates. He simply separated the TG curve of cement paste into two parts: one for CH, the rest of the mass loss is due to the dehydration of C-S-H, which is a very general classification because

Table 1.4: Thermal analyses performed by different researchers.

Ref.	Sha W et. al(Sha *et al.*, 1999)	Zhang and Ye(Zhang and Ye, 2012)	Stepkowska, et. al(Stepkowska *et al.*, 2004)	Vedalakshmi et. al(Vedalakshmi *et al.*, 2003)
experimental parameters	HR(Heating Rate)=10K/min, up to 1000°C	Different HR, from1K/min to 30K/min	HR=1K/min, up to 1000°C	HR=20K/min, up to 900°C
20-100°C	100-140°C, dehydration of C-S-H,one of the two peaks diminished with aging		100-130°C, the release of the absorbed water; 160-185°C, hydrate water released	100-300°C, dehydration of C-S-H and ettringite
100-200°C				
200-300°C			220-440°C, the gel water in jennite-like phase released(Taylor, 1990)(Maravelaki-Kalaitzaki *et al.*, 2003)(Mackenzie, 1970); 450-470°C, the dehydration of CH	290-350°C, the decomposition of calcium aluminate hydrate(Ubbrı aco and Calabrese, 1998);around 350°C, the formation of Fe_2O_3 solution(Monzó *et al.*, 2001);450-501°C, dehydration of CH
300-400°C				
400-500°C	450-550°C, dehydration of CH	450-550°C, dehydration of CH(onset temperature varies with the heating rate)		
500-600°C			500-700°C, the further of dehydration and formation of $CaCO_3$;680-770°C, decomposition of $CaCO_3$	
600-700°C	650-750°C, decarbonation of $CaCO_3$ or other solid-solid reaction(Bhatty, 1991)			
700-800°C				

the dehydration of other hydrates was considered as part of C-S-H dehydration. When the composition of hydrates varies, the parameters to calculate the C-S-H dehydration ought to be re-fitted. Stepkowska did not specifically pointed out the cause for the mass loss in some ranges like 160-185°C and 500-700°C, but she agreed that in the range from 220°C to 440°C, the jennite-like structure, which could be the structural unit of C-S-H, dehydrates(Taylor, 1990)(Maravelaki-Kalaitzaki *et al.*, 2003)(Mackenzie, 1970). R.Vedalakshimi agreed with Lea that the mass loss of cement paste in the range of 100-300°C is due to the dehydration of C-S-H and ettringite(Lea, 1970). However, the dehydration of ettringite could happen below the temperature of 100°C according to (Zhou and Glasser, 2001)(Zhou *et al.*, 2004)(Pourchez *et al.*, 2006).
In the rest of this section, effect of temperature on each main hydrate in cement paste will be introduced.

1.2.3 Effect of temperature on CH

It has been reported that dehydration of portlandite takes place in the temperature range approximately 400-600°C(Vedalakshmi *et al.*, 2003; Sha *et al.*, 1999; Stepkowska *et al.*, 2004; Zhang and Ye, 2012), and follows the reaction:

$$\mathrm{Ca(OH)_2} \rightleftharpoons \mathrm{CaO} + \mathrm{H_2O} \tag{1.14}$$

However, few test was performed on pure CH. In (Zhang and Ye, 2012), the TG curve of CH was separated from the TG curve of cement pastes with a graphic method, which was illustrated in fig.1.10. The large peak in the DTG curve around 400°was considered as a result of the dehydration of CH. Hence, the temperatures where the peak started and ended were considered as the onset temperature and the offset temperature of the dehydration of CH, and the difference between the two tangents at onset and offset temperatures on the TG curve were considered as the mass loss due to the dehydration of CH.

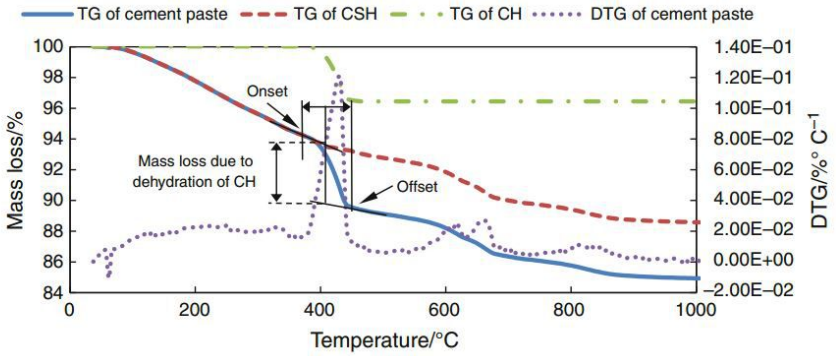

Figure 1.10: The separation of CH from the TG curve of cement paste(Zhang and Ye, 2012)

With that method, the TG curve of CH under different heating rates was shown in fig.1.11

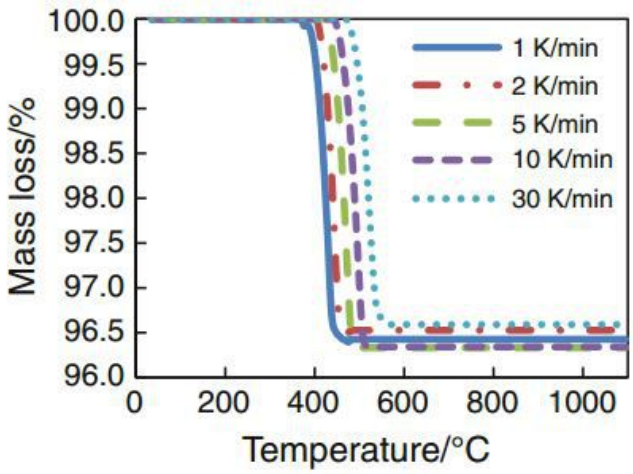

Figure 1.11: The TG curve of CH under different heating rate separated from TG curves of cement pastes(Zhang and Ye, 2012)

which showed that under different heating rates, the dehydration process of CH started at the same temperature but ended at different temperature. Similar result was found by Zelić(Jelica Zelic and Jozic, 2007) using TGA test with pure CH(see fig.1.12). The onset temperature of the reaction could be considered as the same for different heating rates, and samples under higher heating rates had larger temperature range during dehydration. Zelić also performed the TGA test with the cement pastes under the same heating condition with the pure CH. However, for the CH in the cement paste(see fig.1.13), the phenomenon observed was not the same with the pure ones. The onset

temperature was higher than the pure CH and the onset temperature became higher with the increase of the heating rate. Hence, when calculating the dehydration of cement pastes, the onset temperature of the dehydration of CH should be set higher than that of pure CH. The difference between the pure CH and the CH in the cement paste was probably due to both the less crystallinity of the CH in the cement paste and the influence of other hydrates.

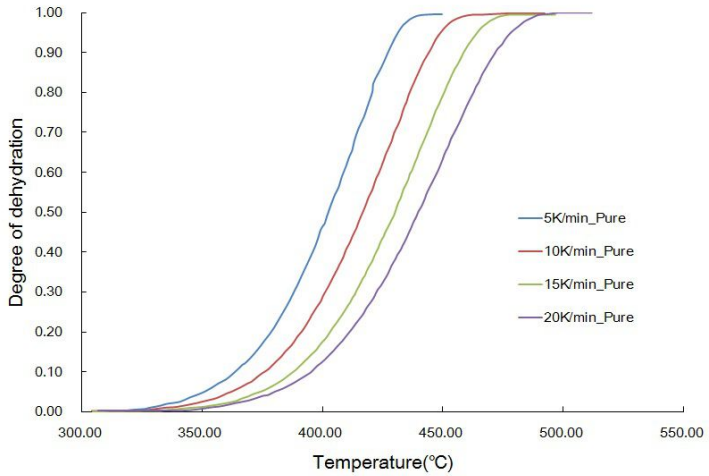

Figure 1.12: The TG curve of CH under different heating rates(Jelica Zelic and Jozic, 2007)

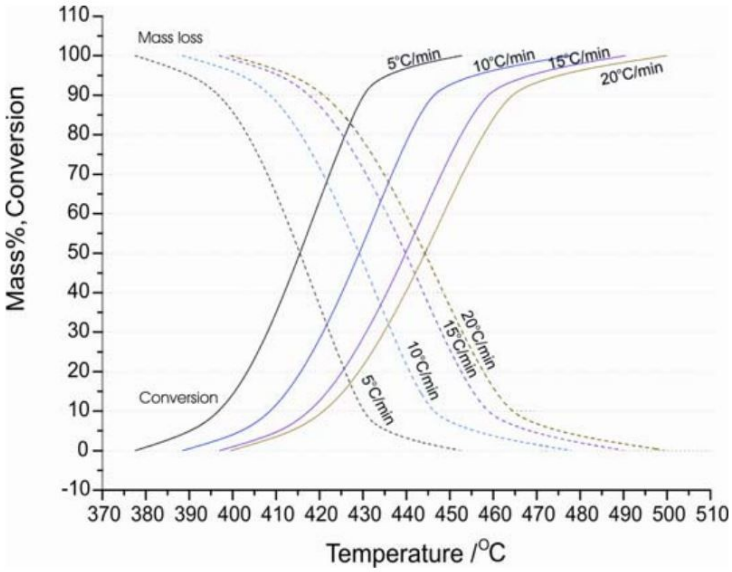

Figure 1.13: The dehydration process of CH in the cement paste(Jelica Zelic and Jozic, 2007)

1.2.4 Effect of temperature on C_3AH_6

J.M. Rivas-Mercury(Rivas-Mercury *et al.*, 2008) synthesized the crystal and performed thermal analysis under a heating rate of 2°C/min.(See fig.1.4)

From fig.1.4, it can be noticed that tricalcium aluminate hexahydrate(C_3AH_6) lost most of the water above 200°C. Horváth proposed that the dehydroxylation of C_3AH_6 occurs in the temperature range 260-400°C, and the activation energy of the reaction is 85.4kJ/mol(Horváth *et al.*, 1977). S.K.Das reported that the peak of the DSC test in the process of dehydration occurred at 310°C and the activation energy was found 35.58kJ/mol(Das *et al.*, 1996). Rivas-Mercury performed the TG test and neutron thermodiffractometry and was convinced that the whole process of the dehydration consists two stages(Rivas-Mercury *et al.*, 2008). Still, most of the mass loss took place in the temperature range 200-300°C (around 80%). It was mentioned that the TG test might be influenced by the presence of $Ca(OH)_2$ introduced during the sample preparation. Besides, comparing with the experimental results mentioned above, the mass loss before 200°C was probably not due to dehydration of C_3AH_6. Hence, the simplification was made that the dehydration of the C_3AH_6 starts from 200°C, and in fig.1.4, only the mass loss between 200°C and 300°C was corresponding to the dehydration of calcium aluminate.

1.2.5 Effect of temperature on Monosulfate

A typical dehydration curve for monosulfate is presented as follows(Taylor, 1990): From which it should be noticed that the TG curve of monosulfate could be separated into several parts. Leisinger performed thermal analysis on synthesized monosulfate as well, and the result was shown in fig.1.15.

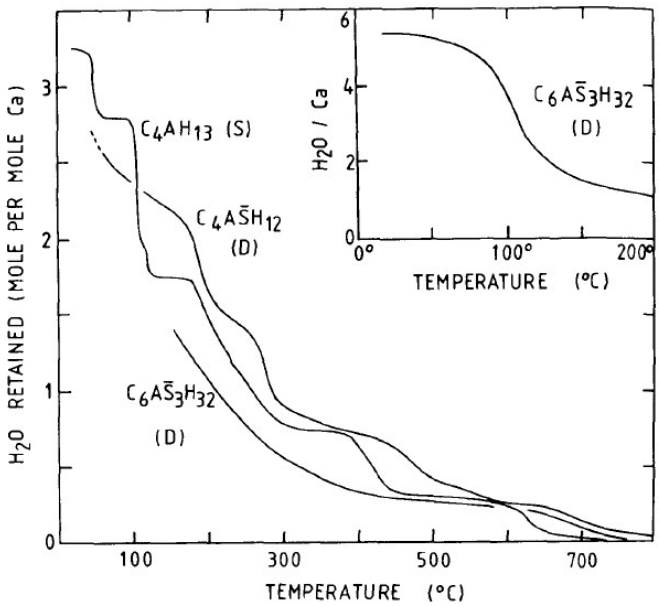

Figure 1.14: Typical TG curve of monosulfate(Taylor, 1990)

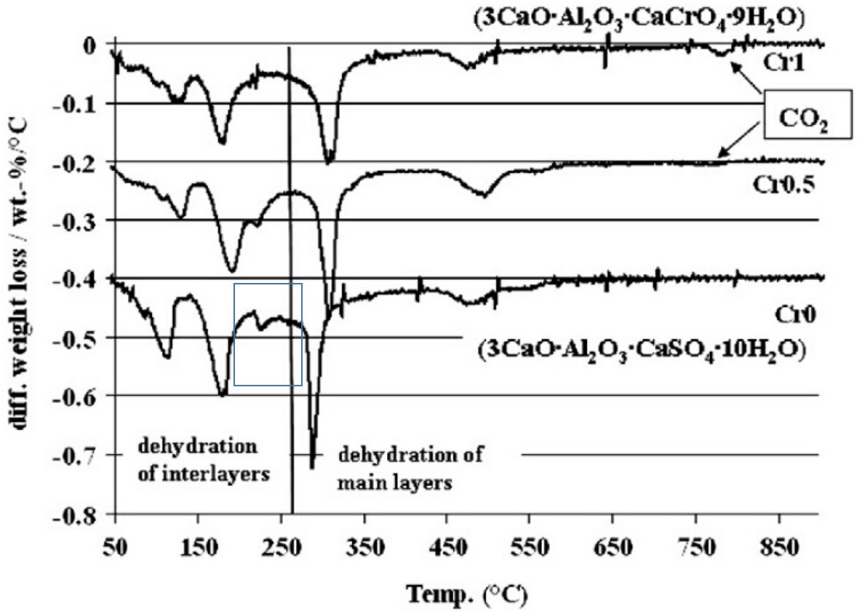

Figure 1.15: The DTGA of the dehydration of monosulfate(Cr0)(Leisinger *et al.*, 2012)

It can be noticed that the dehydration occurred mainly before 350°C, and there was a significant peak in the DTG curve around 300°C. Leisinger (Leisinger *et al.*, 2012) suggested that the dehydration before 250°C causes the mass loss of water in interlayer, while the mainlayer will lose water when temperature is

higher than 250°C. In the DTG test result performed by Dilnesa(Dilnesa *et al.*, 2012) and Pan(Pan Guoyao, 1997), there was also a similar peak in the DTG curve(see fig.1.16and fig.1.17), which could be a support to the proposal. Thus, while modeling the monosulfate dehydration, the model could be separated into two parts for the simplification without losing too much accuracy.

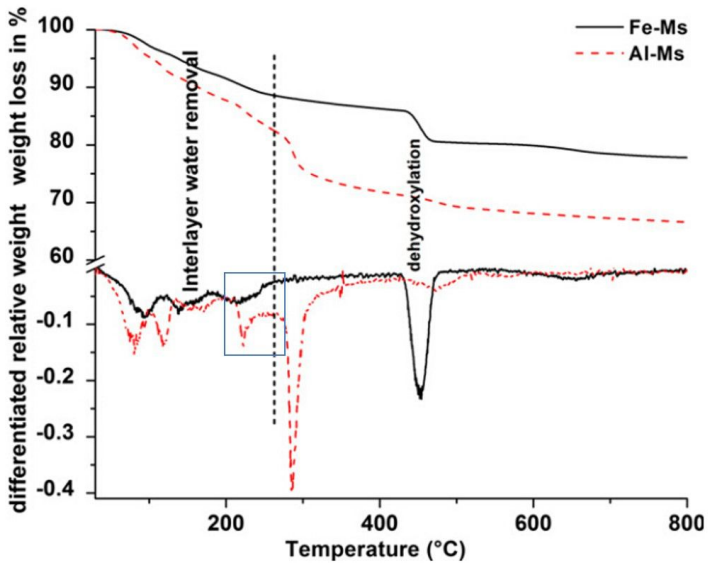

Figure 1.16: Thermal analysis (TGA and DTG) of monosuflate(Dilnesa *et al.*, 2012)

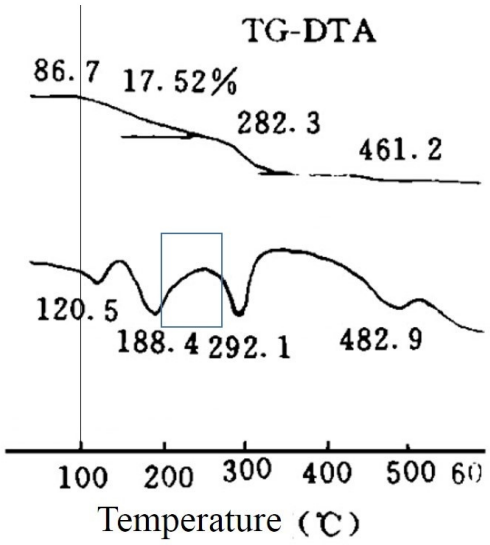

Figure 1.17: TG-DTA of monosulfate(Pan Guoyao, 1997)

1.2.6 Effect of temperature on C-S-H

Some researches on the dehydration of the specific hydrates in cement pastes have been reported. Considering that considerable C-S-H models have been built on the tobermorite-like and jennite-like unit, the dehydration of tobermorite and jennite are shown below.

- Tobermorite: 73% (9%w.t.) of the total stoichiometric amounts of water lost in the range of 50-250°C, and the weight loss continued until 750°C, when all the rest of the stoichiometry water(27%, 3.2%w.t.) had gone.(Pourchez *et al.*, 2006) The experiment performed by P. Yu and R.J. Kirkpatrick showed the similar shape of the TG/DSC curve(Yu and Kirkpatrick, 1999), which pointed out that at around 90°C, 200°C and 260°C, the tobermorite started transformations to 1.18nm, 1.1nm and 0.96nm tobermorite. Considering that the heating rate (25°C/min) was so high, the experimental results he obtained showed higher reacting temperatures than others (i.e., report by Farmer et al.(Farmer *et al.*, 1966))

- Jennite: According to the experiment performed by P. Yu and R.J. Kirkpatrick, the weight loss started at about 130°C may be attributed to the dehydration of metajennite, which continued until 360°C. From 360°C to 460°C, the weight loss and the broad endotherm peak corresponded to the transformation to disordered phase.

However, for the poorly crystalline or amorphous C-S-H, it is difficult to determine the dehydration curve in the thermal analysis graph from the real structure of the C-S-H because of the complexity of its structure like stated before. Fig.1.18 showed a thermal analysis results from of a synthesized C-S-H(Foley *et al.*, 2012). As mentioned in section 1.1.2, there is still some interlayer water in C-S-H after 11%RH drying, so the sample lost more water than that after d-drying since all the water in the sample after d-drying is chemically combined water. It should be noted that the Ca/Si ratio of the specimen(Ca/Si = 1.5) was different from the one that can be adopted for C-S-H issued from Portland cement hydration(Ca/Si = 1.75).

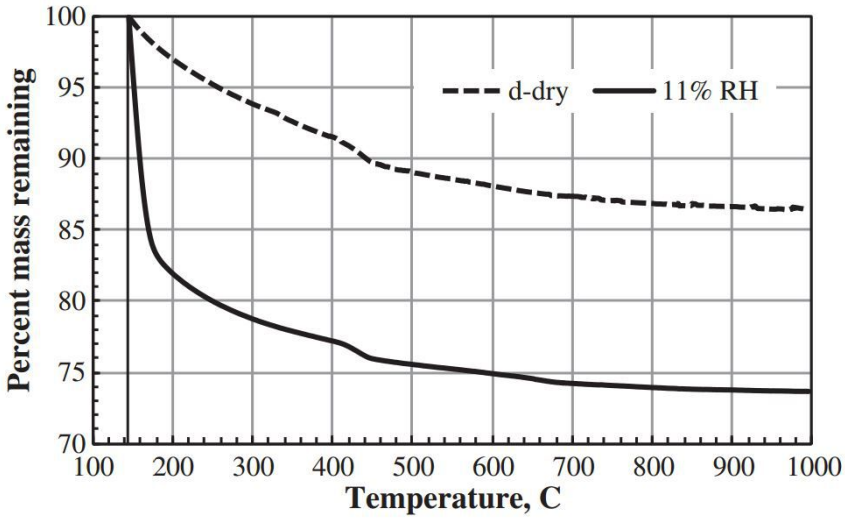

Figure 1.18: TGA curves for C-S-H after d-drying and drying under 11% RH(Foley *et al.*, 2012)

1.3 Modeling of cement hydrate dehydration

To model the water and heat transfer in cement-based material, it is important to calculate both the change of the water content and the local pressure of the matrix. During the dehydration of cement paste, the hydrates release water and bring more water into the matrix to influence the water content in the cement paste. Besides, the pressure will be influenced because of the change of saturation, which may lead to damage to the micro-structure. And all above will change the transfer properties of heat and water, together with the physical properties of the bulk varying. Hence, the dehydration of cement paste should be paid considerable attention to.

1.3.1 linear evolution according to temperature

In many researches, linear functions were used to describe the dehydration process.(Bary *et al.*, 2008)(Bary *et al.*, 2012)(Ranc *et al.*, 2003). In (Bary *et al.*, 2008), a linear function describing the released water due to dehydration of the cement paste in the concrete was adopted(equation.1.15):

$$w_{dehydr}^{concrete} = (0.39(T-60)+1.72)H(T-60) \quad [\mathrm{kg/m^3}] \tag{1.15}$$

where $H(T-60)$ is the Heaviside function, and T is the temperature in Celsius. In 2012, Bary adopted another equation(Bary *et al.*, 2012) from Ranc's work(Ranc *et al.*, 2003), which is a linear function as well:

$$w_{dehydr}^{concrete} = 0.018(T-60)H(T-60) \quad [\mathrm{kg/m^3}] \tag{1.16}$$

The parameters in equation.1.15 and equation.1.16were fitted with the experiments on tested cements, so the equations have good agreement with the experimental results in tested temperature ranges. For the examples above, equation.1.15 was adopted to calculate the water release in the temperature 60-160°C and equation.1.16 was adopted for a wider temperature range up to 200°C. However, some inevitable defects should be noticed. The first is that it is quite a simplification to consider the TG curve as a linear one, because the curvature of it varies a lot during the heating process. Besides, the rate of dehydration calculated with the linear equation will keep constant even when the temperature is quite high, when the dehydration completes, and it is not consistent with the observation. (e.g. When T=1000°C, the rate of d is still 0.39 or 0.018 considering the equation1.15, 1.16).

1.3.2 kinetic models

With their experiment of XRD on the cement paste, Ye and Zhang proposed that the main hydrates of OPC were CH and C-S-H, and the TG curve of the cement paste(see fig.1.19) could be separated in to two parts: CH and C-S-H(Zhang and Ye, 2012).

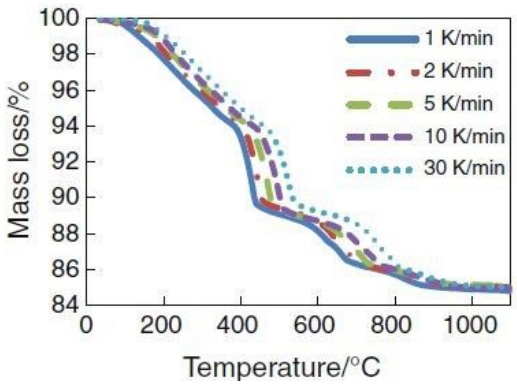

Figure 1.19: The TG curve of cement paste under different heating rates(Zhang and Ye, 2012) after being drying at 105°C

The rate of the dehydration was considered as equation.1.17

$$\frac{\mathrm{d}\xi}{\mathrm{d}t} = K(T)f(\xi) \tag{1.17}$$

Where ξ is the reaction degree, and was defined as:

$$\xi = \frac{m_i - m_0}{m_{final} - m_0} \tag{1.18}$$

with m_i, m_0, and m_{final} representing the mass during dehydration, the initial mass and the final mass after dehydration. $f(\xi) = 1 - \xi$, and the Arrhenius equation was applied to describe the influence of the temperature (equation.1.19):

$$K(T) = A_0 \exp(-E_a/RT) \tag{1.19}$$

For C-S-H, E_a and A_0 were proposed as a function of dehydration degree. while for CH, they were considered constants.
The method of Zhang has its limit that only kinetics of the dehydration was taken into consideration, regardless of the equilibrium. Hence, if the temperature rose to the middle of the whole dehydration process, the calculation of the dehydration process would not stop until the degree of dehydration reached 1 if this method was applied. For example, like what was shown in fig.1.20, the dehydration of the C-S-H was calculated by this method.

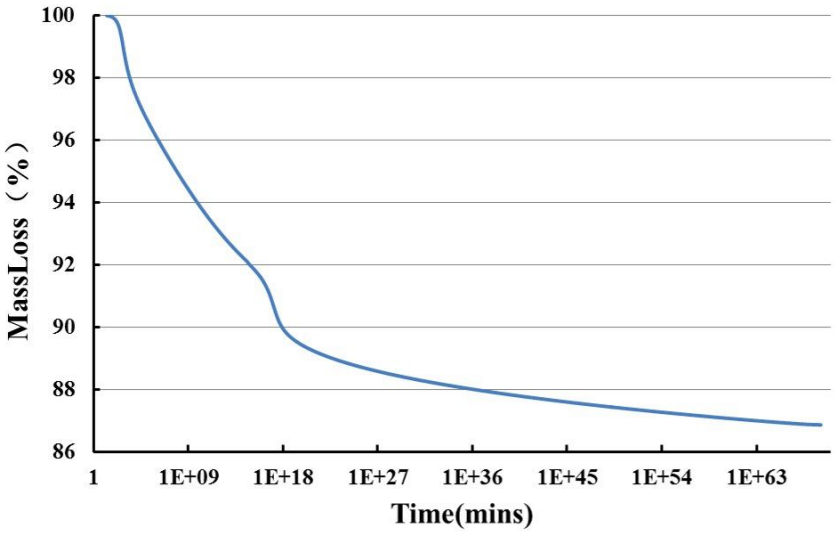

Figure 1.20: Calculation of the dehydration of C-S-H with kinetic model

It was assumed that the C-S-H dehydrate at 105°C for a long time. The water of the C-S-H will be released completely eventually. Consequently, the model from Zhang could be applied if a high temperature(>1000°C) is rapidly reached during the process.

S. Hassen's experiment(Hassen, 2011), in which at each of the four temperature levels the temperature was kept constant until the weight of the sample did not change anymore, proved that the cement paste would not lose all the water at such a low temperature as 105°C, although the equilibrium of dehydration could be reached at such a temperature.

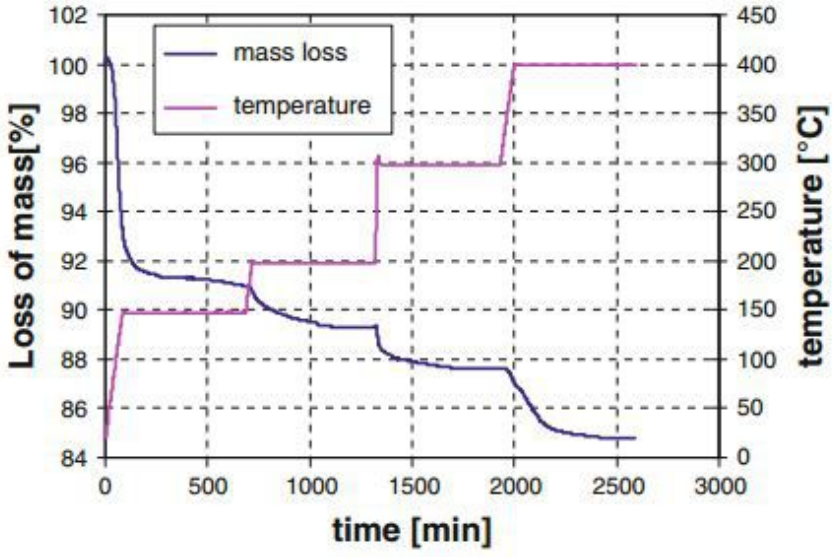

Figure 1.21: Evolution of the mass loss in function of temperature and time

1.3.3 kinetic and equilibrium models

In order to approximate the reality of the dehydration process of cement pastes, a method including both kinetic and equilibrium of the process was proposed by Feraille(Feraille Fresnet, 2000) in the form of:

$$\dot{w} = -\frac{1}{\tau}(w(T) - w_{eq}(T)) \tag{1.20}$$

where the characteristic time τ is 10800[s] for the test cement paste, and the

equilibrium mass $w_{eq}(T)$ was proposed as:

$$\begin{aligned} w_{eq}(T) = & \frac{7.5}{100} m_{eq}^{sample}(105°C)[1-\exp(-\frac{T-105}{200})]H(T-105) \\ & + \frac{2}{100} m_{eq}^{sample}(105°C)[1-\exp(-\frac{T-400}{10})]H(T-400) \\ & + \frac{1.5}{100} m_{eq}^{sample}(105°C)[1-\exp(-\frac{T-540}{5})]H(T-540) \end{aligned} \tag{1.21}$$

where $m_{eq}^{sample}(105°C)$ is the equilibrium mass of sample at 105°C, and the coefficient before that depend on the maturation of the cement paste studied. Equation 1.20 was based on the experimental result, so the accuracy for the specific material used in the experiment was quite high. However, when the equation is applied on different cement pastes, it is difficult to adapt the fitted values to another cement paste. In other words, another set of parameters will be required for the different cement paste.

1.4 Conclusion

The existing models describing the dehydration of cement pastes included:

1) linear evolution, which consider the dehydration rate as constant.

2) kinetic model, which did not consider the equilibrium during the dehydration. It will overestimate the dehydration degree when the temperature was kept lower than the onset temperature of hydrates in the cement paste.

3) kinetic and equilibrium model for specific material, which cannot be adopted for a different cement paste without refitting the parameters.

Hence, a model including both the equilibrium and the kinetic part of the dehydration process and can be applied to different cement pastes without refitting the parameters would be very interesting. Before establishing such a model, a series of dehydration tests were performed in LMDC Toulouse, in order to have a complete set of parameters available to accurately fit the model which will be proposed after.

Chapter 2

Kinetic model for cement paste dehydration

In order to calculate the dehydration process of cement pastes with different compositions of hydrates, the dehydration model considering the dehydration process of each hydrate is going to be established. The scheme to calculate the water release due to dehydration using the dehydration model is shown in fig.2.1

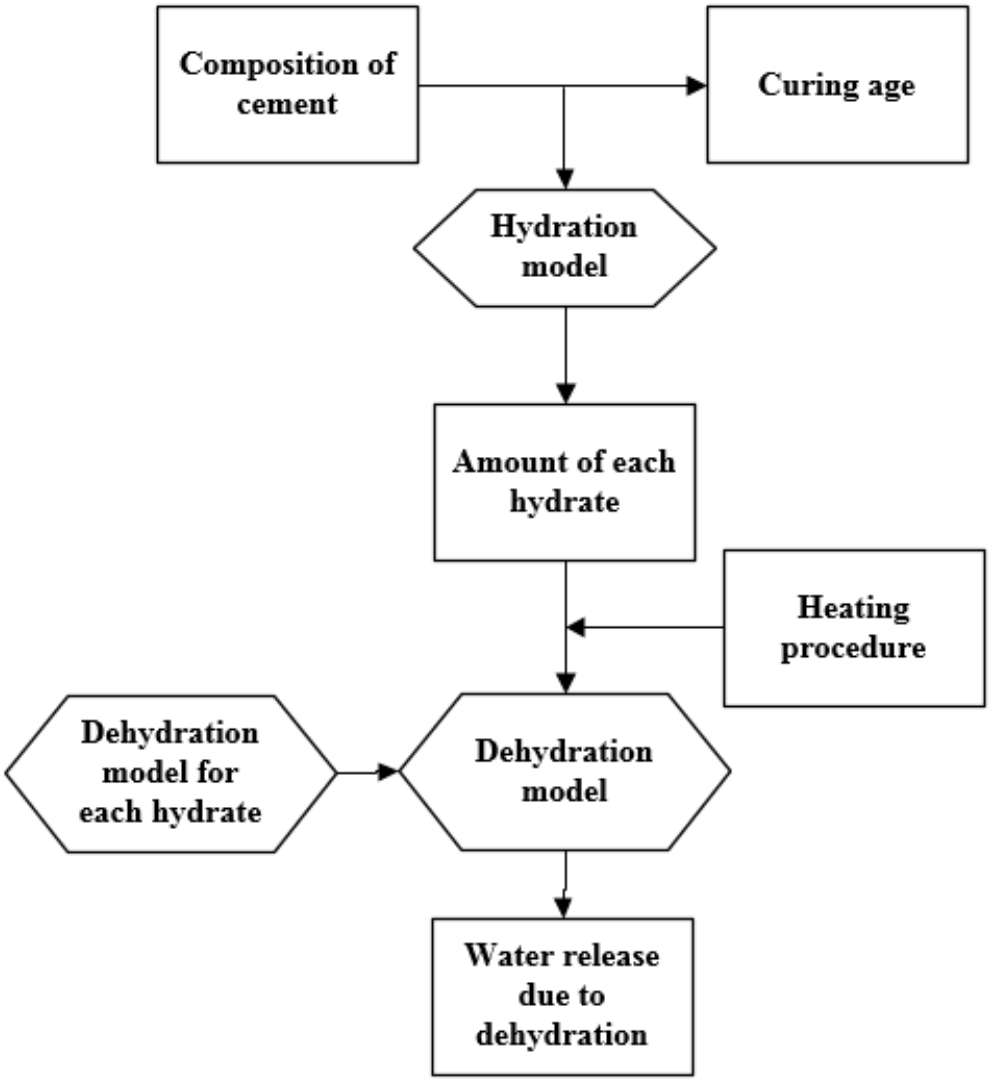

Figure 2.1: Scheme to calculate the water release due to dehydration for cement paste

2.1 General principles

The model proposed by Feraille(Feraille Fresnet, 2000) includes both equilibrium and kinetic, which is closer to the reality of the dehydration process of the cement paste than linear model and kinetic model stated in section 1.3. However, the kinetic and equilibrium model considered the cement paste, in which the content of different hydrates could vary a lot, as a whole during the dehydration process, so it is not appropriate to apply the existing dehydration models on cement pastes with different composition of hydrates without performing additional experiment under low heating rate to fit the coefficients in equation 1.21. To show the different dehydration behaviors for different cement pastes, the comparison of the TGA result between the model proposed by feraille(Feraille Fresnet, 2000) and the experiment mentioned in chapter 3 under heating rate 5K/min was shown in fig.2.2, where the sample weight at 105°C was considered as 1.

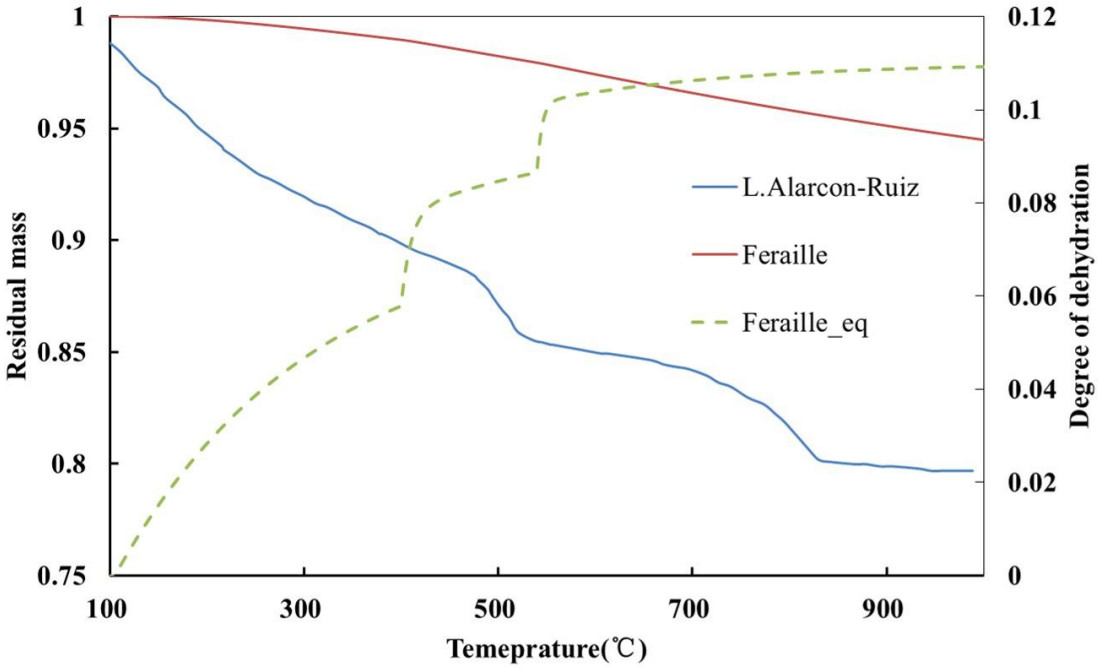

Figure 2.2: The comparison between the kinetic and equilibrium model with the TGA test from Alarcon(Alarcon-Ruiz *et al.*, 2005)

The model was built on the basis that the dehydration started at 105°C, so the TGA test performed by Alarcon(Alarcon-Ruiz *et al.*, 2005), in which the sample was kept in the oven of 105°C for 24h hours, was selected to compare with. The heating rate in the TGA test was 5K/min, and the sample weight

was between 220 and 226mg. The difference between the modeling result and the experimental result was obvious, and it is probably due to the difference in the composition of the hydrates between Alarcon's sample(Alarcon-Ruiz *et al.*, 2005) and Feraille's sample that used to establish the model(the composition of the cement and the hydration degree of the cement paste). In order to expand the use of the dehydration model, the released water of the cement paste due to the dehydration could be described as equation.2.1

$$w_{dehydr} = \sum_i w^i \tag{2.1}$$

where i represents the different hydrates: C-S-H, AFm, TCA(Tricalcium aluminate hexahydrate), CH. The water released during the dehydration of each hydrate could be expressed as a function of the dehydration degree ξ^i and the total chemically bound water w^i_{max}in the hydrate i as:

$$w^i = w^i_{max}\xi^i \tag{2.2}$$

Consequently, the mass loss rate due to dehydration $\dot{w}^i$ can be expressed as

$$w_d\dot{ehydr} = \sum_i \dot{w}^i = \sum_i w^i_{max}\dot{\xi}^i \tag{2.3}$$

The equation to calculate the rate of the dehydration should include both the equilibrium part and the kinetic part as mentioned in section 1.3. The basic idea of Feraille's model including both equilibrium and kinetics was adopted, so the equation is shown in form of a multiplication of the equilibrium part $\xi^i_{eq} - \xi^i$ and the kinetic part. Hence, the dehydration equation of each hydrate could be written as equation.2.4

$$\dot{\xi}^i = \frac{1}{\tau^i}\exp(-\frac{E^i_a}{R}(\frac{1}{T} - \frac{1}{T_{onset}}))(\xi^i_{eq} - \xi^i)H(T - T^i_{onset}) \tag{2.4}$$

Instead of considering the rate of the reaction as a constant, a modified Arrhenius expression was adopted to describe the effect of the temperature on the rate of dehydration. The first part on the right side of the equation $\frac{1}{\tau^i}\exp(-\frac{E^i_a}{R}(\frac{1}{T} - \frac{1}{T^i_{onset}}))$ is the Arrhenius expression with the onset temperature of the dehydration T^i_{onset}, and the ideal gas constant $R = 8.31[\text{J}\cdot\text{mol}^{-1}\cdot\text{K}^{-1}]$. The latter part

$(\xi_{eq}^{i} - \xi^{i})$ represents the equilibrium of hydrate i in the corresponding temperature range during the dehydration.
In numerical form, for step $n+1$,the degree of dehydration follows:

$$\xi_{n+1} = \xi_n + \dot{\xi}_n \Delta t \tag{2.5}$$

where Δt is the time step length of the calculation, and $\dot{\xi}_n$ was calculated with equation.2.4.

The initial temperature was selected to a temperature lower than the onset temperature of dehydration for each hydrate, and the initial dehydration degree $\xi_0 = 0$. The rate of dehydration varies a lot with the time of the reaction, so a varying step-length algorithm was applied to calculate the degree of dehydration. A step-control constant ϵ was introduced to control the time step length of the calculation. After each Δt, the increment of degree of dehydration could not be larger than $1/\epsilon$. The default time step length was set 1min, and $\epsilon = 5 \times 10^4$ was adopted in order to get an accurate result. The scheme of the n_{th} step of the calculation was shown in fig.2.3.

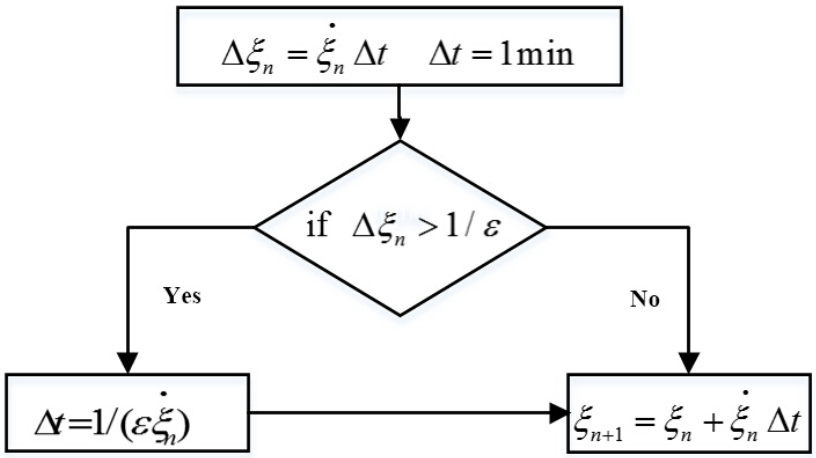

Figure 2.3: The calculation of the ξ_{n+1}

For each hydrate, it is necessary to get all the parameters to calculate the released water during dehydration process before the summation of the results. In this study, the material is the widely used ordinary Portland cement, and the main hydrates are thus CH, TCA, AFm and C-S-H.

2.2 Dehydration of hydrates

2.2.1 CH

For dehydration of CH, we assume that :

1. The onset temperature for CH dehydration T_{onset}^{CH} is constant, and it is independent from the heating rate. The onset temperature of CH dehydration was selected at 300°C according to the experimental results in fig.1.12.

2. All the -OH is able to be released at any temperature higher than the onset temperature. In other words, $\xi_{eq}^{CH} = H(T - T_{onset}^{CH})$.

To calculate the kinetics of the dehydration process, the experimental TG curve of pure CH from Zelić(See Fig.1.12)(Jelica Zelic and Jozic, 2007) was adopted because the result of pure CH could eliminate the influence of other hydration products in the cement paste.

Zelić(Jelica Zelic and Jozic, 2007) chose 4 different heating rates(5K/min, 10K/min, 15K/min, 20K/min) in the TGA test. The purpose of the modeling was to find a set of parameter to fit the *mass loss–T* curve under all the four heating rates.
For CH, equation.2.4 became:

$$\dot{\xi}^{CH} = \frac{1}{\tau^{CH}} \exp(-\frac{E_a^{CH}}{R}(\frac{1}{T} - \frac{1}{T_{onset}^{CH}}))(\xi_{eq}^{CH} - \xi^{CH})H(T - T_{onset}^{CH}) \tag{2.6}$$

The comparison between the model and the experimental results from Zelić was shown in fig.2.4. The legend 'exp 5K' means the experimental result under heating rate of 5K/min, and the legend 'fitting 5K' means the fitting result under heating rate of 5K/min.

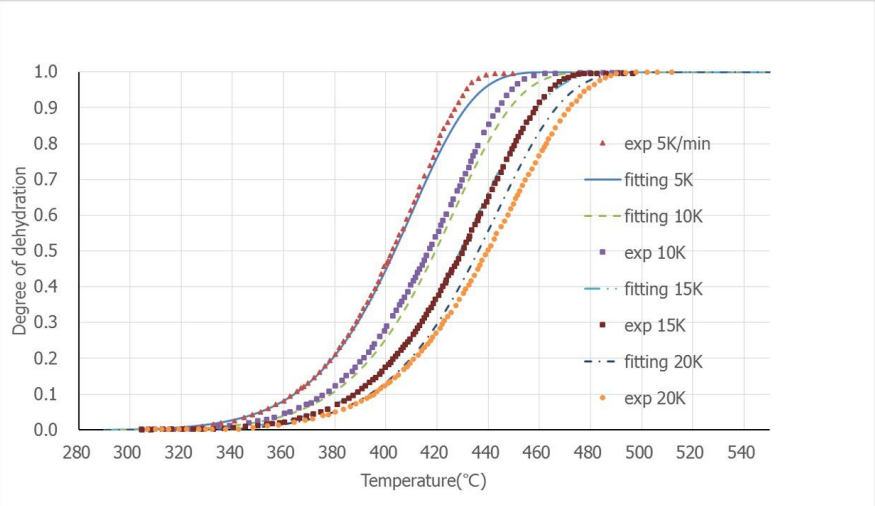

Figure 2.4: The comparison of fitting results and experimental results from Zelić(onset temperature=300°C)

The fitting result of τ^{CH} and E_a^{CH} were 6.25×10^4s and 158.53kJ/mol, respectively. Fig.2.4 presents better fit results under heating rate 5K/min, 10K/min and 15K/min. The result under heating rate 20K/min fit very well when the temperature was no higher than 400°C, but the difference between the fitting result and the experimental result was no greater than 0.1.

Validation of the model

To validate the model, the predicted result of the dehydration model of CH was compared with the result from Zhang(Zhang and Ye, 2012). The sample was made from ordinary Portland cement with W/C = 0.5. The sample was cured 28d and dried 24h at 105°C before the TGA test. As can be seen from fig.2.5, the CH curves were separated from the TG curves of cement pastes.

In the modeling results, the temperature range corresponding to the decomposition of CH was larger than that in the CH results by Zhang. It is probably because of the influence of the carbonation discovered by Morandeau(Morandeau *et al.*, 2014). In (Morandeau *et al.*, 2014), it was implied by the TG-MS experiment(fig.2.6 and fig.2.11). In fig.2.11, the partially carbonated cement paste had a small temperature corresponding to the CH dehydration. It is because of the influence of the carbonation which could occur during the grinding of the cement paste according to his research.If we observe the TG curves by Zhang in the temperature range above 600°C, the mass loss due to

carbonation could be observed. All the evidence showed that the temperature range corresponding to the dehydration of CH was shorter that it should be because of the carbonation of the samples. Hence, the modeling result fit the result of separated CH better than it seems in fig.2.5.

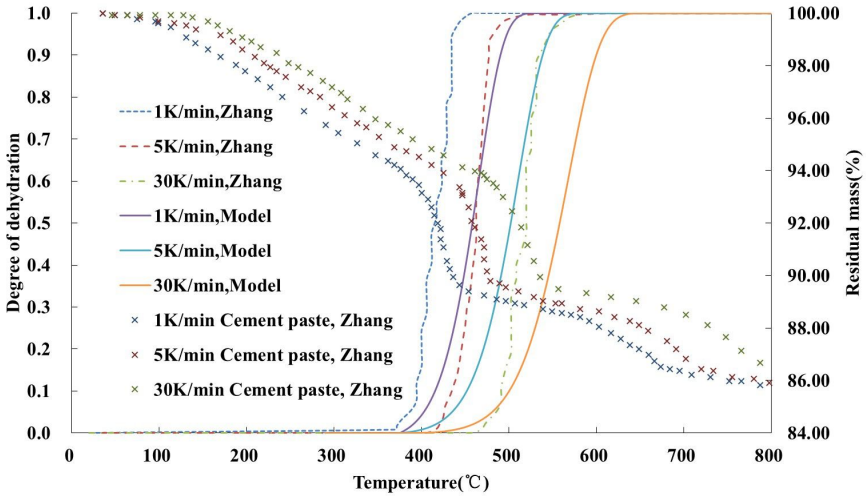

Figure 2.5: Comparison between the modeling result and the experiments by Zhang(Zhang and Ye, 2012)

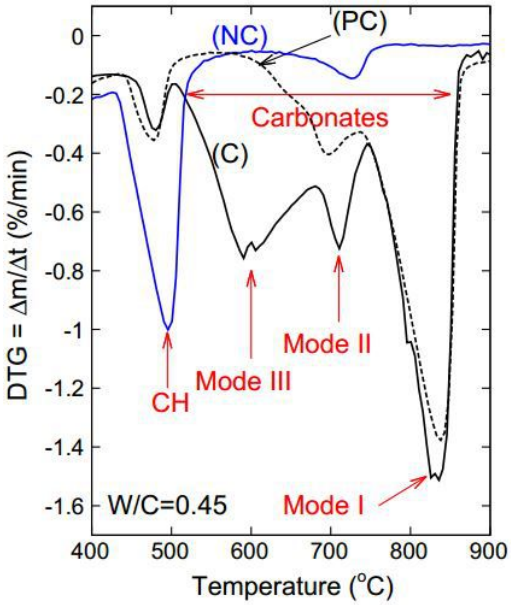

Figure 2.6: DTG results of non-carbonated(NC), partially carbonated(PC) and carbonated(C) cement pastes(Morandeau *et al.*, 2014)

Influence of the onset temperature T_{onset}^{CH}

The onset temperature used for modeling was selected graphically, so the influence of it was studied to improve the reliability of the model. Besides 300°C, 290°C, 295°C, 305°C and 310°C were tested as onset temperature of the dehydration of CH. The results were shown in fig.2.7, which illustrated that 300°C has better accuracy than other onset temperatures. Moreover, the larger the difference between the test temperature and 300°C, the greater difference between the fitting result and the experimental result would be. Hence, 300°C was selected as onset temperature of the dehydration process of the pure CH.

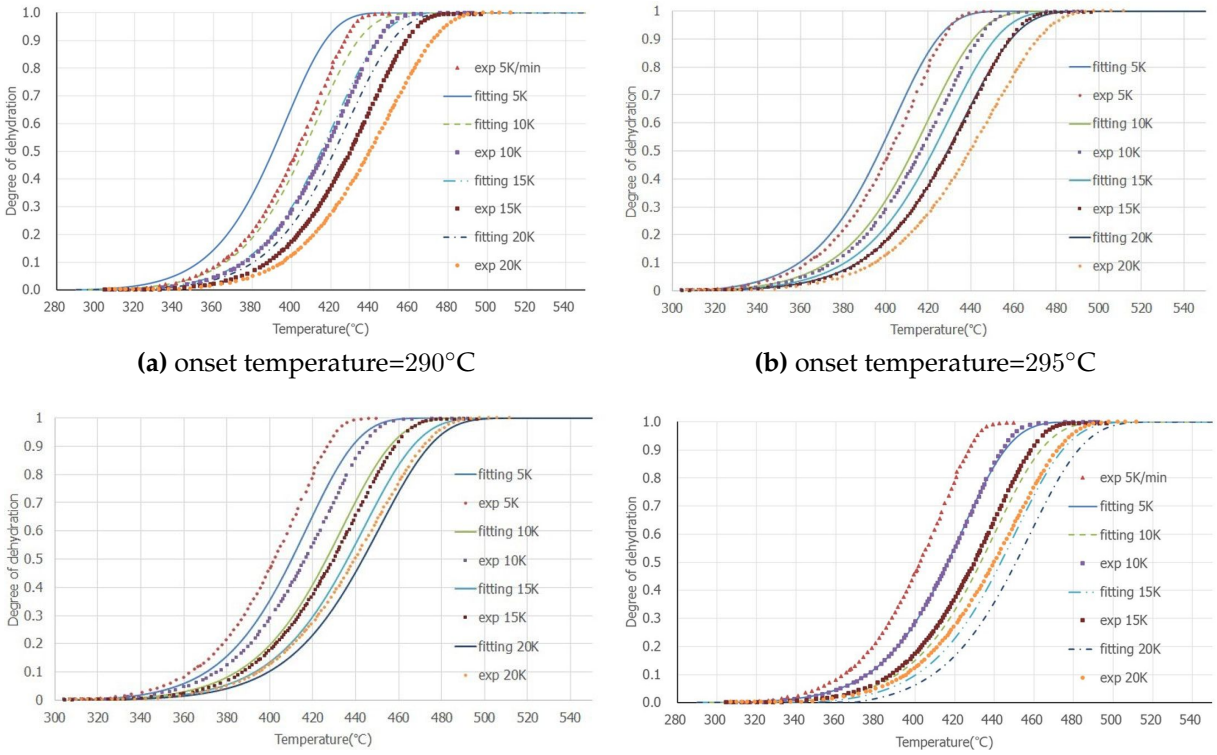

(a) onset temperature=290°C

(b) onset temperature=295°C

(c) onset temperature=305°C

(d) onset temperature=310°C

Figure 2.7: The influence of the onset temperature

The influence of activation energy E_a^{CH}

Five E_a^{CH} in the range of $0.8E_a^{CH}$ to $1.2E_a^{CH}$ were used to investigate the influence of E_a on the dehydration of CH. The interval of the E_a^{CH} was selected 10% of E_a^{CH}, and all the results were compared with TG test by Zelić(Jelica Zelic and Jozic, 2007) in fig.2.8

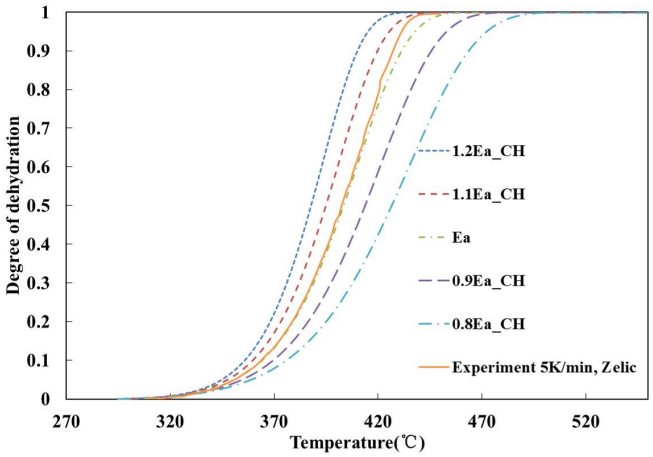

Figure 2.8: The influence of E_a^{CH} on dehydration of CH

E_a^{CH} showed obvious effect on the kinetics of CH dehydration. $T_{0.5}$ of the modeling result increased from 401°C to 425°C if E_a^{CH} increased by 20%. In addition, if E_a^{CH} decreased by 20%, $T_{0.5}$ decreased to 388°C. There were apparent difference between the results with E_a^{CH} other than 158.53kJ/mol and experimental result by Zelić under heating rate of 5K/min.

The influence of characteristic time τ^{CH}

The influence of the characteristic time of the CH dehydration was investigated by comparing the modeling results with τ^{CH} varying from 0.8 τ^{CH} to 1.2τ^{CH}. The comparison is shown in fig.2.9. The increase of the characteristic time represents the slower dehydration rate, which makes the $T_{0.5}$ shift towards higher temperature.

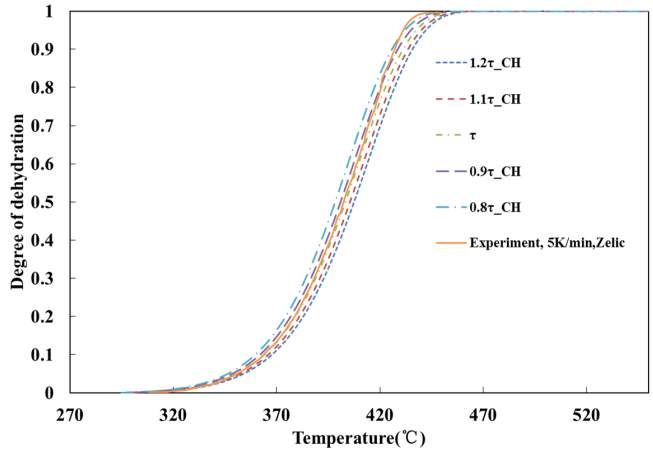

Figure 2.9: The influence of characteristic time τ^{CH} on dehydration of CH

The onset temperature of CH in cement paste

In Zelić's experiments(Jelica Zelic and Jozic, 2007), 340°C-460°C was considered as the temperature range corresponding to the dehydration of CH in cement paste(fig.1.13). As can be seen from fig.1.13, the onset temperature varies with the heating rate as well, and the onset temperature of the dehydration under the lowest heating rate could be considered around 375°C. Hence, 375°C was adopted as $T_{onset}^{CH}{}'$ in our model, and the modeling result was shown in fig.2.10.

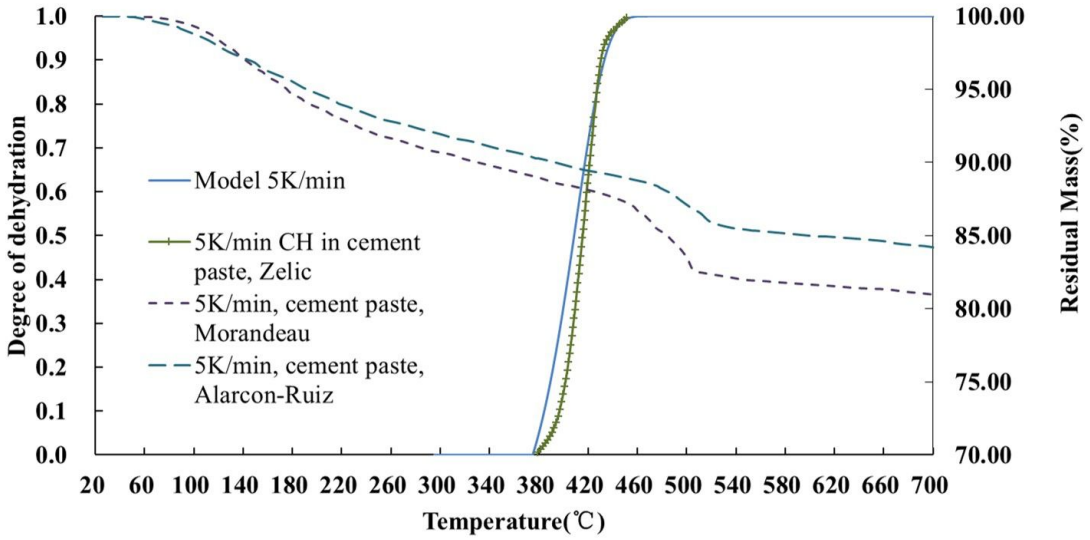

Figure 2.10: Dehydration of cement pastes and CH under heating rate of 5K/min

The modeling result showed obvious difference in kinetics from the experiment by Zelić, but showed acceptable compatibility with experimental result by Morandeau(Morandeau *et al.*, 2014), Alarcon-Ruiz(Alarcon-Ruiz *et al.*, 2005). The TG-MS experiment by Morandeau(Morandeau *et al.*, 2014)also provided evidence that the T_{onset}^{CH} should be around 375°C(fig.2.11).

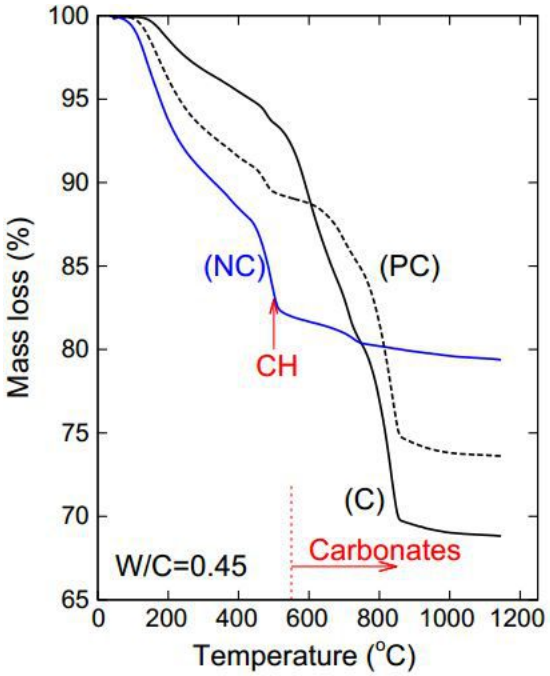

Figure 2.11: TG-MS experiment of cement paste by Morandeau(Morandeau *et al.*, 2014)

Since their has not been direct evidence showed the onset temperature of CH in cement paste, and there is obvious difference between T^{CH}_{onset} in pure CH and in cement paste, the accuracy of T^{CH}_{onset} can be investigated in the future. All the parameters for dehydration of CH are listed in table.2.1.

Table 2.1: Parameters for dehydration of CH

Hydrate	$T_{onset}(°C)$	$\xi_{eq}(H(T-T^i_{onset}))$	E_a(kJ/mol)	$\tau(10^3 s)$
CH	375	1	158.53	62.5

2.2.2 C_3AH_6

For C_3AH_6, equation.2.4 becomes:

$$\dot{\xi}^{TCA} = \frac{1}{\tau^{TCA}} \exp(-\frac{E_a^{TCA}}{R}(\frac{1}{T} - \frac{1}{T^{TCA}_{onset}}))(\xi^{TCA}_{eq} - \xi^{TCA})H(T - T^{TCA}_{onset}) \quad (2.7)$$

With the simplification proposed in section 1.2.4 that the dehydration of C_3AH_6 started at 200°C, and the assumption that the onset temperature of C_3AH_6 de-

hydration be independent of the heating rate, T_{onset}^{TCA} was set 200°C.
Considering that C_3AH_6 is crystalline, $\xi_{eq}^{TCA} = H(T - T_{onset}^{TCA})$ was adopted as the equilibrium mass of dehydration.
For the activation energy E_a^{TCA}, two values in literature mentioned in section 1.2.4 were compared. S.K. Das(Das *et al.*, 1996) suggested $E_a^{TCA} = 35.58$[kJ/mol], while Horváth(Horváth *et al.*, 1977) proposed that $E_a^{TCA} = 85.4$[kJ/mol], and the results were shown in fig.2.12b and fig.2.12a .The fitting result using the activation energy proposed by Horváth had a better fit with the experiment performed by Rivas-Mercury(Rivas-Mercury *et al.*, 2008), so $E_a^{TCA} = 85.4$[kJ/mol] was adopted as activation energy of the dehydration of C_3AH_6, and the corresponding characteristic τ^{TCA}time is 11800[s].

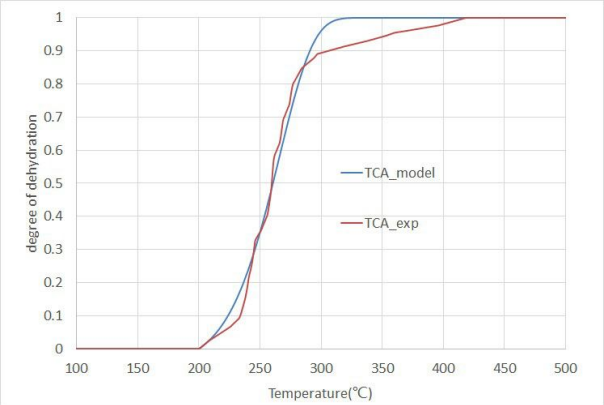

(a) The fitting result with activation energy 85.4kJ/mol(Horváth *et al.*, 1977)

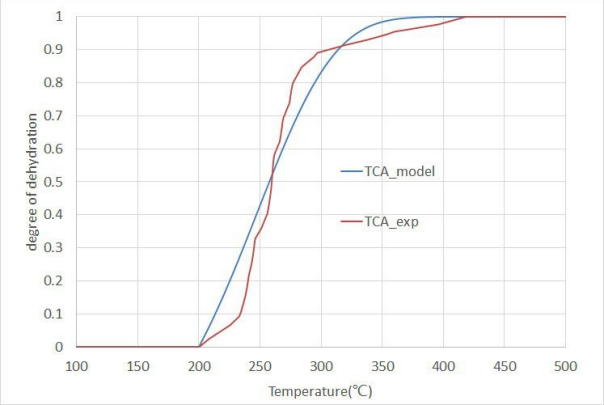

(b) The fitting result with activation energy 35.58kJ/mol(Das *et al.*, 1996)

Figure 2.12: The Fitting of the dehydration of C_3AH_6

Influence of the activation energy E_a^{TCA}

5 different activation energies of TCA dehydration ranging from $0.8E_a^{TCA}$ to $1.2E_a^{TCA}$ with an interval of $0.1E_a^{TCA}$ were used to calculate the dehydration profile to get the influence of that parameter. The comparison was shown in fig.2.13.

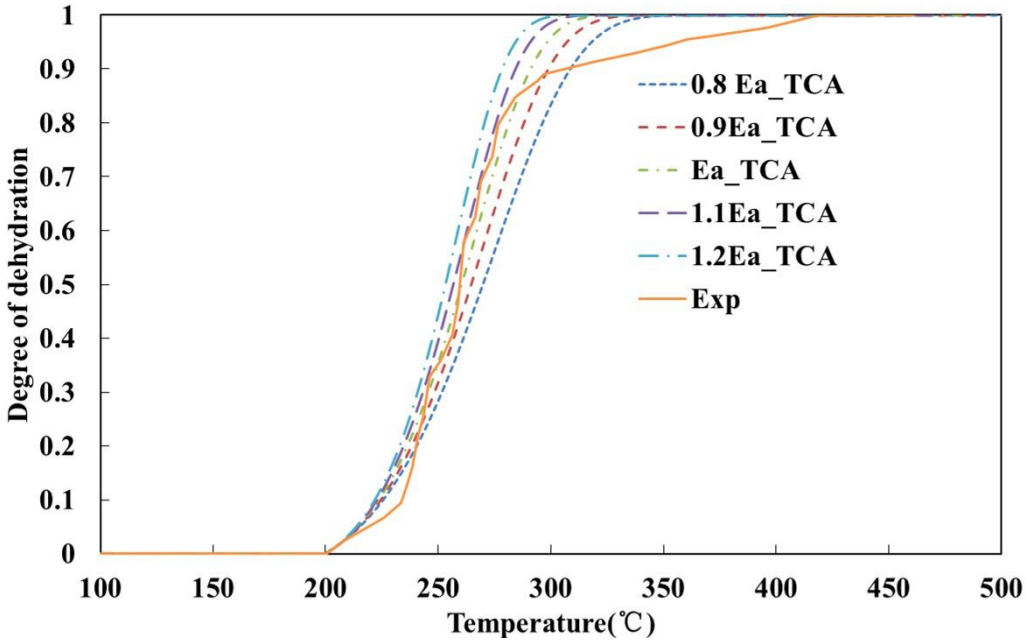

Figure 2.13: The influence of activation energy on TCA dehydration

As can be seen from the diagram, dehydration activation energy showed great influence on the rate of dehydration. $T_{0.95}$, at which temperature dehydration degree=0.95, varied from 306°C to 353°C when activation energy decrease from $1.2E_a^{TCA}$ to $0.8E_a^{TCA}$.

Influence of the characteristic time τ^{TCA}

The comparison between the modeling results using characteristic time from $0.8\tau^{TCA}$ to $1.2\tau^{TCA}$ was shown in fig.2.14. It should be noticed that there is not so large difference between different results as that of activation energy. Difference between $T_{0.95}$ calculated with $0.8\tau^{TCA}$ and $1.2\tau^{TCA}$ was 13°C(318°C and 331°C, respectively).

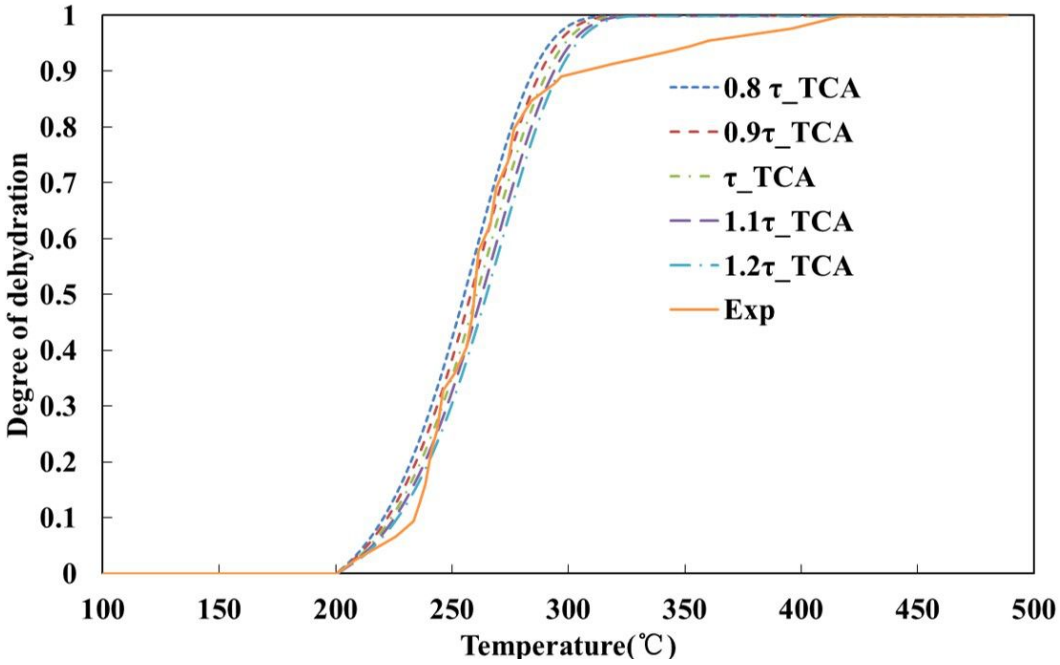

Figure 2.14: Influence of characteristic time on TCA dehydration

All the parameters for dehydration of C_3AH_6 are listed in table.2.2

Hydrate	$T_{onset}(°C)$	$\xi_{eq}(H(T-T^i_{onset}))$	E_a(kJ/mol)	$\tau(10^3 s)$
C_3AH_6	200	1	85.4	11.8

Table 2.2: Parameters for dehydration of C_3AH_6

2.2.3 Monosulfate

As mentioned in section 1.1, the water content of monosulfate depends on the pre-drying method. Hence, the residual water content was chosen to compare the dehydration processes in term of H_2O/Ca ratio. The initial water content could be acquired according to the pre-drying conditions in table.1.1. However, some of the pre-drying conditions were not listed in table.1.1. Assume that :

1) the different pre-drying methods only affected the amount of interlayer water. In other words, the stoichiometry of monosulfate in those experiments could be written as $Ca_4Al_2(OH)_{12}SO_4 \cdot xH_2O$ $(0 \leq x \leq 6)$.

2) all the sample dehydration completely in the TG tests in table.2.3.

The final mass loss in the TG tests can be expressed as:

$$y = \frac{\text{mass loss}}{\text{Initial mass of the sample}} = \frac{204 + 18x}{514 + 18x} \tag{2.8}$$

By this way, the initial interlayer water in each experiment that was adopted to fit or validate the dehydration of monosulfate was calculated and listed in table.2.4

Table 2.3: Experiments for validation of AFm dehydration model

Literature	Heating rate	Temperature	Pre-drying	Maximum mass loss
(Dilnesa *et al.*, 2012)	20K/min	30-980°C	vacuum filtration through 0.45 μm nylon filters	0.333
(Pan Guoyao, 1997)	not mentioned	100-600°C	60°C drying	0.358
(Leisinger *et al.*, 2012)	20K/min	30-980°C	silica gel	not mentioned
(Taylor, 1984)	10K/min	50-700°C	not mentioned	3mol H_2O per 1mol CaO

Table 2.4: Initial amount of interlayer water in experiments

Literature	(Dilnesa *et al.*, 2012)	(Pan Guoyao, 1997)	(Leisinger *et al.*, 2012)	(Taylor, 1984)[1]
interlayer water(x)	5.3	6	4.5	6

[1] The H_2O/Ca ratio was considered 3 under initial condition

Simplified dehydration model for monosulfate

According to the DTG diagrams in the literature(Dilnesa *et al.*, 2012)(Pan Guoyao, 1997)(Leisinger *et al.*, 2012)(fig.1.16-fig.1.17), there were several peaks in the DTG diagrams, and the equilibrium dehydration degree of AFm increased when the temperature increased. Hence, the best way to model AFm dehydration should be the combination of all the sub-processes represented by peaks in the DTG diagrams. Yet, the model would be very complicated if AFm dehydration was modeled by that method. For the simplification, dehydration of AFm was first modeled as a whole reaction(marked "method1"), and the kinetics of the dehydration process follows equation.2.9:

$$\dot{\xi}^{AFm} = \frac{1}{\tau^{AFm}} \exp(-\frac{{E_a}^{AFm}}{R}(\frac{1}{T} - \frac{1}{T^{AFm}_{onset}}))(\xi^{AFm}_{eq} - \xi^{AFm})H(T - T^{AFm}_{onset}) \quad (2.9)$$

where the onset temperature of AFm dehydration T^{AFm}_{onset} was the room temperature 20°C .
In order to reproduce the effect of several peaks in DTG diagram, the equilibrium of the dehydration was considered as a function of temperature as equation.2.10 to model the increased equilibrium dehydration degree with increased temperature instead of a constant for portlandite.

$$\xi^{AFm}_{eq} = (1 - \exp(a^{AFm}(T - T_{ref})^{b^{AFm}}))H(T^{AFm}_{onset}) \quad (2.10)$$

Where T_{ref} was the room temperature(20°C) as well. The parameters a^{AFm}, b^{AFm}, τ^{AFm} and E^{AFm}_a were fitted with the TG test by Dilnesa(Dilnesa *et al.*, 2012). The TG test was performed under heating rate of 20K/min, over the temperature range from 30°C to 980°C. The fitting result was shown in fig.2.15 under the assumption that the dehydration equilibrium is greater than the test result.

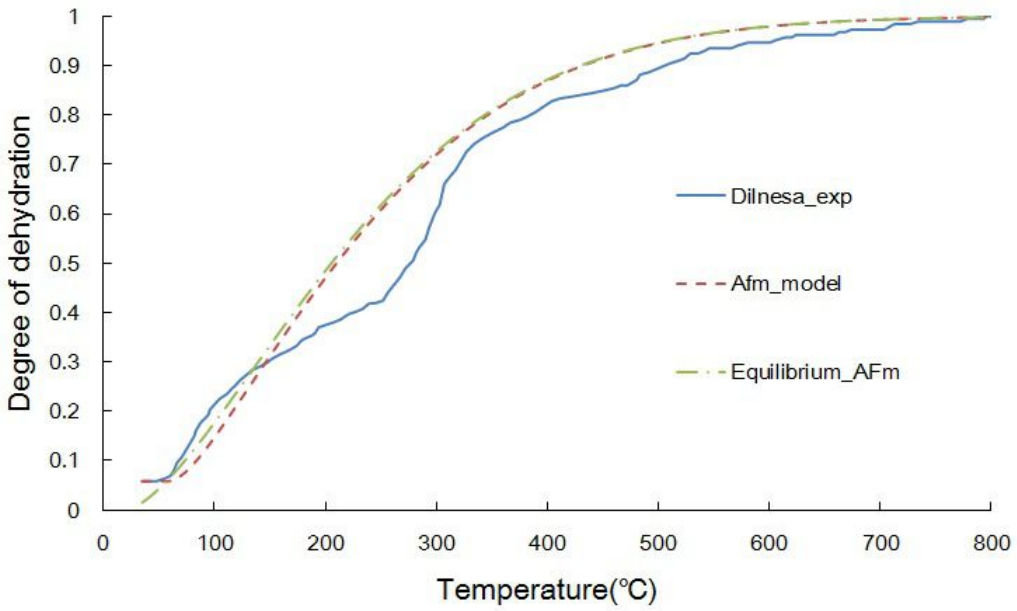

Figure 2.15: The evolution of equilibrium and dehydration degree of AFm

The model fit the test result best in the temperature range of 300-400°C, and seemed acceptable in higher temperature. However, in the temperature range below 300°C, which was interesting in the nuclear safety field, the model could not fit the test result very well. Before 167°C, the modeling dehydration degree was lower than the test result. Yet, the modeling result went higher than the test result when temperature went higher than 167°C.

Enhanced model for dehydration of monosulfate

To pursue a more accurate model, the dehydration process of AFm was finally modeled as more than one part, and each part was denoted j(marked "method2"). The total mass loss due to the dehydration follows:

$$w^{AFm} = \sum_{j} w_j^{AFm} \tag{2.11}$$

Although the dehydration process could be separated into several parts. the releasable water in the monosulfate was usually considered as two types, which are the interlayer water and the mainlayer water, due to their different crystal

structures(Dilnesa *et al.*, 2012)(Leisinger *et al.*, 2012)(Pan Guoyao, 1997), and the mechanism of the dehydration of those two types of water were different(Leisinger *et al.*, 2012) .Hence, the dehydration of monosulfate was considered as two processes:

- Interlayer water($j = 1$) takes up half of the water in the monosulfate $3CaO \cdot Al_2O_3 \cdot CaSO_4 \cdot 12H_2O$, and the equilibrium of the interlayer dehydration $\xi_{eq,1}^{AFm} = 0.5(1 - \exp(a_1^{AFm}(T - T_{onset,1}^{AFm})))H(T - T_{onset,1})$.
- Mainlayer water($j = 2$) consisted the other half of water in the monosulfate. which is part of the main layers $[Ca_2Al(OH)_6]^+$, so the equilibrium of the main layer dehydration $\xi_{eq,2}^{AFm} = 0.5H(T - T_{onset,2})$as well.

Therefore, equation2.11 could be written as:

$$w^{AFm} = w_1^{AFm} + w_2^{AFm} \tag{2.12}$$

where

$$w_j^{AFm} = w_{max}^{AFm}(0.5 - \xi_j^{AFm}) \tag{2.13}$$

and the rate of the dehydration $\dot{\xi_j^{AFm}}$

$$\dot{\xi}_j^{AFm} = \frac{1}{\tau_j^{AFm}} \exp(-\frac{E_{aj}^{AFm}}{R}(\frac{1}{T} - \frac{1}{T_{onset,j}^{AFm}}))(\xi_{eq,j}^{AFm} - \xi_j^{AFm})H(T - T_{onset,j}^{AFm}) \tag{2.14}$$

At room temperature, when the relative humidity was 12%, $n = 12$ in $3CaO \cdot Al_2O_3CaSO_4 \cdot nH_2O$. Besides, no obvious mass loss was observed in the thermal analysis performed by Dilnesa(Dilnesa *et al.*, 2012) before 40°C. Hence, the onset temperature ought to be higher than room temperature. Given all that, the onset temperature was approximately considered as 40°C.
The TGA test done by Dilnesa(Dilnesa *et al.*, 2012) was shown in fig.1.16. The dotted line was TGA and DTG curves of the Al-monosulfate, and 260°C was selected as the boundary between the interlayer water removal and the water removal of the mainlayer.In the research done by Leisinger(Leisinger *et al.*, 2012) and Pan(Pan Guoyao, 1997), the experimental results of which were shown in fig.1.15 and fig.1.17, 290°C and 292°C was considered as the onset temperature of the water release due to the main layer.

The most interesting finding was that on the DTG and DTA curves in fig.1.16, 1.17 and 1.15, the values of the sections marked by enclosed boxes were not 0.

It was probably due to the fact that they were overlapped area of dehydration of both interlayer and main layer. Hence, the onset temperature of the main layer dehydration ought to be lower that the peak of the reaction. According to the experimental results above, 200°C, which would probably be the onset temperature of the first peak of the DTG and DTG peak of the main layer dehydration, was approximately selected as the onset temperature of the main layer dehydration. Given all that, 40°C and 200°C were selected as onset temperatures of dehydration for interlayer and main layer to fit the experimental result from Dilnesa(Dilnesa *et al.*, 2012), in which the sample was synthesized monosulfate(See fig.1.16). For the dehydration of interlayer, the characteristic time τ_1^{AFm} is 713s and the activation energy $E_{a,1}^{AFm}$ is 2.51kJ/mol; for the main-layers, the characteristic time τ_2^{AFm} is 2500s and the activation energy $E_{a,2}^{AFm}$ is 72.31kJ/mol. The comparison between this method and the previous one is shown in fig.2.16.

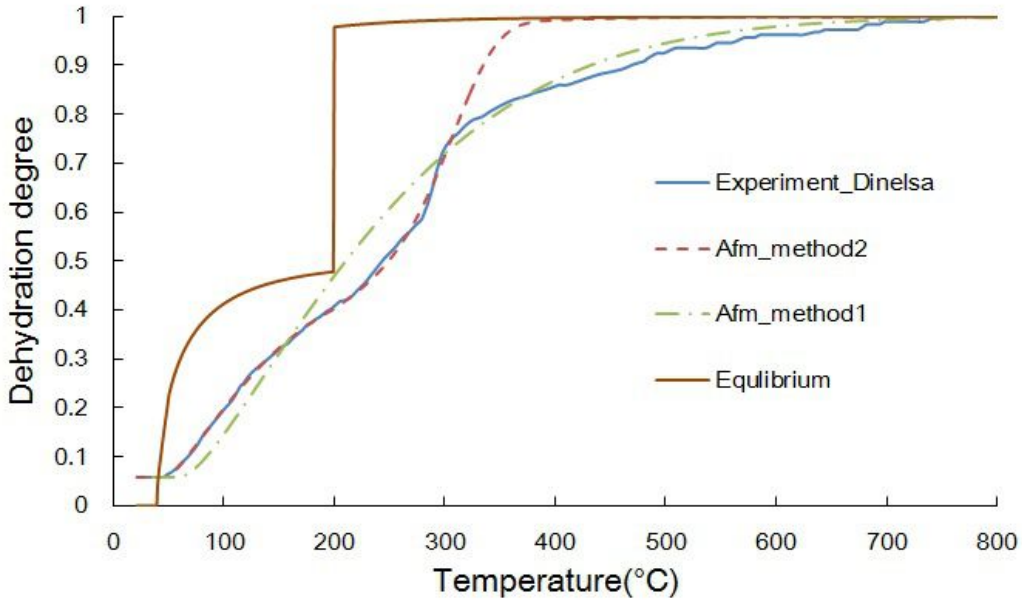

Figure 2.16: The fitting result of the dehydration of monosulfate

According to table.2.4, before the experiment, every mol of monosulfate used in (Dilnesa *et al.*, 2012) included 5.3 mols of interlayer water, which means the initial dehydration degree $\xi_0^{AFm} = (6 - 5.3)/12 = 0.058$. The "·−" line represented the previous model considering the AFm dehydration as a whole (method1), and the "··" line represented the latter model considering the pro-

cess as 2 parts (method2). As can be seen from fig.2.16, in the temperature range lower than 300°C, method2 fit the experimental result much better than method1, method1 had advantage over method2 while above 300°C. Method2 shows better fitting in the temperature range that our research interested in,so the evolution of the dehydration degree of monosulfate should be modeled as interlayer and mainlayer, respectively.

Validation of the model

In order to validate the dehydration model, the predicted water loss during the increasing of temperature was compared with some experimental results of TG tests. The experiments used for the validation of the model are introduced in table.2.3.

The comparison between the experimental results and the modeling result were shown in fig.2.17. The calculation tried to reproduce the result of Dilnesa under heating rate of 20K/min, and it showed less difference under 300°C. All the experimental results showed a rapid mass loss between 200°C and 400°C, which corresponds to the dehydration of main layer. Taylor's(Taylor, 1984) result contains apparent 4 "stage", which are probably due to the lower heating rate than that for Dilnesa's(Dilnesa *et al.*, 2012) and Leisinger's(Leisinger *et al.*, 2012) results. Pan(Pan Guoyao, 1997) did not mention the heating rate of the TG test in the literature, and the TG curve given was in the relatively narrow temperature(100-600°C), which perhaps would add some error when we re-plot his test result. With given fact that the sample lost 17.5% of the weight at the end of the peak at 188.4°C, and the assumption that all the water lost before 188.4°C was contributed by the dehydration of interlayer, the curve was re-plot in fig.2.17, and showed similar shape to the results from both Dilnesa and Leisinger. Above 300°C, the model showed greater error than before probably because the defect of the crystals and the assumption that all the water in mainlayer follow the same law during the dehydration process.

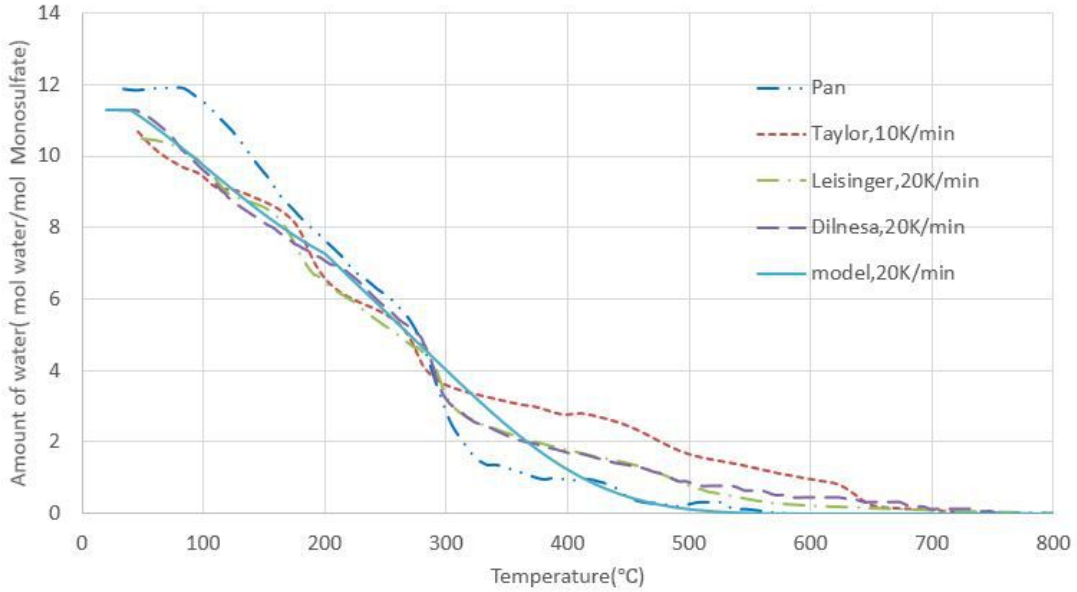

Figure 2.17: The modeling result and the experimental results of water content during the dehydration under heating rate of 20K/min

The influence of onset temperature

- interlayer dehydration onset temperature $T_{onset,1}^{AFm}$
  Four different onset temperatures between 25°C and 40°C were compared with the experimental result, which was shown in fig.2.18.

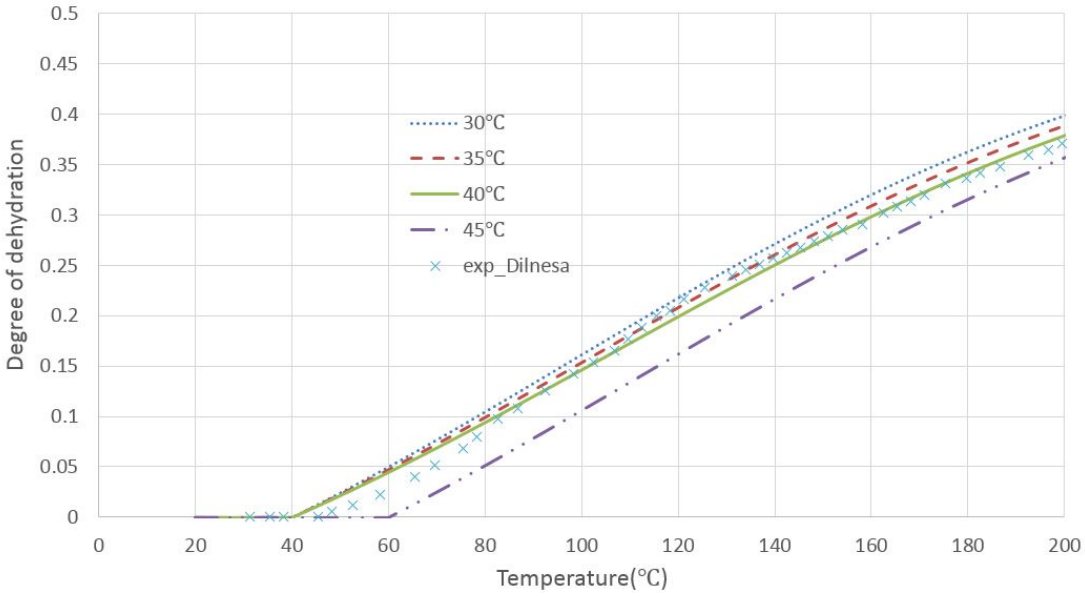

Figure 2.18: The influence of the interlayer dehydration onset temperature

The model fit the experiment best when $T^{AFm}_{onset,1} = 40$°C, and the difference among 30°C, 35°C and 40°C are apparently less than that of 45°C.

- main layer dehydration onset temperature $T^{AFm}_{onset,2}$
  The influence of main layer dehydration onset temperature $T^{AFm}_{onset,2}$ was shown in fig.2.19. In the temperature range 200-300°C, the higher onset temperature 210 °C fit better than lower onset temperatures, but the situation was the opposite in temperature range 300-400°C, where the lower onset temperature 190°C fit best. When the temperature was higher than 400°C, the influence of the $T^{AFm}_{onset,2}$ became less than that when temperature was below 400°C. Therefore, the onset temperature 200°C, which has least square error to the experimental result in the temperature range 200-400°C, was selected as main layer dehydration onset temperature.

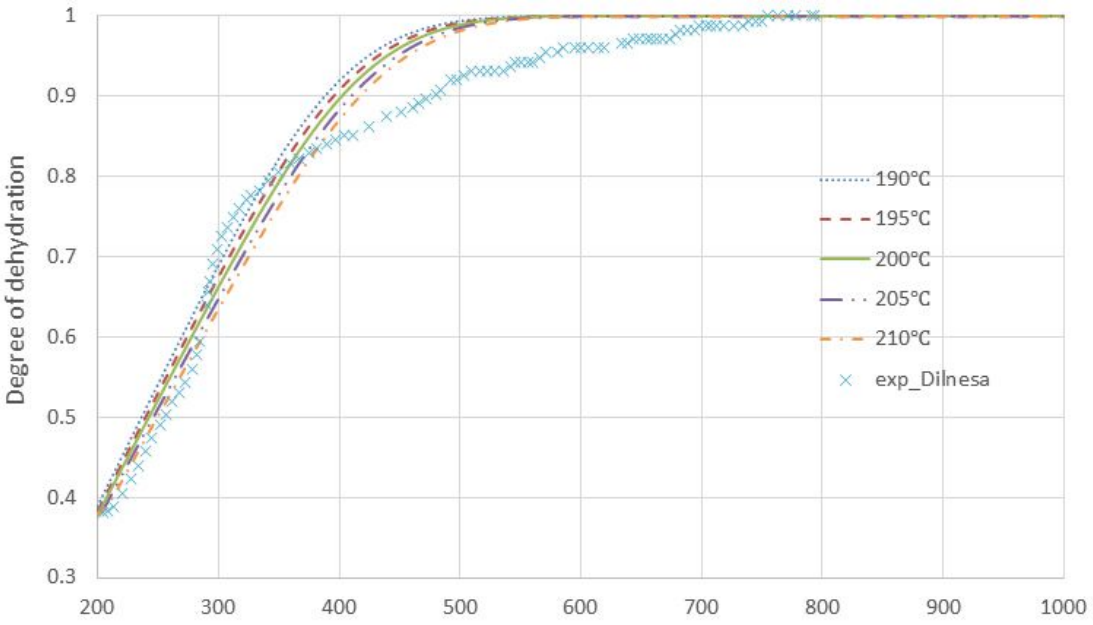

Figure 2.19: Influence of main layer dehydration onset temperature

The influence of the activation energy E^{AFm}_a

- Interlayer dehydration activation energy $E^{AFm}_{a,1}$
  Fig.2.20 showed the comparison of the different results calculated by the dehydration model with various activation energy of the interlayer dehydration process.

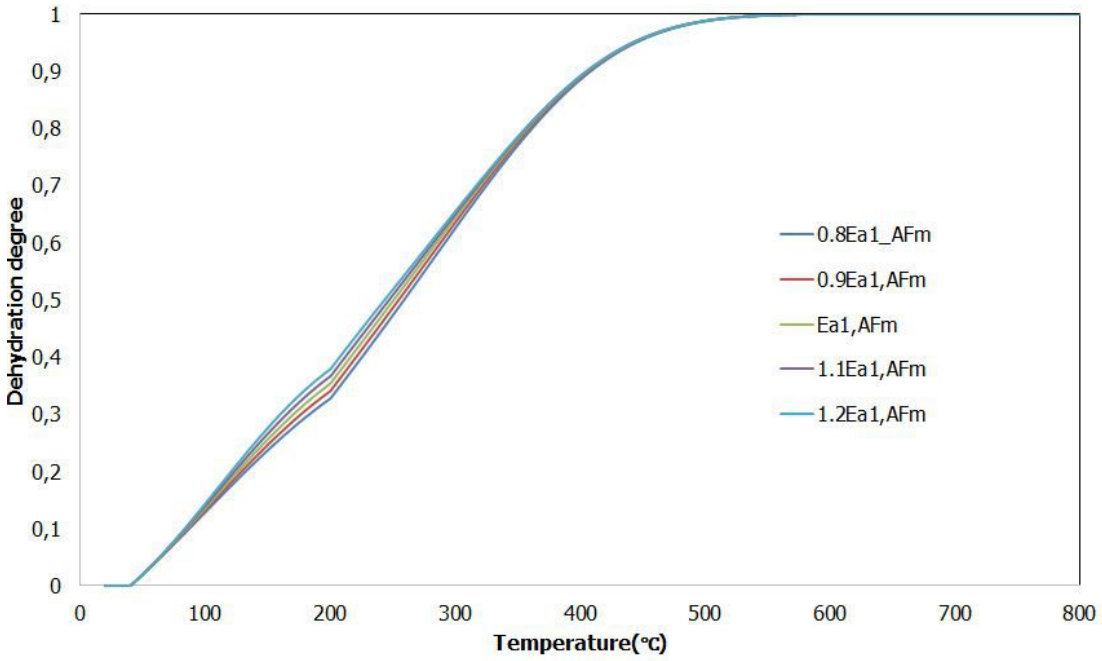

Figure 2.20: The influence of the interlayer dehydration activation energy on monosulfate dehydration

The interlayer dehydrated in the lower temperature than mainlayer, so the influence was obviously below 300°C. Furthermore, the influence became less as temperature rose to higher than the onset temperature of mainlayer dehydration, and the largest difference between results with different activation energy ranging from $0.8E_{a,1}^{AFm}$ to $1.2E_{a,1}^{AFm}$ occurred at 200°C, which was 0.04 in dehydration degree of the sample.

- Mainlayer dehydration activation energy $E_{a,2}^{AFm}$
  $E_{a,2}^{AFm}$ showed influence on the monosulfate dehydration above 200°C, which was shown in fig.2.21. However, the dehydration rate of mainlayer was very small at beginning of the reaction, difference between difference activation energy was not easy to observe until 250°C.

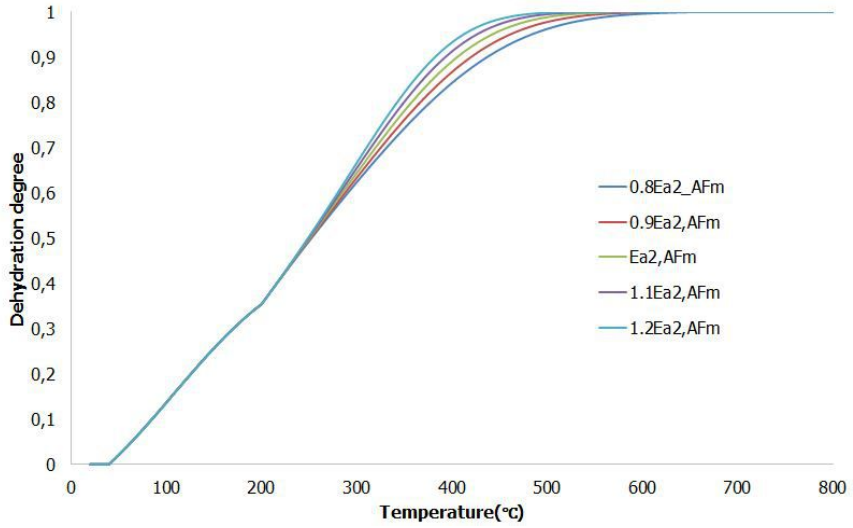

Figure 2.21: The influence of the mainlayer dehydration activation energy on monosulfate dehydration

The influence of the characteristic time τ^{AFm}

- the characteristic time of interlayer dehydration τ_1^{AFm}
  The influence of the characteristic time of interlayer dehydration was shown in fig.2.22

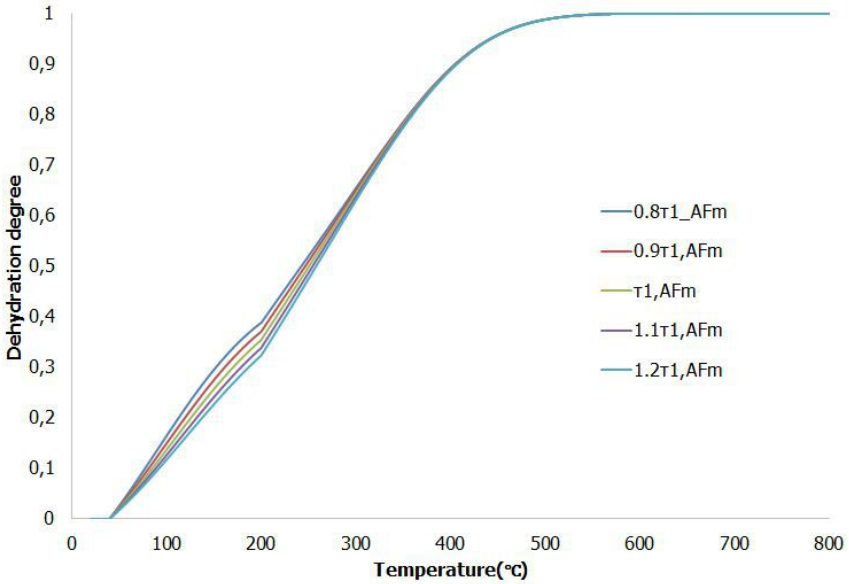

Figure 2.22: The influence of characteristic time of interlayer dehydration on monosulfate dehydration

It showed same tendency with the influence of $E_{a,1}^{AFm}$, but with a greater effect. At 200°C, the difference between the results with least characteristic time and that with the most characteristic time was more than 0.05 in dehydration degree of monosulfate.

- the characteristic time of mainlayer dehydration τ_2^{AFm}
  Like the interlayer dehydration, the influence of τ_2^{AFm} showed similar tendency with the influence of $E_{a,2}^{AFm}$. The comparison between the different modeling results was shown in fig.2.23.

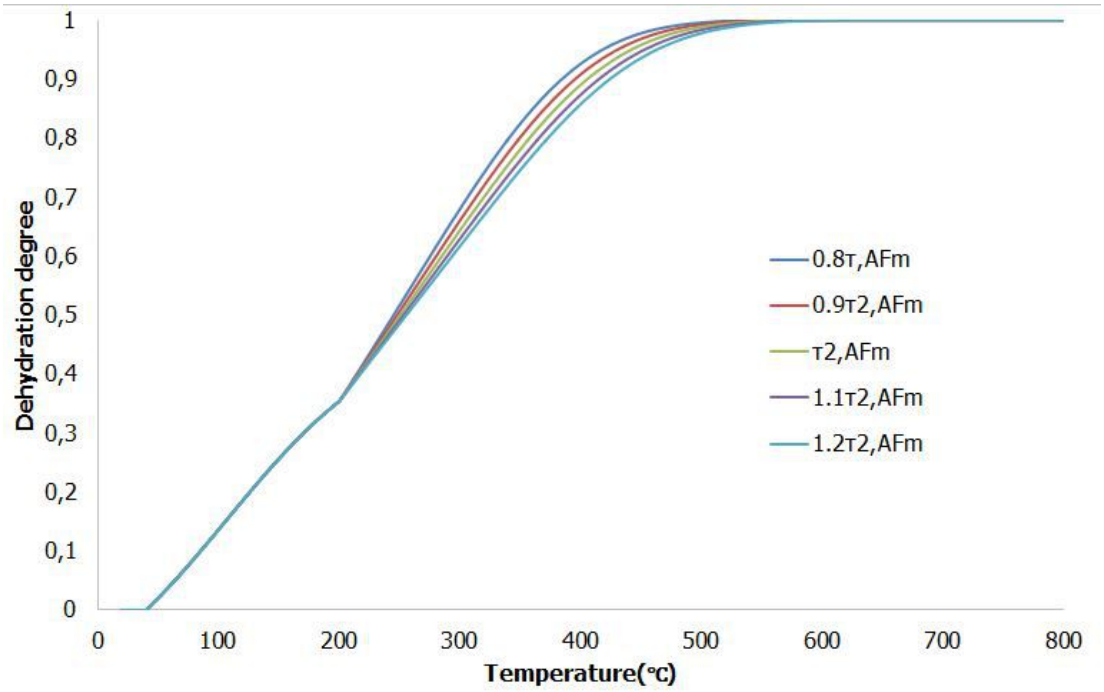

Figure 2.23: The influence of characteristic time of mainlayer dehydration on monosulfate dehydration

All the parameters for dehydration of monosulfate are listed in table.2.5

Table 2.5: Parameters for dehydration of AFm

Hydrate	$T_{onset}(°C)$	$\xi_{eq}(H(T-T_{onset}^i))$	E_a(kJ/mol)	$\tau(10^3 s)$
AFm(Interlayer)	40	$0.5(1-e^{-0.15(T-40)^{0.6}})$	9.30	0.713
AFm(Mainlayer)	200	0.5	25.15	2.5

2.2.4 C-S-H

Because of the poor crystallinity and the complexity of its structure, it is difficult to distinguish the dehydration process of C-S-H in hydrates of cement paste with pure C-S-H. As mentioned in section. 1.1.3, there are different types of water in C-S-H. Besides, C-S-H gel in cement paste is always poor crystallized. Hence, the equilibrium equation of dehydration could not be considered as constant in certain temperature ranges. An equation with constant a and b was proposed to describe the equilibrium of C-S-H in the process of dehydration(see equation.2.15).

$$\xi_{Eq}^{CSH} = (1 - \exp(a^{CSH}(T - T_{onset}^{CSH})^{b^{CSH}}))H(T - T_{onset}^{CSH}) \tag{2.15}$$

The TG curve used for the fitting of the C-S-H was the experimental result of chapter 3.2.3, under the heating rate of 5K/min. According to the experimental result from Korpa(Korpa and Trettin, 2006), the relative percentages of the removed water after d-drying and freeze-drying were 57.14% and 56.61%. Assume that all the hydrates except monosulfate lose the same content of water after both drying methods, the interlayer water left in monosulfate after freeze-drying could be considered as much as that after d-drying, so the stoichiometry of monosulfate after freeze-drying could be written as same as that after d-drying $C_4A\bar{S}H_8$.

There have not been so many directly studies on the dehydration of C-S-H in cement pastes, Foley(Foley *et al.*, 2012) synthesized C-S-H(Ca/Si=1.5) samples and dried them with d-drying method and 11%RH environment. However, the actual stoichiometry of the d-dried C-S-H and 11%RH dried C-S-H were calculated with the experimental result and considered as $C_{1.2}SH_{0.7}$, and $C_{1.2}SH_{2.4}$, respectively. Furthermore, there were $Ca(OH)_2$(14.5% and 9.6%) and $CaCO_3$(2.9% and 2.4%) in the d-dried and 11%RH dried samples, respectively. The TGA results of samples with both pre-drying methods are shown in fig.2.24. The data started at 145°C, but the interesting temperature to this study is from room temperature to 200°C, which means that the the behavior of C-S-H dehydration in major part of the interesting temperature range cannot be obtained from that experimental result. However, the TGA result can be used validate the model.

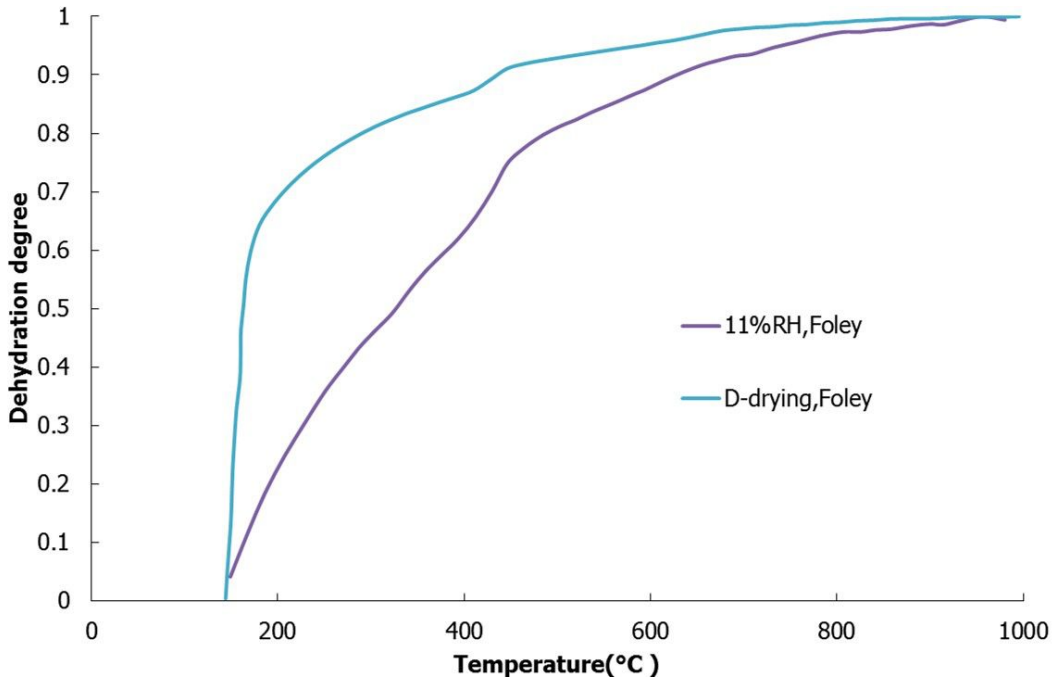

Figure 2.24: TGA of synthesized C-S-H that were dried with d-drying and 11%RH environment(Foley *et al.*, 2012)

Since we have the dehydration models for other hydrates in the cement paste, the model of the dehydration of the C-S-H was fitted as following steps:

1. Get the TG results of the cement paste with known composition.

$$w_{dehydr} = w_{dehydr}(T) \tag{2.16}$$

   In this study, $w_{dehydr}(T)$ is the data of TGA test under heating rate of 5K/min performed in LMDC, which is introduced in chapter.3.

2. Get TG results of the hydrates other than C-S-H.

$$\sum_i w^i = \sum_i w^i(T) \tag{2.17}$$

   where i=CH, AFm, TCA in this study.

3. Remove the mass loss of other hydrates from the result of cement paste to get the TG results of C-S-H.

$$w^{CSH}(T) = w_{dehydr}(T) - \sum_i w^i(T) \tag{2.18}$$

4. Fit the TG results of C-S-H to get the equilibrium equation ξ_{Eq}^{CSH}, activation energy E_a^{CSH} and characteristic time of the dehydration of C-S-H τ^{CSH}.

Given all that, The fitting result of C-S-H up to 200°C is shown in Fig.2.25a, with $a^{CSH} = -0.658, b^{CSH} = 0.252, E_a^{CSH} = 44.80\text{kJ/mol}, \tau^{CSH} = 23000\text{s}$, with the step-control constant $\epsilon = 5 \times 10^4$. The legend "exp_CSH" means the dehydration curve obtained with equation.2.18 and the TG test in LMDC Toulouse under heating rate of 5K/min.

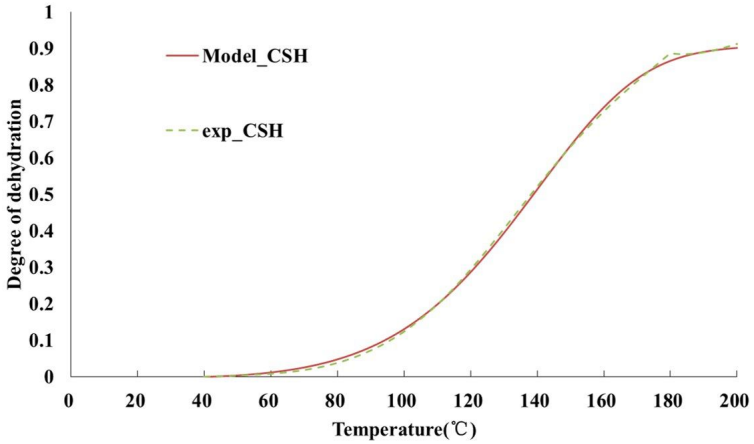

(a) Fitting result of C-S-H

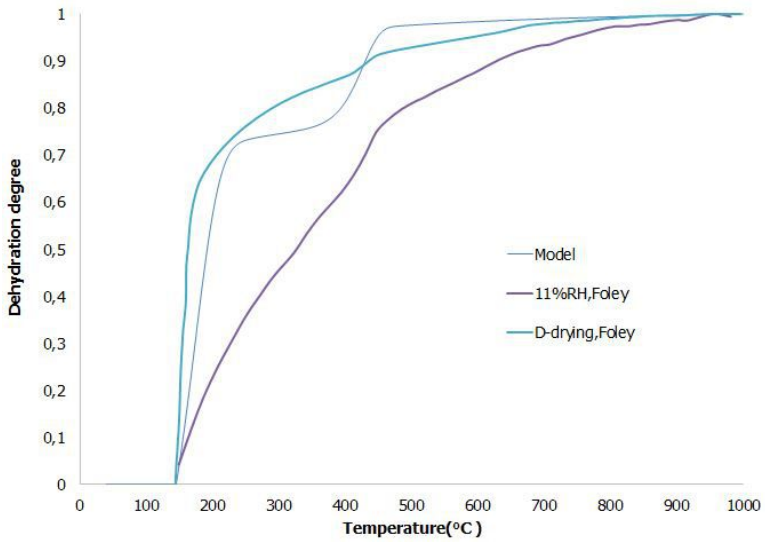

(b) Modeling and experimental result of dehydration of C-S-H under heating rate of 10K/min(Foley *et al.*, 2012)

Figure 2.25: Fitting results and validation of the model with synthesized C-S-H(Foley *et al.*, 2012)

Validation of the C-S-H dehydration model

To make a more reasonable comparison, some assumptions were made according to the experiments in (Foley *et al.*, 2012):

1. The modeling result consists dehydration process of both CH and C-S-H($C_{1.75}SH_{1.4}$).

2. the sample for modeling contain:85.5% C-S-H, 12% $Ca(OH)_2$ and 2.5%$CaCO_3$

3. The mass loss of $CaCO_3$ was not modeled because of the complexity that it would introduce.

4. The mass loss before 145°C was not considered as the dehydration of C-S-H in order to keep the same assumption as that in the literature.

5. $Ca(OH)_2$ starts to dehydrate at 300°C since the delay of the onset temperature in the experiment was not as much as in cement pastes.

During the TGA tests, the samples were heated from 25°C to 1000°C. The author argued that the dehydration of C-S-H started from 125-150°C and the mass loss became negligible at the temperature range between 350°C and 400°C. The comparison between the modeling result and the experimental results was shown in fig.2.25b. The modeling line was between the two experimental results because the water content of the C-S-H and the content of CH used in the calculation was close to the average of the two samples in the experiments. Above 430°C, the modeling dehydration degree was slightly larger than experimental result of d-dried sample and it is probably because the dehydration process of $CaCO_3$ was not considered in the model.

Influence of onset temperature of C-S-H dehydration T_{onset}^{CSH}

4 different onset temperatures (30°C, 35°C, 40°C, 45°C) were tested. The results are compared with the experimental result mentioned in fig.2.25b. The comparison was shown in fig.2.26. when the temperature was higher than 200°C, the influence of the onset temperature of the C-S-H dehydration almost vanished. However, obvious differences could be observed below 200°C, and $T_{onset}^{CSH} = 40$°C fit the experiment best.

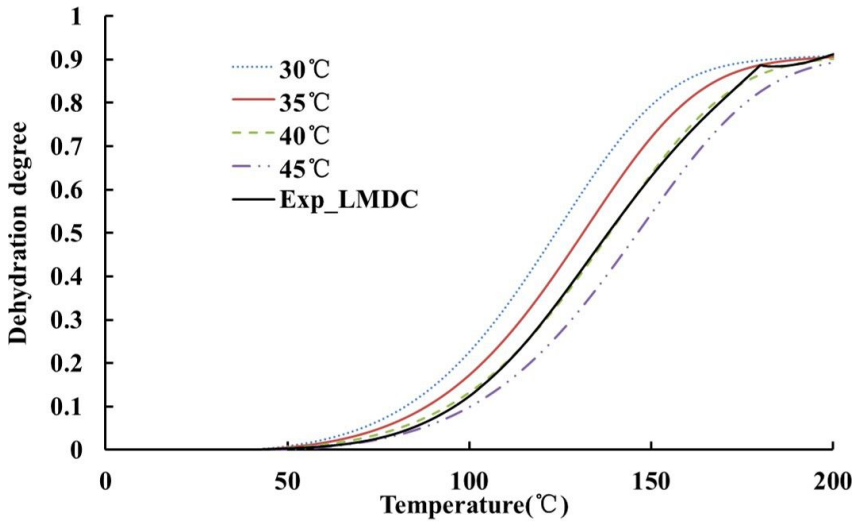

Figure 2.26: Influence of onset temperature of C-S-H dehydration

Influence of activation energy E_a^{CSH}

The comparison of modeling result with various activation energy ranging from $0.8E_a^{CSH}$ to $1.2E_a^{CSH}$ was shown in fig.2.27. $T_{0.5}$ will decrease to 131°C if the the activation energy was 20% greater than E_a^{CSH}, and increase to 168°C if 20% less.

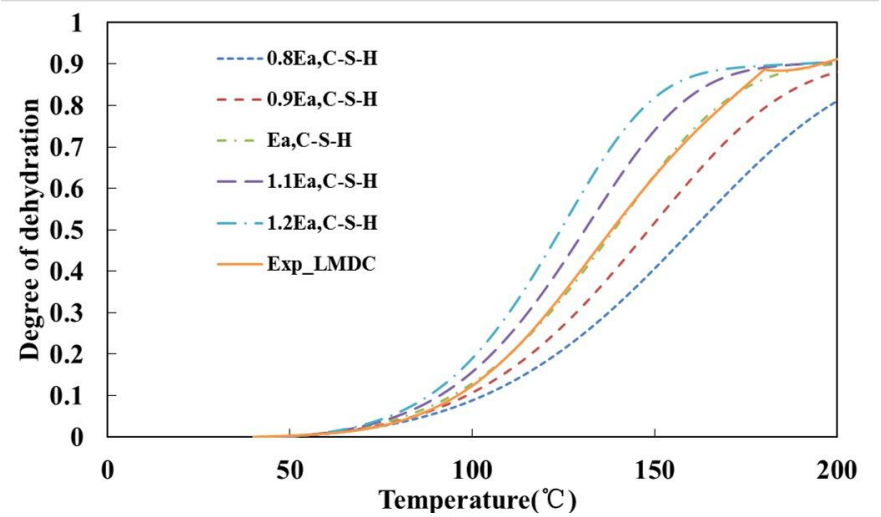

Figure 2.27: Influence of activation energy on dehydration of C-S-H

Influence of characteristic time τ^{CSH}

Characteristic time of C-S-H dehydration showed less influence on the dehydration profile. Again, τ^{CSH} was augmented and shrunk at most 20% to

show the influence of characteristic time. The comparison was shown in fig.2.28

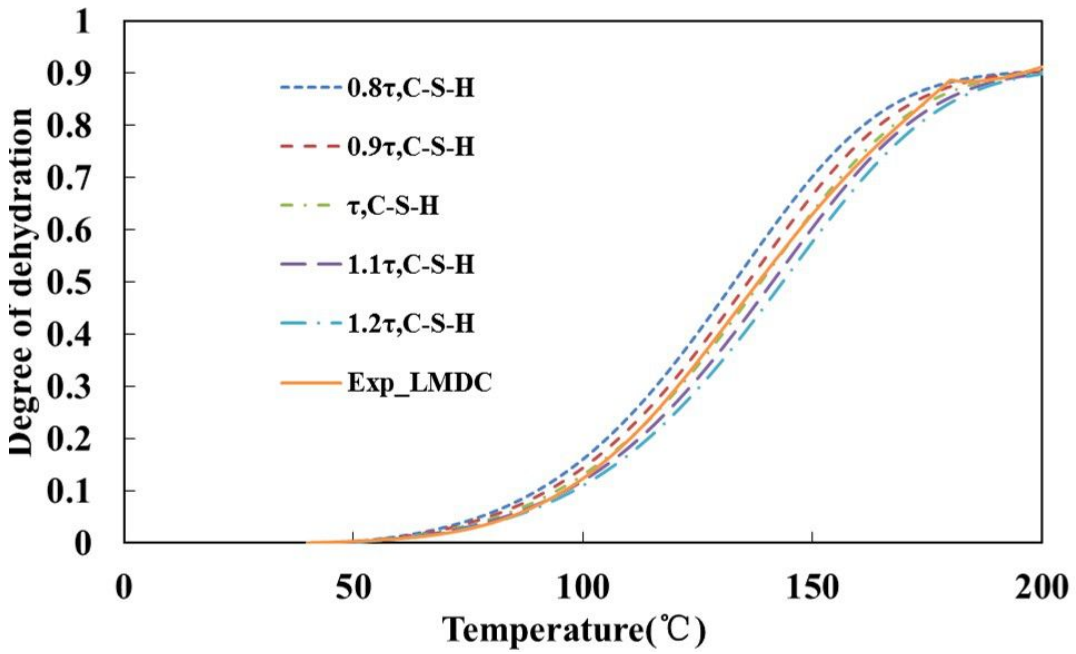

Figure 2.28: Influence of characteristic time τ^{CSH}

There's no significant differences between different results. The characteristic time showed limited influence on the rate of C-S-H dehydration process. All the calculation implied that the dehydration degree will be greater than 85% at 200°C.

A summary for the parameters that were used to model the dehydration of cement pastes were shown in table.2.6. The equilibrium equation of each hydrate is valid when the temperature is higher than the onset temperature, so the Heaviside function is applied to each equation.

Table 2.6: Parameters for model of dehydration of the cement paste

Hydrate	CH	AFm Interlayer|Mainlayer	TCA	C-S-H
$T_{onset}(^{\circ}\mathrm{C})$	375	40| 200	200	40
$\xi_{eq}(H(T-T^{i}_{onset}))$	1	$0.5(1-e^{-0.15(T-40)^{0.6}})$ | 0.5	1	$1-e^{-0.658(T-40)^{0.252}}$
E_a(kJ/mol)	158.53	9.30|25.15	85.4	44.80
$\tau(10^3\mathrm{s})$	62.5	0.713| 2.5	11.8	23

Chapter 3

Validation of the dehydration model

With all the dehydration models of hydrates in the cement paste, the dehydration model of the cement paste could be established by adding dehydration process of each hydrate following equation.2.1. To validate the dehydration model, two aspects including heating rate and different composition of the paste were taken into consideration.

3.1 Numerical method

To predict mass loss during dehydration process of cement paste, the scheme in fig.2.3 was used to calculate dehydration degree of each hydrate. At n_{th} time step, the rate of dehydration of hydrate i $\dot{\xi}_n^i$ follows:

$$\dot{\xi}_n^i = \frac{1}{\tau^i} \exp(-\frac{E_a^i}{R}(\frac{1}{T_n} - \frac{1}{T_{onset}}))(\xi_{eq,n}^i - \xi_n^i) \tag{3.1}$$

and

$$\xi_{n+1}^i = \xi_n^i + \dot{\xi}_n^i \Delta t \tag{3.2}$$

Δt was selected to 1min by default and ϵ was also used to control the accuracy of the calculation. The influence of ϵ on different hydrates was shown in fig.3.1, 3.2, and 3.3

- **Influence of ϵ on CH**
  Using varying time step length could lead to better reliability than constant time step length method. Different step-control constant ϵ could resulted in different accuracy and calculation efficiency. Fitting results with

different ϵ was shown in fig.3.1, where $\epsilon 1 = 1 \times 10^5, \epsilon 2 = 5 \times 10^4, \epsilon 3 = 1 \times 10^4, \epsilon^4 = 5 \times 10^3$. As shown in fig.3.1, the higher heating rate resulted in large differences between different ϵ. When the heating rate was lower than 20K/min, $\epsilon 1$ and $\epsilon 2$ lead to the same fitting result. Hence, the smaller step-control constant should be selected in order to get a higher calculation efficiency. Not until the heating rate was raised to 30K/min, could a small difference between the result using $\epsilon 1$ and $\epsilon 2$ be observed at the beginning of the dehydration. Therefore, $\epsilon 2 = 5 \times 10^4$ was adopted as the step-control constant. Comparison between the modeling result with parameters above and the experimental result was shown in fig.3.1.

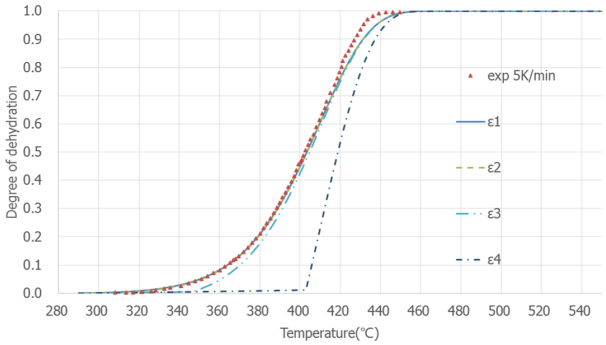

(a) The influence of ϵ under heating rate 5K/min

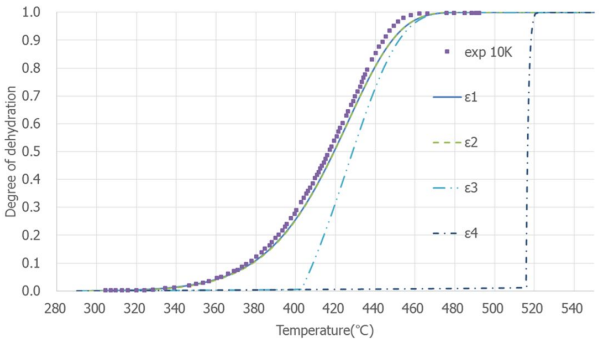

(b) The influence of ϵ under heating rate 10K/min

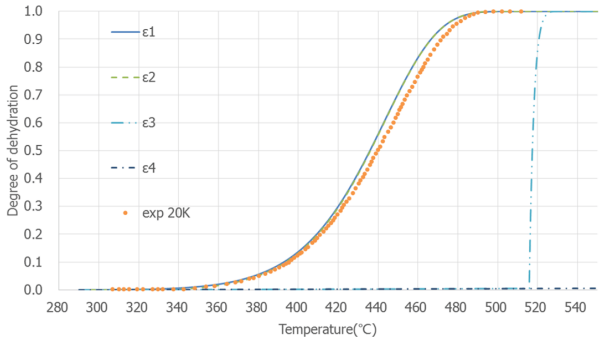

(c) The influence of ϵ under heating rate 20K/min

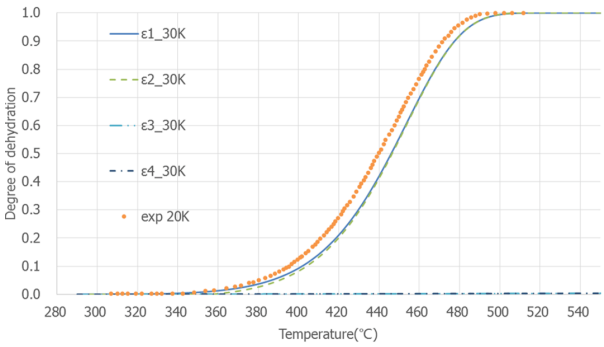

(d) The influence of ϵ under heating rate 30K/min

Figure 3.1: The influence of ϵ on dehydration of pure CH

- **Influence of ϵ on AFm**
  Like in the calculation the dehydration of CH, four different ϵ $\epsilon 1 = 1 \times 10^5, \epsilon 2 = 5 \times 10^4, \epsilon 3 = 1 \times 10^4, \epsilon 4 = 5 \times 10^3$ were tested to find the best one for the calculation. The comparison was shown in fig.3.2. The result of $\epsilon = 5 \times 10^4$ was overlapped with that of $\epsilon = 1 \times 10^5$, and was different

with other two curves. Therefore, $\epsilon = 5 \times 10^4$ was selected as time step control constant of dehydration of monosulfate.

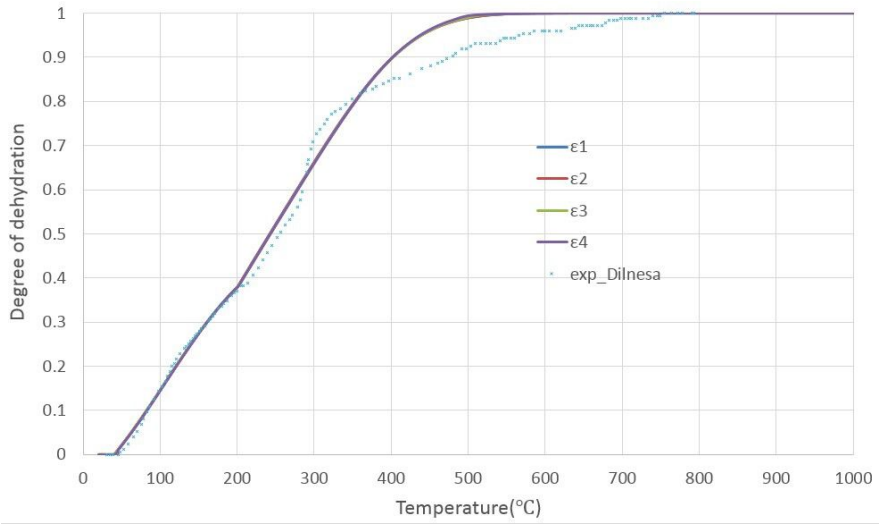

Figure 3.2: The influence of ϵ

- **Influence of ϵ on TCA**
  Again, the influence of the ϵ was tested and the comparison of the four ϵ ($1 \times 10^5, 5 \times 10^4, 1 \times 10^4, 5 \times 10^3$) was shown in fig.3.3. The influence of the step-control constant in the selected range was quite small. However, if part of fig.3.3 was zoomed in, small differences could be observed(see fig.3.4). The modeling curve using $\epsilon = 5 \times 10^4$ was the only one that was overlapped with that using $\epsilon = 1 \times 10^5$. Hence, $\epsilon = 5 \times 10^4$ was selected as time step control constant of the dehydration of C_3AH_6.

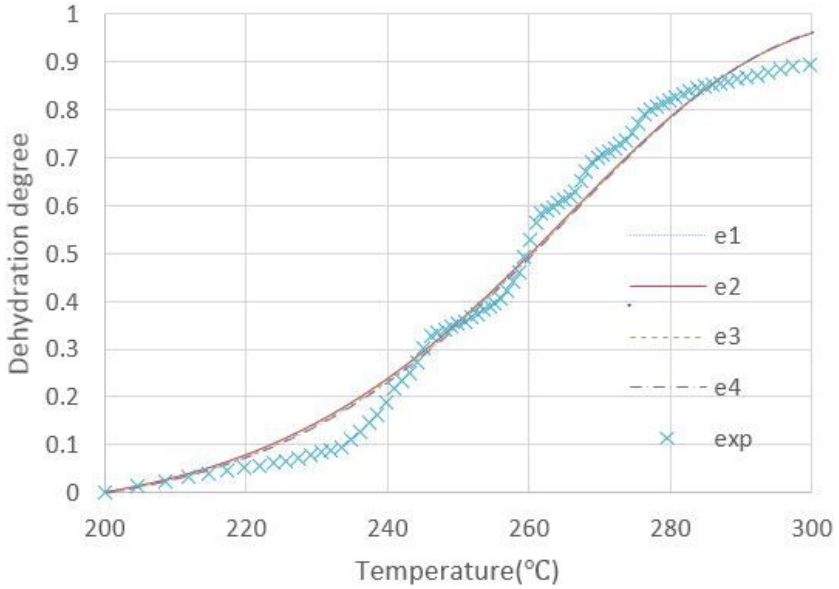

Figure 3.3: The influence of $\epsilon(e1 = 1\times10^5, e2 = 5\times10^4, e3 = 1\times10^4, e4 = 5\times10^3)$

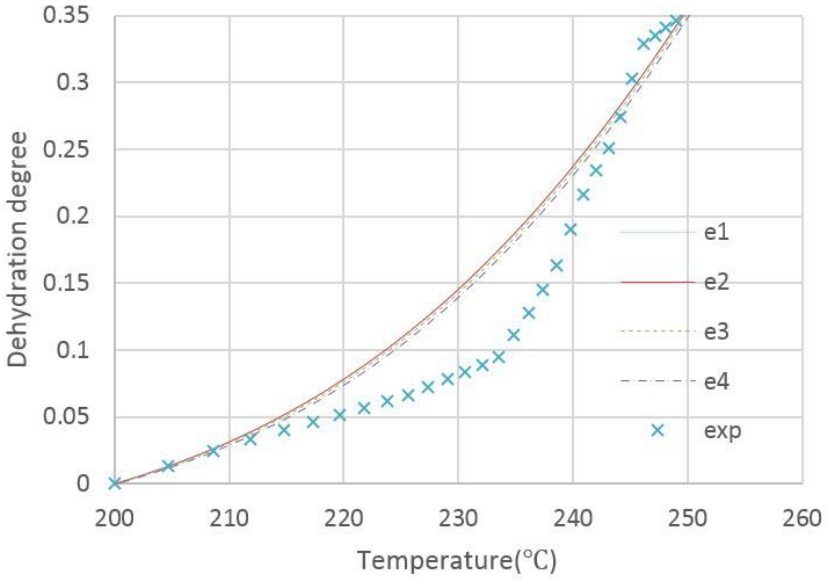

Figure 3.4: The influence of ϵ in temperature range 200-260°C

- **Influence of** ϵ on C-S-H
  The same 4 step-control constants with other hydrates were tested for dehydration of C-S-H as well($\epsilon_1 = 1 \times 10^5, \epsilon_2 = 5 \times 10^4, \epsilon_3 = 1 \times 10^4, \epsilon_4 = 5 \times 10^3$). The comparison of the calculation with those four step-control constants was shown in fig.3.5

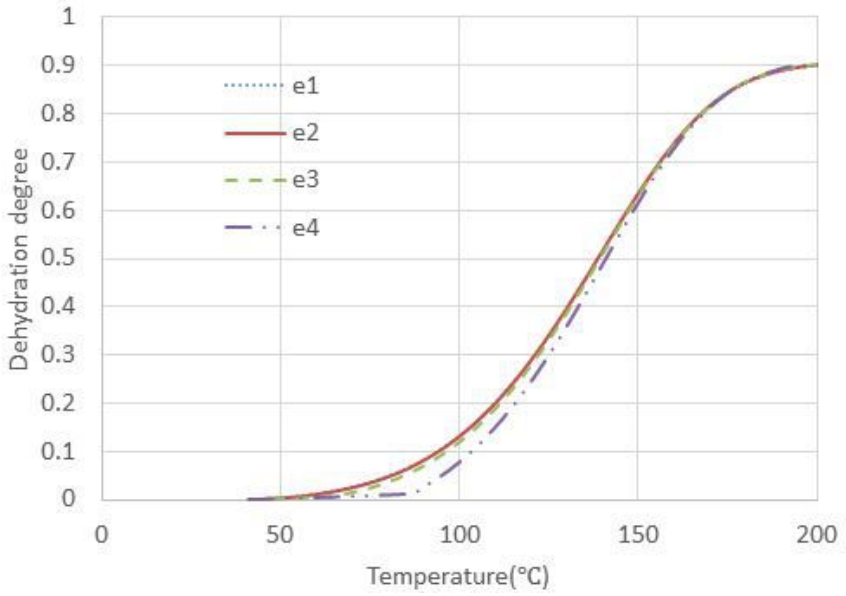

Figure 3.5: Influence of step-control constant on dehydration of C-S-H

Like other hydrates, when $\epsilon = 5 \times 10^4$, the curve was overlapped with the curve using $\epsilon = 1 \times 10^5$, while other curves showed a little difference with those two curves. Hence, $\epsilon = 5 \times 10^4$ was selected as the step-control constant of the C-S-H dehydration.

According to the comparisons above, the ϵ could be set $\epsilon = 5 \times 10^4$ during calculations.

3.2 Validation with the LMDC tests performed at two different heating rates

To validate the model with different heating rates, the modeling result was compared with the the same cement paste after the same freeze-drying procedure.

3.2.1 Experimental procedures

In order to get the dehydration model for each hydrate, the amount of the hydrates should be acquired first. Hence, the hydration model proposed by Buffo-Lacarrière (Kolani *et al.*, 2012)(Buffo-Lacarrière *et al.*, 2007) was adopted

to compute the amount of each hydrate. To use the model, the heat of hydration, which could be measured by Langavant semi-adiabatic test according to the European standard NF EN 196-9, has to be obtained. After that, the dehydration of cement paste was measured with thermogravimetry test for both modeling and validation of the model.

3.2.2 Material

The composition of mortar used for Lagavant method is given in table 3.2, with W/C=0.5, and CEM I 52.5 cement for Project MACENA was used used for the test. The chemical composition of the cement is in the table 3.1. The sand and water used in the experiment were normalized sand following the Norm EN 196-1 and tap water. Besides, the superplastisizer (SP) SIKAPLAST TECHNO 80 was added in the mortar.

Table 3.1: Chemical composition of the cement(w.t.%)

elementary composition/w.t.%	
LOI	2.1
SiO_2	20.6
Al_2O_3	4.5
Fe_2O_3	2.3
TiO_2	0.3
MnO	0.1
CaO	63.2
MgO	2.1
SO_3	3.3
K_2O	0.73
Na_2O	0.16
P_2O_5	0.3
S^{2-}	0.02
Cl^-	0.05

Table 3.2: The composition of mortar for Langavant Method(kg/m^3 mortar)

Cement	Sand	water	SP
450	1350	235	3.375

The composition of the cement paste used in the thermogravimetry was the same as that used in the Langavant test.

3.2.3 Characterization of hardened cement paste

One of the advantage of the dehydration model is that once the amounts of the hydrates are determined, the water content evolution due to dehydration then can be calculated without any experiment. Here, the initial content of water is calculated with the hydration model proposed in (Buffo-Lacarrière *et al.*, 2007), which has been experimentally proved. Before dehydration, the quantity of water per m^3 cement paste can be written as a function of degree of hydration:

$$w_{max} = \sum_i w^i_{max} = \sum_i M_w \cdot n^i_{w,initial} \tag{3.3}$$

where w_{max} is the quantity of water in cement paste[kg/m^3 cement paste], w^i_{max} is the quantity of water of hydrate i in cement paste[kg/m^3 cement paste], and $n^i_{w,initial}$ is the amount of water of hydrate i before dehydration[mol/ (m^3 cement paste)]

$$n^i_{w,initial} = n^i_w \cdot n^i_v \tag{3.4}$$

with

- n^i_w the content of water in hydrate i[mol /mol hydrate]
- n^i_v the amount of hydrate i in cement paste [mol /m^3 cement paste].

The content of water in each hydrate is listed in table.3.3

The amount of hydrate i can be calculated as a function of hydration degree α^i. If the hydration degrees of all hydrates are the same,which means $\alpha^i = \alpha$, n^i_v can be written as:

$$n^i_v = n^i_{max} \cdot \alpha_{initial} \tag{3.5}$$

Table 3.3: The water content in each hydrate [mol / mol hydrate]

Hydrate	Water content(mol / mol hydrate)
CH	1
$C_4A\bar{S}H_{12}$	12
C_3AH_6	6
C-S-H	1.4

where n^i_{max} is the amount of hydrate when the cement paste is completely hydrated. According to equation.1.9 with $m = 1.75$, n^i_{max} can be calculated with equation.3.6 or equation.3.7:

$$\begin{cases} n^{CSH}_{max} = n_{SiO_2} \\ n^{CH}_{max} = n_{CaO} - 1.75n_{SiO_2} - n_{SO_3} - 3n_{Al_2O_3} \\ n^{AFm}_{max} = n_{SO3} \\ n^{C_3AH_6}_{max} = n_{Al_2O_3} - n_{SO_3} \end{cases} \tag{3.6}$$

$$\begin{cases} n^{CSH}_{max} = n_{SiO_2} \\ n^{CH}_{max} = n_{CaO} - 1.75n_{SiO_2} - n_{SO_3} - 3n_{Al_2O_3} - n_{SO_3} \\ n^{AFm}_{max} = 1.5n_{SO3} - 0.5n_{SO_3} \\ n^{AFt}_{max} = 0.5n_{SO_3} - 0.5n_{Al_2O_3} \end{cases} \tag{3.7}$$

The kinetic law of cement hydration, which can be used to calculate the hydration degree α, was express as(Buffo-Lacarrière *et al.*, 2007):

$$\dot{\alpha} = A \cdot g \cdot \pi \cdot h \cdot S \tag{3.8}$$

where A is a calibration constant, g is the chemical activation term, π represents the water accessibility to anhydrous phase, h is the thermal activation and $S = 1$ for clinker. For clinker, the chemical activation term was expressed as:

$$g = \frac{\alpha C_{p0clinker}}{MIN(W_{ps}, W_p)} \tag{3.9}$$

with

- α degree of hydration

- $C_{p0clinker}$ initial volumetric concentration of clinker

- W_p the volumetric concentration of water.

The accessibility of water to anhydrous phase follows:

$$\pi = \exp\left[-\frac{1}{n}\left(\frac{\bar{r}_m}{r_k}\right)^n\right] \tag{3.10}$$

with

- n, r_k calibration parameters

- $\bar{r}_m$ the current thickness of hydrate layers around anhydrous grain.

The thermal activation item h is described with Arrhenius law:

$$h = \exp\left(-\frac{E_a}{R}\left[\frac{1}{T} - \frac{1}{T_0}\right]\right) \tag{3.11}$$

with

- E_a activation energy of clinker

- T temperature in Kelvin[K]

- R the ideal gas constant(8.314[J·mol^{-1}·K^{-1}])

The kinetics of hydration thus could be calculated with equation.3.8–3.11. The three calibration parameters A, r_k and n were fitted with Lagavant test. To sum, as long as we know

1) the composition of the cement

2) the heat release due to hydration(from Langavant test)

3) the curing age

the initial water content in cement paste before dehydration can be calculated. Then, with known pre-drying condition, the initial dehydration degree for monosulfate can be determined according to table.1.1. The dehydration described in last chapter then can be applied to calculate the water release of cement paste due to dehydration.

For the cement in this study, the composition is shown in table.3.1. The fitting result with Langavant test is shown in fig.3.6, with $A = 2.153$, $r_k = 1.343$ and $n = 0.414$.

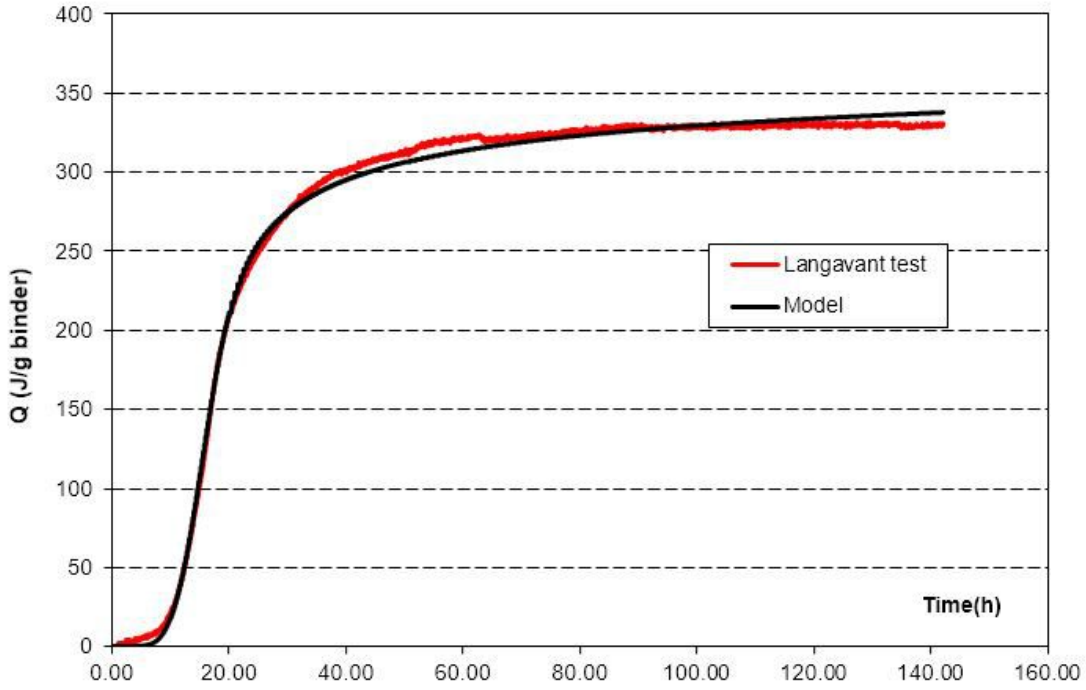

Figure 3.6: The fitting results with Langavant test

With hydration model mentioned above, the hydration degree after 60d curing was 0.861. Hence, the composition of the cement paste is shown in table.3.4

Table 3.4: composition of cement paste and water in hydrate

hydrate	CH	AFm	C_3AH_6	C-S-H
water in hydrate(kg/m^3 cement paste)	65.06	90.94	3.16	88.30

3.2.4 Pre-drying and thermal test procedure

To measure the dehydration of the cement paste, thermogravimetric analysis(TGA) was applied on the cement paste which has been cured in sealed cylinder plastic tubes(ϕ30mm$\times$60mm) under 20°C for 60 days.
To remove the free water, the vacuum drying methods mentioned in section.1.2 are preferable. Here, a kind of freeze-drying method was adopted. The samples were soaked into liquid nitrogen for 5 minutes just after being taken out of the tube, and then dried by lyophilization under -50°C with the lyophilizer Labconco Free Zone 4.5 for 48h. With this method, the initial dehydration degree of monosulfate $\xi_0^{AFm} = 1/3$. After drying, the samples were ground until all of them passed the 80μm sieve before the TGA test. The TGA was run by the analyzer STA 449 F3 manufactured by Netzsch. The temperature range for the test was 40-1000°C under heating rate 5K/min and 10K/min.

3.2.5 Results and analysis

The result of the tests is shown in fig.3.7. The effect of temperature was the same as that mentioned in section 1.2.1. The sample under lower heating rate(5K/min) lost more weight at given temperature compared to the higher heating rate(10K/min) during the heating process until 950°C, when both of samples lost all the bound water. The discrepancy of the total mass loss for the two experiments may be due to the experimental error.

It can be noticed that there were three obvious peaks in the DTG curve. The first peak was between around 100°C–300°C, which is due to the dehydration of monosuflate, C_3AH_6 and C-S-H, and it is difficult to separate them from each other in the experimental result. After that, the dehydration of CH resulted in obvious weight loss in the temperature range 400–600°C, and the increased rate of dehydration above 600°C was due to the decarbonation according to the previous report. These results will now be used, in addition to the ones already found in the literature, to clarify our dehydration model.
The comparison between the model and the TGA result was shown in fig.3.8.

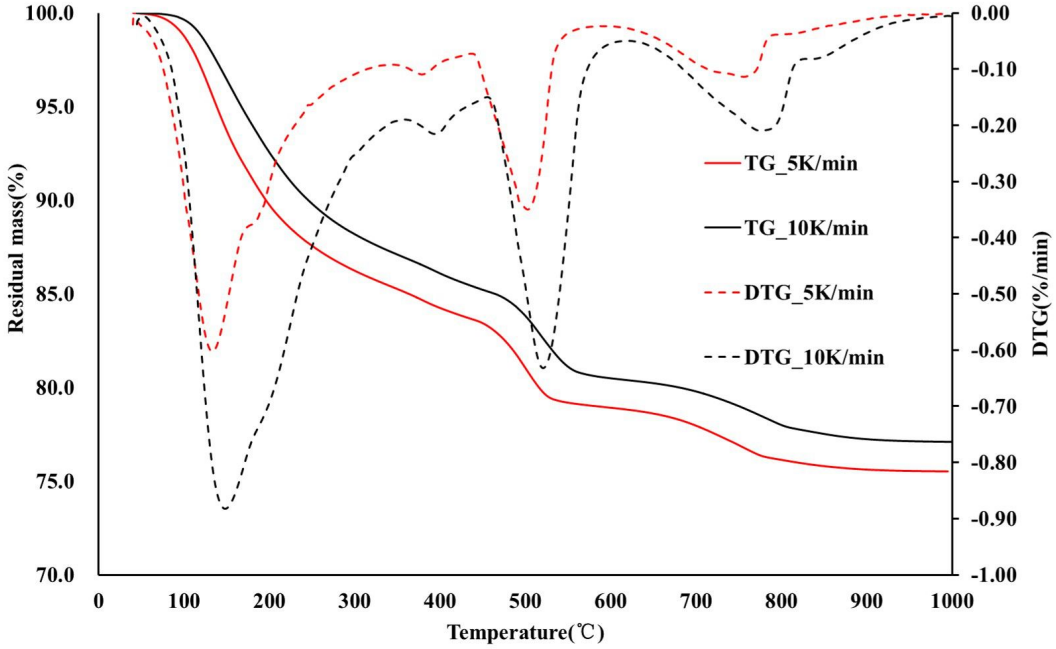

Figure 3.7: The result of TG/DTG test under heating rate 5K/min and 10K/min

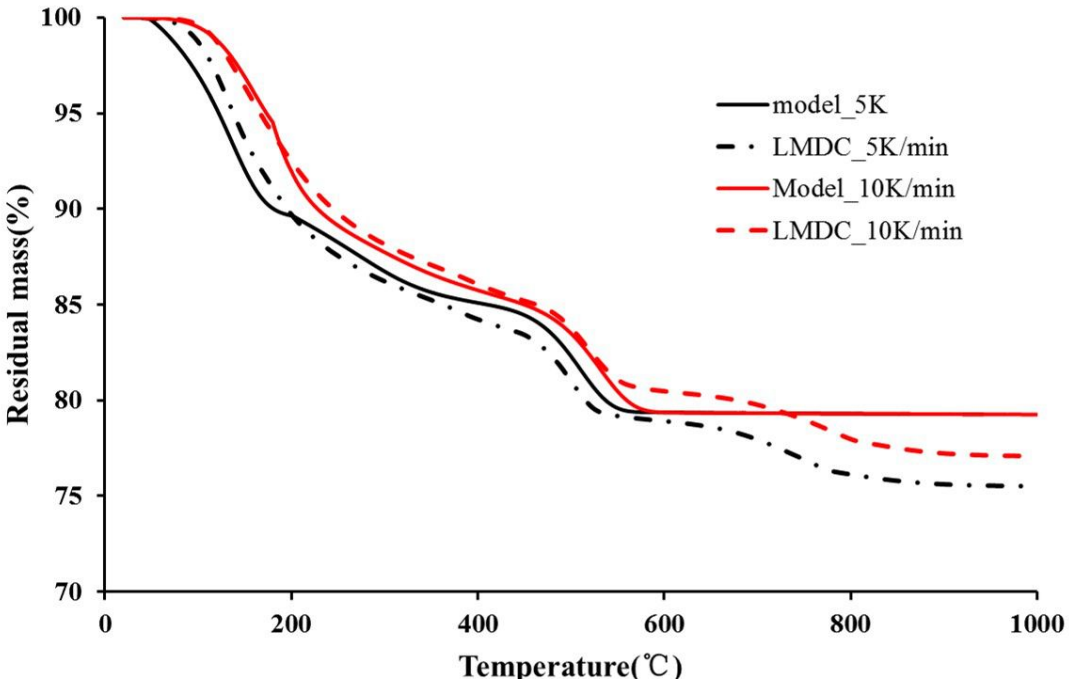

Figure 3.8: Comparison with TGA test under 10K/min

The model predicted the dehydration under heating rate of 10K/min very well before 550°C, and showed difference in the higher temperature range,

which is probably due to the carbonation of the sample.

3.3 Comparison with other experiments

The modeling result was first compared with existing TGA result in literature. The composition of cements used in the experiments were listed in table.3.5.

Table 3.5: Composition of cements in the TGA tests in literature

Literature	SiO_2%w.t.	Al_2O_3%w.t.	CaO%w.t.	SO_3%w.t.	W/C
(Morandeau *et al.*, 2014)	22.12	3.69	65.03	2.94	0.45
(he Shui *et al.*, 2010)	21.02	5.70	60.10	2.35	0.35
(Alarcon-Ruiz *et al.*, 2005)	19.45	4.80	59.00	2.95	0.33
(Menéndez *et al.*, 2012)	20.50	5.09	62.04	2.83	0.50
(Alonso and Fernandez, 2004)	19.60	4.43	62.61	3.29	0.40

In addition, some information that might influence the experimental results were in table.3.6

Table 3.6: Experimental conditions of TGA tests in literature

literature	Heating condition	drying method	Curing method and complementary information
(Morandeau *et al.*, 2014)	20°C-1150°C, 10K/min	freeze-drying	6-month cured in sealed plastic bottles, then was oven-dried at 45°C before put in a desiccator at RH62±5% and 20°C
(he Shui *et al.*, 2010)	From around 60°C to 1000°C,10K/min	–	Cured at RH>95% and 20°C for 28d
(Alarcon-Ruiz *et al.*, 2005)	5K/min	oven-dried at 105°C for 24h	Cured under water at 20°C for at least 28d
(Menéndez *et al.*, 2012)	up to 1050°C, 10K/min	–	Interior part of the matured specimen(4-year exposure to 20°C 60%RH)
(Alonso and Fernandez, 2004)	20°C-1000°C. 4K/min	–	The samples were sealed and cured for 70 days at room temperature (20± 2°C) inside the tubes

Because the hydration model used in section.3.2.3 requires the Langavant test, which has not been used in literature in table.3.6, to determine the fitting parameters, the hydration degree then was assumed as 0.8 for all of them due to their curing procedures. The water content in each hydrate per m^3 of cement paste thus could be calculated, and was listed in table.3.7 And this is used as the maximum mass of water that can be released due to dehydration w^i_{max}.

Table 3.7: Water content of each hydrate in cement paste (kg per 1 m^3 cement paste) in literature

hydrate	CH	AFm	C_3AH_6	AFt	C-S-H
(Morandeau *et al.*, 2014)	69.04	80.30	-	1.33	96.07
(he Shui *et al.*, 2010)	56.24	75.35	33.99	-	104.85
(Alarcon-Ruiz *et al.*, 2005)	67.90	97.49	13.46	-	99.98
(Menéndez *et al.*, 2012)	56.80	74.22	15.24	-	83.63
(Alonso and Fernandez, 2004)	74.61	98.21	2.75	-	91.00

As can be noticed in table.3.7, the calculated hydrates in (Morandeau *et al.*, 2014) includes some AFt instead of C_3AH_6. However, since the content of water in AFt only takes up 0.5% of all the water in the cement paste, it was neglected in the calculation.

In (Alarcon-Ruiz *et al.*, 2005), a reference sample being not dried and several samples heated at different temperatures were tested. Because 105°C was considered as common temperature for drying samples, samples pre-heated at higher temperatures were not used for the comparison. All the experimental result were shown in fig.3.9

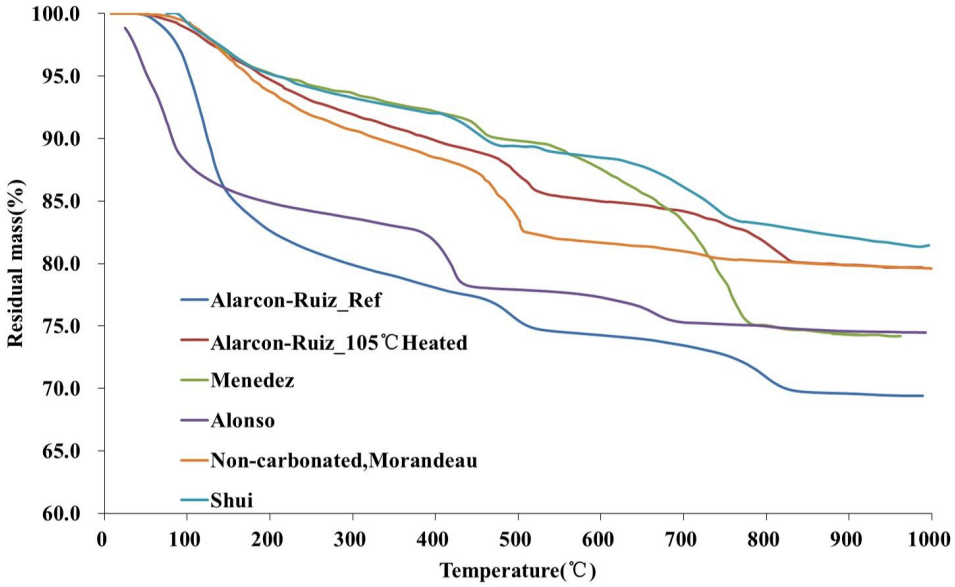

Figure 3.9: TGA tests of cement pastes in literature

TG results from Alonso and Alarcon-Ruiz (without pre-heating) showed rapid mass change below 200°C, which was due to the free water in the sample. The different dehydration profiles above 500°C may be caused by the carbonation. The comparison between the experimental results and the modeling results were shown in fig.3.10-fig.3.14.

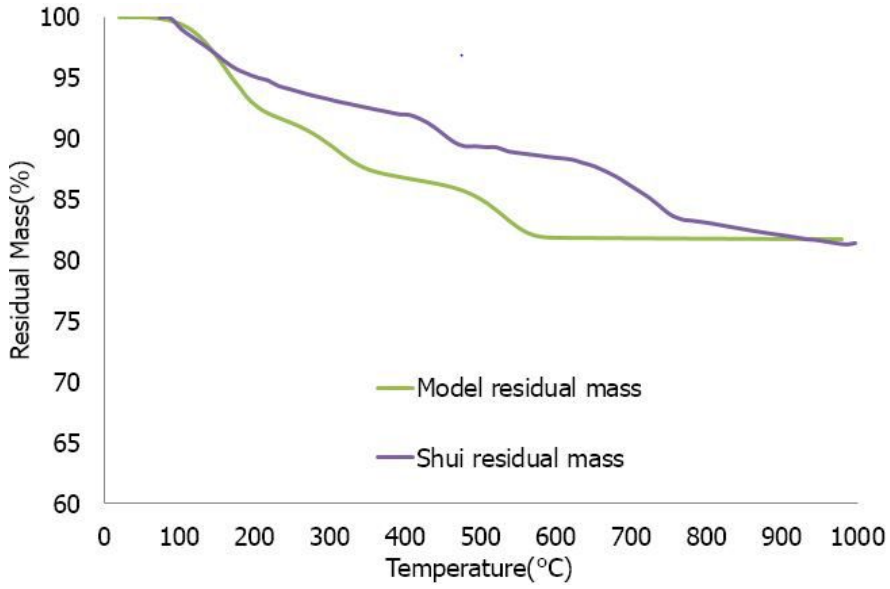

Figure 3.10: Comparison between shui, heating rate=10K/min(he Shui *et al.*, 2010)

From fig.3.10, it could be noticed that the modeling result showed well fit until 150°C. In addition,it shows similar temperature range for dehydration of CH. The deviation of the model was probably because the sample used in (he Shui *et al.*, 2010) was carbonated. Thus the TG curve showed small quantity of mass loss in temperature range around 450°C, which is considered as dehydration of CH. Instead, it showed rapid decline in the temperature afterwards, which corresponds to decarbonation.

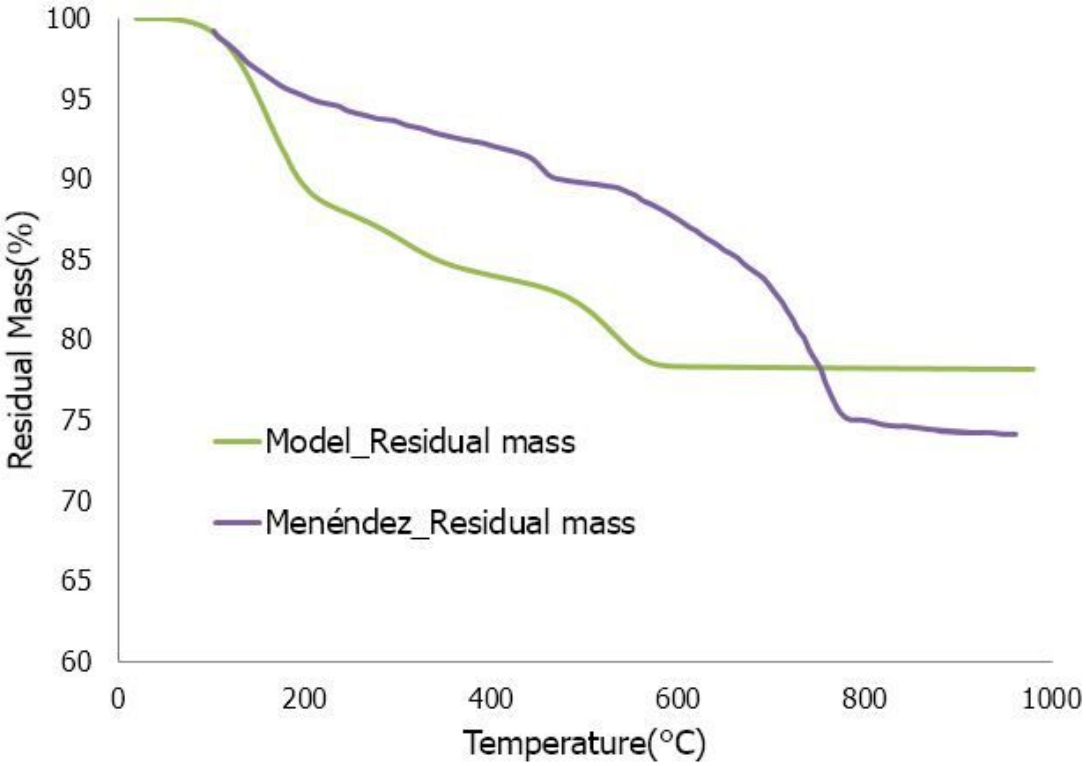

Figure 3.11: Comparison between Menéndez

Fig.3.11 illustrated another carbonated sample, which was exposed in the environment at 60% and 20°C. It showed some similarity with the TG result in fig.3.10. After dehydration of CH, an obvious decline corresponding to $CaCO_3$ was observed in the diagram. Moreover, $CaCO_3$ lost more weight than $Ca(OH)_2$ if the initial weights were the same. Therefore, the mass loss before dehydration of $CaCO_3$ should be more than that in fig.3.11 if the sample was non-carbonated, which might be closer to the result from modeling.

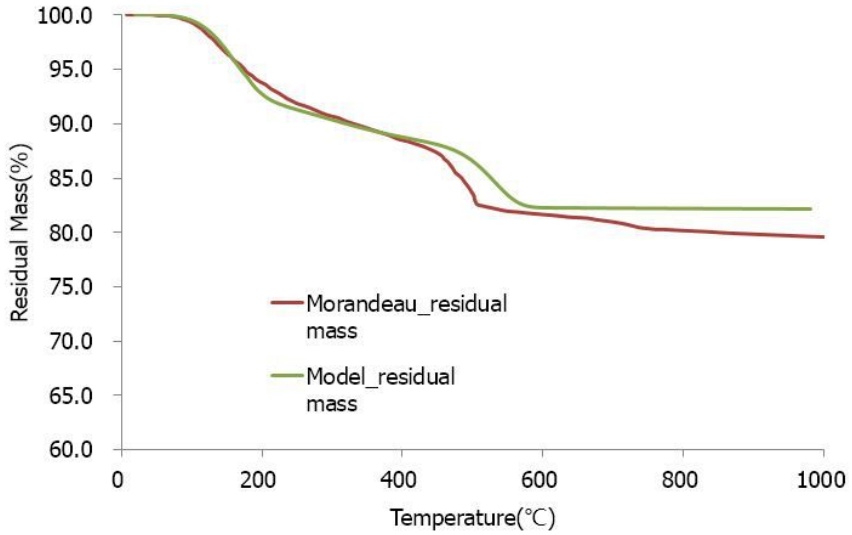

Figure 3.12: Comparison between Morandeau

Morandeau(Morandeau *et al.*, 2014) studied the influence of carbonation on cement paste, and the TG result of the non-carbonated sample was shown in fig.3.12. As explained in(Morandeau *et al.*, 2014), the carbonation was almost inevitable during the grinding of the sample, a little mass loss still could be observed around 700°C. However, it was better than experiments before. The modeling produced the TG curve with less error in the whole range than previous comparisons.

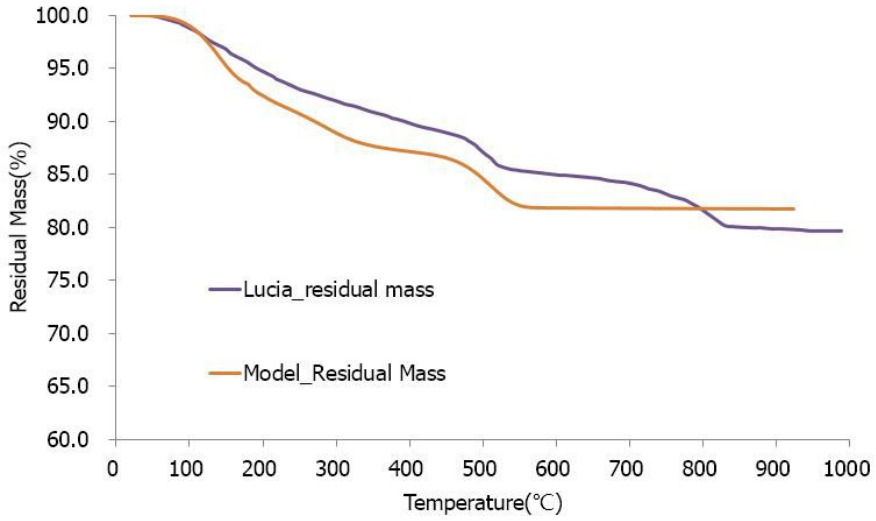

Figure 3.13: Comparison between Lucia

Alarcon-Ruiz(Alarcon-Ruiz *et al.*, 2005) performed the TG test under a different heating rate(5K/min), and the comparison was shown in fig.3.13. Modeling result showed the same tendency with the experimental result except for the part above 600°C, which could be considered as the mass loss due to decomposition of $CaCO_3$.

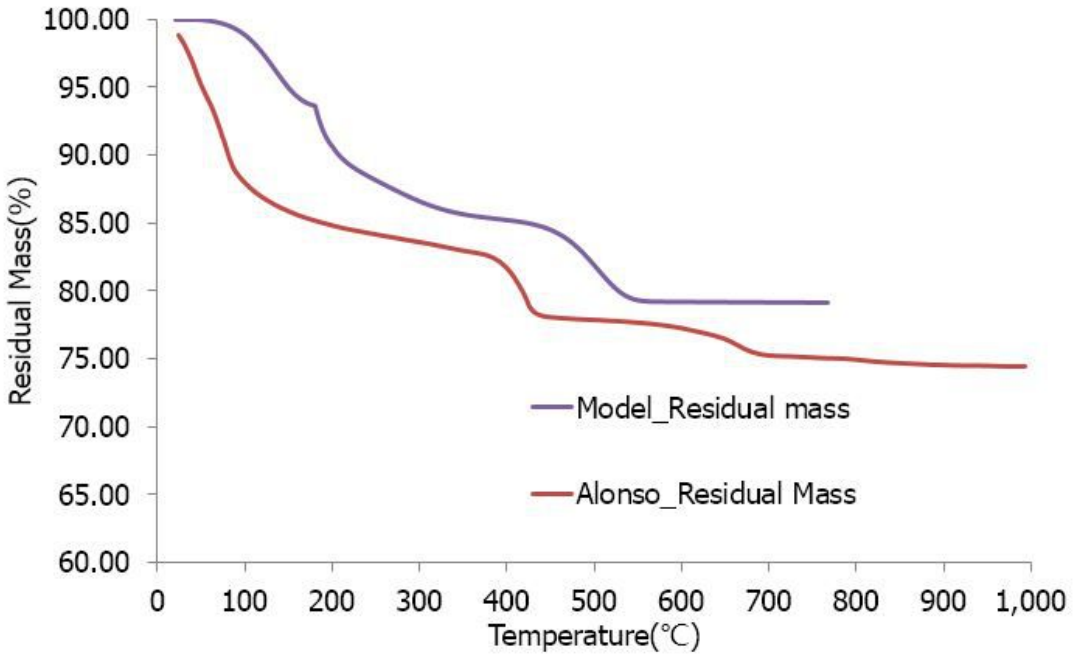

Figure 3.14: Comparison between Alonso

In (Alonso and Fernandez, 2004), there was obvious difference between experimental result and modeling result before. It is because the sample used in fig.3.14 was tested after curing process without pre-drying method, so the water in the sample contained free water as well. Moreover, carbonation, which could influence dehydration of CH, can be observed above 600°C. Since some details of the experiments were not clear, the modeling result sometimes showed obvious difference. However, as long as the important information like the drying condition of the sample and heating history was given, the predicted result could be rather accurate. In order to validate the model with different heating rate and different compositions of cement pastes, some TG tests were performed.

Conclusion of Part I

In this part, models for dehydration of hydrates in cement paste were built, with which the dehydration model for dehydration of paste was established.
To study the dehydration process of cement paste, the first step is to determine the hydrates that are of most influence in the problem. In this case, C-S-H, CH, TCA and AFm are chosen as hydrates to study.
The existing models to calculated the mass loss due to dehydration could be categorized as: 1) linear model; 2) kinetic model; 3) kinetic model with equilibrium. Each of them have their limit, so a new dehydration model for concrete is proposed in this study. The model contains both equilibrium and kinetic parts, and is able to be applied on cement paste with different composition without re-fit the parameters.
Dehydration models for CH, AFm and TCA were based on experiments on pure crystals, and the dehydration model for C-S-H was deducted by subtract the mass loss of all the other hydrates from the TG curve of cement paste. The experimental data for that was under the heating rate 5K/min.
The model was compared with experiments 1) under different heating rate; 2) with different composition of cement; 3) use different heating method, and showed good capability to predict the dehydration process of cement paste without carbonation. In next chapter, the dehydration will be implemented in the water and heat transfer model and applied to a concrete structure.

The dehydration model will be implemented in a transfer model, and the detailed water and heat transfer model for concrete under temperature up to 200°C will be explained in Part II. The model will be applied for mock-up MAQBETH(Bary *et al.*, 2012) without considering the mechanical aspects.

Part II

HEAT AND WATER TRANSFER

Introduction

The objective of this part is to simulate the coupled mass and heat transfer in concrete exposed up to 200°C with the dehydration model developed in Part. I, and study the influence of different parameters on the temperature, relative humidity and pressure evolution.
Chapter.1 introduced and compared the existing models and concerning parameters in Hygro-thermal modeling for concrete. Chapter.2 describes the hygro-thermal model that is to use for the simulation in this thesis, the simulation is then validated with the MAQBETH mock-up. Chapter.3 discussed the influence of concrete permeability and heat of dehydration on the temperature and vapor pressure profiles, and it finishes by an application to the simulation for structures with different thickness and under different thermal loadings.

Chapter 1

Literature review

In order to study the behavior of concrete under high temperature, there have been a number of models for water and heat transfer in concrete developed. Z. P. Bazant(Bažant and Thonguthai, 1979), Schrefler(Schrefler *et al.*, 2002), Bary(Bary *et al.*, 2012)(Bary *et al.*, 2008) and Dal Pont(Dal Pont *et al.*, 2011) all proposed their own models to describe the water and heat transfer process in concrete exposed to high temperature. One of the obvious difference between those models is that some of them consider the composition of the gaseous phase as vapor(Bažant and Thonguthai, 1979)(Bary *et al.*, 2008)(Bary *et al.*, 2012), while others consider it as a mixture of both vapor and dry air(Baroghel-Bouny, 2007),(Gawin *et al.*, 1999),(Gawin *et al.*, 2002),(Dal Pont and Ehrlacher, 2004),(Schrefler *et al.*, 2002).

1.1 Water transfer

1.1.1 Water transfer at ambient temperature

The mass balance equation for water transfer is

$$\frac{\partial m}{\partial t} = -\nabla \cdot (\boldsymbol{J}) + \dot{f} \tag{1.1}$$

with:

- m mass of fluid per m^3 of concrete[kg/m^3]
- $\boldsymbol{J}$ the flow term of liquid[$kg/m^2/s$]
- $\dot{f}$ the source term[$kg/m^3/s$]

If the gaseous phase is considered as water vapor, equation.1.1 becomes:

$$\begin{aligned} \frac{\partial}{\partial t}(m_l) &= -\nabla \cdot (m_l \boldsymbol{v_l}) - \mu_{l\to v} + \dot{d} \\ \frac{\partial}{\partial t}(m_v) &= -\nabla \cdot (m_v \boldsymbol{v_v}) - \mu_{v\to l} \end{aligned} \tag{1.2}$$

where $\boldsymbol{v_l}$ and $\boldsymbol{v_v}$ are velocities of water liquid and vapor[m/s], respectively. $\dot{d}$ is the water release rate due to dehydration [kg/(m$^3 \cdot s$)], and $\mu_{l\to v}$ and $\mu_{v\to l}$ are rate of vaporization and condensation[kg/(m$^3 \cdot s$)], respectively. If the gaseous phase was considered as the mixture of dry air and water vapor, the conservation equation for dry air is required, so Equation.1.1 becomes(Dal Pont and Ehrlacher, 2004):

$$\begin{aligned} \frac{\partial m_w}{\partial t} &= -\nabla \cdot (m_l \boldsymbol{v_l} + m_v \boldsymbol{v_v}) + \dot{d} \\ \frac{\partial m_a}{\partial t} &= -\nabla \cdot (m_a \boldsymbol{v_a}) \end{aligned} \tag{1.3}$$

with

- m_w Mass of water per m^3 concrete [kg/m^3]
- m_a Mass of dry air per m^3 concrete [kg/m^3]
- $m_a \boldsymbol{v_a}$ Flux of dry air [kg/m^2/s]

1.1.2 Effect of high temperature

High temperatures have influence on some fluid properties(density, dynamic viscosity,...), concrete property(permeability), and desorption properties of concrete(desorption,isotherm). Thermal loading at high temperature therefore is able to exert some influence on the mass transfer in concrete.

Desorption isotherm

When exposed to an environment of high temperature, the concrete undergoes a process of desorption. To describe the relationship between water content and relative humidity(or vapor pressure) at certain temperature during the process, different desorption isotherms were proposed.
Bazant and Thonguthai(Bazant and Thonguthai, 1978) proposed that the water content follows:

- For relative humidity $h_r < 0.96$,

$$\frac{m_w}{c} = \left(\frac{m_{w,sat}(25°\mathrm{C})}{c} h_r\right)^{1/m(T)} \quad m(T) = 1.04 - \frac{T'}{22.3 + T'} \quad T' = \left(\frac{T+10}{T_0+10}\right)^2 \tag{1.4}$$

  where c is the mass of anhydrous cement per m^3 of concrete, and m_w is the mass of water per m^3 of concrete, and $T_0 = 25°\mathrm{C}$.

- For $h_r \geq 0.96$ The water content w linearly increases as h_r rises from 0.96 to 1.04.

The isotherms following that method was illustrated in fig.1.1, with concrete density=2300[kg/m^3], cement content=300[kg/m^3] and free water content=100[kg/m^3]. This model made clear difference between the desorption isotherm behavior between RH<0.96 and RH>0.96 based on the fact that when the relative humidity is higher than certain value(here is 0.96), the water content will increase much more rapidly than that at lower relative humidity. This phenomena was also observed by Foley(Foley *et al.*, 2012).

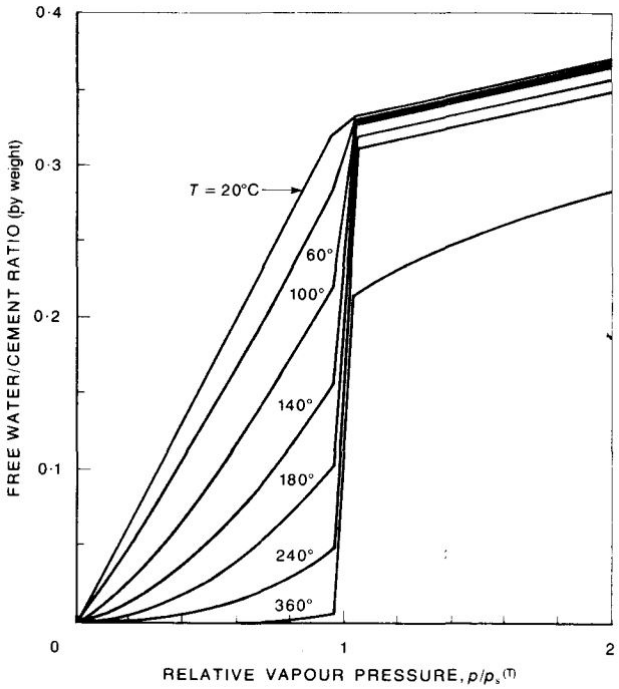

Figure 1.1: Calculated relation between free water/cement ratio and vapor pressure at various temperatures(Bažant and Thonguthai, 1979)

In (Bary *et al.*, 2012), when the relative humidity $h_r < 0.94$, Bary used the same isotherms as in (Poyet, 2009), and the details of the experiments results were presented in (Poyet, 2009). In that method, the relative humidity in concrete at arbitrary temperature followed:

$$h_r(T, w) = h_r(T_0, w)\frac{p_{vs}(T_0)}{p_{vs}(T)} \exp\left(-\frac{Q_{st}}{R}\frac{T_0 - T}{TT_0}\right) \tag{1.5}$$

with

- $p_{vs}(T_0), p_{vs}(T)$ saturated vapor pressure at reference temperature and at temperature T[K] in [Pa]. The evolution of p_{vs} as a function of T follows equation.1.26
- Q_{st} the energy involved in the process[kJ/mol]
- T_0 reference temperature, which is 303.15[K].

Q_{st} represents the latent heat of desorption, and it is a function of the thickness of the water layers. That is to say, $Q_{st} = Q_{st}(w/w_m)$, where w_m is the water content when there is only one layer of water on the pore walls of the concrete. For a specific sample, if the desorption isotherm(water content as a function of relative humidity) at two different temperatures are known, Q_{st} can be obtained with equation.1.5. In (Bary *et al.*, 2012), the value of Q_{st} was calculated with the experiments performed by Poyet at 30°C and 80°C, and the result is shown in fig.1.2.

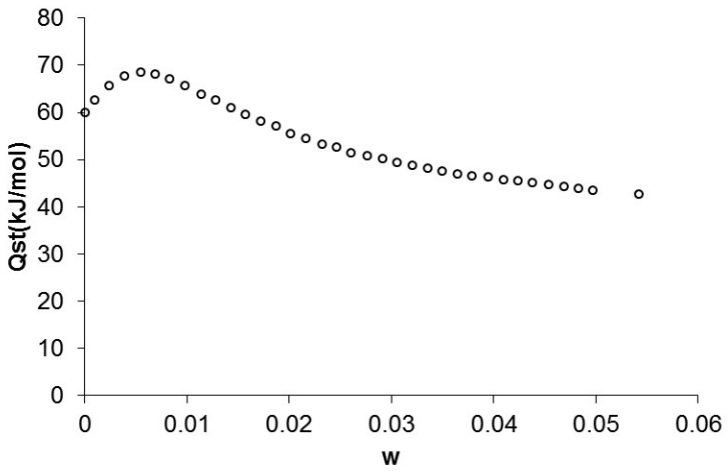

Figure 1.2: Q_{st} according to experiments by Poyet(Poyet, 2009)

GAB model can also be adopted to describe the isotherm at reference temperature $h(w, T_0)$ in equation.1.5. The model was built based on the experimental result from (Poyet, 2009).

$$w(h_r) = \frac{C_G k_G w_m h_r}{(1 - k_G h_r)(1 + (C_G - 1)k_G h_r)} \tag{1.6}$$

with $C_G = 4.69, k_G = 0.592, w_m = 0.02534$.

When $h_r \geq 0.94$, the water content was considered having a parabolic relationship with the relative humidity.

The isotherm proposed by Bary(Bary *et al.*, 2012) was shown in fig.1.3, in which the dot lines represented the results following equation.1.6 and equation.1.5

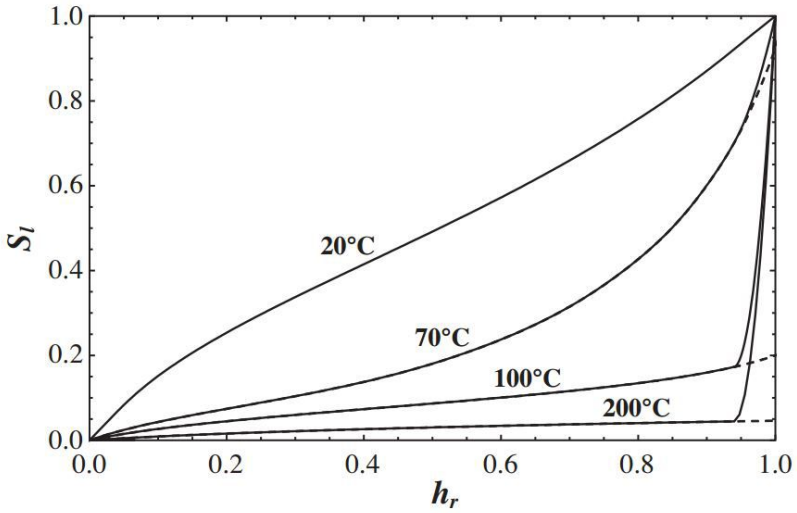

Figure 1.3: Numerical desorption curves obtained at different temperatures ranging from 20 to 200°C.(Bary *et al.*, 2012)

Assume that the sample be saturated when the water content reached the maximum value, the comparison between the results in Bary(Bary *et al.*, 2012) and the converted results based on the experiments by Poyet(Poyet, 2009) are shown in fig.1.4. The round and square dots are the experimental results from Poyet(Poyet, 2009) and the lines are the modeling results.

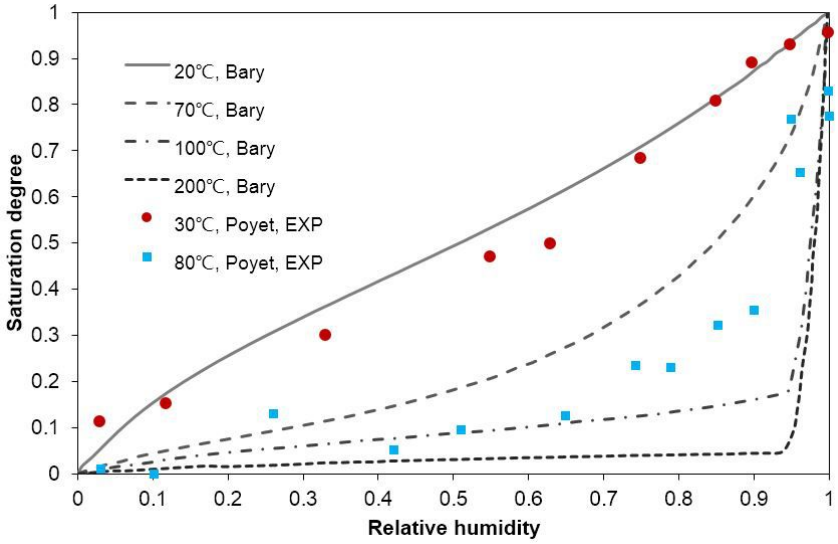

Figure 1.4: The converted results according to (Poyet, 2009) and the calculated results from (Bary *et al.*, 2012)

When the temperature is elevated, two phenomena were observed. First, the increasing rate of saturation degree with relative humidity decreases. The other one is that the saturation degree will increase rapidly when relative humidity goes higher, which can cause convergence problems during the simulation. The explanation of this difficulty was given in (Bary *et al.*, 2012). During my first attempts with this isotherm, I found it difficult to get the calculation converged. Hence, it was not adopted in the final simulation.

The two methods above established a direct relationship between water content and vapor pressure/relative humidity, and both of them set a "critical relative humidity"($h_r = 0.94$ in (Bažant and Thonguthai, 1979) whilst $h_r = 0.96$ in (Bary *et al.*, 2008)).

In some researches, the capillary pressure curve was used to establish the relationship between saturation degree and capillary pressure/relative humidity. Based on Van Genuchten water retention curve(Van Genuchten, 1980), considering the effect of temperature on the sorption curve of cementitious material, Dal Pont(Dal Pont and Ehrlacher, 2004) proposed the equation to calculate capillary pressure $p_c(S_l, T)$, which follows:

$$p_c = \frac{\sigma(T)}{\sigma(T_0)} a_c (S_l^{-b_c} - 1)^{(1-\frac{1}{b_c})} \tag{1.7}$$

with

- surface tension $\sigma(T) = \sigma_0(1 - \frac{T}{T_{cr}})^{n_\sigma}$
- a_c, b_c capillary curve coefficients determined experimentally from experimental curve(Baroghel-Bouny, 1994).

Table 1.1: Parameters used in equation.1.7

Parameters	Value
a_c	46.9364 MPa
b_c	2.0601
σ_0	$155.8 \times 10^{-3}\mathrm{N} \cdot \mathrm{m}^{-1}$
T_{cr}	647.15K
n_σ	1.26

The comparison with Poyet's experiments were shown in fig.1.5,

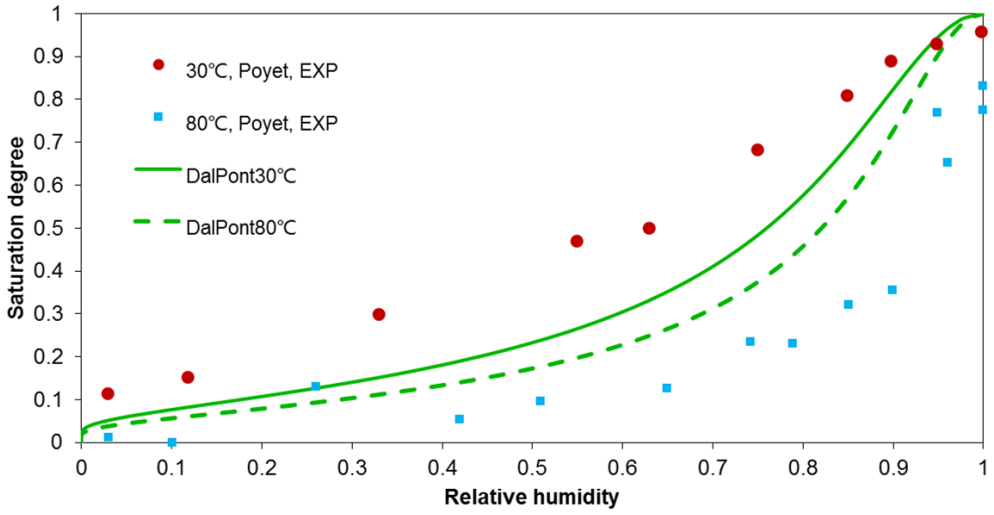

Figure 1.5: The desorption isotherm comparison between the experiments in(Poyet, 2009) and calculation with the method in Dal Pont and Ehrlacher (2004)

It illustrated that comparing with the experimental results in (Poyet, 2009), the calculation results under estimated the effect of the temperature on the evolution of the desorption isotherm, and the difference between at 30°C was probably due to that there were experimentally determined parameters in the

method in (Dal Pont and Ehrlacher, 2004), and the materials used in those two researches were not the same. With the method using equation.1.7 , the drastic change of saturation degree S_l with the variation of relative humidity can be avoid. Hence, it was adopted as the method in this thesis to describe the desorption isotherm.

Permeability

The permeability of concrete is another very important property in transfer problems in concrete. The permeability of concrete k_i was commonly expressed as:

$$k_i = k_{ri} k_i^0 \tag{1.8}$$

where k_i represents the permeability of concrete to liquid i, which means $i = a$ for air, $i = v$ for vapor, $i = l$ for liquid water. The relative permeability k_{ri} was considered as function of saturation degree of liquid water. k_i^0 is the intrinsic permeability, which is independent from the saturation degree of concrete.

- **Relative permeability**
  The relative permeability k_{ri} was considered as a function of saturation degree.
  Based on Mualem model(Mualem, 1976), Van Genuchten(Van Genuchten, 1980) proposed that the relative permeability to liquid follows:

$$k_{rl}(S_l) = \sqrt{S_l}(1 - (1 - S_l^{1/m})^m)^2 \tag{1.9}$$

  Similarly, the permeability to gaseous phase could be deducted as:

$$k_{rv}(S_l) = (1 - S_l)^{1/2}(1 - S_l^{1/m})^{2m} \tag{1.10}$$

  Bary(Bary *et al.*, 2008)(Bary *et al.*, 2012)adopted the corrected function for cementitious material proposed by Monlouis-Bonnaire JP(Monlouis-Bonnaire *et al.*, 2004). The relative permeability thus follows:

$$k_{rv} = (1 - S_l)^p(1 - S_l^{1/m})^{2m} \tag{1.11}$$

where $p = 5.5, m = 0.56$. Baroghel-Bouny (Baroghel-Bouny, 2007)used the same corrected equations for relative permeability with different coefficients $m = 0.4854, 0.4396$ for liquid water and vapor, respectively. Besides, Luckner(Luckner *et al.*, 1989) proposed that $p = 1/3$.

J.H. Chung(Chung and Consolazio, 2005) proposed that the relative permeabilities of concrete were a function of both porosity and saturation degree of liquid water. The relative permeability to gas was written

$$k_{rg} = 10^{S_w \lambda} - 10^{\lambda} S_w \tag{1.12}$$

with :

- S_w Saturation degree of liquid water
- $\lambda = 0.05 - 22.5\phi$, and ϕ is porosity of concrete

The relative permeability to liquid water was approximately expressed in equation.1.13 as:

$$k_{rl} = k_{rg}(1 - S_w) \tag{1.13}$$

Taking the form from(Bear, 1972)(Forsyth and Simpson, 1991)(Perré and Degiovanni, 1990),Dal Pont (Dal Pont *et al.*, 2007)(Dal Pont *et al.*, 2011)used the following equations to calculate the relative permeabilities of concrete to liquid water and gas:

$$k_{rl} = \left(\frac{S_l - S_{ir}}{1 - S_{ir}}\right)^{A_w} \tag{1.14}$$

$$k_{rg} = 1 - \left(\frac{S_l}{S_{cr}}\right)^{A_g} \tag{1.15}$$

Equation.1.14 is valid when the saturation degree S_l is greater than the irreducible saturation degree S_{ir}, which is often assumed as $S_{ir} = 0$, and A_w is a constant usually in the range <1, 3>. Equation.1.15 is valid when $S < S_{cr}$, which is the critical saturation value which is the maximum saturation value for a concrete to let gas flow the medium. The constant A_g is in the range <1, 3> as well. In order to compare those different

equations to calculate relative permeability of water liquid and vapor, following assumptions are made:

1. The porosity of the concrete is 0.1;
2. The gas will flow the medium until the saturation degree reaches 1. In other words, $S_{cr} = 1$;
3. The irreducible saturation degree is 0($S_{ir} = 0$);
4. The constants both A_w and A_g were tested with value 1 and 3.

The relative permeability of gas was compared with the experimental results from Monlouis-Bonnaire(Monlouis-Bonnaire *et al.*, 2004), in which a concrete made of OPC with a $W/C = 0.48$) was tested, which is similar to the concrete that is going to be used for the validation in this thesis. The comparison is shown in fig.1.6

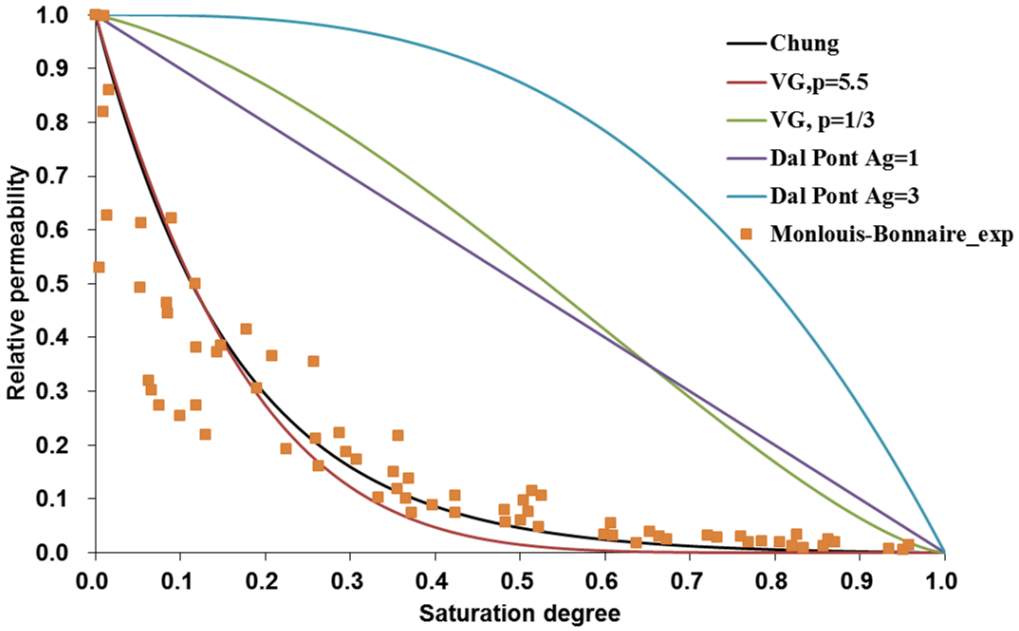

Figure 1.6: Relative permeability of concrete to gas

Table.1.2 is the correspondance of the source of equations and legends in fig.1.6: It is illustrated in fig.1.6 that the results calculated with equation.1.12, 1.15 and equation.1.11 with $p = \frac{1}{3}$ are not suitable for the tested concrete in (Monlouis-Bonnaire *et al.*, 2004). In equation.1.12, the effect of

Table 1.2: Correspondence of legends and equations in fig.1.6

Legend	Equation
Chung	Equation.1.12
VG, p = 5.5	Equation.1.11 with $p = 5.5$
VG, p = 1/3	Equation.1.11 with $p = \frac{1}{3}$
Dal Pont Ag = 1	Equation.1.15 with $A_g = 1$
Dal Pont Ag = 3	Equation.1.15 with $A_g = 3$
Monlouis-Bonnaire_exp	Experimental data from (Monlouis-Bonnaire *et al.*, 2004)

porosity was taken into account in the estimation of relative permeability. In order to emphasize that the relative permeability is the permeability variation with saturation degree of concrete, equation.1.12 was not preferred in the following work. The effect of the variation of porosity will be taken into account in other parts of the transfer model. Hence, the modified Van-Genuchten equations with $p = 5.5$(equation.1.11) were adopted to calculate the relative permeability of concrete to vapor. Correspondingly, the relative permeability of liquid water was estimated with equation.1.9, and the variation with the saturation degree was shown together with that of gas relative permeability in fig.1.7

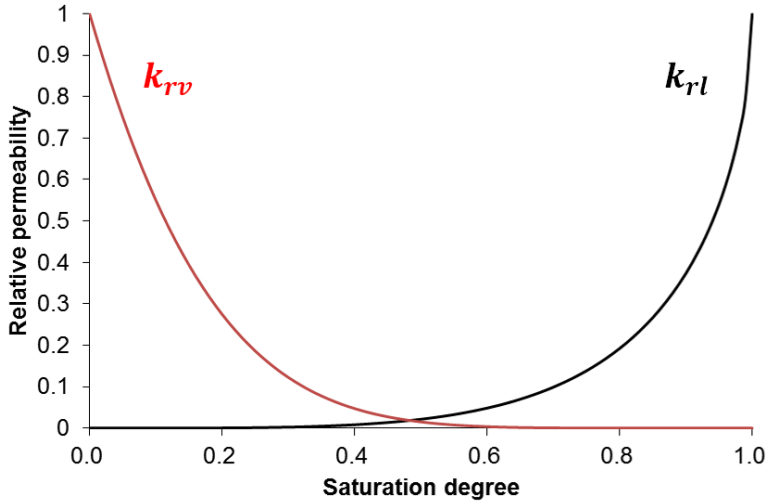

Figure 1.7: Relative permeabilities of concrete to water liquid and vapor

- **Klinkenberg constant**
  Kundt and Warburg(Kundt and Warburg, 1875) proved that the layer of gas adjacent to the wall was in motion while the gas flowing along a solid wall. Based on that, Klinkenberg proposed the theory of slippage, which described the velocity of the gas flow. With that theory, the permeability of the idealized porous media to the gaseous phase was deducted as:

$$k_g = K\left(1 + \frac{b}{\bar{p}}\right) \tag{1.16}$$

  with:

  - k_g Permeability to gaseous phase[m^2]
  - K Permeability constant[m^2]
  - b Klinkenberg constant[atm]
  - $\bar{p}$ Mean pressure of the inlet and outlet pressure[atm].

  Equation.1.16 describes
  "a relation between the apparent and true permeability of an idealized porous system to gas."(Klinkenberg *et al.*, 1941)

  For cementious material, various values for Klinkenberg constant have been proposed.
  Studied the test data of permeability by Whiting(Whiting, 1988) and relationships between the intrinsic gas permeability and water permeability of near-surface concrete presented by Dhir et al.(Dhir *et al.*, 1989), Chung(Chung and Consolazio, 2005) developed the function describing the relationship between Klinkenberg constant, which is

$$b = \exp(-0.5818 \ln(K_{gas}) - 19.1213) \quad [\text{atm}] \tag{1.17}$$

  where K_{gas} is the intrinsic permeability to gaseous phase in [m^2]. Monlouis-Bonnaire(Monlouis-Bonnaire *et al.*, 2004) tested the evolution of effective permeability of concrete with gas pressure under different saturation degree. The experimental results were shown in Fig.1.8.

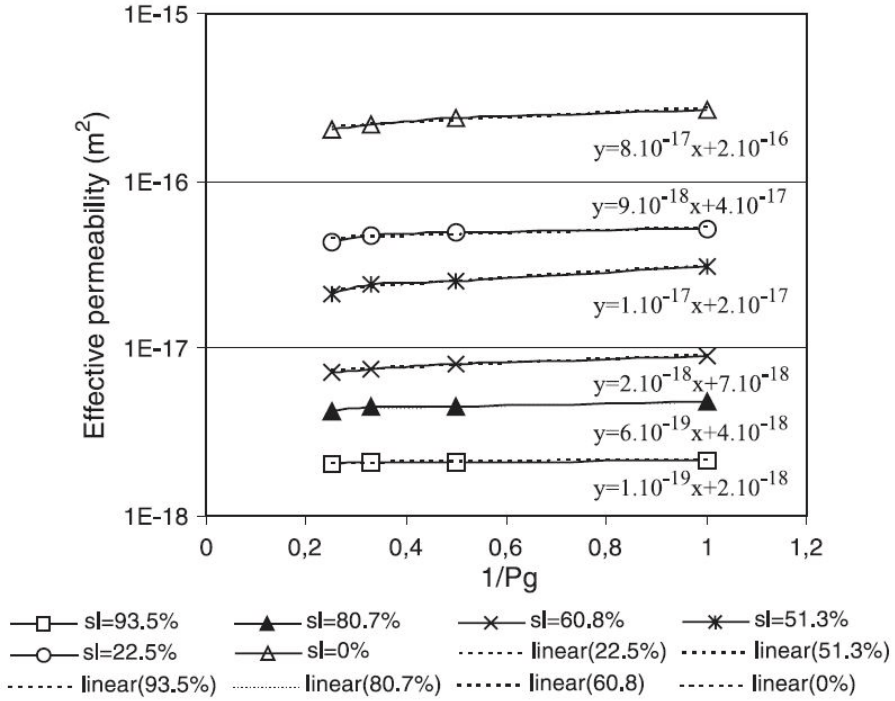

Figure 1.8: Effective permeability for different degree of saturation and gas pressures.(Monlouis-Bonnaire *et al.*, 2004)

The permeability evolution were linear with pressure, which was a confirmation of equation.1.16. The Klinkenberg constant b thus could be calculated at different saturation degree with the fitting equations in Fig.1.8, and the results were listed in table.1.3, with an average value of 0.275[atm].

Table 1.3: Klinkenberg constant at different saturation degree

Saturation degree	Klinkenberg Constant (atm)
0	0.0524
0.225	0.149
0.513	0.296
0.608	0.55
0.807	0.225
0.935	0.381

Assume that the intrinsic permeability of concrete to gas be in the range

1×10^{-17}—1×10^{-16}[m^2], the klinkenberg constant calculated with equation.1.17 is between 10[atm] and 38[atm]. And in (Chung and Consolazio, 2005), fig.1.9 showed the relations between klinkenberg constant and intrinsic gas permeability from different experiments and equations.

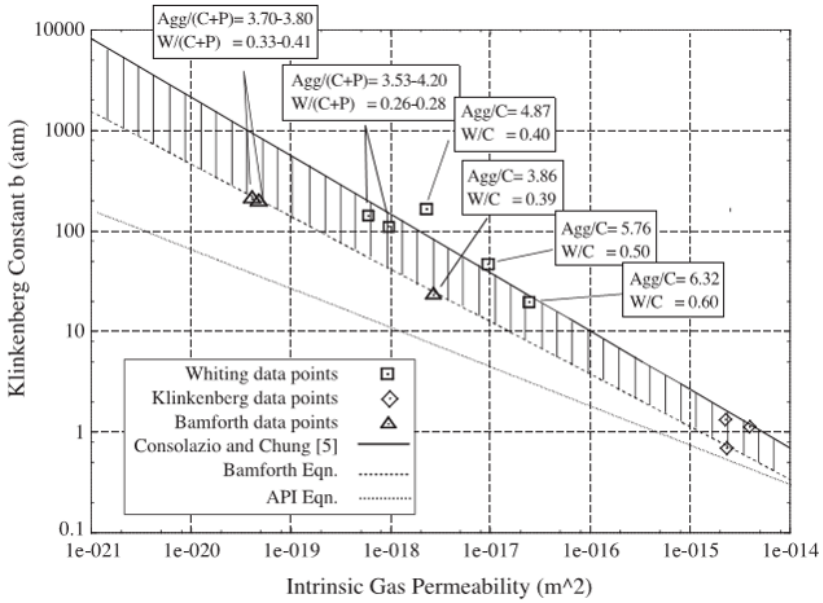

Figure 1.9: Klinkenberg constant vs. gas permeability of concrete(Chung and Consolazio, 2005)

It was reported that the results from Bamforth(Bamforth, 1987), which was shown in fig.1.10, approximately bounded the lower end Klinkenberg constant of concrete.

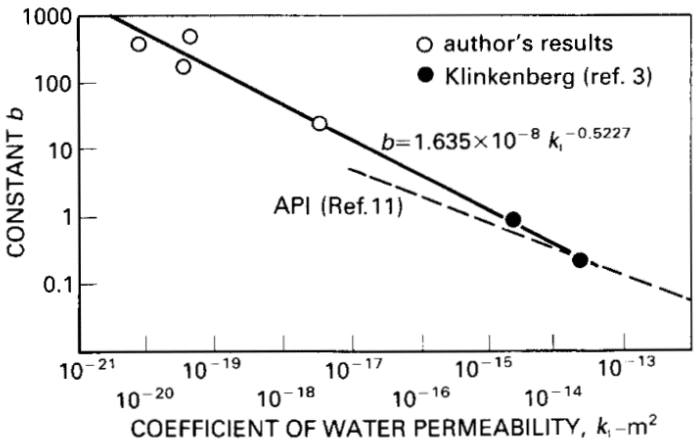

Figure 1.10: Klinkenberg constants in (Bamforth, 1987)

However, Bamforth used the intrinsic water permeability as permeability constant in equation.1.16 to calculate the Klinkenberg constant, which means the intrinsic gas permeability of concrete follows:

$$k_g^0 = k_l^0(1 + \frac{b}{\bar{p}}) \tag{1.18}$$

and the "Bamforth data points" were actually points representing (k_l^0, b).

For concrete with W/C ranging from 0.4 to 0.7, Dhir(Dhir *et al.*, 1989) established the relation between the intial intrinsic gas permeability and intrinsic water permeability. The experimental results are shown in fig.1.11

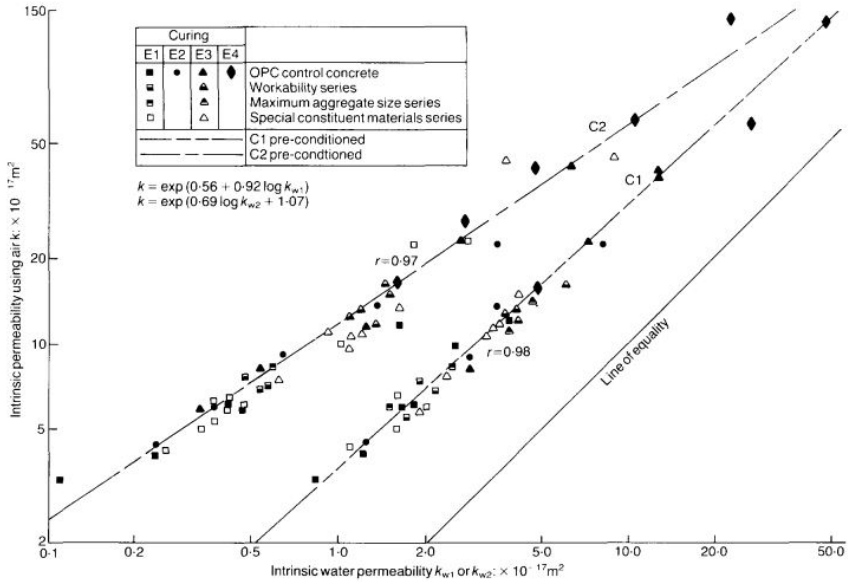

Figure 1.11: Relationship between initial intrinsic air permeability and intrinsic water permeability(Dhir *et al.*, 1989)

Where C1 was first dried under 105°C, and C2 was kept at room temperature and 55% RH before vacuum drying procedure. Here the result of C2 was taken into consideration because 105°C would probably cause damage to the structure of the specimens.
For C2, the relation follows:

$$K_g = 10^{0.69\,\lg(k_l)+1.07} \tag{1.19}$$

And the Kg/k_l^0 ratio ranges from 0.04 to 0.287. Hence, if K_g in equa-

tion.1.17 is going to be adopted to calculate the intrinsic permeability of gas k_g, which means the intrinsic gas permeability k_g^0 follows:

$$k_g^0 = K_g(1 + \frac{b}{\bar{p}}) \tag{1.20}$$

, $(1+\frac{b}{\bar{p}})$ should be approximately 1 or 2 orders smaller than the presented value calculated with k_l^0. According to the equation.1.21 in (Bamforth, 1987), if the water intrinsic permeability ranges from 1×10^-17[m^2] to 1×10^-16[m^2] , then $3.77[\text{atm}] \leq b \leq 12.6[\text{atm}]$.

$$b = 1.635 \times 10^{-8} k_l^0 - 0.5227 \tag{1.21}$$

Since $(1 + \frac{b}{\bar{p}}) > 1$, the average value of $b = 0.275$[atm] in (Monlouis-Bonnaire *et al.*, 2004) seems in the reasonable range. Because the concrete used in (Monlouis-Bonnaire *et al.*, 2004) was similar to that in the thesis and for the sake of simplification, $b = 0.275$[atm] was adopted in the following simulation.

- **Intrinsic permeability**
  Dal Pont(Dal Pont and Ehrlacher, 2004) used one function for the intrinsic permeability of concrete to both liquid and gas, which is:

$$k(T, p_g) = k_0 \cdot 10^{A_T(T-T_0)} \left(\frac{p_g}{p_0}\right)^{A_p} \tag{1.22}$$

  where $A_T = 0.05, A_p = 0.368$, and $k_0 = 2 \times 10^{-17}$ m^2 are the constants depending on the type of concrete.

  Some researchers used separated value for different phases. Bary(Bary *et al.*, 2012) proposed that the intrinsic permeability is a function of the mass loss due to dehydration, which is

$$k_{mv}(S_l = 0) = k_{mv}^0 \exp(0.2d) \tag{1.23}$$

  where d is the mass loss due to dehydration and $k_{mv}^0 = 1 \times 10^{-17}$ [m^2] is the initial intrinsic permeability to vapor. As for liquid water, the intrinsic permeability $k_{ml}^0(S_l = 1)$ was considered proportional to that of

vapor, which was $k_{ml}^0 = \alpha k_{mv}^0$, with $\alpha = 3 \times 10^{-5}$. This method was used by Chung(Chung and Consolazio, 2005) as well. He proposed α between 0.068 and 0.038 based on the research from Dhir(Dhir *et al.*, 1989) and Whiting(Whiting, 1988). The obvious difference between those two researches is due to that in (Bary *et al.*, 2012), K_g and α are both fitting parameters with the specific experiment. If the estimation of K_g was different from the real K_g, α would compensate that effect by differing from the real value as well. The experiment of gas permeability is not necessary, but both α and K_g cannot be used for another concrete.
Since the permeability of concrete to liquid and to gas are of great difference, it is more straightforward to consider them separately, which means to estimate them with the proportional relation with corresponding α for different concrete.

Physical properties of fluids

- **Density of liquid and vapor of water** ρ_l and ρ_v
  If the liquid water was considered as incompressible, the density of liquid water was dependent on temperature, and could be expressed as (Raznjevic, 1978)

$$\rho_l = 314.4 + 685.6 \left[1 - \left(\frac{T - 273.15}{374.14}\right)^{\frac{1}{0.55}}\right]^{0.55} \quad [\mathrm{kg/m^3}] \tag{1.24}$$

  If the vapor of water is considered as ideal gas, the density of vapor of water ρ_v can be calculated with Clapeyron equation, and will depend on both pressure and temperature. ρ_v can be expressed as

$$\rho_v = \frac{M_w p_v}{RT} \tag{1.25}$$

  where $M_w = 18$[g·mol^{-1}] is the molar mass of water.

  Both equation.1.24 and equation.1.25 are valid for the temperature lower than critical temperature of water $T_{cr} = 647.096$[K], and their variations with temperature were shown in fig.1.12. The densities from (Keenan *et al.*, 1969) were compared, and it was illustrated that when the temperature approaches T_{cr}, equation.1.24 and equation.1.25 showed more discrepancy with the values from (Keenan *et al.*, 1969). However, in the

temperature range from 293.15K to 473.15K, which is interesting to this thesis, both equations are acceptable for the calculation.

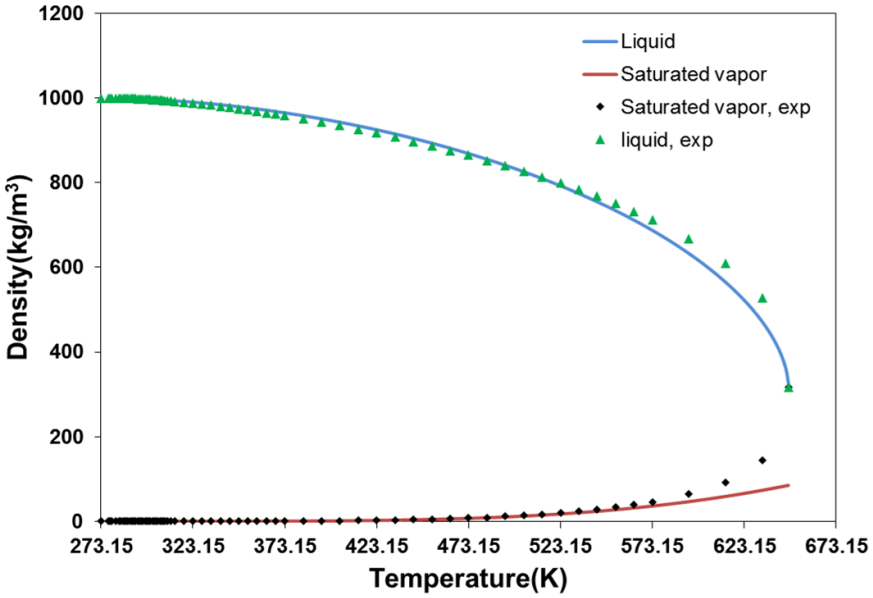

Figure 1.12: Density of liquid water and water vapor

- **Saturated vapor pressure** p_{vs} The saturated vapor pressure of water could be calculated with Clausius-Clapeyron equation as

$$p_{vs}(T) = p_{atm} \exp\left(\frac{\Delta H}{R}\frac{T - 373.15}{373.15T}\right) \tag{1.26}$$

In (Dal Pont and Ehrlacher, 2004), Dal Pont adopted $\Delta H = 39583.85[\text{J·mol}^{-1}]$(ASHRAE *et al.*, 2001). Bary(Bary *et al.*, 2012)adopted the tabulated results in (Raznjevic, 1978), and proposed the function in equation.1.27, which is of the same type with equation.1.26:

$$p_{vs}(T) = p_{atm} \exp\left(4871.3\frac{T - 373.15}{373.15T}\right) \tag{1.27}$$

The comparison of the two above are shown in fig.1.13, and there is not apparent difference between them.

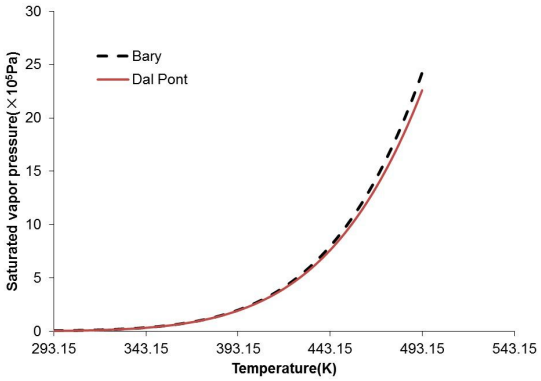

Figure 1.13: Saturated vapor pressure of water from Bary(Bary *et al.*, 2012) and Dal Pont(Dal Pont and Ehrlacher, 2004)

- **Dynamic viscosity of liquid and vapor of water η_l and η_v**
  Schmidt and Mayinger(Schmidt and Mayinger, 1963) performed tests to measure the dynamic viscosity of water under high pressures and high temperatures, and plotted their results with experimental results from Kestin(Kestin and Moszynski, 1958) and Timroth(Timroth and Vargaftik, 1940)(Timroth D. L. and Vargaftik, 1958). Fig.1.14 showed the comparison of those results, and there was not significant change when the pressure was raised from less than 10[atm] to more than 300[atm] comparing to the dramatic increase of dynamic viscosity due to the change of temperature in the range from 73°C to 300°C.

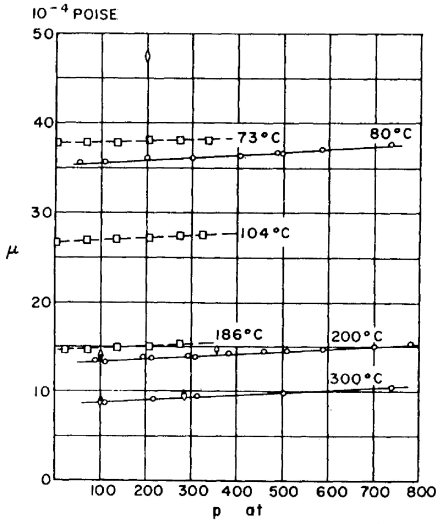

Figure 1.14: Dynamic viscosity of water(Schmidt and Mayinger, 1963)

The viscosity of liquid water is dependent on temperature(Reid *et al.*, 1987), and Dal Pont(Dal Pont and Ehrlacher, 2004) adopted the Watson formula(Thomas and Sansom, 1995), which is

$$\eta_l(T) = 0.6612(T - 229)^{-1.562} \tag{1.28}$$

Bary(Bary *et al.*, 2012) used the value in (ASHRAE *et al.*, 2001), which is

$$\eta_l(T) = 2.414 \times 10^{-5} \exp\left(\frac{570.58058}{T + 133.15}\right) \quad [\mathrm{kg}/(\mathrm{m} \cdot \mathrm{s})] \tag{1.29}$$

Where temperature T was in Celsius. Al-Shemmeri(Al-Shemmeri, 2012) proposed that the dynamic viscosity of liquid water follows

$$\eta_l(T) = 2.414 \times 10^{-5} \cdot 10^{(\frac{247.8}{T-140})} \quad [\mathrm{kg}/(\mathrm{m} \cdot \mathrm{s})] \tag{1.30}$$

The experimental results under 300[atm] in (Schmidt and Mayinger, 1963) was compared with the expressions above, and was plotted in fig.1.15

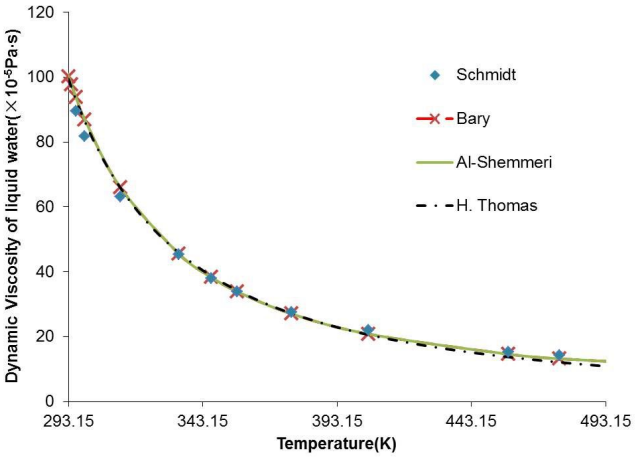

Figure 1.15: Experimental(Schmidt and Mayinger, 1963) and calculated(Bary *et al.*, 2012)(Al-Shemmeri, 2012)(Thomas and Sansom, 1995) values of dynamic viscosity of liquid water

From (PEZZANI, 1992), the dynamic viscosity of water vapor was dependent only on temperature, and was expressed as

$$\eta_v(T) = 3.85 \times 10^{-8} T + 10^{-5} \quad [\mathrm{kg}/(\mathrm{m} \cdot \mathrm{s})] \tag{1.31}$$

Dal Pont(Dal Pont, 2004) used a similar linear relation between the temperature and dynamic viscosity of water vapor with reference temperature $T_0 = 20°C$(equation.1.32)

$$\eta_v = \eta_{v0} + \alpha_v(T - T_0) \quad [\mathrm{Pa \cdot s}] \tag{1.32}$$

with $\eta_{v0} = 8,85 \times 10^{-6}[\mathrm{Pa \cdot s}]$, $\alpha_v = 3.53 \times 10^{-8}[\mathrm{Pa \cdot s \cdot K^{-1}}]$, the variation of dynamic viscosity of water vapor according to equation.1.32 and equation.1.31 were shown in fig.1.16. The square dots in fig.1.16 are the extracted data from Appendix B in (Sengers and Kamgar-Parsi, 1984), which was the critically evaluated experimental data. It illustrated that the dynamic viscosity of water vapor increased linearly with temperature in the tested temperature range, and equation.1.32 was very close to the experimental data with small discrepancy. In order to get a more precise function to describe the variation of η_v, a new set of parameters in equation.1.32 was proposed: $\eta_{v0} = 9.846 \times 10^{-6}[\mathrm{Pa \cdot s}]$, $\alpha_v = 3.53 \times 10^{-8}[\mathrm{Pa \cdot s \cdot K^{-1}}]$, and the result was shown in fig.1.16 labeled "Fit".

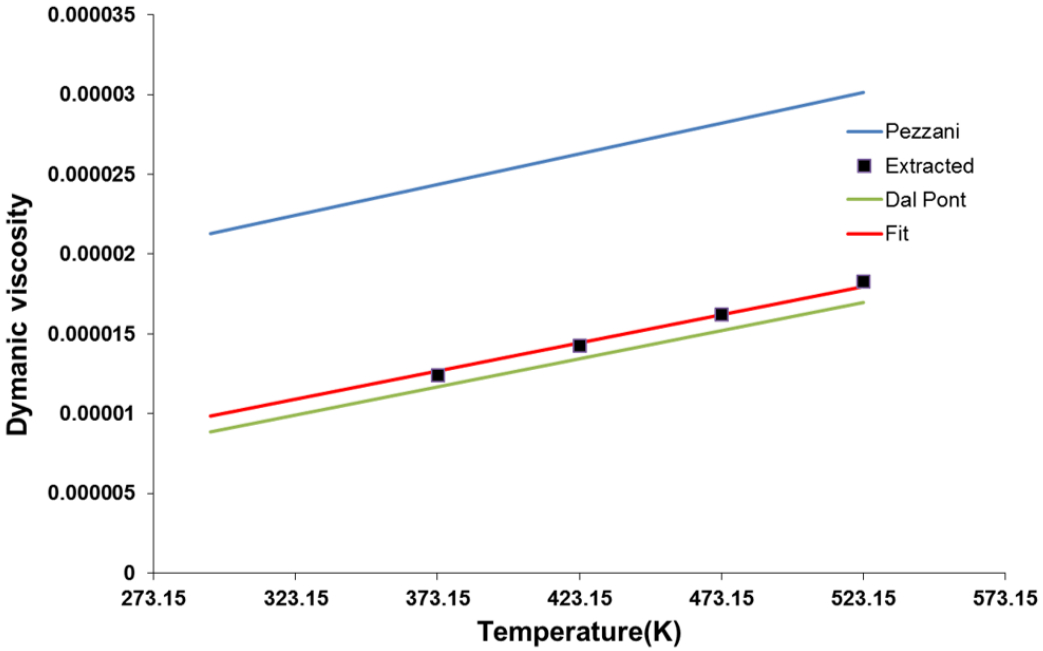

Figure 1.16: Dynamic viscosity of water vapor

1.2 Heat transfer

1.2.1 Conservation law of energy

The conservation equation for heat in concrete can be written as(Lienhard, 2013):

$$\frac{\partial(\rho\hat{u})}{\partial t} + \nabla \cdot (\rho\vec{u}\hat{h}) - \nabla \cdot \lambda\nabla T - Q = 0 \tag{1.33}$$

with

- $\hat{u}$ specific internal energy of the volume.[J/kg]
- $\vec{u}$ the velocity of the flow.[m/s]
- $\hat{h}$ specific enthalpy of the volume. [J/kg]
- Q inner heat source in the volume. [W/m^3]
- λ thermal conductivity of the volume [W/m^{-1}/K]

Neglecting the effect of pressure,

$$\mathrm{d}(\rho\hat{u}) = \mathrm{d}(\rho\hat{h}) = \rho\mathrm{d}\hat{h} + \hat{h}\mathrm{d}\rho \tag{1.34}$$

Then, equation.1.33 becomes

$$\rho\left(\frac{\partial\hat{h}}{\partial t} + \vec{u}\cdot\nabla\hat{h}\right) + \hat{h}\left(\frac{\partial\rho}{\partial t} + \nabla\cdot(\rho\vec{u})\right) - \nabla\cdot(\lambda\nabla T) = Q \tag{1.35}$$

Assumptions are made that 1) the flux is almost incompressible flow, which means $\nabla\cdot\vec{u} \approx 0$; 2) The density change was slow enough to be neglected, which means $\frac{\partial\rho}{\partial t} \approx 0$. Neglecting the effect of pressure, $\mathrm{d}\hat{h} \approx c_p\mathrm{d}T$, equation.1.35 thus can be written as:

$$\rho c_p\left(\frac{\partial T}{\partial t} + \vec{u}\cdot\nabla T\right) - \nabla\cdot(\lambda\nabla T) = Q \tag{1.36}$$

For the studied system, it is written as

$$c\frac{\partial T}{\partial t} = -(C_{pl}\boldsymbol{J}_l + C_{pg}\boldsymbol{J}_g)\nabla T + \nabla\cdot(\lambda\nabla T) + Q \tag{1.37}$$

with

- c Thermal capacity of the volume [J/m^3/K], including the concrete matrix and water in it.

- C_{pl} and C_{pg} Specific heat of liquid water and gaseous phase[J/kg/K]

- $\boldsymbol{J}_l$ and $\boldsymbol{J}_g$ Flux of liquid water and gaseous phase[kg/m^2/s]

- λ Thermal conductivity of concrete[W/m^{-1}/K]

Assume that the gaseous phase contains only water vapor, in Equation.1.37 $C_{pg}\boldsymbol{J}_g = C_{pv}\boldsymbol{J}_v$, where the subscript v represents water vapor. Likewise, if the gaseous phase is considered as a mixture of water vapor and dry air, in Equation.1.37 $C_{pg}\boldsymbol{J}_g = C_{pv}\boldsymbol{J}_v + C_{pa}\boldsymbol{J}_a$, where the subscript a represents dry air.

1.2.2 Effect of high temperature

Thermal conductivity λ

In (Gawin *et al.*, 1999), the thermal conductivity of concrete was described as a function of saturation degree of water and temperature:

$$\lambda(S_l, T) = \lambda_d(T)\left(1 + \frac{4\phi\rho_l S_l}{(1-\phi)\rho_s}\right) \tag{1.38}$$

where ϕ is the porosity of concrete, ρ_l and ρ_s are the density of liquid water and the matrix, respectively. λ_d is thermal conductivity of dry concrete, which varies with temperature as well, can be expressd as(Harmathy and Allen, 1973):

$$\lambda_d(T) = \lambda_d(T_{ref})\left(1 + A_\lambda(T - T_{ref})\right) \tag{1.39}$$

where A_λ is an coefficient that equals 0.0005[K^{-1}], $\lambda(T_{ref})$ is the thermal conductivity of dry concrete at reference temperature $T_{ref} = 298.15$K.
Dal Pont(Dal Pont and Ehrlacher, 2004) adopted the function that was used in Eurocode4. The thermal conductivity of concrete considering condensation/vaporization was solely dependent on temperature, and was written as:

$$\lambda(T) = 2 - 0.24\left(\frac{T - 273.15}{120}\right) + 0.012\left(\frac{T - 273.15}{120}\right)^2 \quad [\mathrm{W}\cdot\mathrm{m}^{-1}\cdot\mathrm{K}^{-1}] \tag{1.40}$$

where T is the temperature in [K].
Bary(Bary *et al.*, 2012) adopted the experimental function proposed in(Ranc *et al.*, 2003):

$$\lambda(S_l, d) = \lambda_{60} + (\lambda_{20} - \lambda_{60})(S_l/S_{l0}) - k_d d \tag{1.41}$$

where $k_d = 9.83 \times 10^{-3}$, $\lambda_{60} = \lambda_{60}(S_l = 0, d = 0) = 2.3[\mathrm{W/m/K}]$, $\lambda_{20} = \lambda_{20}(S_{l0}, d = 0) = 2.7[\mathrm{W/m/K}]$, and $d[\mathrm{kg/m^3}]$ is the water release due to dehydration.

The latent heat of phase change from liquid water to vapor $L_{l\to v}$

The latent heat equals to the enthalpy of evaporation, which is temperature-dependent. Dal Pont(Dal Pont *et al.*, 2007) adopted Watson formula to approximate it(See. Equation.1.42).

$$L_{l\to v} = 2.672 \times 10^5 (T - T_{cr})^{0.38} [\mathrm{J/mol}] \tag{1.42}$$

where T_{cr} is the critical temperature of water. Tabulated values from (Bergman *et al.*, 2011) was compared with calculated results by equation.1.42. In fig.1.17, and we can notice that there is still some difference between the tabulated value and the value calculated with Watson formula.

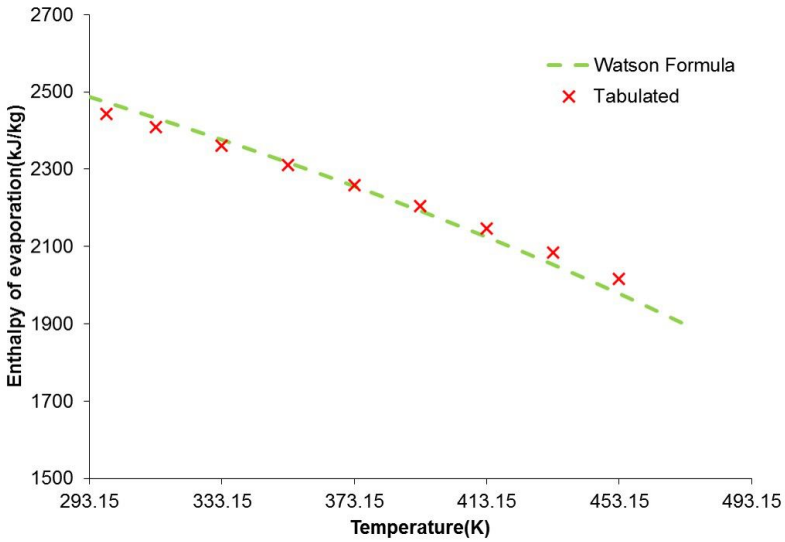

Figure 1.17: Comparison between tabulated(Bergman *et al.*, 2011) and calculated(Dal Pont *et al.*, 2007) enthalpy of evaporation

1.3 Review of modeling approaches for hygro-thermal behavior of concrete at high temperature

1.3.1 Effect of the composition of the fluids

Marcus V.G. de Morais made a comparative analysis of coupled THM model for concrete(De Morais *et al.*, 2009), and one of his aims was to compare the effect of the composition of the fluids. One of his models considered the fluids in the concrete included liquid water and water vapor, which was named "THMs" model; The other model named "THHM" considered the dry air as the third fluid in the concrete. Mass conservation equation for water, which included both liquid and vapor, and that for dry air were established, respectively. Hence, one more variable was required. The variables for THMs model were liquid water pressure, temperature, and nodal displacement, and the variables for THHM model were gas pressure, capillary pressure, temperature and nodal displacement.

A concrete cylinder($\phi 16\text{cm} \times 32\text{cm}$) was heated up to 200°C. Evolutions of gas pressure in the median plan at the axis of the specimen and that near the surface of the specimen were compared with the simulation results. It was worth being noticed that the ratio of intrinsic permeability of gas and liquid and the coefficient to calculate the permeability evolution of gas was adjusted to fit the experimental results of mass loss during the test before being used for simulations. The set of the two parameters were adjusted for both models(THMs and THHM), respectively. The results were shown in Table.1.4

Table 1.4: Permeabilities of concrete adjusted for THMs model and THHM model(De Morais *et al.*, 2009)

Parameters	Simulation I: THMs adjusted	Simulation II: THHM adjusted
Gas intrinsic permeability K_g	$K_g = K_{g0}\exp(0.425(w^{1.0}_{dehydr}))$	$K_g = K_{g0}\exp(0.176(w^{1.3}_{dehydr}))$
Liquid intrinsic permeability K_w	$K_w = 1.0 \times 10^{-4} K_g(w_{dehydr})$	$K_w = 2.0 \times 10^{-4} K_g(w_{dehydr})$

The simulation results with both sets of parameters were shown in Fig.1.18 in terms of gas pressure. THMs model reproduced the gas pressure evolution closer to the experimental result in the center of the specimen while the THHM

model returned a better result near the surface of the specimen. Near the surface, the maximum gas pressure calculated from both models were close to the experimental results; In the center of the specimen, the maximum gas pressure from THHM model showed obvious discrepancy than the experimental results, while the THMs model calculated the closer maximum gas pressure than the experiment. In the first 20 hours, the two models did not show much disparity. The apparent difference between the two models started around the time when the gas pressure of the THMs model reached its peak.

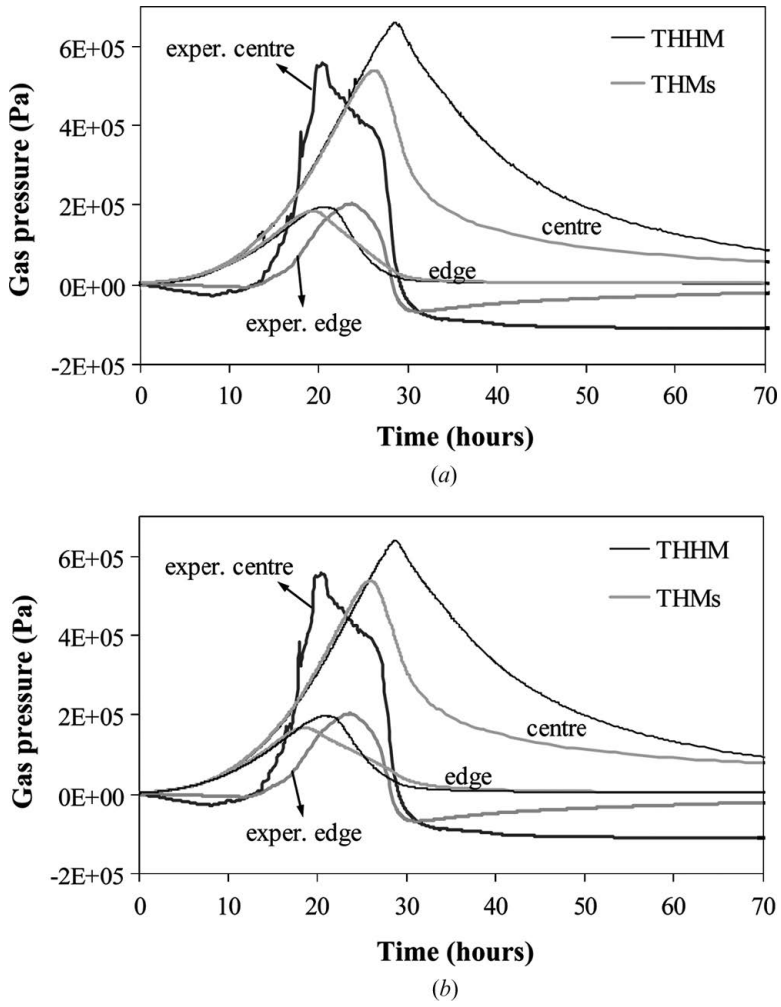

Figure 1.18: Experimental and numerical gas pressure evolution at the center and 0.5cm from the surface in the median plan of the specimen for both THMs and THHM models, for (*a*) simulations I and (*b*) II.(De Morais *et al.*, 2009)

As can be seen, the results with the two sets of parameters had analogous tendency of evolution, so for the purpose of comparing the different models, De Morais(De Morais *et al.*, 2009) only adopted the set of parameter Simulation

I for the following comparison.
The evolution of the water saturation degree and relative humidity in the center of the specimen were shown in Fig.1.19, from which it could be seen that in the first 10 hours, both models had the same resaturation process due to water released by the dehydration. After that, a rapid decrease followed and before around 25 hours, the prediction by model THHM desaturated faster while the contrary took place after that until 70h.

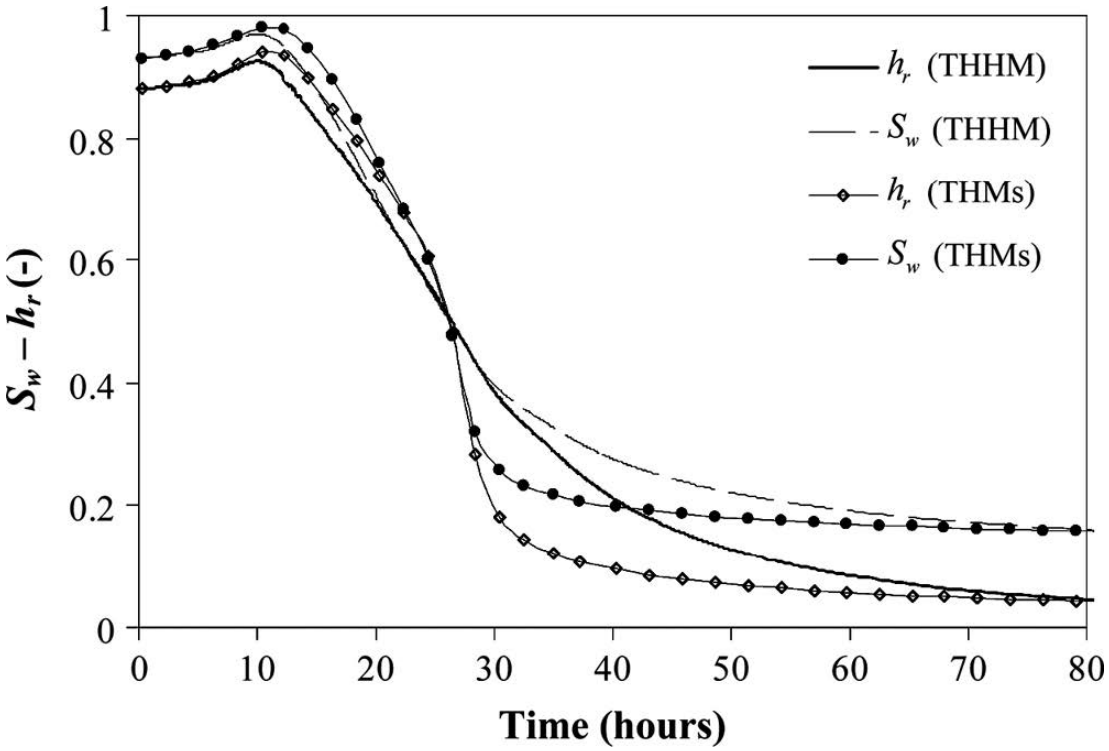

Figure 1.19: Evolution of S_l and relative humidity in the center of the specimen (De Morais *et al.*, 2009)

All in all, from the evolution of gas pressure, we can notice that both model well predicted the tendency of the evolution, but did not predicted the peak position accurately while the amplitude were close to the experimental results. The saturation degree in the center developed similarly in the two predictions with some disparity between 30 hours and 70hours. Considering both models predicted reasonably well the evolution of the gas pressure and the predictions of water saturation degree had the same tendency, the less CPU-time-consuming THMs model was preferable in this study.

1.3.2 Diffusion contribution in water transfer

One of the differences between the THHM model and THMs model is that in THMs model, the diffusion of the water vapor is not taken into consideration explicitly because there is only one gaseous phase. In (De Morais *et al.*, 2009), THHM model was applied to study the diffusion of vapor, and the predicted gas pressure with and without diffusion could not be distinguished. Gawin compared predicted temperature, saturation degree and gas pressure with different simplifications with those from a reference model(Gawin *et al.*, 2011). In the first few minutes of simulation, the simulation without considering the vapor diffusion showed little difference with the reference. However, when the temperature started to change rapidly, the simulation could not get converged.

Chapter 2

Model of hygro-thermal behavior of concrete until 200°C

In this chapter, we are going to implement the dehydration model in the mass and heat transfer model. Here some basic assumptions are made:

1. The fluid in the concrete contains only liquid water and water vapor.
2. The matrix of concrete does not deform.
3. Liquid water is incompressible.

The conservation equations for mass transfer and heat transfer will be deducted separately. Then the desorption isotherm and the permeability of concrete, which are very important in transfer process, will be discussed. COMSOL Multiphysics was then used to simulate the modified MAQBETH mock-up.

2.1 Conservation laws and coupling

2.1.1 Mass transfer

The mass change of the fluid in the concrete per unit volume depends on the flow $\vec{F}$ and source of mass $\dot{w}_{in}$. Hence, the widely used conservation equation for water transfer in concrete was adopted(Bary *et al.*, 2012)(Coussy, 2004):

$$\frac{\partial m}{\partial t} = -\nabla \cdot \vec{F} + \dot{w}_{in} \tag{2.1}$$

where m is the mass of water per unit volume, $\vec{F}$ is the flux of water through unit surface, $\dot{w}_{in}$ is the internal source of mass(phase change, dehydration) per volume.

As stated above, the fluid in concrete are assumed composed of water and vapor only, the saturation degree of liquid water S_l thus has the following relation with vapor saturation degree S_v(Equation.2.2). m_{sat} is the mass of fluid when the matrix is saturated with the fluid.

$$S_l = 1 - S_v \tag{2.2}$$

Consider concrete a homogeneous, the mass of water could be expressed as

$$m_i = \rho_i \phi S_i \tag{2.3}$$

where the subscript $i = \mathrm{l}, \mathrm{v}$ represents liquid water and vapor, respectively.

Because the liquid phase of the fluid contains only liquid water, and the gaseous phase contains only vapor, the diffusive force will not be consider in this study. Darcy's law was adopted to describe the flux of water in concrete, which means the flux of the liquid and the gaseous phases follow:

$$\vec{F_l} = -\rho_l \frac{k_{ml}}{\eta_l} \nabla p_l \tag{2.4}$$

$$\vec{F_v} = -\rho_v \frac{k_{mv}}{\eta_v} \nabla p_v \tag{2.5}$$

where k_{mv} and k_{ml} are permeabilities of concrete to vapor and liquid water, respectively. η_l and η_v are dynamic viscosities of liquid water and vapor.

The source term $\dot{w}_{in}$ represents the mass change per unit volume due to phase change and dehydration. The mass change due to dehydration is calculated with the dehydration model in Part. I. Hence, the mass conservation equations for liquid water and vapor can be written as:

$$\begin{aligned} \frac{\partial}{\partial t}(m_l) &= -\nabla \cdot (-\rho_l \frac{k_{ml}}{\eta_l} \nabla p_l) - \mu_{l \to v} + \dot{w}_{dehydr} \\ \frac{\partial}{\partial t}(m_v) &= -\nabla \cdot (-\rho_v \frac{k_{mv}}{\eta_v} \nabla p_v) - \mu_{v \to l} \end{aligned} \tag{2.6}$$

With

- $\mu_{l\to v}$ and $\mu_{v\to l}$ are the rate of evaporation and rate of condensation, respectively. [kg/m^3/s]

- $\dot{w}_{dehydr}$ the mass loss due to dehydration. [kg/m^3/s]

Adding the two equations in Equation.2.6, and substitute m_l and m_v with Equation.2.3, we can get:

$$\begin{aligned}&(S_v\rho_v + S_l\rho_l)\frac{\partial\phi}{\partial t} + \phi\Big(\rho_l\frac{\partial S_l}{\partial t} + \rho_v\frac{\partial S_v}{\partial t} + S_l\frac{\partial\rho_l}{\partial t} + S_v\frac{\partial\rho_v}{\partial t}\Big)\\ &-\nabla\cdot\Big(\rho_l\frac{k_{ml}}{\eta_l}\nabla p_l + \rho_v\frac{k_{mv}}{\eta_v}\nabla p_v\Big) = \dot{w}_{dehydr}\end{aligned} \tag{2.7}$$

According to Equation.2.2, Equation.2.7 could be expressed as:

$$\begin{aligned}&[(1-S_l)\rho_v + S_l\rho_l]\frac{\partial\phi}{\partial t} + \phi(\rho_l-\rho_v)\frac{\partial S_l}{\partial t} + S_l\phi\frac{\partial\rho_l}{\partial t} + (1-S_l)\phi\frac{\partial\rho_v}{\partial t}\\ &-\nabla\cdot\Big(\rho_l\frac{k_{ml}}{\eta_l}\nabla p_l + \rho_v\frac{k_{mv}}{\eta_v}\nabla p_v\Big) = \dot{w}_{dehydr}\end{aligned} \tag{2.8}$$

where $\dot{w}_{dehydr}$ is the mass loss rate due to dehydration, and is calculated with equation.2.37 in part I.

2.1.2 Heat transfer and coupling

Considering the flux of water, phase change between liquid water and vapor, latent heat of dehydration, and thermal conduction, the conservation equation for heat transfer in concrete is written

$$\begin{aligned}&c(S_\mathrm{l},d)\frac{\partial T}{\partial t} + \underbrace{(\vec{F}_l C_{pl} + \vec{F}_v C_{pv})\nabla T}_{\text{flux of water}}\\ &= \underbrace{-\nabla\cdot\vec{q}}_{\text{thermal conduction}} \quad \underbrace{\underbrace{-L_{\mathrm{l}\to\mathrm{v}}\mu_{\mathrm{l}\to\mathrm{v}}}_{\text{phase change}}\ \underbrace{-L_{\mathrm{s}\to\mathrm{l}}\dot{w}_{dehydr}}_{\text{dehydration}}}_{\text{inner source of heat}}\end{aligned} \tag{2.9}$$

where $c(S_l,d)$ is the thermal capacity of concrete per volume, which is

$$c(S_\mathrm{l},d) = m_{\mathrm{ds}}C_{\mathrm{ds}} + \phi\rho_\mathrm{l}S_\mathrm{l}C_{pl} + \phi\rho_\mathrm{v}(1-S_\mathrm{l})C_{pv} + (w_{max}-w_{dehydr})TC_{\mathrm{bw}} \tag{2.10}$$

with:

- $C_{\mathrm{ds}}, m_{\mathrm{ds}}$ mass and specific heat of cement and aggregates per volume

- $C_{\mathrm{pl}}, C_{\mathrm{pv}}$ specific heat of liquid water and vapor.

- C_{bw} is the specific heat of bound water of cement paste

Bary(Bary *et al.*, 2008)(Bary *et al.*, 2012) cited the conclusion in(Bazant and Kaplan, 1996) that the heat due to flux of water $(\vec{F}_l C_{\mathrm{pl}} + \vec{F}_v C_{\mathrm{pv}})\nabla T$ could be neglected. The thermal conduction follows Fourier's law, which is

$$\vec{q} = -\lambda(s_l, w_{dehydr})\nabla T \tag{2.11}$$

where $\lambda(S_l, d)$ is the thermal conductivity of concrete. The energy conservation equation for concrete is then written as

$$c(S_l, w_{dehydr})\frac{\partial T}{\partial t} = -\nabla \cdot (-\lambda(S_l, w_{dehydr})\nabla T) - L_{\mathrm{l}\to\mathrm{v}}\mu_{\mathrm{l}\to\mathrm{v}} - L_{\mathrm{s}\to\mathrm{l}}\dot{w}_{dehydr} \tag{2.12}$$

If temperature T and vapor pressure p_v were selected as dependent variables, the partial derivatives in Equation.2.8 should be expressed as partial derivatives with respect to T and/or p_v. Once Equation.2.8 was rewritten as

$$\begin{aligned}
&\left[\phi(\rho_l - \rho_v)\frac{\partial S_l}{\partial p_v} + (1 - S_l)\frac{\partial \rho_v}{\partial p_v}\right]\frac{\partial p_v}{\partial t} + \nabla \cdot \left[-\left(\rho_l \frac{k_{ml}}{\eta_l}\frac{\partial p_l}{\partial p_v} + \rho_v \frac{k_{mv}}{\eta_v}\right)\nabla p_v\right] \\
&+ \left[\phi(\rho_l - \rho_v)\frac{\partial S_l}{\partial T} + ((1 - S_l)\rho_v + S_l\rho_l)\frac{\partial \phi}{\partial T} + \phi\left(S_l\frac{\partial \rho_l}{\partial T} + (1 - S_l)\frac{\partial \rho_v}{\partial T}\right)\right]\frac{\partial T}{\partial t} \\
&+ \nabla \cdot \left[-\left(\rho_l \frac{k_{ml}}{\eta_l}\frac{\partial p_l}{\partial T}\right)\nabla T\right] = \dot{w}_{dehydr}
\end{aligned} \tag{2.13}$$

2.2 Expression of physical characteristics as function of state variables T and p_v

2.2.1 Desorption isotherm

In this study, the capillary pressure curve in (Dal Pont and Ehrlacher, 2004) was adopted to calculate the desorption isotherm.

The capillary pressure follows(Dal Pont and Ehrlacher, 2004):

$$p_c = \frac{\sigma(T)}{\sigma(T_0)} a_c (S_l^{-b_c} - 1)^{(1-\frac{1}{b_c})} \tag{2.14}$$

where $\sigma(T) = \sigma_0(1 - \frac{T}{T_{cr}})^{n_\sigma}$. The values of concerning parameters are listed in table.1.1. Considering the vapor as ideal gas, the vapor pressure thus can be written as:

$$p_v = p_{vs}(T) \exp(-\frac{p_c M_w}{\rho_l RT}) \tag{2.15}$$

Hence, the relative humidity in the pores $h_r = p_v/p_{vs}$ can be written as a function of S_l and T. The desorption isotherm calculated with Equation.1.7 and Equation.2.15 at 20°C and 80°C are compared with the isotherm from some other literature in Fig.2.1

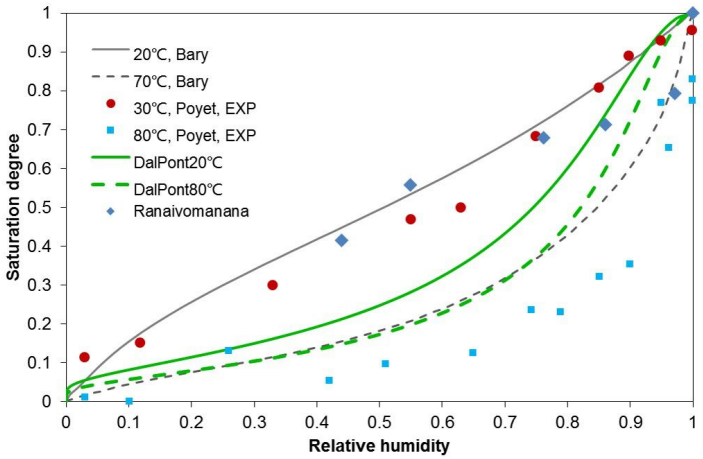

Figure 2.1: Comparison among different desorption isotherms

- The experimental data from Poyet at 30°C(Poyet, 2009).
- The experimental data from Poyet at 80°C(Poyet, 2009).
- The experimental data of desorption isotherm from Ranaivomanana with sample B1 at 20°C(Ranaivomanana, 2010).

—, - - - Calculated value using the method by Bary mentioned in section.1.1.2 at 20°C and 70°C, respectively(Bary *et al.*, 2012).

—,- - - Calculated results with Equation.1.7 and Equation2.15 at 20°C and 80°C, respectively.

The desorption isotherms are affected by pore structure of concrete, so it may vary a lot from one concrete to another. All the curves showed the same

tendency when the temperature was elevated. The saturation degree increased faster with the relative humidity at higher temperature.

The hysteresis of the desorption/adsorption loop have been observed and studied for many researchers(McBain, 1935)(Brunauer *et al.*, 1967)(Ranaivomanana, 2010)(Baroghel-Bouny, 2007)(Ishida *et al.*, 2007). There have been several explanations to this phenomenon:

- The ink bottle effect(McBain, 1935). Because smaller pores can keep the meniscus under lower relative humidity, the ink-bottle-shape pores prevent the water in the pore from moving through the narrow neck during the process of desorption.
- The temperature of water condensation in pores is different from that of evaporation.(Brunauer *et al.*, 1967)
- Under low relative humidity, the hysteresis can be explained due to structural change due to the loss of interlayer water in C-S-H(Baroghel-Bouny, 2007).

This phenomenon was showed in Fig.2.2 with the experimental data in (Ranaivomanana, 2010). The sorption curve started from the dry state, whilst the desorption curve started from the saturated state. There is a apparent difference between the two curves, and the sorption curve which is more commonly used lies between the desorption and the sorption curve.

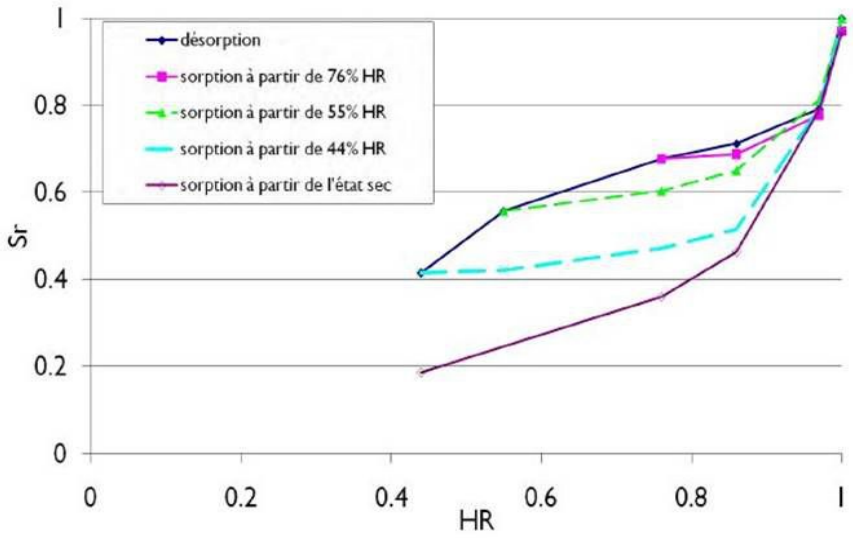

Figure 2.2: Hysteresis of desorption-sorption process(Ranaivomanana, 2010)

From this point of view, the isotherm used in this study corresponds to a mean value between sorption and desorption at each temperature. Besides, equation.2.14 and equation.2.15 were adopted to simulate the mean isotherm because it is more numerically convenient as it avoids rapid changes on the isotherm at higher temperature. Fig.2.3 shows the comparison of the experimental data and calculated curves.

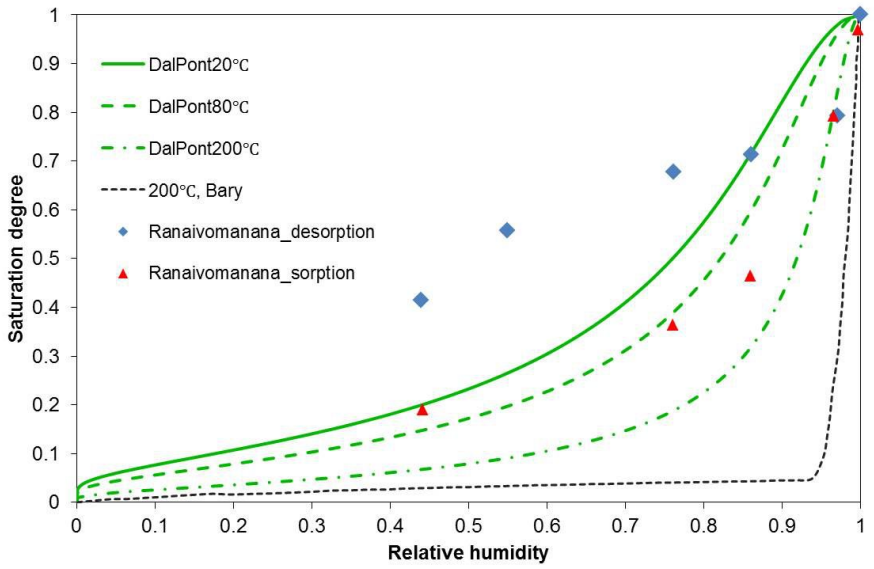

Figure 2.3: Comparison with desorption and sorption isotherms from Ranaivomanana(Ranaivomanana, 2010)

◆ The desorption isotherm from Ranaivomanana with sample B1 at 20°C(Ranaivomanana, 2010).
▲ The sorption isotherm from Ranaivomanana with sample B1 at 20°C(Ranaivomanana, 2010).
–·– Calculated results with Equation.1.7 and Equation2.15 at 200°C
- - - Calculated value using the method by Bary mentioned in section.1.1.2 at 200°C(Bary *et al.*, 2012).

2.2.2 Permeabilities

Permeability of unsaturated concrete to vapor

Considering the Klinkenberg effect, the permeability of concrete to vapor is written as

$$k_{mv} = k_{mv}^{0} k_{rv} (1 + \frac{\beta}{p_v}) \tag{2.16}$$

where β is the Klinkenberg constant, the value is in Table.2.1

The relative permeability was dependent on the saturation degree of water. In this study, the function proposed Van Genuchten(Van Genuchten, 1980) was adopted(Equation.2.17).

$$k_{rv}(S_l) = (1 - S_l)^p (1 - S_l^{1/m})^{2m} \tag{2.17}$$

The original value of parameter m was for soil, and for different matrix, the value of m is different, so $m = 0.56$ (Bary *et al.*, 2012) , which was used for cementitious material(Monlouis-Bonnaire *et al.*, 2004), is adopted in this study.

During the dehydration process, the network of pores in concretes changes as the decomposition of the hydrates. Hence, the intrinsic permeability k_{mv} here used the function that is in (Bary *et al.*, 2012), which is

$$k_{mv}(S_l = 0) = k_{mv}^0 \exp(0.2 w_{dehydr}) \tag{2.18}$$

where k_{mv}^0 is the the intrinsic permeability to vapor without dehydration, and listed in table.2.1.

Permeability of unsaturated concrete to liquid water

The permeability of concrete to liquid water could be described as product of the permeability of concrete at saturated state and relative permeability of liquid water.(See Equation.2.19).

$$k_{ml} = k_{ml}^0 (S_l = 1) k_{rl} \tag{2.19}$$

Same with the relative permeability of concrete to vapor, the relative permeability to liquid water k_{rl} was described by Van Genuchten equation(Van Genuchten, 1980) as well(See Equation.2.20).

$$k_{rl}(S_l) = \sqrt{S_l}(1 - (1 - S_l^{1/m})^m)^2 \tag{2.20}$$

The intrinsic permeability of concrete to liquid water k_{ml}^0 was considered being related to the k_{mv}^0. In this study, k_{ml}^0 and k_{mv}^0 were considered having the following relation(Bary *et al.*, 2012)

$$k_{ml}(S_l = 1) = a_k k_{mv}(S_l = 0) \tag{2.21}$$

with $a_k = 1.1 \times 10^{-3}$.

Table 2.1: Parameters to evaluate the permeabilities of concrete to liquid water and vapor

Parameter	Value
Klinkenberg constant β	$0.275[\mathrm{atm}]$
m	0.56
p	5.5

2.2.3 Hygral parameters

- **Density of liquid water** was considered as a function of temperature, which is(Raznjevic, 1978):

$$\rho_l = 314.4 + 685.6 \left[1 - \left(\frac{T - 273.15}{374.14}\right)^{\frac{1}{0.55}}\right]^{0.55} \quad [\mathrm{kg/m^3}] \tag{2.22}$$

- **Density of water vapor** was determined with Clapeyron equation(See equation.1.25), and with R=8.31$[\mathrm{J \cdot mol^{-1} \cdot K^{-1}}]$ and M_w=18$\mathrm{g \cdot mol^{-1}}$, it was rewritten as:

$$\rho_v = 2.167 \times 10^{-3} \frac{p_v}{T} \quad [\mathrm{kg/m^3}] \tag{2.23}$$

- **Saturated vapor pressure** was calculated with Clausius-Clapeyron equation, and the function used in (Bary *et al.*, 2012) was adopted:

$$p_{vs}(T) = p_{atm} \exp\left(4871.3 \frac{T - 373.15}{373.15T}\right) \tag{2.24}$$

- **Dynamic viscosity of liquid water** follows(Al-Shemmeri, 2012)

$$\eta_l(T) = 2.414 \times 10^{-5} \times 10^{\left(\frac{247.8}{T-140}\right)} \quad [\mathrm{kg \cdot m^{-1} \cdot s^{-1}}] \tag{2.25}$$

- **Dynamic viscosity of water vapor** follows

$$\eta_v(T) = 3.53 \times 10^{-8}(T - 293.15) + 9.846 \times 10^{-5} \quad [\mathrm{kg \cdot m^{-1} \cdot s^{-1}}] \tag{2.26}$$

2.2.4 Thermal parameters

- **Thermal conductivity** of concrete was considered as a function of S_l and T, and follows(Gawin *et al.*, 1999):

$$\lambda(S_l, T) = \lambda_d(T)\left(1 + \frac{4\phi\rho_l S_l}{(1-\phi)\rho_s}\right) \tag{2.27}$$

where ρ_s is the density of matrix, which can be calculated with following equation:

$$\rho_s = \frac{m_{cp} + m_{aggr}}{\frac{m_{cp}}{\rho_{cp}} + \frac{m_{aggr}}{\rho_{aggr}}} \tag{2.28}$$

where the m_{cp} and m_{aggr} are the masses of cement paste and aggregates per unit volume of concrete, ρ_{aggr} is the density of aggregates and ρ_{cp} is density of cement paste, which is calculated with the hydration model proposed by L. Buffo-Lacarrière(Buffo-Lacarrière, 2007).

$\lambda_d(T)$ is the thermal conductivity of dry concrete, which is dependent on temperature as well(Harmathy and Allen, 1973):

$$\lambda_d(T) = \lambda_d(T_\lambda)\left(1 + A_\lambda(T - T_\lambda)\right) \tag{2.29}$$

with

- $\lambda_d(T_\lambda)$ thermal conductivity of dry concrete at reference temperature T_λ.
- T_λ reference temperature, which is 298.15K.
- A_λ constant depends on the type of concrete, which the value 0.0005K^{-1} is adopted(Gawin *et al.*, 1999)

- **Latent heat of vaporization**
From Fig.1.17, we can notice that there is still some difference between the formula-based curve and the tabulated value. Hence, a polynomial expression was adopted to fit the tabulated value(Equation.2.30):

$$L_{l\to v} = \Delta h_{phase} = 3.664 \times 10^{-3} T^2 + 2767.1931 \quad [\mathrm{kJ/kg}] \tag{2.30}$$

The curve calculated with equation.2.30 was shown in Fig.2.4, and it has better consistency with the tabulated value.

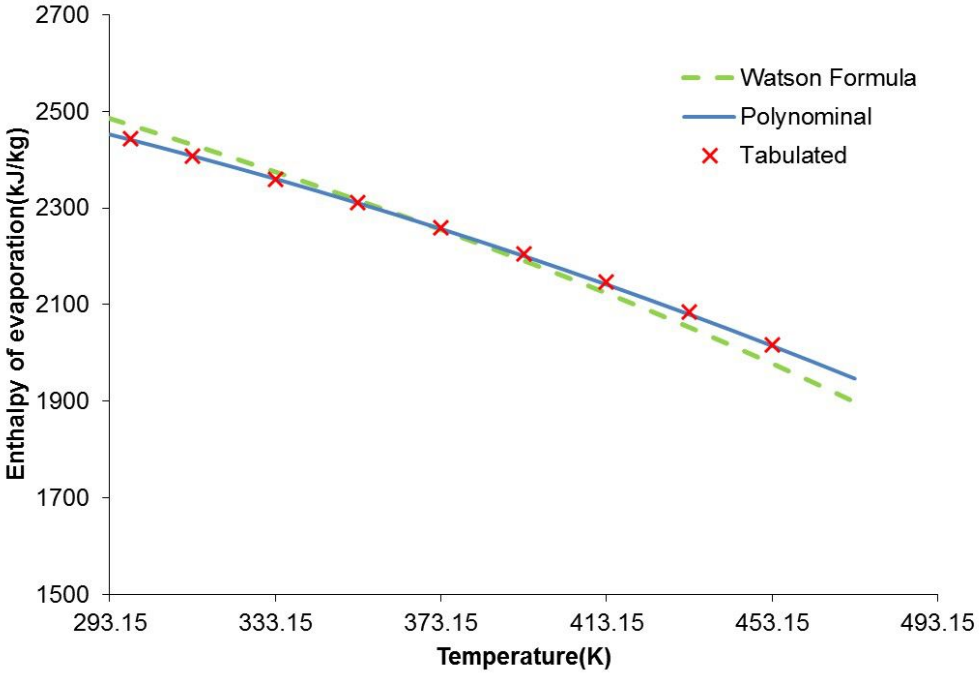

Figure 2.4: Enthalpy of vaporization of water from 293.15K to 473.15K

Watson formula
Fitting result with polynomial expression.
× Tabulated value in (Bergman *et al.*, 2011)

- **Rate of vaporization**
  From Equation.1.2, it can be deducted that the rate of evaporation

$$\mu_{l\to v} = \nabla \cdot \left(\rho_v \frac{k_{mv}}{\eta_v} \nabla p_v\right) - \frac{\partial m_v}{\partial t} \tag{2.31}$$

- **Latent heat of dehydration** can be calculated as sum of the latent heat of each hydrate. For the simplification, a constant value $L_{s\to l} = 2500\text{kJ/kg}$ was used(Kanema *et al.*, 2007)(Bary *et al.*, 2012) in this study.

2.3 Application on MAQBETH mock-up

2.3.1 MAQBETH mock-up

The water and heat transfer model was then validated with the experimental data of MAQBETH mock-up(Bary *et al.*, 2012). The general view of MAQBETH and the reinforcement inside was shown in Fig.2.5

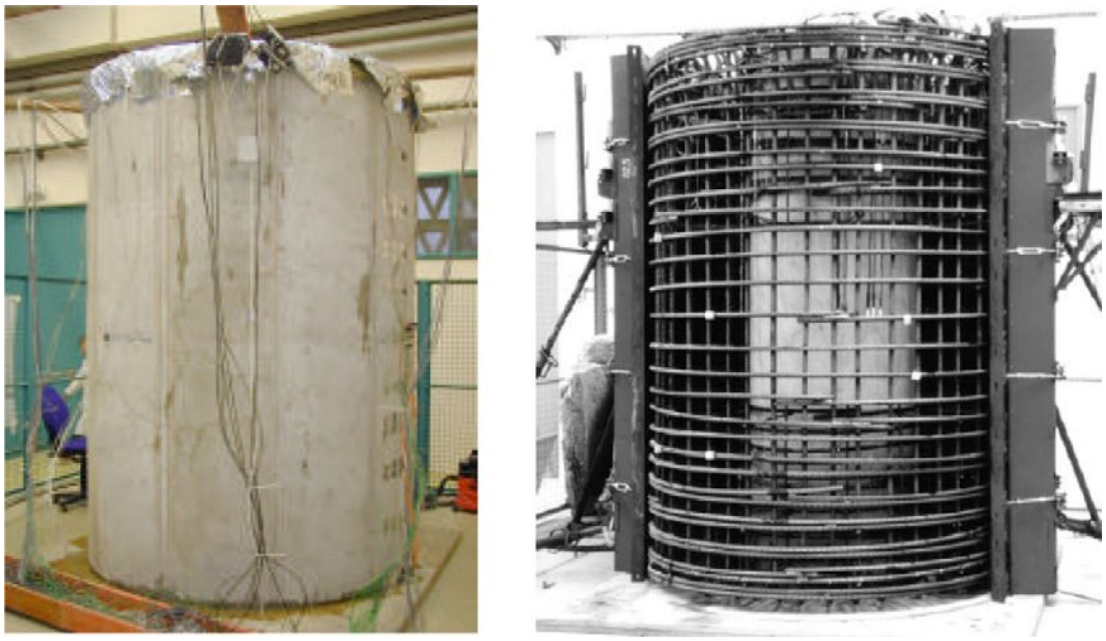

Figure 2.5: General view of the MAQBETH mock-up(left) and the steel reinforcement inside(right)(Ranc *et al.*, 2003)

The MAQBETH mock-up is a hollow reinforced concrete cylinder, with an interior diameter of 100cm, outer diameter 220cm, and a height of 300cm. The mock-up sat on a wooden plate which is 60mm thick, and was covered with with a 20mm thick insulator layer and a 30mm thick wooden layer on its top. The shape and the 2D-characteristics of the MAQBETH mock-up are shown in fig.2.5. The thickness of the cylinder allows us to observe the high temperature gradient through the wall, as well as to avoid the size-effect so that the test data can reflect the performance of the real structure. Besides, the axisymmetric structure, the setup of the heating source and insulator layers make it possible for us to consider the water and heat flow as one-dimensional if only the middle part of the section was taken into account during the simulation.
The reinforcement was not considered specifically in this study, and more detail about the MAQBETH mock-up can be found in (Bary *et al.*, 2012) and (Ranc

et al., 2003).

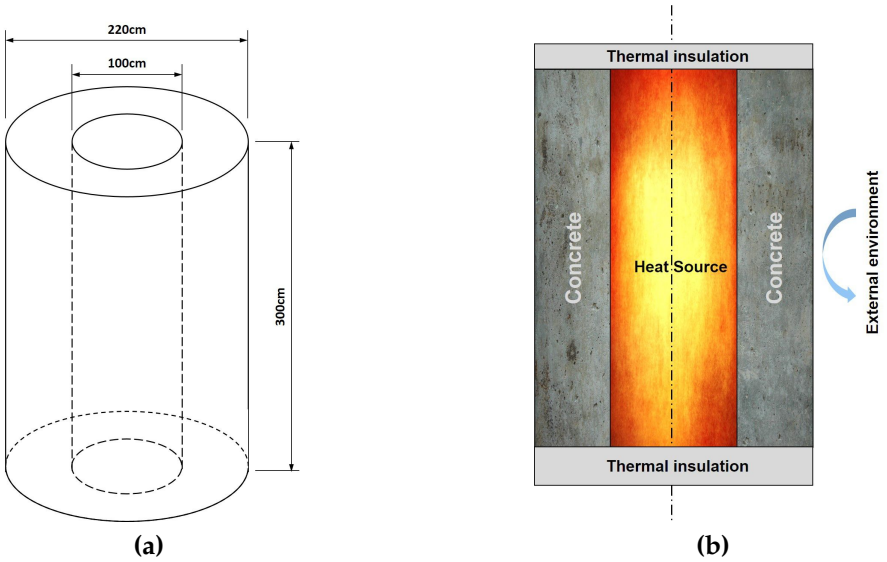

Figure 2.6: The shape(a) and 2D-characteristics(b) of MAQBETH mock-up
The texture of the heat source is from https://www.flickr.com/photos/37753256@N08/4740760966

2.3.2 Boundary conditions and initial conditions

In Section.2.3.1, it was mentioned that the water and heat flow can be considered as one-dimensional if only the middle section of the structure was studied. Hence, the schema of the numerical model could be simplified as that demonstrated in Fig.2.7a.

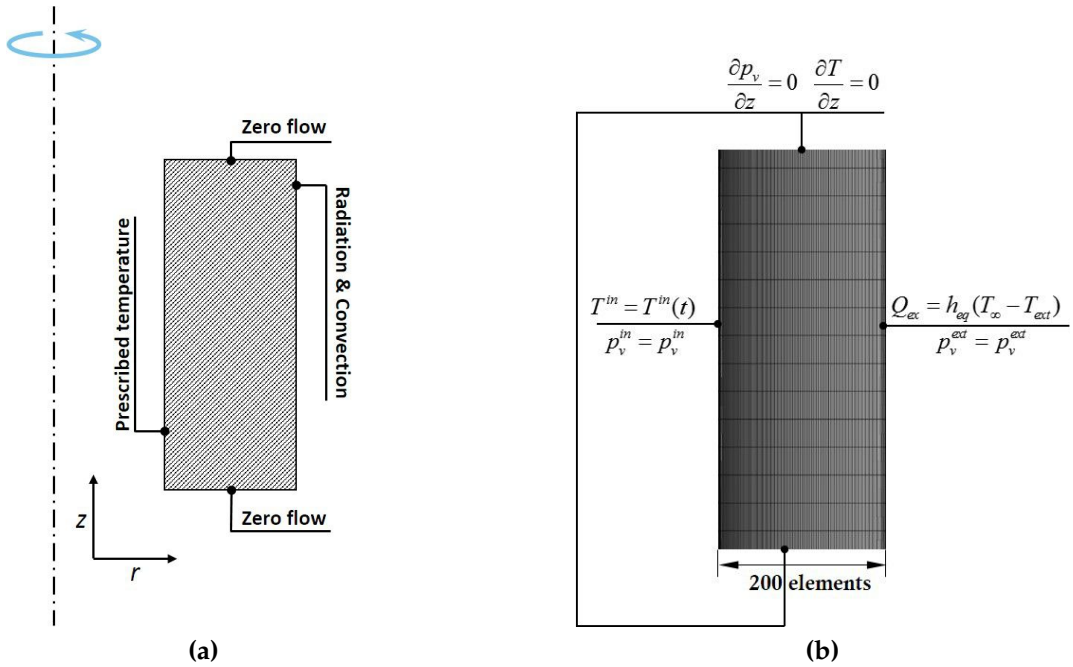

Figure 2.7: Schema of the model used for simulation(a) and boundary conditions of the simulation(Bary *et al.*, 2012)

There is no heat or mass flow through the bottom and the top of the structure, and the inner surface of the sample had prescribed temperature due to the heating source in the cylinder. The mass and heat exchange with the external environment was controlled by radiation and convection.

- Boundary conditions
  As can be seen from Fig.2.7b, the top and the bottom of the geometry was considered insulated. In other words, there are no flux though them. The temperature on the inner surface T^{in} followed the same heating scheme with that in (Bary *et al.*, 2012), which is plotted in Fig.2.8.

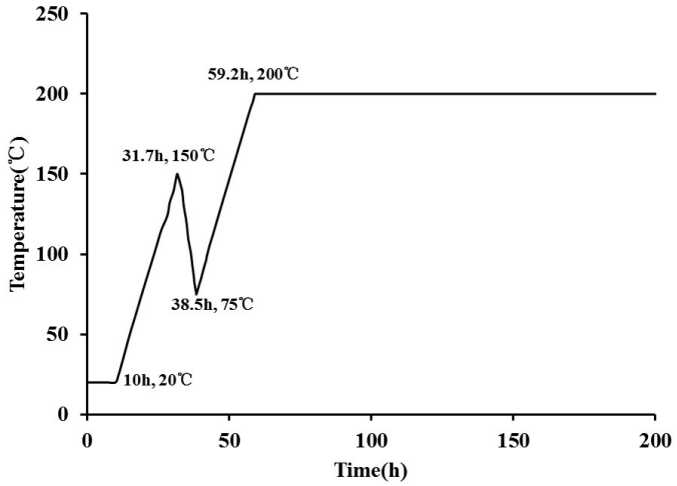

Figure 2.8: Heating scheme on the inner boundary(Bary *et al.*, 2012)

The vapor pressure p_v on inner and exterior boundary was prescribed as 2500Pa, which lead that the relative humidity on the boundary would change as temperature varied during the simulation. The heat exchange with the external environment was considered due to the radiation and convection, which follows Equation.2.32

$$Q_{ex} = h_{eq}(T_\infty - T_{ext}) \tag{2.32}$$

with

- $h_{eq} = 10$[W/m^2/K] the equivalent heat exchange coefficient which includes the contribution from both radiation and convection.
- $T_\infty = 20$°C the temperature at the infinity.
- T_{ext} the temperature on the external boundary of the structure.

- Initial conditions
  The independent variables in the simulation were vapor pressure p_v and temperature T.
  The initial condition was set as follows: Assume that the structure be kept in the environment with the same temperature and vapor pressure as that of external boundary condition for a period of time which make the vapor pressure and the temperature were uniform in the whole structure, the initial vapor pressure was the same as the vapor pressure on

the interior and the exterior boundaries, which is 2500 Pa. The initial temperature of the structure was set 293.15K, which represented room temperature.

2.3.3 Simulation in COMSOL Multiphysics

The properties of the concrete in the simulation

The mix proportions of the concrete was list in table.2.2(Bary *et al.*, 2012).

Table 2.2: Mix proportions of the concrete for MAQBETH mock-up(Bary *et al.*, 2012)

composition	value
Cement mass (CEM I 52.5 Lafarge)	354 kg/m^3
Aggregates mass	1877 kg/m^3
Mix water	154 kg/m^3
water cement ratio	0.43

According to the dehydration model established in Chapter.2, in the simulation for the MAQBETH mock-up(no higher than 200°C), the dehydration of C-S-H and the interlayer water of monosulfate were taken into consideration.

Assuming that the composition of the cement is the same as in table.3.1and the concrete had been cured for 60d, via the hydration model in (Buffo-Lacarrière, 2007), the amount of C-S-H and monosulfate were 2.96 mol/kg cement and 0.358 mol/kg cement, respectively. The density of the cement paste was 3.186$\times$ 10^3 kg/m^3.

The implementation of the model

The simulation was run with the help of the finite element analysis software COMSOL Multiphysics 4.4. Meshing were made to get convergence, and was shown in Fig.2.7b. The coupled model was implemented with coefficient PDE, which has a form:

$$d_a \frac{\partial \mathbf{u}}{\partial t} + \nabla \cdot (-c\nabla \mathbf{u}) = f \tag{2.33}$$

with

$$c = \begin{bmatrix} B11 & B12 \\ B21 & B22 \end{bmatrix}, \quad d_a = \begin{bmatrix} A11 & A12 \\ A21 & A22 \end{bmatrix}, \quad \text{and } f = \begin{bmatrix} f1 \\ f2 \end{bmatrix}$$

According to equation.2.12 and equation.2.13, $\mathbf{u} = \begin{bmatrix} p_v \\ T \end{bmatrix}$

$$\begin{aligned} B11 &= \left(\rho_l \frac{k_{ml}}{\eta_l}\frac{\partial p_l}{\partial p_v} + \rho_v \frac{k_{mv}}{\eta_v}\right) \\ B12 &= \left(\rho_l \frac{k_{ml}}{\eta_l}\frac{\partial p_l}{\partial T}\right) \\ B21 &= 0 \\ B22 &= \lambda(S_l, d) \end{aligned} \tag{2.34}$$

$$\begin{aligned} A11 &= \phi(\rho_l - \rho_v)\frac{\partial S_l}{\partial p_v} + (1 - S_l)\frac{\partial \rho_v}{\partial p_v} \\ A12 &= \phi(\rho_l - \rho_v)\frac{\partial S_l}{\partial T} + ((1 - S_l)\rho_v + S_l\rho_l)\frac{\partial \phi}{\partial T} + \phi\Big(S_l\frac{\partial \rho_l}{\partial T} + (1 - S_l)\frac{\partial \rho_v}{\partial T}\Big) \\ A21 &= 0 \\ A22 &= c(S_l, d) \end{aligned} \tag{2.35}$$

$$\begin{aligned} f1 &= \dot{w}_{dehydr} \\ f2 &= -L_{l\to v}\mu_{l\to v} - L_{s\to l}f1 \end{aligned} \tag{2.36}$$

where $\dot{w}_{dehydr}$ was the rate of mass loss due to dehydration, including the contribution of C-S-H $\dot{w}^{CSH}_{dehydr}$ and monosulfate $\dot{w}^{AFm}_{dehydr}$. $\dot{w}^{AFm}_{dehydr}$ and $\dot{w}^{CSH}_{dehydr}$ were calculated via

$$\begin{aligned} \dot{w}^{AFm}_{dehydr} &= w^{AFm}_{max}\dot{\xi}^{AFm} \\ \dot{w}^{CSH}_{dehydr} &= w^{CSH}_{max}\dot{\xi}^{CSH} \end{aligned} \tag{2.37}$$

w^{AFm}_{max} and w^{CSH}_{max} were the maximum mass of water that can be released during the dehydration. $\dot{\xi}^{AFm}$ and $\dot{\xi}^{CSH}$ were rates of dehydration of monosulfate and C-S-H and could be calculated via the dehydration model in Part I. $f1$ in equation.2.36 therefore, for the temperature lower than 200°C, as CH and C_3AH_6 are not affected, becomes $f1 = w^{CSH}_{max}\dot{\xi}^{CSH} + w^{AFm}_{max}\dot{\xi}^{AFm}$.

In the software, Newton's method was selected to solve the equations, with initial damping factor = 10^{-4}, minimum damping factor = 10^{-8}. The default time step was 0.1h, which was adjusted automatically during calculation with the relative tolerance 10^{-5}. The iteration for each step terminated according to tolerance factor = 10^{-3}.

The parameters that are used in the simulation are listed in table.2.3

Table 2.3: Parameters that are used in the simulation

Parameter	value
Initial intrinsic permeability to water vapor k^0_{mv}	1×10^{-17} [m^2]
Intrinsic permeability to liquid water k^0_{ml}	$1.1 \times 10^{-3} k^0_{mv}$
Initial porosity ϕ_0	0.1
Thermal conductivity of dry concrete at 25°C $\lambda_d(T_\lambda)$	1.9[W/m/K]
Thermal capacity of anhydrous cement C_c	750[J/kg/K]
Thermal capacity of aggregates C_a	800[J/kg/K]
Thermal capacity of bound water C_{bw}	3760[J/kg/K]
Thermal capacity of liquid water C_{pl}	4184[J/kg/K]
Thermal capacity of water vapor C_{pv}	4184[J/kg/K]

All of the parameters in table.2.3 were data in (Bary *et al.*, 2012) except k^0_{ml} and $\lambda_d(T_\lambda)$. The value of k^0_{ml} was selected to best fit the relative humidity profile, which was the same method that used in (Bary *et al.*, 2012). $\lambda_d(T_\lambda)$ was the experimental result at 60°C in (Bary *et al.*, 2012), and following the assumption that the thermal conductivity of dry concrete does not change in 20°C –60°C, the value obtained at 60°C was adopted as $\lambda_d(T_\lambda)$ here. For the dehydration of the cement paste in the concrete, the dehydration model can be directly used here without additional experiment. If the temperature was elevated from 20°C to 200°C with a heating rate of 0.1K/min, the mass change during the process is shown in fig.2.9.

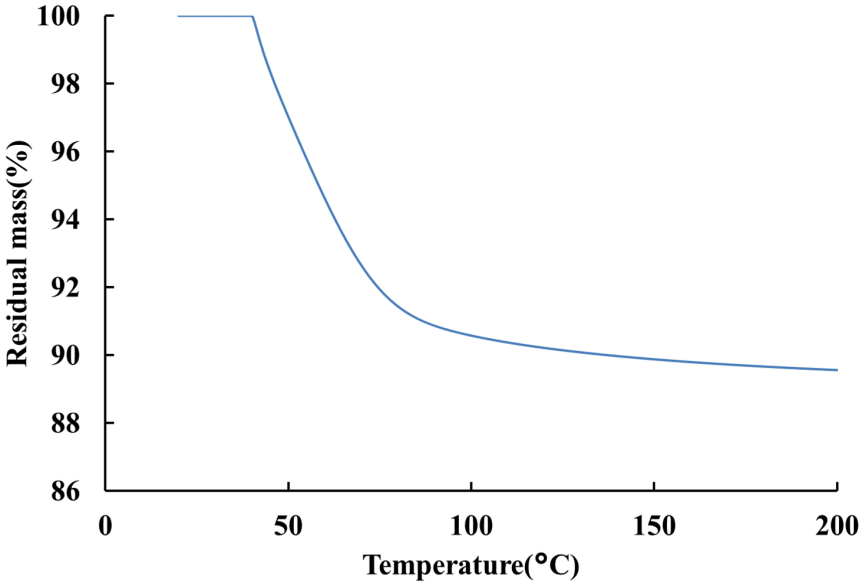

Figure 2.9: Mass change from 20°C to 200°C.(Heating rate = 0.1K/min)

2.3.4 Result and discussion

Here we are going to compare the simulation results with experimental results in (Bary *et al.*, 2012). The evolutions of temperature, gas pressure(vapor pressure in this study), and relative humidity at different time along the radius of the structure (See Fig.2.10)were compared.

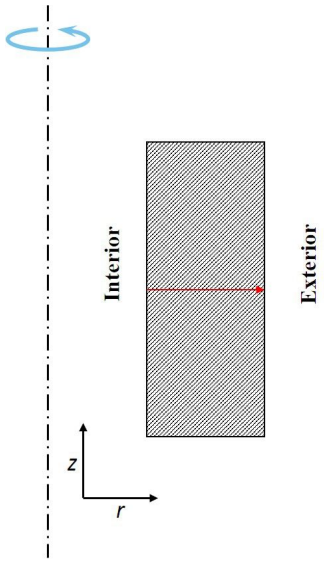

Figure 2.10: Comparison was made along the direction of the red arrow

The temperature distribution along the radius of the structure at 19.5h, 30.5h, 41.8h and 61.3h were shown in Fig.2.11. The x-axis represented the distance to the interior boundary, and y-axis was temperature in Celsius, which means that for the interior boundary, the distance to the interior boundary $x = 0\mathrm{m}$ and for the exterior boundary, $x = 0.6\mathrm{m}$.

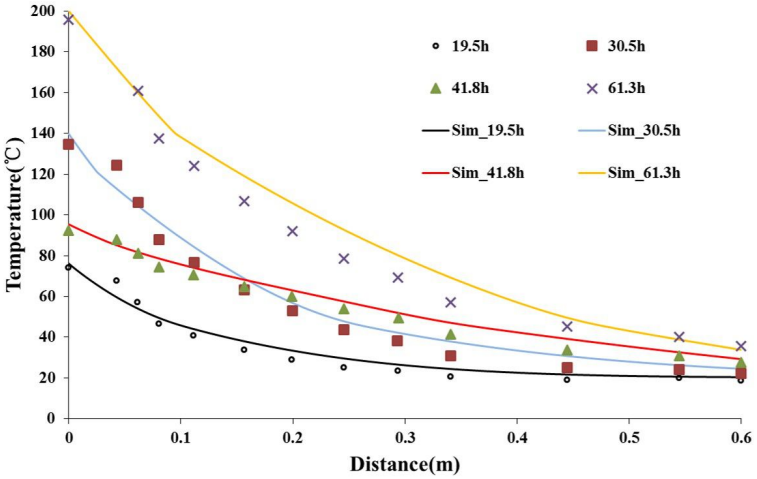

Figure 2.11: Evolution of temperature profile of the simulation and experimental data(Bary *et al.*, 2012)

The result of the simulation was generally in good agreement with the experimental results. Some difference occurred when the heating time reached 61.3h. It is probably due to the overestimation on permeability and thermal conductivity at high temperature in this study.

The comparison of the simulation and experiments in terms of relative humidity was shown in Fig.2.12, and the corresponding saturation degree profiles was shown in Fig.2.13.

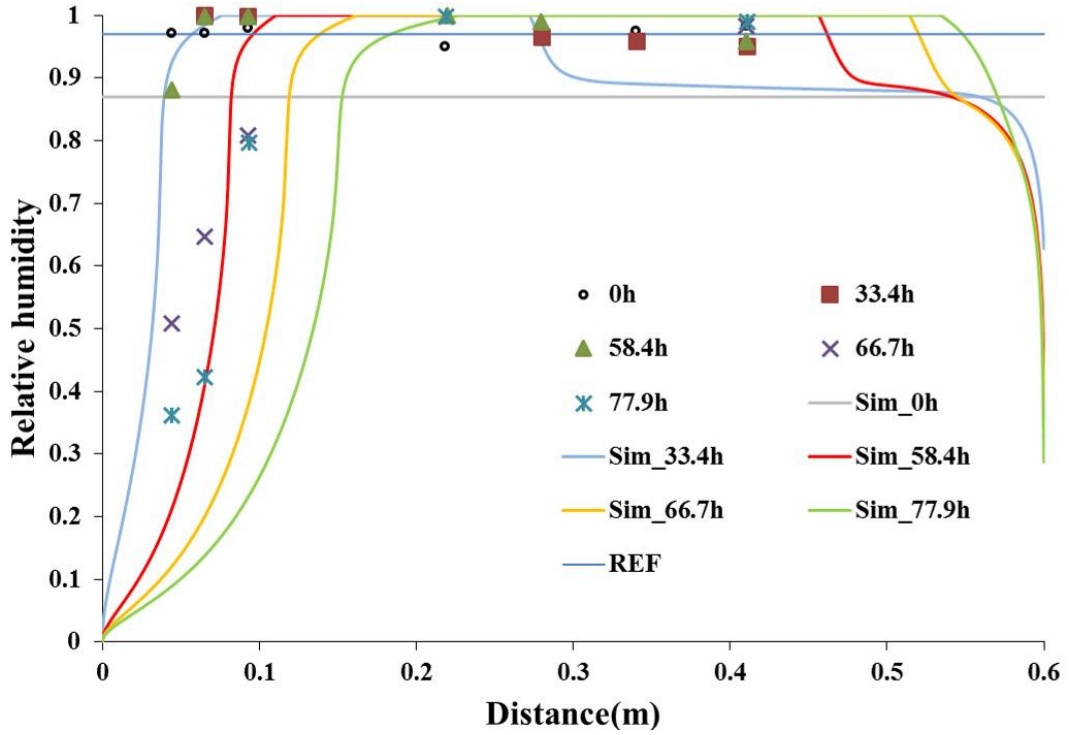

Figure 2.12: Evolution of relative humidity profile of the simulation and experimental data(Bary *et al.*, 2012)

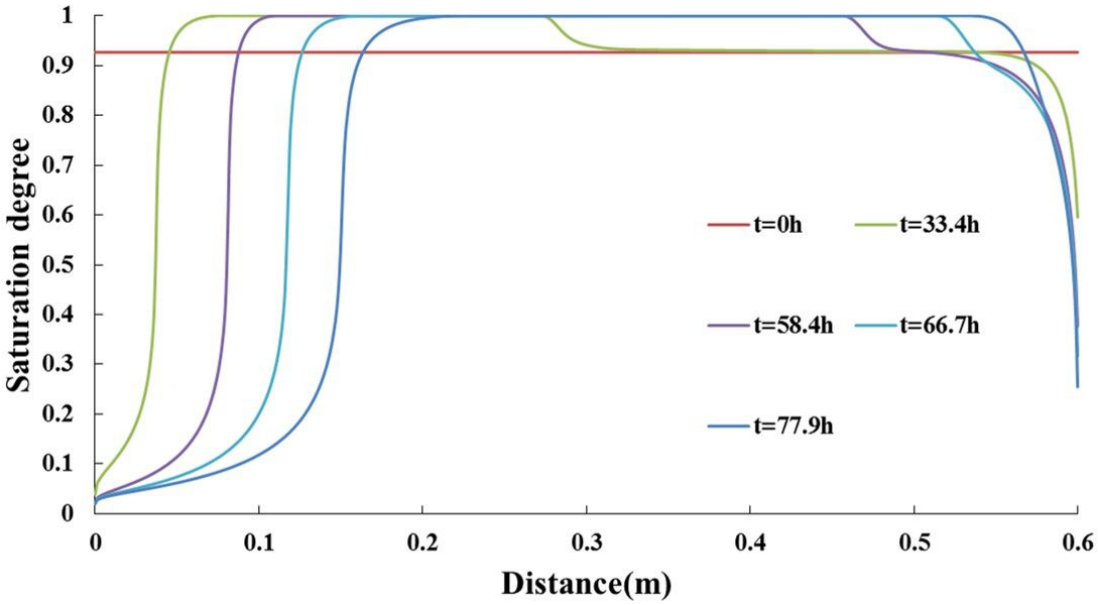

Figure 2.13: Evolution of simulated saturation degree of concrete at different time

As fig.2.12 illustrated, the simulation results of relative humidity was lower

than experimental results. The possible explanation of the difference is that with the initial condition that was mentioned before, the initial relative humidity was 0.874, while the measured value was more than 0.95(line with legend "REF"). Moreover, the desorption isotherm used in the simulation might be different from the real desorption isotherm of the concrete which was used for the experiment, because the fitting parameters a_c, b_c in Equation.1.7 depends on the type of concrete. The desorption isotherm is a very important property of concrete for the simulation, which may lead to quite different profile of saturation degree even two different simulations get same profile of relative humidity, and vice versa.
The intrinsic permeability of vapor was not obtained with experiment. According to the research from Chung(Chung, 2003), the Klinkenberg constant of concrete varies with the intrinsic permeability, so that might be one of the error sources as well(Equation.1.17).

The evolution of the gas pressure, which is vapor pressure in this study, was plotted in Fig.2.14. The peak of the pressure profile moved from interior boundary towards the exterior boundary. Generally, the simulated vapor pressure was 1-1.5 bar less than the experimental result, which could be the consequence of not considering dry air as component of the gas. Gawin(Gawin *et al.*, 2011) calculated the gas pressure evolution in a heated concrete cylinder. The gas was considered as mixture of air and vapor, so the vapor pressure was part of the gas pressure. The difference between gas pressure and vapor pressure could reach around 1.5 bar, which is almost the difference between the experimental value from (Bary *et al.*, 2012) and the simulation here. However, it should be noted that during the simulation in (Gawin *et al.*, 2011), the vapor pressure was almost as same as gas pressure, which means that the vapor pressure was dominant. It is also the one of reasons why the assumption that the gaseous phase consists only vapor is interesting and of acceptable accuracy when the vapor pressure is dominant in the gas pressure. However, the discrepancy between the vapor pressure and the real gas pressure cannot be ignored for the rest of the situation. For example, in Fig.25 in (Gawin *et al.*, 2011), when the temperature was elevated from room temperature at rate of 5K/min, the difference between the vapor pressure and gas pressure were notable in the first 1-2 hours.

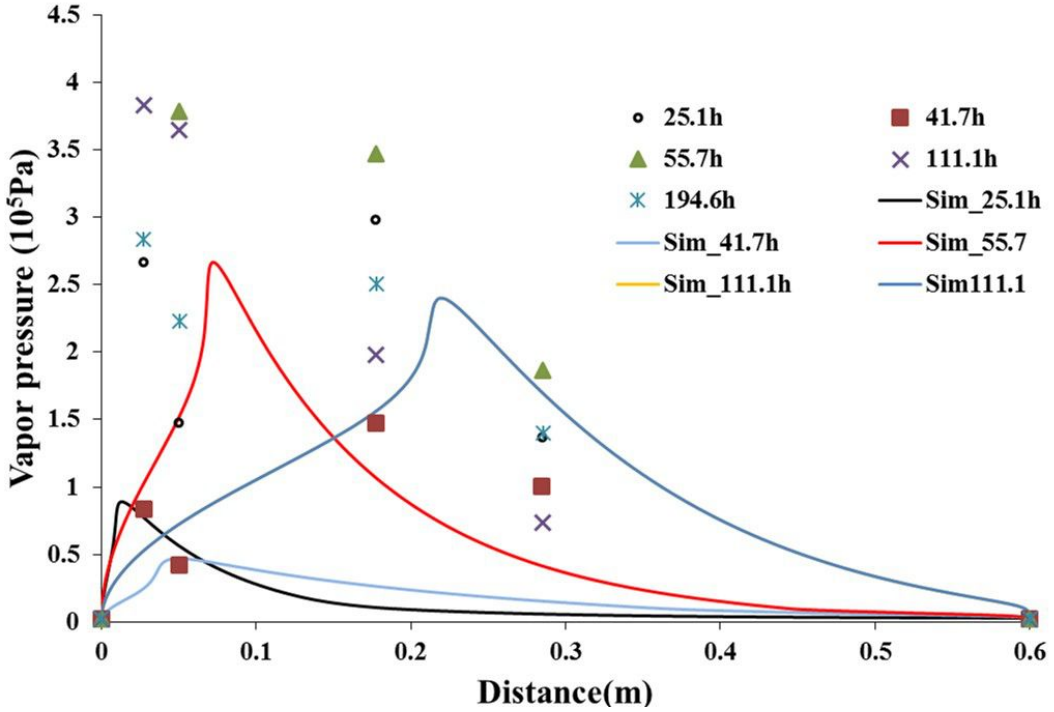

Figure 2.14: Evolution of vapor pressure profile of the simulation and experimental data(Bary *et al.*, 2012)

In order to get a better understanding of the model, the influence of some parameters is studied in the next chapter as well as some applications with different thermal boundary conditions and size of the structure.

Chapter 3

Parametric study and applications

In this chapter, the influence of heat of dehydration and permeabilities on thermo-hygral transfer in concrete are studied. Besides, different thermal boundary conditions are applied on the inner surface to see their influence. At last, the model was applied to structures with different thicknesses in order to study the influence of the thickness on the distribution of pressure temperature and water distribution in the structure. The reference simulations in this chapter are based on MAQBETH mock-up mentioned in section 2.3.1, while the thermal loading was adjusted to have a less calculation time. The temperature on the inner boundary was elevated from 20°C to 200°C at a heating rate of 0.1 K/min, and then the temperature was kept 200°C until the end of the simulation(see fig.3.1).

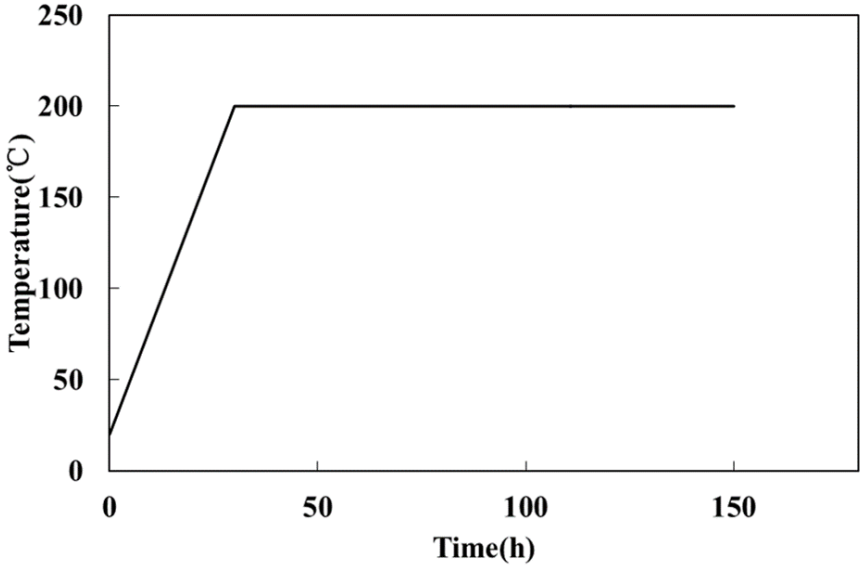

Figure 3.1: Temperature boundary condition for parametric study

3.1 Parametric Study

3.1.1 Latent heat of dehydration

In the thermo-hygral model that used in this study, the latent heat of dehydration $L_{s\to l}$ is considered as constant 2500[kJ/kg]. However, $L_{s\to l}$ for different cement paste may vary because the composition of hydrates may be different and the latent heat of dehydration for each hydrate differs from each other. Hence, the influence of $L_{s\to l}$ is interesting and is investigated by comparing the evolutions of temperature, relative humidity and gas pressure profiles, which are calculated with and without considering the latent heat of dehydration. The simulation without considering the latent heat of dehydration is denoted "no-H_dhy", and are shown in fig.3.2–fig.3.5

Fig.3.2 shows the evolution of temperature profiles. The temperature profile of "no-H_dhy " is higher than the reference in general because dehydration is an endothermic process. In the first 10h of the simulation, the difference between the two simulations are not so obvious except the part of the structure close to the inner surface. It is because the onset temperature of dehydration for the hydrates that are considered in the dehydration model T_{onset}^{CSH} and T_{onset}^{AFm} are both 313.75[K], and the dehydration does not take place in most part of the structure. The difference between the ” no-H_dhy” becomes more obvious as

the temperature goes higher. In the center of the structure, if $L_{s\to l}$ is neglected, the temperature difference will reach up to around 20°C at 30h. As the dehydration degree reached equilibrium, the rate of dehydration slows down and the "no-H_dhy" was overlapped eventually.

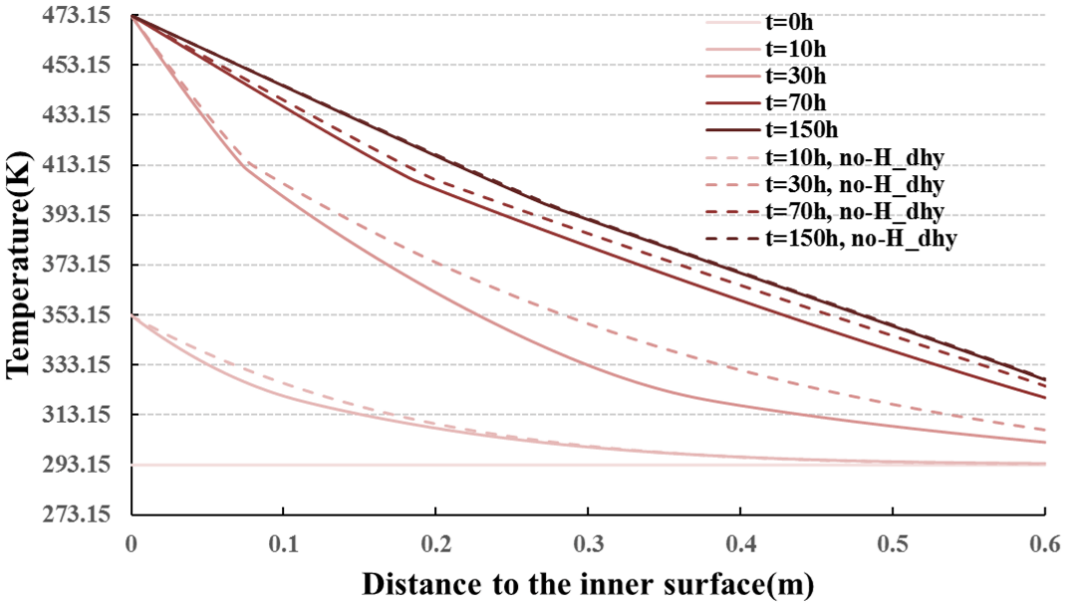

Figure 3.2: Evolution of temperature distribution without taking heat of dehydration into account

The evolution of relative humidity h_r and saturation degree of liquid water S_l are shown in fig.3.3 and fig.3.4. The tendency of the evolution of h_r and S_l for "no-H_dhy" are the same as that for the reference simulation. h_r near the interior surface increases at first. After that, when the temperature near the surface goes higher, the water transfer rate increases and a drying front is formed. The drying front moves towards the exterior surface during the simulation. The h_r and S_l drop at 70h and 150h is due to the constant vapor pressure boundary condition on the exterior surface. When the temperature on the exterior boundary increases, the saturated pressure p_{vs} increases as well. Hence, $h_r = p_v/p_{vs}$ decreases and forms an obvious drop. The drying front of "no-H_dhy" moves slightly faster than the reference simulation, because the temperature is higher than the reference simulation as mentioned above.

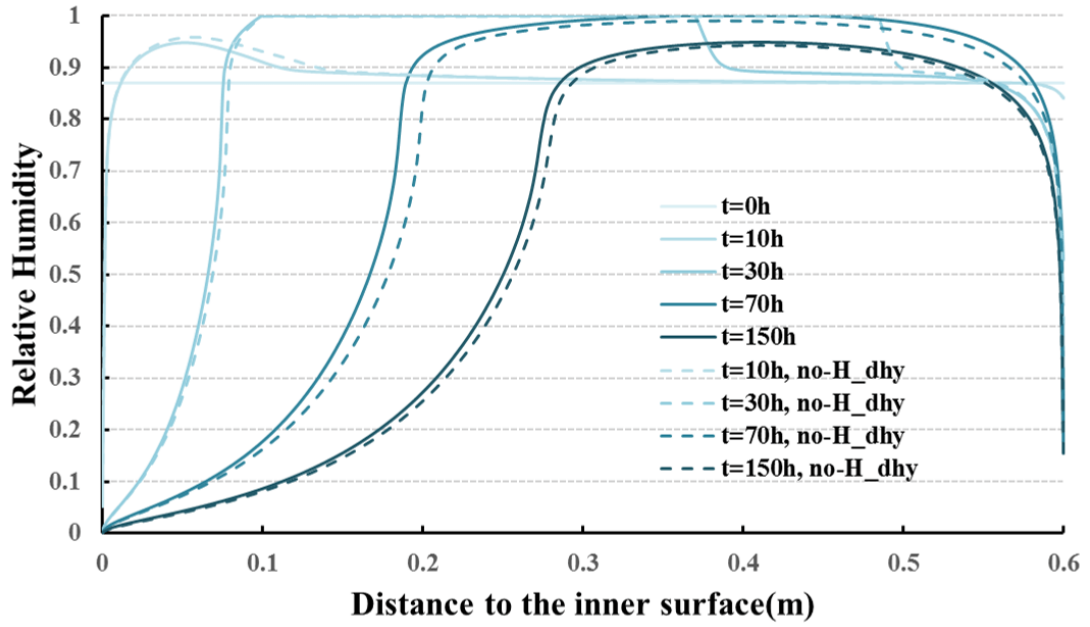

Figure 3.3: Evolution of relative humidity distribution without taking heat of dehydration into account

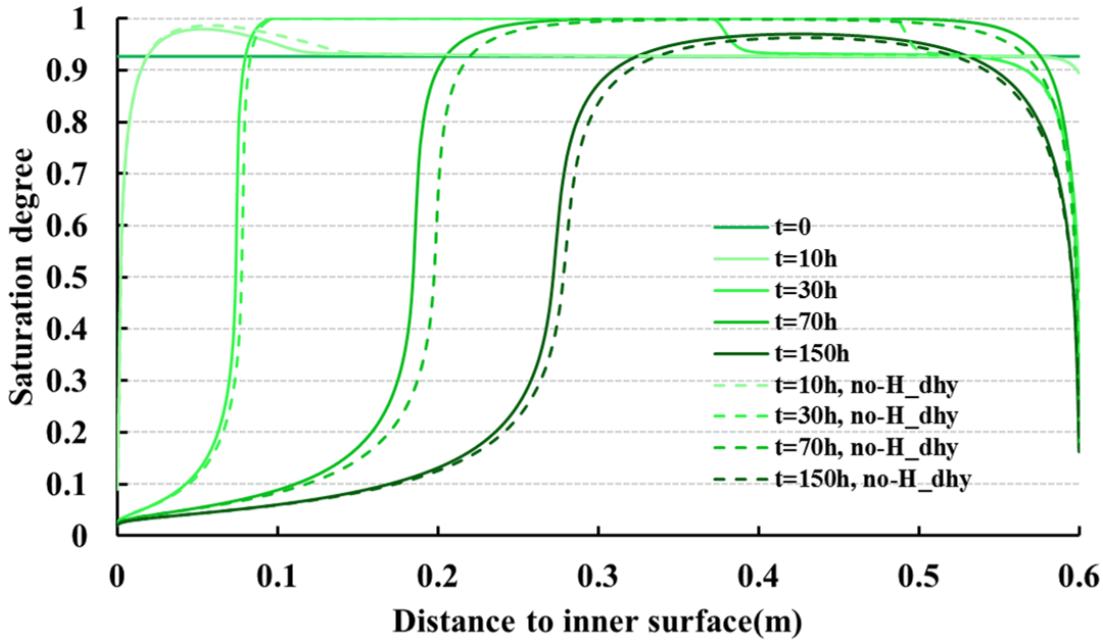

Figure 3.4: Evolution of saturation degree distribution without taking heat of dehydration into account

As can be seen from fig.3.5, the maximum gas pressure of ”no-H_dhy” is a little higher than the reference simulation, and reaches 3.3 [bar]. However,

at 70h, the difference of maximum gas pressure between the two simulations become negligible with a peak shifting towards the exterior boundary.
If the relative humidities are the same, the higher temperature will lead to higher gas pressure. Correspondingly, higher relative humidity will lead to higher gas pressure as well. By comparing the temperature and relative humidity profile at 70h, it could be noticed that, the temperature of "no-H_dhy" is higher than the reference, while the relative humidity is lower than the reference. The two effects on the gas pressure compensate around 70h, so the gas pressure curve showed the same peak value. Similarly, at 150h, when temperature profiles of the two simulations are the same, "no-H_dhy" predicted a lower gas pressure peak.

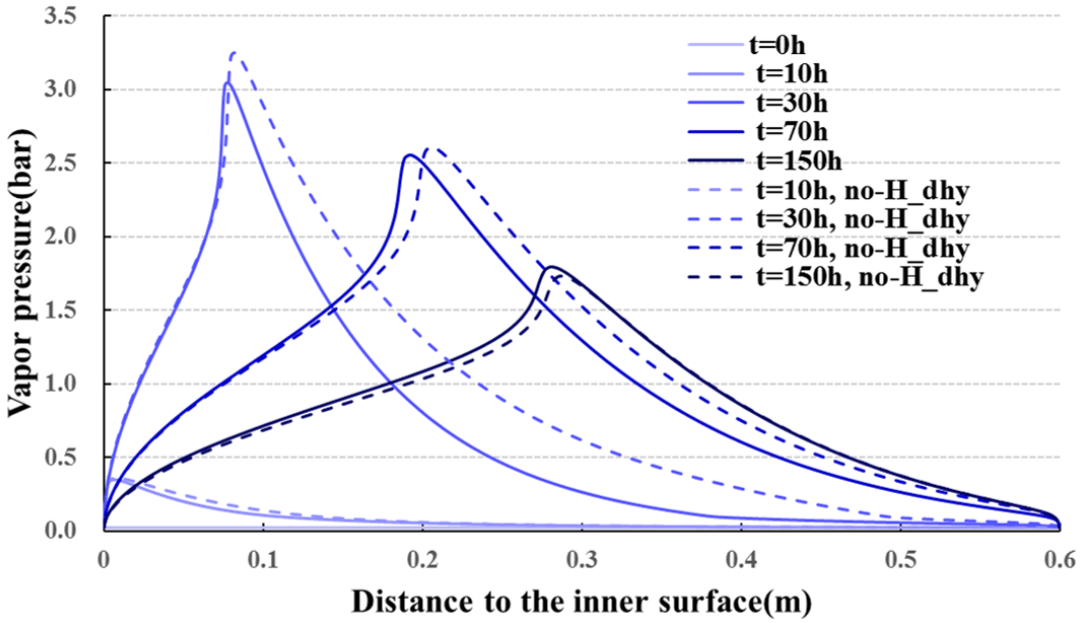

Figure 3.5: Evolution of vapor pressure distribution without taking heat of dehydration into account

3.1.2 Permeabilities

The permeabilities in the thermo-hygral model used in this study is not directly fitted by experiments. The initial intrinsic permeability to vapor $k_{mv}^0$was considered the same as that in (Bary *et al.*, 2012), and the intrinsic permeability to water k_{ml}^0 was calculated with equation.2.21, in which k_{ml}^0 is proportional to k_{mv}^0 with a coefficient a_k. In (Bary *et al.*, 2012), k_{mv}^0 and a_k were fitted to reproduce the h_r profiles, so here the effects of those two parameters on the transfer

process is investigated.

Different coefficient a_k

In this section, two different values of a_k($a_k = 9 \times 10^{-4}$ and $a_k = 1.3 \times 10^{-3}$) are adopted to compare with the value in section 2, $a_k = 1.1 \times 10^{-3}$. Both simulations were denoted with their values of a_k. From fig.3.6, the temperature profiles of all the simulations overlap with each other. Hence, for the studied thermal loading and material, a_k has little effect on the heat transfer.

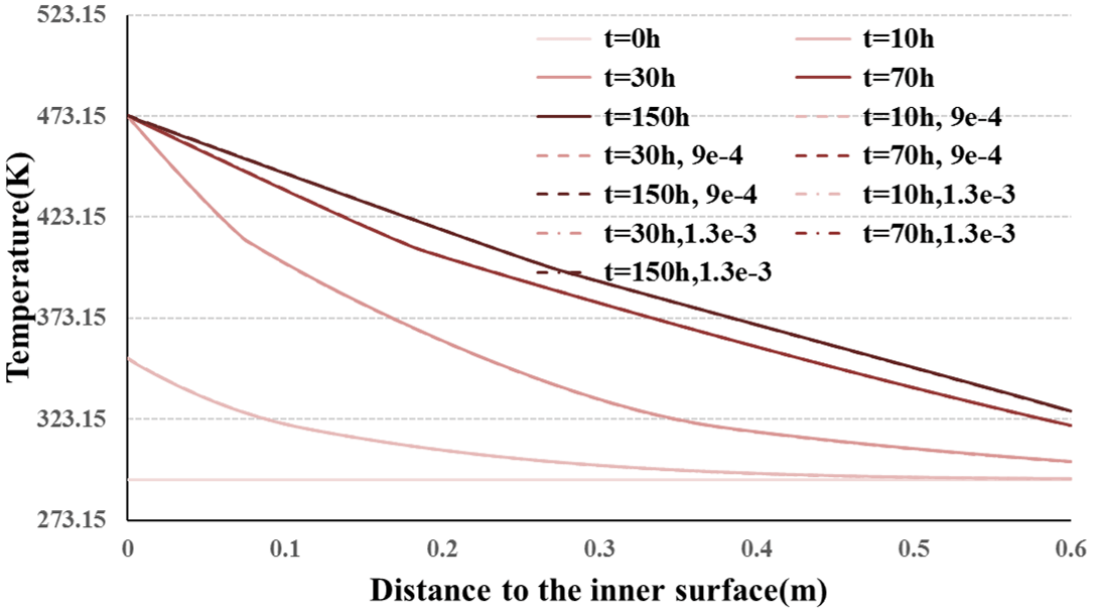

Figure 3.6: Evolution of temperature distribution with different coefficient

The evolutions of h_r and S_l profiles are shown in fig.3.7 and fig.3.8. On the inner side of the drying front, there is no difference that can be observed among "9e-4", "1.3e-3" and the reference; on the other side, some disparity can be observed, and "9e-4" predicted higher h_r and S_l. This is because a_k reflects the rate of liquid water transfer. The comparison indicates a variation of nearly 20% of the coefficient does not play an important role in the water immigration towards the high temperature boundary. Instead, it affects the water transfer in the part of the structure which is between the drying front and the exterior surface. For different concretes, investigations with larger variations could be carried out.

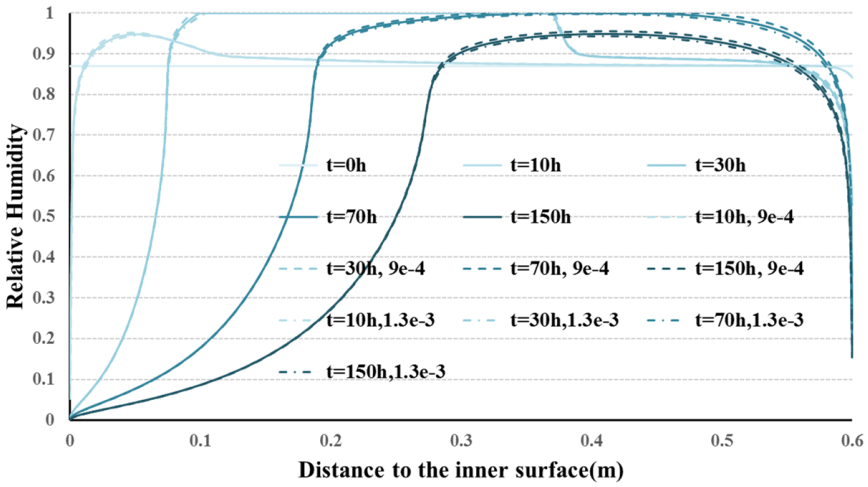

Figure 3.7: Evolution of relative humidity distribution with different coefficient

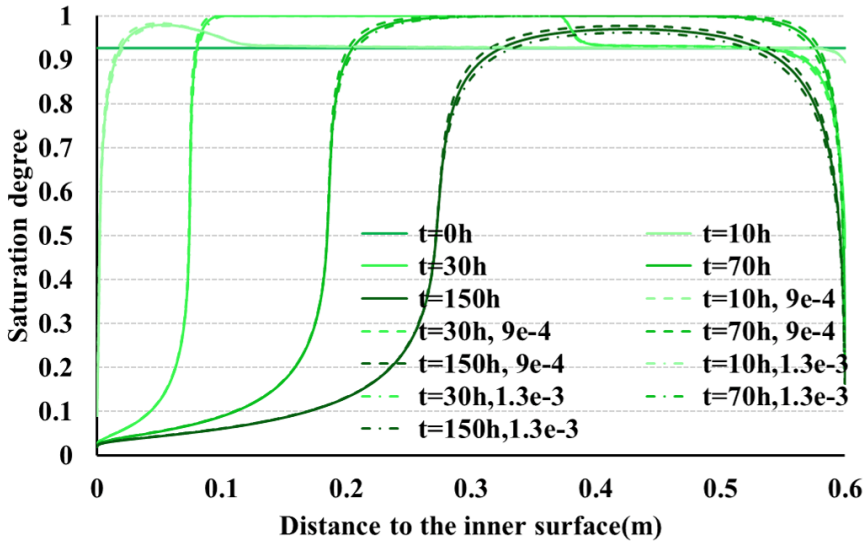

Figure 3.8: Evolution of saturation degree distribution with different coefficient

Fig.3.9 illustrates the influence of a_k on vapor pressure distribution. There is no obvious difference among the three simulation except at 30h, where "9e-4" predicted slightly higher vapor pressure where $r > 0.1$[m].

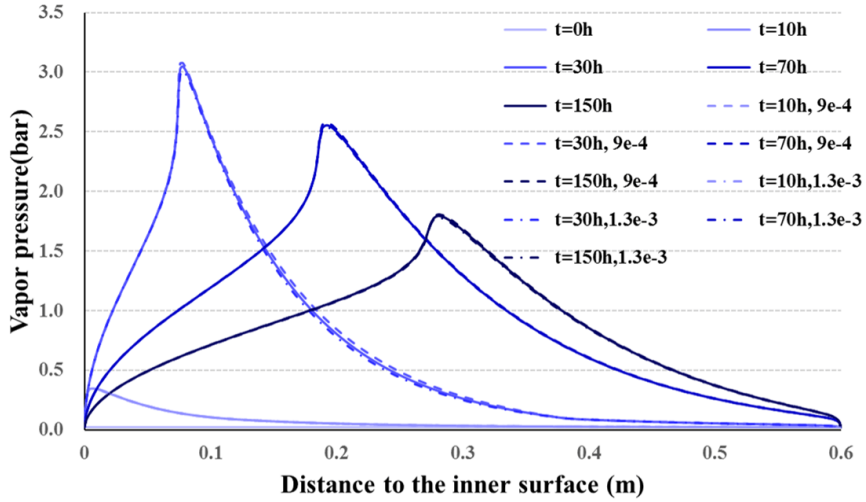

Figure 3.9: Evolution of vapor pressure distribution with different coefficient

Different initial intrinsic permeabilityk_{mv}^0

To investigate the influence of initial intrinsic permeability k_{mv}^0, the adopted value in section 2 1×10^{-17}[m^2] is multiplied by 0.8("0.8kv") and 1.2("1.2kv"). The evolutions of temperature are shown in fig.3.10. There is only a very little effect of water vapor transfer on heat transfer in studied concrete in the first 70h.

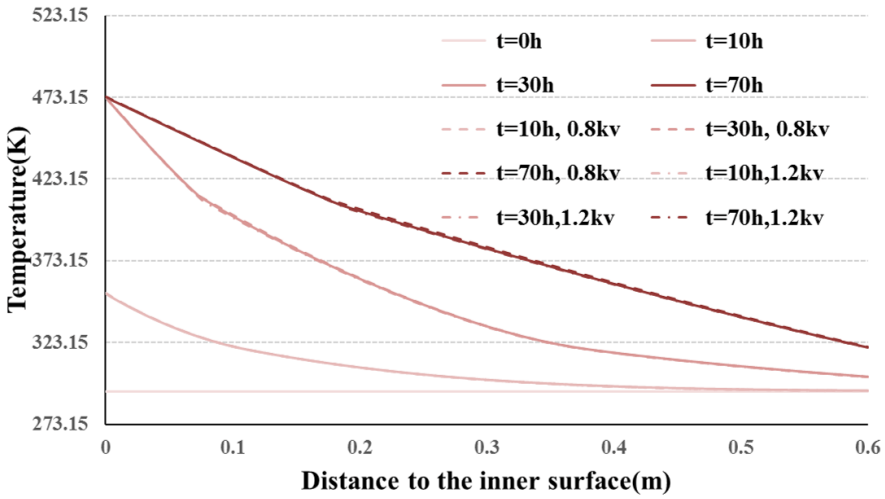

Figure 3.10: Evolution of temperature distribution with different intrinsic permeability to vapor k_{mv}^0

For the evolutions of h_r and S_l, the comparisons are shown in fig.3.11 and fig.3.12. The lower h_r and S_l profiles predicted by "1.2kv" means the higher

permeability to water vapor accelerates the water migration towards the interior surface. Besides, the difference between "1.2kv" and reference in the center of the structure, where the structure is nearly saturated, is smaller than that at the drying front.

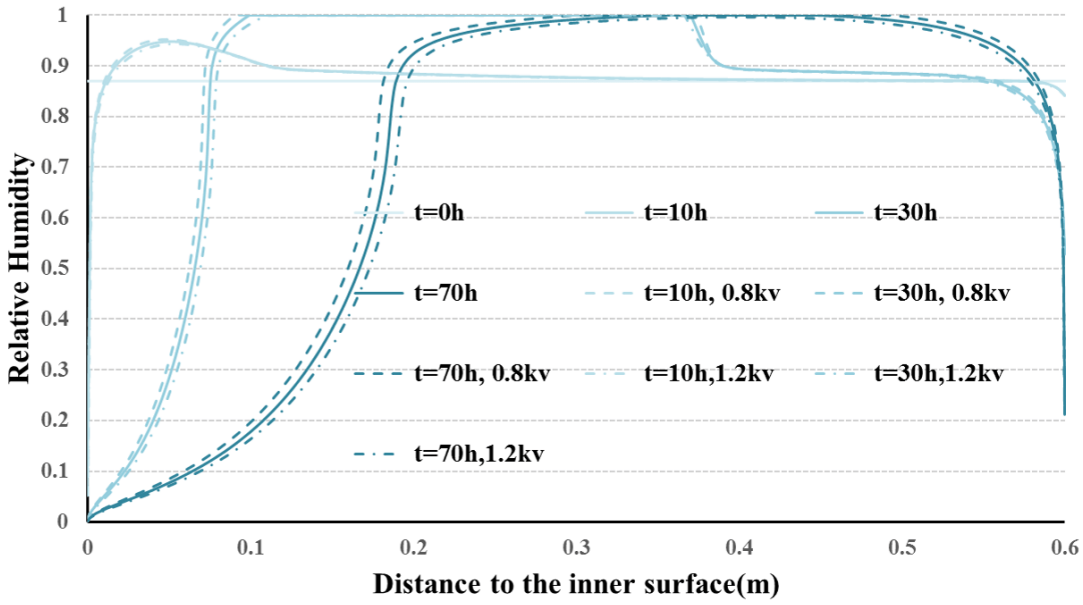

Figure 3.11: Evolution of relative humidity distribution with different intrinsic permeability to vapor k_{mv}^0

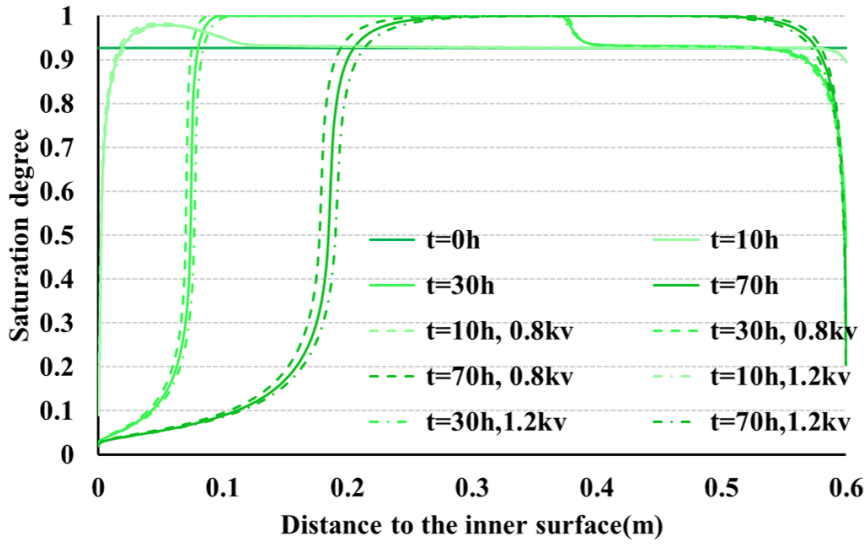

Figure 3.12: Evolution of saturation degree distribution with different intrinsic permeability to vapor k_{mv}^0

Unlike the liquid water, vapor transfer rate distinctly affects the vapor pressure. The maximum vapor pressure increases more than 0.2[bar] if k^0_{mv} is reduced to 80% of the reference, and decreases more than 2.5[bar] if k^0_{mv} increases 20%.

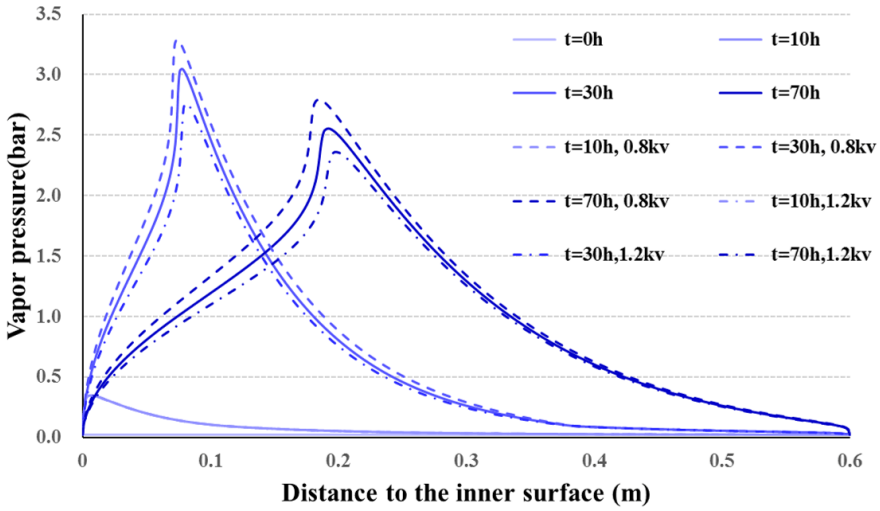

Figure 3.13: Evolution of vapor pressure distribution with different intrinsic permeability to vapor k^0_{mv}

3.2 Applications

In order to get a better understanding of the thermo-hygral transfer of concrete under different thermal loadings, which means different heating rates on the interior boundary, two different boundary conditions were adopted to simulate the transfer process, and compared with the reference. Besides, the size of the structure, especially the thickness of the structure is interesting for the nuclear containment. Two simulations are made to get the temperature, gas pressure and relative humidity distribution in structures with different thickness.

3.2.1 Effect of heating rate on the interior boundary

Two different heating rates, 0.2K/min(denoted by "0.2K") or 0.05K/min(denoted by "0.05K"), were adopted to compare the simulation result with the reference(0.1K/min). The thermal loadings on the inner surface are shown in fig.3.14

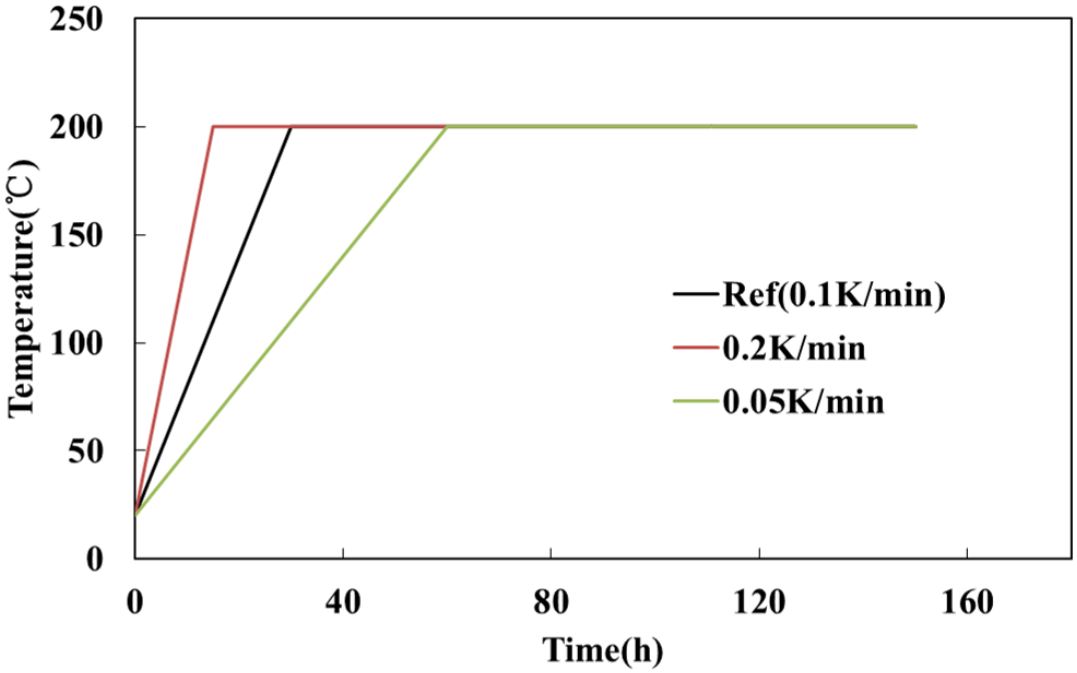

Figure 3.14: Boundary conditions with different heating rates

The comparison of evolutions of temperature profiles between the reference and ”0.05K” and ”0.2K” is shown in fig.3.15.
As can be seen from fig.3.15a, when the temperature on the surface is rising, there is large temperature difference between ”0.05K” and reference, especially near the inner surface. When the inner boundary temperature reaches 200°C, the difference between those two simulations starts to decrease. At 150h, there is only very slight difference between ”0.05K” and the reference. Fig.3.15b shows the comparison between ”0.2K” and the reference. Similarly, the difference between the two simulations decreases when the inner boundary reaches 200°C. At 70h, although ”0.2K” has longer time when the inner boundary reaches the highest temperature, it still has some difference from the temperature profile at 150h. The much smaller difference than that between 30h and 70h means that at 70h, the temperature distribution in the structure becomes quasi-independent of the heating rate.

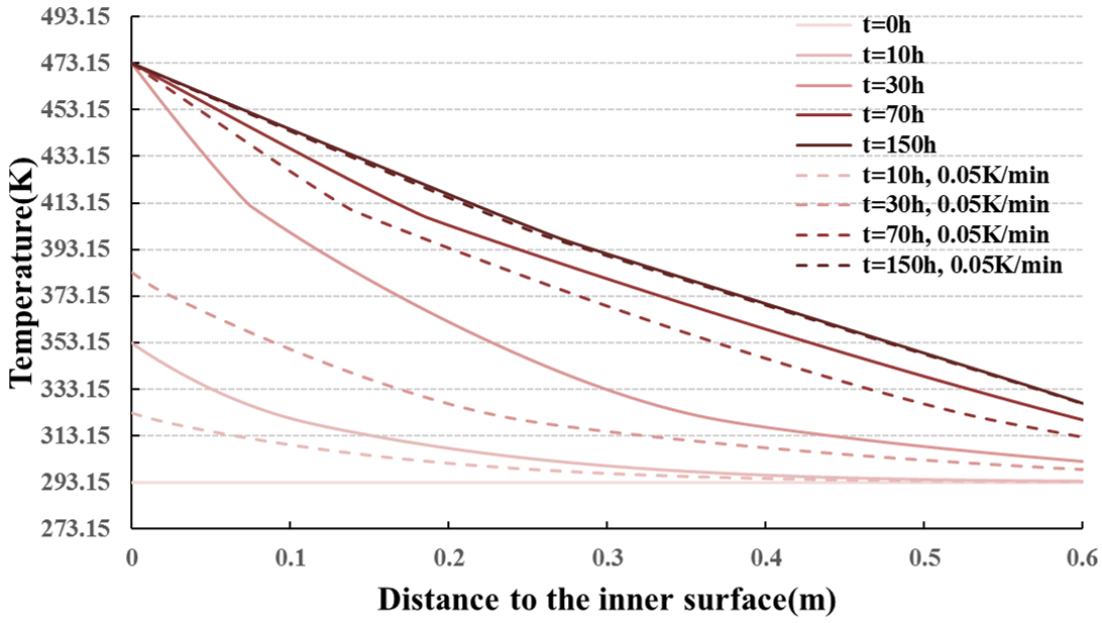

(a)

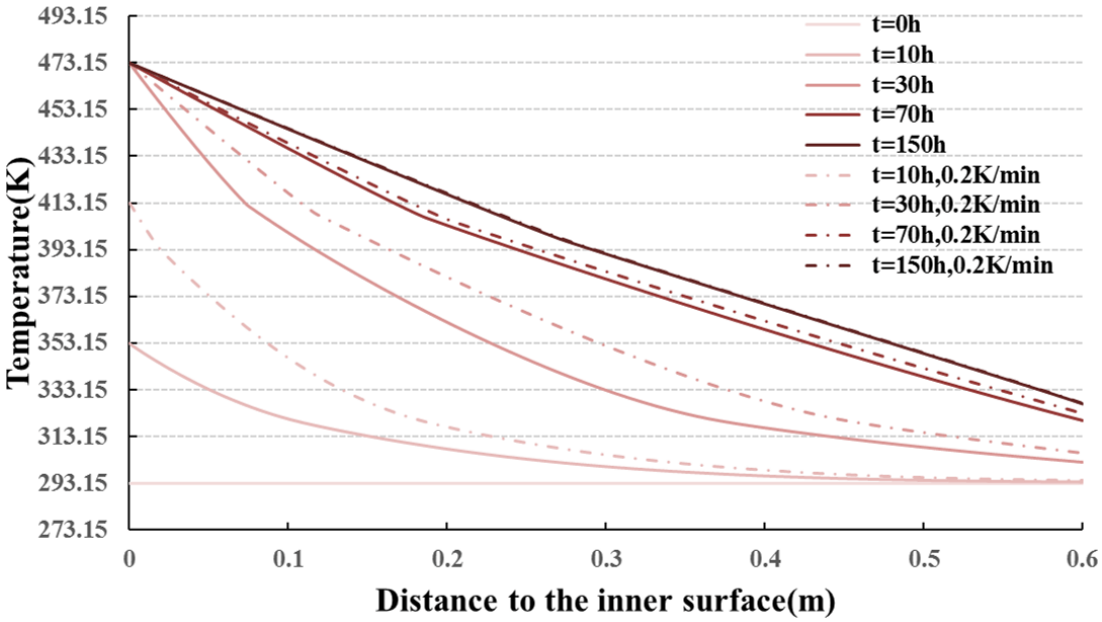

(b)

Figure 3.15: Evolution of relative humidity distribution in the structure under heating rate of (a)0.05K/min (b)0.2K/min

The comparison of h_r and S_l are shown in fig.3.16 and fig.3.17. As can be seen from fig.3.16 and fig.3.17. "0.05K" shows delayed water distribution evolution comparing to the reference. h_r and S_l is no lower than that of the reference except at 10h. It is because of the effect of the dehydration, which

releases water to the structure. From fig.3.15a, it can be noticed that at around r<0.15[m] at 10h, the temperature of reference is higher than the onset temperature of dehydration. It explains the peak in the corresponding part in fig.3.16 and fig.3.17. Similar to the evolution of temperature profile, h_r profiles of different heating rates will have less and less difference once the boundary temperature reaches 200°C. However, at 150h, when the difference of the temperature profiles between different heating rates vanishes, there is still observable disparity in the h_r and S_l profile. For the simulation with faster heating rate "0.2K"(fig.3.16 and fig.3.17), the difference from the reference is less than that of "0.05K". At 150h, h_r and S_l of "0.2K" are still lower than the reference in general. However, the difference is smaller than "0.05K", and for the parts near boundaries(r<0.1[m] and r>0.4[m]), there is hardly any disparity that can be observed between "0.2K" and the reference.

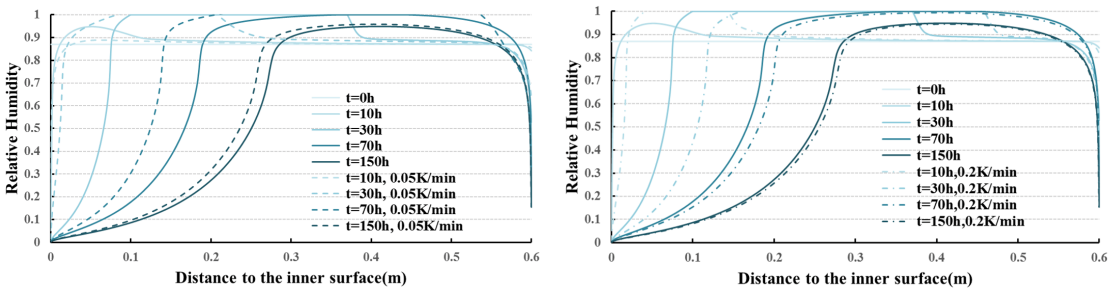

Figure 3.16: Evolution of relative humidity distribution in the structure under heating rate of (a)0.05K/min (b)0.2K/min

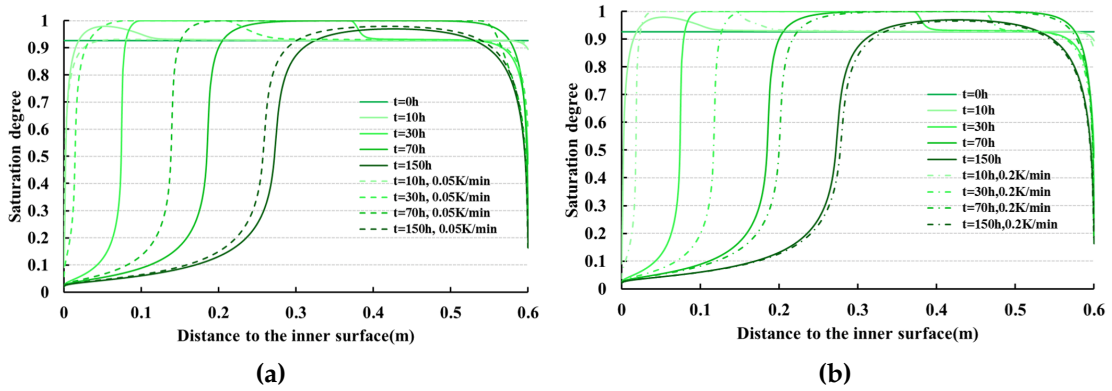

Figure 3.17: Evolution of saturation degree of liquid water S_l distribution in the structure under heating rate of (a)0.05K/min (b)0.2K/min

The vapor pressure evolutions are shown in fig.3.18. The position of the vapor pressure peak is affected by heating rate. The slower heating rate on the inner boundary shifts the peak towards the inner surface, while the faster heating rate shifts the vapor peak towards the exterior surface.

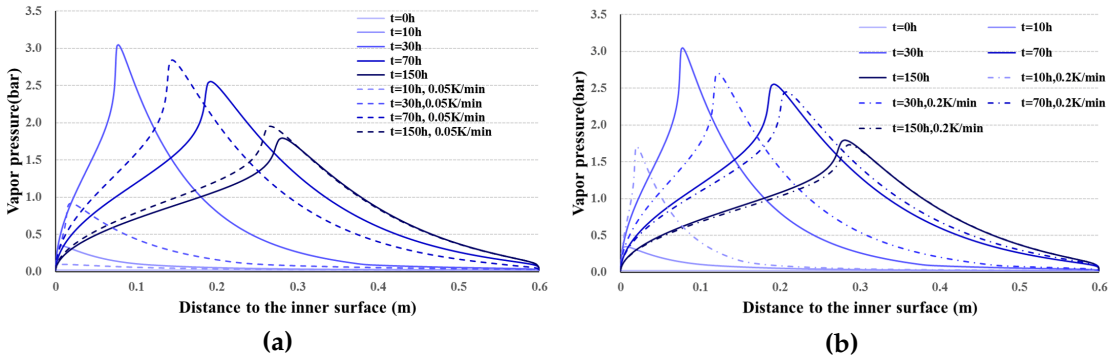

Figure 3.18: Evolution of vapor pressure p_v distribution in the structure under heating rate of (a)0.05K/min (b)0.2K/min

As can be see from fig.3.18a, the vapor pressure of "0.05K" increase much slower than the reference. At 10h, the peak value of p_v for "0.05K" is less than 0.2[bar], which is only half of the corresponding value for the reference. The difference increases at first and then, like the evolution of temperature and water content, it diminishes gradually. In the end of the simulation at 150h, the peak vapor pressure of "0.05K" was around 10% larger than the reference. It is worth being noticed that during all the simulations, the value of the peak vapor pressure increases at first, and then decreases because the loss of water, so "0.05K" always shows a "delay" effect, but the effect becomes less and less after 70h. Compared to "0.05K", "0.2K" shows the opposite effect. From fig.3.18b, it shows that the vapor pressure reached more than 1.5[bar] near the surface at 10h. Since the maximum vapor pressure of "0.05K"appeared later than the reference(at around 70h), the maximum vapor pressure should be appeared earlier than 30h. The maximum vapor pressure was found at around 16h(see. fig.3.19), and heating rate does not affect the maximum vapor pressure.

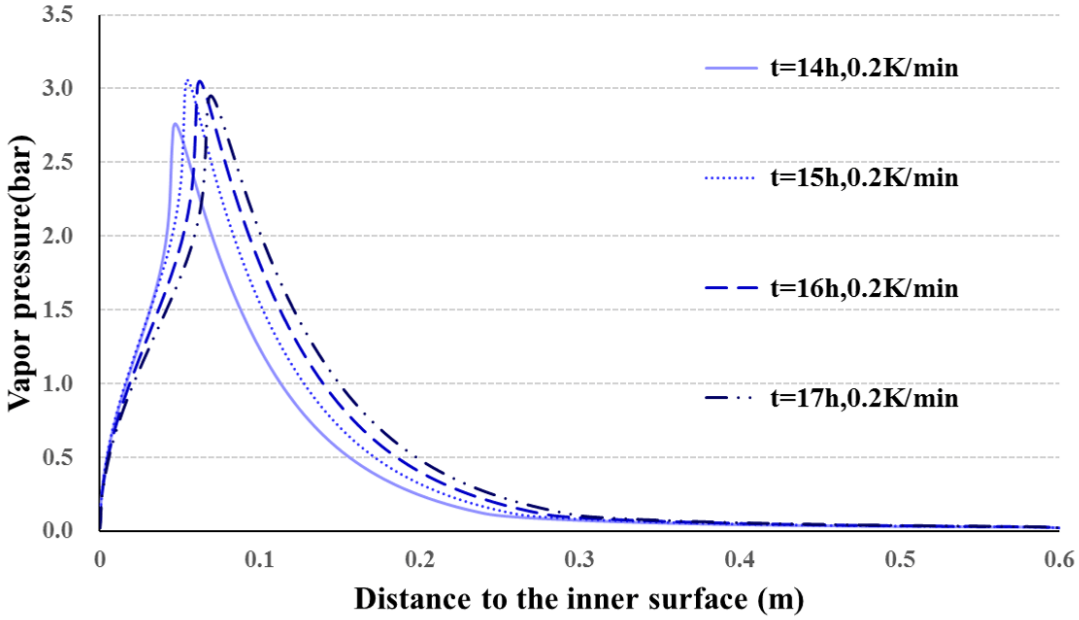

Figure 3.19: Vapor pressure evolution of ”0.2K”

3.2.2 The size of the structure

The thermo-hygral transfer in structures with different thicknesses were simulated. Two thickness of the structure were adopted: 0.2[m](”0.2m”) and 0.4[m](”0.4m”). Both of them are compared with the reference simulation in which the thickness of the structure is 0.6[m].
The temperature evolutions are shown in fig.3.20. In the first 10h, the temperature distributions among the three simulations do not show obvious difference if T is considered as a function of distance to the inner surface r. At 30h, ”0.2m” exhibits some differences from the other two, the temperature at the position where $r > 0.1$[m] is lower than that ”0.4m ” and the reference. This difference becomes more obvious afterwards. In general, although the thinner structure has the lower temperature at the exterior surface, it has greater temperature gradient in the simulation.

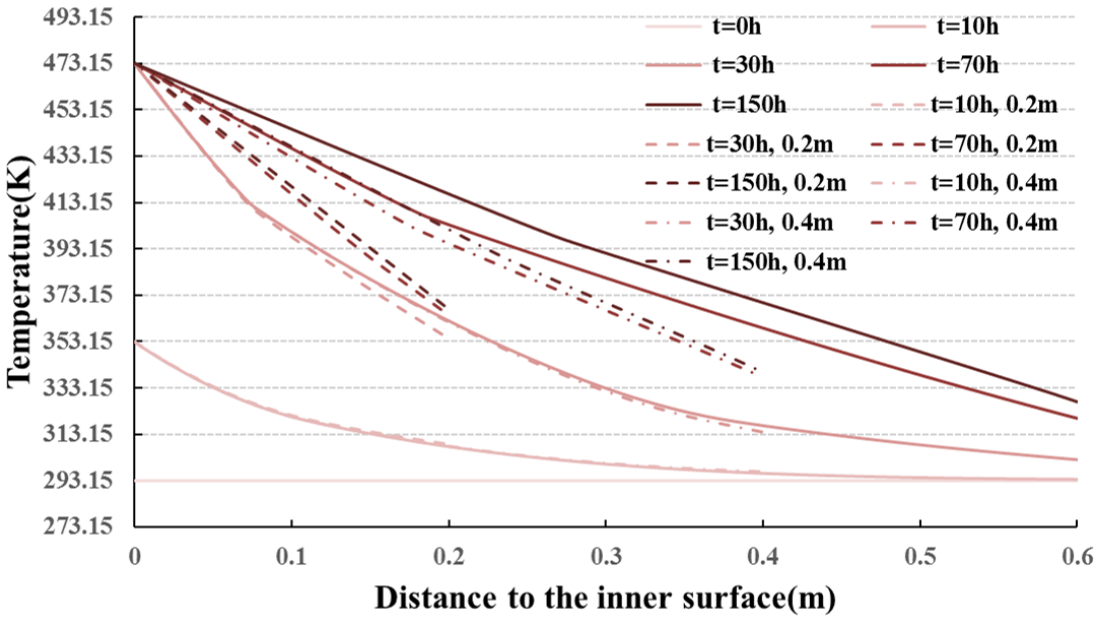

Figure 3.20: Evolution of temperature distribution in structures of different thickness

The comparison of h_r and S_l are shown in fig.3.21 and fig.3.22. The thinner structure is dried faster than the thicker ones in general. However, in the beginning of the simulation, it is not obvious, especially at the the drying front. As can be seen from fig.3.21a and fig.3.22a, the h_r and S_l distribution at $r < 0.05$[m] are almost the same as that of the reference at 10h. The difference at the drying front between "0.4m" and the reference will not be noticed until 70h, when the disparity is still very small(see. fig.3.21b and fig.3.22b). When the simulation is over 70h, "0.2m"shows a strong drying effect, and the maximum saturation degree is 0.5 at 70h. Furthermore, at 150h, the maximum saturation degree of "0.2m" drops to around 0.1, which means it is at a very dry state while "0.4m" still has a maximum saturation degree of 0.87.

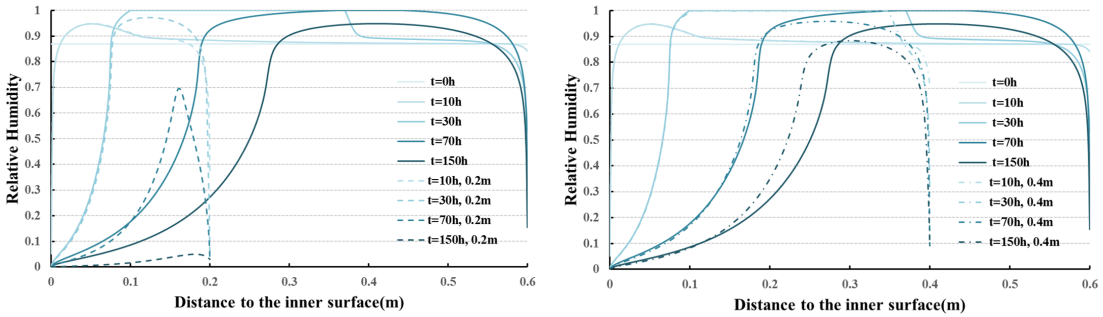

Figure 3.21: Evolution of temperature distribution in structures of different thickness (a)0.2m (b)0.4m

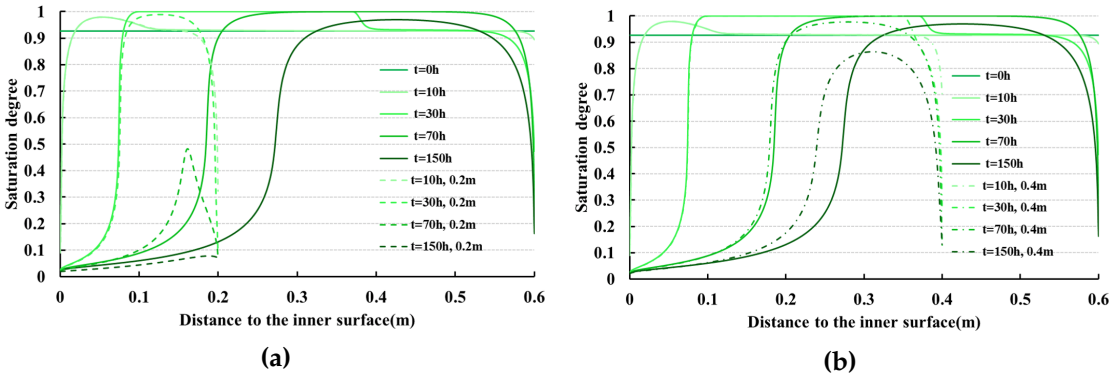

Figure 3.22: Evolution of saturation degree distribution in structures of different thickness (a)0.2m (b)0.4m

The evolutions of the vapor pressure are shown in fig.3.23 and fig.3.24.

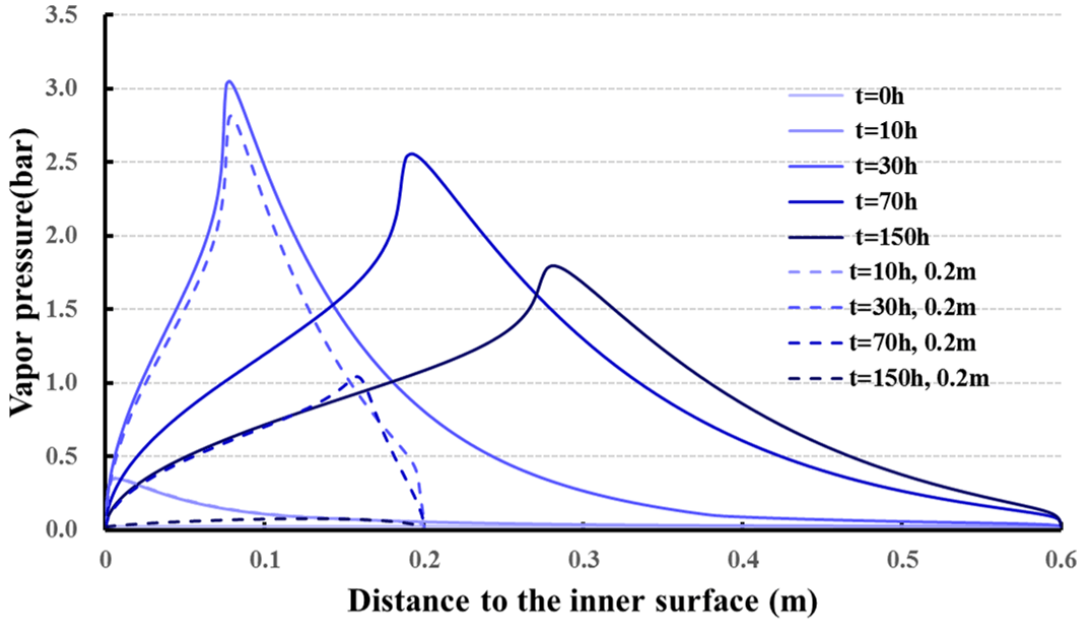

Figure 3.23: Evolution of relative humidity distribution in structures with thickness of 0.2m

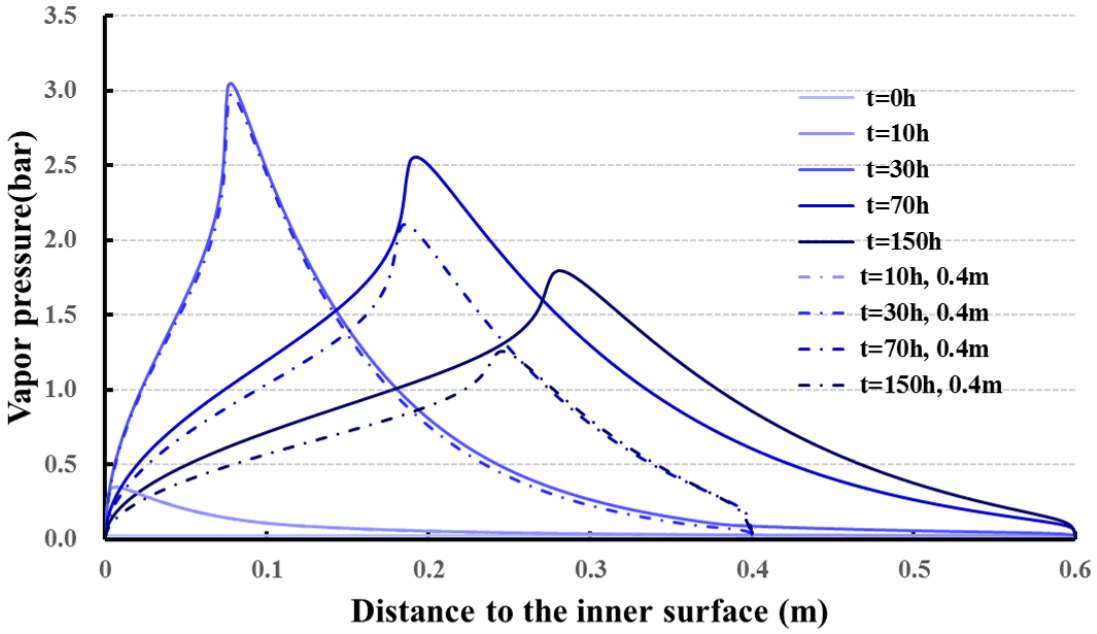

Figure 3.24: Evolution of relative humidity distribution in structures with thickness of 0.4m

Since the temperature and relative humidity distributions show no difference among the three simulations at 10h, the vapor pressure profiles at 10h

overlap each other. Between 0.2[m] and 0.6[m], the thickness does not affect the maximum vapor pressure a lot. The maximum vapor pressure of "0.2m" is slightly smaller than the reference, and "0.4m" has closer maximum vapor pressure to the reference than "0.2m". However, the thinner the structure is, the faster the peak of the p_v drops, because water has shorter path to move out. Besides, the higher temperature gradient means lower saturated vapor pressure. Hence, at 150h, the vapor pressure of "0.2m" is lower than 0.1[bar].

Conclusion of Part II

In this part, the dehydration model was implemented in the thermo-hygral model for concrete up to 200°C. The model was validated with MAQBETH mock-up(Bary *et al.*, 2012) via a simulation with the finite element software COMSOL Multiphysics.

Some assumptions were made for the thermo-hygral model: 1)only liquid water and water vapor were considered as composition of fluid. 2) liquid water is incompressible 3) the skeleton of concrete has no deformation. 4) Since the temperature is up to 200°C, only the dehydration of C-S-H and the interlayer of monosulfate was taken into consideration.

The profiles of temperature, relative humidity, saturation degree of liquid water and vapor pressure were used to evaluate the simulation.

In general, the simulation well predicted the temperature evolution. The disparities between the predicted results and the experimental results from (Bary *et al.*, 2012) are mainly due to following reasons: 1) the permeabilities of the concrete in the model are not obtained from experiment. 2) the initial relative humidity in the simulation was set to make the initial pressure identical to boundary condition to reduce the numerical difficulty, and it was not the same as that in the experiment. 3) the assumption that only water vapor is the gaseous phase, which affects the gas pressure distribution.

The effects of latent heat of dehydration $L_{s\rightarrow l}$, initial intrinsic permeability to vapor k_{mv}^0 and the coefficient a_k, which is used to calculate the permeability to liquid water, on the thermo-hygral transfer were investigated by comparing with a reference simulation.

The parametric study has shown that for the value tested in this study 1) a_k did not have much effect on the temperature, water content and gas pressure in the concrete. 2) k_{mv}^0 almost have no influence on the evolution of temperature profile, but the increase of k_{mv}^0 led to lower gas pressure and made the drying front move faster towards the exterior. 3) Without considering the la-

tent heat of dehydration, temperature was overestimated, drying front moved faster and the maximum gas pressure increase at first, but decreased afterwards. The thermo-hygral model then was applied to the simulations with different thermal loadings and different thicknesses for the structure to investigate the heat and mass transfer in different conditions. For a 0.6m thick wall, the heating rates investigated have low influence; on the other hand, the wall thickness has a great influence as a drying effect amplifier, as expected with thinner walls.

Modeling of Concrete Dehydration and Multiphase Transfer in Nuclear Containment Concrete Wall during Loss of Cooling Accident

Abstract

Nuclear power plant now takes an important part in the world's electricity generation. In human history, there have already been two tragic accidents in Chernobyl and Fukushima causing severe radioactive matter leakage. To prevent this kind of accident from happening again, concrete structure plays an important role as material of containment building, which is the last barrier to isolate the radioactive matter from the environment. Hence, the transfer properties of concrete under severe circumstances, especially high temperature, are important for this usage. This PhD thesis aims to investigate the behavior of the concrete under high temperature up to 200°C. In the first part, a dehydration model was proposed. The model consists of different dehydration sub-models for main hydrates in the cement paste. In the second part, the dehydration model was implemented in a thermo-hygral model. The thermo-hygral model was then used to simulate a mock-up for which experimental results are available in the literature, without considering the mechanical behaviors. At last, parametric studies were performed to investigate the influence of some parameters, and the model was then applied to structures under different heating rates, and structures with different thicknesses to compare the temperature and gas pressure profiles across a wall.

Keywords: concrete, cement paste, dehydration, high temperature, thermo-hygral model, non saturated porous media.

Conclusion and perspective

The main object of this thesis is to proposed a dehydration model for cement paste, and implement it in the thermo-hygral model for concrete.
In part I, the dehydration model for cement paste was proposed. The dehydration model includes the kinetics and the equilibrium of the dehydration. Since it consists of four main hydrates in the paste of ordinary Portland cement(CH, C-S-H, C_4ASH_8, C_3AH_6), it can be applied to another cement pastes with known composition.

It takes following steps to calculate the water release due to dehydration with this model:

1. Use the hydration model(Buffo-Lacarrière *et al.*, 2007)(Kolani *et al.*, 2012) to calculate the amount of the C-S-H, CH, AFm and C_3AH_6.

2. Determine the amount of interlayer water in monosulfate according to the drying condition.

3. Use the dehydration model for each hydrate to calculate the water release of them.

The dehydration model was validated with experiments in literature, and showed good compatibility predicting the dehydration process without considering decarbonation. It was also compared with the experiment in LMDC Toulouse under different heating rate, and able to predicted the dehydration process as well. The dehydration model for CH and C_3AH_6 have constant equilibrium dehydration degree because of their crystallized structure. The dehydration model for $C_4A\bar{S}H_{12}$ was separately into dehydration of interlayer water and mainlayer water because of their different dehydration mechanism. The dehydration model was in the similar form as the bound water

of $C_4A\bar{S}H_{12}$, and the parameters were determined by using the experimental results and the calculation of dehydration for other three hydrates.

In part II, the dehydration model was implemented in a thermo-hygral(TH) model. The main simplification of the TH model is that only water vapor was considered as the gaseous phase during mass and heat transfer in concrete.
The model was validated with the MAQBETH mock-up without considering the mechanical aspects. The finite element software COMSOL Multiphysics was adopted to implement the governing equations and then for the simulation, the temperature, relative humidity and vapor pressure profiles were compared with the experimental results in (Bary *et al.*, 2012). Despite the misunderstanding of the real permeabilities, and initial vapor pressure, the predicted results showed acceptable agreement. The parametric study for the TH model showed the influence of latent heat of dehydration, intrinsic permeabilities on heat and mass transfer in concrete. The higher initial intrinsic permeability leads to lower gas pressure and faster movement of the drying front. The higher intrinsic permeability to water makes the drying front move faster as well. If the latent heat of dehydration is not taken into consideration, the temperature will be overestimated and drying front will move faster, and the maximum gas pressure will be larger than the reference and then decrease to become smaller than the reference. At last, the model was applied to structures with different thickness and different heating rates on inner boundary to investigate the influence of size and thermal loading on the heat and mass transfer in concrete.

There are still some aspects that should be paid attention to in the future.
First of all, not all the hydrates are taken into consideration. To get a more accurate prediction, dehydration of other hydrates should be studied, specifically if composite binders are used.
For the mass and heat model, the mechanical aspects should be taken into consideration, mainly the cracks, which can significantly change the permeabilities, and consequently the fluid pressure. Besides, if the composition of fluids can reflect the real fluids in the concrete, the accuracy can be improved as well.
The hysteresis of isotherm was neglected in this study, so further effort can be put into this part.

Bibliography

F. Adenot. *«Durabilité du béton: caractérisation et modélisation des processus physiques et chimiques de dégradation du ciment»*. Ph.D. thesis, Université d'Orléans, 1992.

S. Ahmed and H. Taylor. Crystal structures of the lamellar calcium aluminate hydrates. *Nature*, pages 622–623, 1967.

T. Al-Shemmeri. *Engineering fluid mechanics*. Bookboon, 2012.

L. Alarcon-Ruiz, G. Platret, E. Massieu, and A. Ehrlacher. The use of thermal analysis in assessing the effect of temperature on a cement paste. *Cement and Concrete Research*, 35(3):609 – 613, 2005.

R. Allmann. Refinement of the hybrid layer structure $[Ca_2Al(OH)_6]^+[1/2SO_4 \cdot 3H_2O]^-$. *Neues Jahrbuch für Mineralogie Monatshefte*, pages 136–143, 1977.

C. Alonso and L. Fernandez. Dehydration and rehydration processes of cement paste exposed to high temperature environments. *Journal of Materials Science*, 39(9):3015–3024, 2004.

ASHRAE *et al.* Handbook: Fundamentals. *American Society of Heating, Refrigerating and Air Conditioning Engineers, Atlanta*, 111, 2001.

P. Bamforth. The relationship between permeability coefficients for concrete obtained using liquid and gas. *Magazine of Concrete Research*, 39(138):3–11, 1987.

P. Barnes and J. Bensted. *Structure and performance of cements*. CRC Press, 2002.

V. Baroghel-Bouny. *Caractérisation microstructurale et hydrique des pâtes de ciment et des bétons ordinaires et à très hautes performances*. Ph.D. thesis, ENPC, 1994.

V. Baroghel-Bouny. Water vapour sorption experiments on hardened cementitious materials: Part i: Essential tool for analysis of hygral behaviour and its relation to pore structure. *Cement and Concrete Research*, 37(3):414 – 437, 2007.

B. Bary, M. V. de Morais, S. Poyet, and S. Durand. Simulations of the thermo-hydro-mechanical behaviour of an annular reinforced concrete structure heated up to 200°C. *Engineering Structures*, 36:302–315, 2012.

B. Bary, G. Ranc, S. Durand, and O. Carpentier. A coupled thermo-hydro-mechanical-damage model for concrete subjected to moderate temperatures. *International journal of heat and mass transfer*, 51(11):2847–2862, 2008.

Z. P. Bazant and M. F. Kaplan. *Concrete at high temperatures: material properties and mathematical models*. Longman Group Limited, 1996.

Z. P. Bazant and W. Thonguthai. Pore pressure and drying of concrete at high temperature. *Journal of the Engineering Mechanics Division*, 104(5):1059–1079, 1978.

Z. P. Bažant and W. Thonguthai. Pore pressure in heated concrete walls: theoretical prediction. *Magazine of Concrete Research*, 31(107):67–76, 1979.

J. Bear. *Dynamics of Fluids in Porous Media*. DOVER PUBLICATIONS, INC., New York, 1972.

T. L. Bergman, F. P. Incropera, and A. S. Lavine. *Fundamentals of heat and mass transfer*. John Wiley & Sons, 2011.

H. Berman and E. Newman. Heat of formation of calcium aluminate monosulfate. *J. Res. Natl. Bur. Stand., A Phys. Chem. A*, 67:1–13, 1963.

J. Bernal. The structures of cement hydration compounds. In *Proc. 3rd Int. Symp. Chem. Cem., London*, volume 1954, pages 216–236. 1952.

J. I. Bhatty. A review of the application of thermal analysis to cement-admixture systems. *Thermochimica Acta*, 189(2):313–350, 1991.

H. Brouwers. The work of powers and brownyard revisited: Part 1. *Cement and Concrete Research*, 34(9):1697–1716, 2004.

S. Brunauer, R. Mikhail, and E. Bodor. Some remarks about capillary condensation and pore structure analysis. *Journal of Colloid and Interface Science*, 25(3):353 – 358, 1967.

L. Buffo-Lacarrière. *Prévision et évaluation de la fissuration précoce des ouvrages en béton*. Ph.D. thesis, Université de Toulouse, 2007.

L. Buffo-Lacarrière, B. Kolani, A. Sellier, and G. Escadeillas. Modélisation de l'hydratation des liants composés à base de laitiers. In *Treizième édition des Journées scientifiques du Regroupement Francophone pour la Recherche et la Formation sur le Béton (RF)2B*. 2012.

L. Buffo-Lacarrière, A. Sellier, G. Escadeillas, and A. Turatsinze. Multiphasic finite element modeling of concrete hydration. *Cement and Concrete Research*, 37(2):131–138, 2007.

J. J. Chen, J. J. Thomas, H. F. Taylor, and H. M. Jennings. Solubility and structure of calcium silicate hydrate. *Cement and Concrete Research*, 34(9):1499–1519, 2004.

M. Chino, H. Nakayama, H. Nagai, H. Terada, G. Katata, and H. Yamazawa. Preliminary estimation of release amounts of 131i and 137cs accidentally discharged from the fukushima daiichi nuclear power plant into the atmosphere. *Journal of nuclear science and technology*, 48(7):1129–1134, 2011.

J. H. Chung. *Numerical simulation of hydro-thermo-mechanical behavior of concrete structures exposed to elevated temperatures*. Ph.D. thesis, University of Florida, 2003.

J. H. Chung and G. R. Consolazio. Numerical modeling of transport phenomena in reinforced concrete exposed to elevated temperatures. *Cement and Concrete Research*, 35(3):597–608, 2005.

N. J. Clayden, C. M. Dobson, C. J. Hayes, and S. A. Rodger. Hydration of tricalcium silicate followed by solid-state 29si nmr spectroscopy. *J. Chem. Soc., Chem. Commun.*, 21:1396–1397, 1984.

L. E. Copeland and R. Bragg. The hydrates of magnesium perchlorate. *The Journal of Physical Chemistry*, 58(12):1075–1077, 1954.

L. E. Copeland and J. C. Hayes. The determination of non-evaporable water in hardened portland cement paste. Technical report, Portland Cement Association, 1953.

O. Coussy. *Poromechanics*. John Wiley & Sons, 2004.

S. Dal Pont. *Lien entre la perméabilité et l'endommagement dans les bétons à haute température*. Ph.D. thesis, ECOLE NATIONALE DES PONTS ET CHAUSSEES, 2004.

S. Dal Pont, S. Durand, and B. Schrefler. A multiphase thermo-hydro-mechanical model for concrete at high temperaturesï£¡finite element implementation and validation under loca load. *Nuclear Engineering and Design*, 237(22):2137–2150, 2007.

S. Dal Pont and A. Ehrlacher. Numerical and experimental analysis of chemical dehydration, heat and mass transfers in a concrete hollow cylinder submitted to high temperatures. *International journal of heat and mass transfer*, 47(1):135–147, 2004.

S. Dal Pont, F. Meftah, and B. Schrefler. Modeling concrete under severe conditions as a multiphase material. *Nuclear engineering and design*, 241(3):562–572, 2011.

S. K. Das, A. Mitra, and P. D. Poddar. Thermal analysis of hydrated calcium aluminates. *Journal of thermal analysis*, 47(3):765–774, 1996.

M. V. De Morais, B. Bary, G. Ranc, S. D. Pont, and S. Durand. Comparative analysis of coupled thermo-hydro-mechanical models for concrete exposed to moderate temperatures. *Numerical Heat Transfer, Part A: Applications*, 55(7):654–682, 2009.

R. Dhir, P. Hewlett, and Y. Chan. Near surface characteristics of concrete: intrinsic permeability. *Magazine of Concrete Research*, 41(147):87–97, 1989.

B. Z. Dilnesa, B. Lothenbach, G. Renaudin, A. Wichser, and D. Kulik. Synthesis and characterization of hydrogarnet $\mathrm{Ca_3(Al_xFe_{1-x})_2(SiO_4)_y(OH)_{4(3-y)}}$. *Cement and Concrete Research*, 59:96 – 111, 2014.

B. Z. Dilnesa, B. Lothenbach, G. Renaudin, A. Wichser, and E. Wieland. Stability of monosulfate in the presence of iron. *Journal of the American Ceramic Society*, 95(10):3305–3316, 2012.

V. Farmer, J. Jeevartnam, and K. Speakman. Thermal decomposition of 14 a tobermorite from crestmore. *Highway Research Board Special Report*, 90, 1966.

A. Feraille Fresnet. *Le rôle de l'eau dans le comportement à haute température des bétons*. Ph.D. thesis, ENPC, 2000.

E. M. Foley, J. J. Kim, and M. R. Taha. Synthesis and nano-mechanical characterization of calcium-silicate-hydrate $(\mathrm{C-S-H})$ made with 1.5 $\mathrm{CaO/SiO_2}$ mixture. *Cement and Concrete Research*, 42(9):1225 – 1232, 2012.

P. A. Forsyth and R. Simpson. A two-phase, two-component model for natural convection in a porous medium. *International journal for numerical methods in fluids*, 12(7):655–682, 1991.

K. Fujii and W. Kondo. Heterogeneous equilibrium of calcium silicate hydrate in water at 30 c. *J. Chem. Soc., Dalton Trans.*, 2:645–651, 1981.

K. Fujii and W. Kondo. Communications of the american ceramic society estimation of thermochemical data for calcium silicate hydrate (c-s-h). *Journal of the American Ceramic Society*, 66(12):C–220, 1983.

D. Gawin, C. Majorana, and B. Schrefler. Numerical analysis of hygro-thermal behaviour and damage of concrete at high temperature. *Mechanics of Cohesive-frictional Materials*, 4(1):37–74, 1999.

D. Gawin, F. Pesavento, and B. Schrefler. Simulation of damage–permeability coupling in hygro-thermo-mechanical analysis of concrete at high temperature. *Communications in numerical methods in engineering*, 18(2):113–119, 2002.

D. Gawin, F. Pesavento, and B. A. Schrefler. What physical phenomena can be neglected when modelling concrete at high temperature? A comparative study. part 2: Comparison between models. *International Journal of Solids and Structures*, 48(13):1945–1961, 2011.

P. J. Haines. *Principles of thermal analysis and calorimetry*, volume 30. Royal society of chemistry, 2002.

T. Harmathy and L. Allen. Thermal properties of selected masonry unit concretes. In *ACI Journal Proceedings*, volume 70. ACI, 1973.

S. Hassen. On the modeling of the dehydration induced transient creep during a heating–cooling cycle of concrete. *Materials and structures*, 44(9):1609–1627, 2011.

Z. he Shui, R. Zhang, W. Chen, and D. xing Xuan. Effects of mineral admixtures on the thermal expansion properties of hardened cement paste. *Construction and Building Materials*, 24(9):1761 – 1767, 2010.

I. Horváth, I. Proks, and I. Nerád. Activation energies of the thermal decompositions of C_3AH_6 and C_3AD_6 by the isothermal tg method. *Journal of thermal analysis*, 12(1):105–110, 1977.

T. Ishida, K. Maekawa, and T. Kishi. Enhanced modeling of moisture equilibrium and transport in cementitious materials under arbitrary temperature and relative humidity history. *Cement and concrete research*, 37(4):565–578, 2007.

Y. A. Izrael, M. De Cort, A. Jones, I. Nazarov, S. D. Fridman, E. Kvasnikova, E. Stukin, J. Kelly, I. Matveenko, Y. M. Pokumeiko, *et al.* The atlas of caesium-137 contamination of europe after the chernobyl accident. In *The Radiological Consequences of the Chernobyl Accident. Proceedings of the First International Conference, Minsk, Belarus*. 1996.

L. U. Jelica Zelic and D. Jozic. Application of thermal mmethod in the chemistry of cement: Kinetic analysis of portlandite from non-isothermal thermogravimetric data. In *The First International Proficiency Testing Conference*. 2007.

H. M. Jennings. A model for the microstructure of calcium silicate hydrate in cement paste. *Cement and Concrete Research*, 30(1):101–116, 2000.

H. M. Jennings. Colloid model of C-S-H and implications to the problem of creep and shrinkage. *Materials and structures*, 37(1):59–70, 2004.

H. M. Jennings. Refinements to colloid model of C-S-H in cement: Cm-ii. *Cement and Concrete Research*, 38(3):275–289, 2008.

M. Kanema, M. De Morais, A. Noumowe, J. Gallias, and R. Cabrillac. Experimental and numerical studies of thermo-hydrous transfers in concrete exposed to high temperature. *Heat and Mass Transfer*, 44(2):149–164, 2007.

J. H. Keenan, F. G. Keyes, P. G. Hill, and J. G. Moore. *Steam Tables*. Wiley, 1969.

J. Kestin and J. Moszynski. An instrument for the measurement of the viscosity of steam and compressed water. *TRANS. ASME*, 80:1009, 1958.

L. Klinkenberg *et al.* The permeability of porous media to liquids and gases. In *Drilling and production practice*. American Petroleum Institute, 1941.

E. Knapen, O. Cizer, K. Van Balen, and D. Van Gemert. Effect of free water removal from early-age hydrated cement pastes on thermal analysis. *Construction and Building Materials*, 23(11):3431–3438, 2009.

B. Kolani, L. Buffo-Lacarrière, A. Sellier, G. Escadeillas, L. Boutillon, and L. Linger. Hydration of slag-blended cements. *Cement and Concrete Composites*, 34(9):1009–1018, 2012.

A. Korpa and R. Trettin. The influence of different drying methods on cement paste microstructures as reflected by gas adsorption: comparison between freeze-drying (f-drying), d-drying, p-drying and oven-drying methods. *Cement and concrete research*, 36(4):634–649, 2006.

A. Kundt and E. Warburg. Über reibung und wärmeleitung verdünnter gase. *Poggendorfs ann Physik.*, pages 155, 337, 525, 1875.

H. Kurczyk, H.G Schwiete. Concerning the hydration products of C_3S and β-C_2S. In *4th ISCC*. 1962.

F. M. Lea. *The chemistry of cement and concrete*. Butterworth-Heinemann, 1970.

S. M. Leisinger, B. Lothenbach, G. Le Saout, and C. A. Johnson. Thermodynamic modeling of solid solutions between monosulfate and monochromate $3\mathrm{CaO} \cdot \mathrm{Al_2O_3} \cdot \mathrm{Ca}[(\mathrm{CrO_4})_\mathrm{x}(\mathrm{SO_4})_{1-\mathrm{x}}] \cdot \mathrm{nH_2O}$. *Cement and Concrete Research*, 42(1):158–165, 2012.

J. H. Lienhard. *A heat transfer textbook*. Courier Corporation, 2013.

B. Lothenbach, L. Pelletier-Chaignat, and F. Winnefeld. Stability in the system CAO–AL_2O_3–H_2O. *Cement and Concrete Research*, 42(12):1621–1634, 2012.

P. Lu, G. Sun, and J. F. Young. Phase composition of hydrated dsp cement pastes. *Journal of the American Ceramic Society*, 76(4):1003–1007, 1993.

L. Luckner, M. T. Van Genuchten, and D. Nielsen. A consistent set of parametric models for the two-phase flow of immiscible fluids in the subsurface. *Water Resour. Res*, 25(10):2187–2193, 1989.

R. C. Mackenzie. *Differential thermal analysis*. Academic Press, 1970.

M. Manolopoulou, S. Stoulos, A. Ioannidou, E. Vagena, and C. Papastefanou. Radiation measurements and radioecological aspects of fallout from the fukushima nuclear accident. *Journal of Radioanalytical and Nuclear Chemistry*, 292(1):155–159, 2012.

P. Maravelaki-Kalaitzaki, A. Bakolas, and A. Moropoulou. Physico-chemical study of cretan ancient mortars. *Cement and Concrete Research*, 33(5):651–661, 2003.

T. Matschei, B. Lothenbach, and F. Glasser. The AFm phase in portland cement. *Cement and Concrete Research*, 37(2):118–130, 2007a.

T. Matschei, B. Lothenbach, and F. P. Glasser. Thermodynamic properties of portland cement hydrates in the system $\mathrm{CaO} - \mathrm{Al_2O_3} - \mathrm{SiO_2} - \mathrm{CaSO_4} - \mathrm{CaCO_3} - \mathrm{H_2O}$. *Cement and Concrete Research*, 37(10):1379–1410, 2007b.

J. W. McBain. An explanation of hysteresis in the hydration and dehydration of gels. *Journal of the American Chemical Society*, 57(4):699–700, 1935.

H. D. Megaw and C. Kelsey. Crystal structure of tobermorite. *Nature*, 1956.

P. K. Mehta. *Concrete. Structure, properties and materials*. McGraw-Hill, 1986.

E. Menéndez, C. Andrade, and L. Vega. Study of dehydration and rehydration processes of portlandite in mature and young cement pastes. *Journal of Thermal Analysis and Calorimetry*, 110(1):443–450, 2012.

A. Mesbah, C. Cau-dit Coumes, G. Renaudin, F. Frizon, and F. Leroux. Uptake of chloride and carbonate ions by calcium monosulfoaluminate hydrate. *Cement and Concrete Research*, 42(8):1157–1165, 2012.

MEXT. Preparation of distribution map of radiation doses, etc. (maps of concentration of tellurium 129m and silver 110m in soil) by mext. Technical report, MEXT (Ministry of Education, E., Culture, Sports, Science & Technology in and Japan, 2011.

J. Monlouis-Bonnaire, J. Verdier, and B. Perrin. Prediction of the relative permeability to gas flow of cement-based materials. *Cement and Concrete Research*, 34(5):737–744, 2004.

J. Monzó, J. Payá, M. Borrachero, E. Mora, and S. Velázquez. Fluid catalytic cracking residue (fc3r) as a new pozzolanic material: Thermal analysis monitoring of fc3r/portland cement reactions, seventh canmet. In *ACI., International Conference on Fly Ash, Silica Fume, Slag and Natural Pozzolans in Concrete, Suplementary papers, India*. 2001.

A. Morandeau, M. Thiery, and P. Dangla. Investigation of the carbonation mechanism of CH and CSH in terms of kinetics, microstructure changes and moisture properties. *Cement and Concrete Research*, 56:153–170, 2014.

Y. Mualem. A new model for predicting the hydraulic conductivity of unsaturated porous media. *Water Resources Research*, 12(3):513–522, 1976. doi: 10.1029/WR012i003p00513.

A. Nonat. The structure and stoichiometry of CSH. *Cement and Concrete Research*, 34(9):1521–1528, 2004.

A. Nonat and X. Lecoq. The structure, stoichiometry and properties of CSH prepared by C_3S hydration under controlled condition. In *Nuclear magnetic resonance spectroscopy of cement-based materials*, pages 197–207. Springer, 1998.

Z. h. Pan Guoyao, Mao Ruoqing. Research of dehydrated calcium sulphoaluminate hydrates(AFm) and its hydration. *Journal of Wuhan University of Technology*, 19(3):28–30, 1997.

R. B. Peppler and L. S. Wells. The system of lime, alumina, and water from 50 to 250°C. *J. Res. Natl. Bur. Stand*, 52(2):75–92, 1954.

P. Perré and A. Degiovanni. Simulation par volumes finis des transferts couplés en milieux poreux anisotropes: séchage du bois à basse et à haute température. *International Journal of Heat and Mass Transfer*, 33(11):2463–2478, 1990.

F. Perrot, P. Hubert, C. Marquet, M. Pravikoff, P. Bourquin, H. Chiron, P.-Y. Guernion, and A. Nachab. Evidence of 131
uppercaseli and (134,137)Cs activities in bordeaux, france due to the fukushima nuclear accident. *Journal of environmental radioactivity*, 114:61–65, 2012.

P. PEZZANI. Propriétés thermodynamiques de l'eau. *Techniques de l'ingénieur. Technologies de l'eau*, 1(W120), 1992.

J. Pourchez, F. Valdivieso, P. Grosseau, R. Guyonnet, and B. Guilhot. Kinetic modelling of the thermal decomposition of ettringite into metaettringite. *Cement and concrete research*, 36(11):2054–2060, 2006.

T. Powers. Physical properties of cement paste. In *4th ISCC*, volume 2, page 577. 1962.

S. Poyet. Experimental investigation of the effect of temperature on the first desorption isotherm of concrete. *Cement and Concrete Research*, 39(11):1052–1059, 2009.

H. Ranaivomanana. *Tranferts dans les milieux poreux réactifs non saturés: application à la cicatrisation de fissure dans les matériaux cimentaires par carbonatation*. Ph.D. thesis, Toulouse 3, 2010.

G. Ranc, J. Sercombe, and S. Rodrigues. Comportement à haute température du béton de structure: impact de la fissuration sur les transferts hydriques. *Revue française de génie civil*, 7(4):397–424, 2003.

K. Raznjevic. *Thermodynamic tables and diagrams*. Technical Publishing, Romanian, 1978.

R. C. Reid, J. M. Prausnitz, and B. E. Poling. *The properties of gases and liquids*. McGraw Hill Book Co., New York, NY, 1987.

I. Richardson. The nature of CSH in hardened cements. *cement and concrete research*, 29(8):1131–1147, 1999.

I. Richardson. The nature of the hydration products in hardened cement pastes. *Cement and Concrete Composites*, 22(2):97–113, 2000.

I. Richardson. Tobermorite/jennite-and tobermorite/calcium hydroxide-based models for the structure of CSH: applicability to hardened pastes of tricalcium silicate, β-dicalcium silicate, portland cement, and blends of portland cement with blast-furnace slag, metakaolin, or silica fume. *Cement and Concrete Research*, 34(9):1733–1777, 2004.

I. Richardson. The calcium silicate hydrates. *Cement and Concrete Research*, 38(2):137–158, 2008.

I. Richardson and G. Groves. Models for the composition and structure of calcium silicate hydrate (c s h) gel in hardened tricalcium silicate pastes. *cement and concrete research*, 22(6):1001–1010, 1992.

I. Richardson and G. Groves. The incorporation of minor and trace elements into calcium silicate hydrate (c s h) gel in hardened cement pastes. *Cement and Concrete Research*, 23(1):131–138, 1993a.

I. Richardson and G. Groves. Microstructure and microanalysis of hardened ordinary portland cement pastes. *Journal of Materials Science*, 28(1):265–277, 1993b.

J. Rivas-Mercury, P. Pena, A. de Aza, and X. Turrillas. Dehydration of $\mathrm{Ca_3Al_2(SiO_4)_{4(3-y)}}$(0< y< 0.176) studied by neutron thermodiffractometry. *Journal of the European Ceramic Society*, 28(9):1737–1748, 2008.

T. Sato, J. Beaudoin, V. Ramachandran, L. Mitchell, and P. Tumidajski. Thermal decomposition of nanoparticulate $\mathrm{Ca(OH)_2}$-anomalous effects. *Advances in cement research*, 19(1):1–7, 2007.

E. H. Schmidt and F. Mayinger. Viscosity of water and steam at high pressures and temperatures up to 800 atmospheres and 700°c. In *Modern Developments in Heat Transfer*, volume 1, page 265. 1963.

B. Schrefler, P. Brunello, D. Gawin, C. Majorana, and F. Pesavento. Concrete at high temperature with application to tunnel fire. *Computational Mechanics*, 29(1):43–51, 2002.

A. Sellier, L. Buffo-Lacarrière, M. E. Gonnouni, and X. Bourbon. Behavior of hpc nuclear waste disposal structures in leaching environment. *Nuclear Engineering and Design*, 241(1):402–414, 2011.

J. Sengers and B. Kamgar-Parsi. Representative equations for the viscosity of water substance. *Journal of physical and chemical reference data*, 13(1):185–205, 1984.

W. Sha, E. O'Neill, and Z. Guo. Differential scanning calorimetry study of ordinary portland cement. *Cement and Concrete Research*, 29(9):1487–1489, 1999.

L. Shpynova, N. ID, and N. Belov. Microstructure of alite cement stone (hydrated tricalcium silicate). *SOVIET PHYSICS CRYSTALLOGRAPHY, USSR*, 11(6):747, 1967.

E. Stepkowska, J. Blanes, F. Franco, C. Real, and J. Pérez-Rodrıguez. Phase transformation on heating of an aged cement paste. *Thermochimica acta*, 420(1):79–87, 2004.

L. SUEUR. Chemical and morphological studies of the hydration of tricalcium silicate. In *Proc. Br. Ceram. Soc.*, 35, page 177. 1984.

H. Taylor. Studies on the chemistry and microstructure of cement pastes. In *Proc. Br. Ceram. Soc.*, 35, page 65. 1984.

H. Taylor. Nanostructure of C-S-H: Current status. *Advanced cement based materials*, 1(1):38–46, 1993.

H. Taylor and J. Howison. Relationships between calcium silicates and clay minerals. *Clay Minerals Bull*, 3(16):98–111, 1956.

H. Taylor and D. Newbury. Calcium hydroxide distribution and calcium silicate hydrate composition in tricalcium silicate and β-dicalcium silicate pastes. *Cement and concrete research*, 14(1):93–98, 1984.

H. F. Taylor. *Cement chemistry*. Thomas Telford, 1990.

E.-i. Tazawa, S. Miyazawa, and T. Kasai. Chemical shrinkage and autogenous shrinkage of hydrating cement paste. *Cement and concrete research*, 25(2):288–292, 1995.

H. R. Thomas and M. R. Sansom. Fully coupled analysis of heat, moisture, and air transfer in unsaturated soil. *Journal of Engineering Mechanics*, 121(3):392–405, 1995.

D. Timroth and N. Vargaftik. The thermal conductivity and viscosity of steam at high temperatures and pressures. *Journal of Physics*, pages 101–111, 1940.

S. Timroth D. L., Rivkin and Vargaftik. Steam table of the all-union heat engineering research institute. Moscow, 1958.

P. Ubbrı aco and D. Calabrese. Solidification and stabilization of cement paste containing fly ash from municipal solid waste. *Thermochimica acta*, 321(1):143–150, 1998.

M. T. Van Genuchten. A closed-form equation for predicting the hydraulic conductivity of unsaturated soils. *Soil science society of America journal*, 44(5):892–898, 1980.

R. Vedalakshmi, A. Sundara Raj, S. Srinivasan, and K. Ganesh Babu. Quantification of hydrated cement products of blended cements in low and medium strength concrete using tg and dta technique. *Thermochimica Acta*, 407(1):49–60, 2003.

L. S. Wells, W. Clarke, and H. McMurdie. Study of the system $\mathrm{CaO} - \mathrm{Al_2O_3} - \mathrm{H_2O}$ at temperatures of 21 and 90°c. *Journal of Research of the National Bureau of Standards*, 30:367–409, 1943.

D. Whiting. Permeability of selected concretes. *ACI Special Publication*, 108, 1988.

J. F. Young and W. Hansen. Volume relationships for CSH formation based on hydration stoichiometries. In *MRS Proceedings*, volume 85, page 313. Cambridge Univ Press, 1986.

P. Yu and R. Kirkpatrick. Thermal dehydration of tobermorite and jennite. *Concr Sci Eng*, 1:185–191, 1999.

Q. Zhang and G. Ye. Dehydration kinetics of portland cement paste at high temperature. *Journal of thermal analysis and calorimetry*, 110(1):153–158, 2012.

Q. Zhou and F. Glasser. Thermal stability and decomposition mechanisms of ettringite at< 120°C. *Cement and Concrete Research*, 31(9):1333–1339, 2001.

Q. Zhou, E. Lachowski, and F. Glasser. Metaettringite, a decomposition product of ettringite. *Cement and concrete research*, 34(4):703–710, 2004.

Modeling of Concrete Dehydration and Multiphase Transfer in Nuclear Containment Concrete Wall during Loss of Cooling Accident

Abstract

Nuclear power plant now takes an important part in the world's electricity generation. In human history, there have already been two tragic accidents in Chernobyl and Fukushima causing severe radioactive matter leakage. To prevent this kind of accident from happening again, concrete structure plays an important role as material of containment building, which is the last barrier to isolate the radioactive matter from the environment. Hence, the transfer properties of concrete under severe circumstances, especially high temperature, are important for this usage. This PhD thesis aims to investigate the behavior of the concrete under high temperature up to 200°C. In the first part, a dehydration model was proposed. The model consists of different dehydration sub-models for main hydrates in the cement paste. In the second part, the dehydration model was implemented in a thermo-hygral model. The thermo-hygral model was then used to simulate a mock-up for which experimental results are available in the literature, without considering the mechanical behaviors. At last, parametric studies were performed to investigate the influence of some parameters, and the model was then applied to structures under different heating rates, and structures with different thicknesses to compare the temperature and gas pressure profiles across a wall.

Keywords: concrete, cement paste, dehydration, high temperature, thermo-hygral model, non saturated porous media.

AUTEUR: WANG Jin
TITRE: Modélisation de la déshydratation du béton et des transferts dans les murs d'enceinte de confinement de centrale nucléaire sous LOCA
DIRECTEUR DE THESE: Alain SELLIER, Laurie BUFFO-LACARRIÈRE
LIEU ET DATE DE SOUTENACE: Salle 110 du département de Génie civil de INSA 10h00, 8 june 2016.

Résumé

Les centrales nucléaires jouent un rôle important au niveau modial dans la production d'electricité aujourd'hui. Dans l'histoire humaine, deux accidents tragiques ont déjà eu lieu, à Tchernobyl et Fukushima, provoquant des fuites des matières radioactives. Pour éviter ce genre d'accident dans la future, la construction en béton prend un rôle important en tant que matériau de construction de confinement qui est la dernière barrière pour isoler la matière radioactive de l'environment. La compréhension des transferts dans le béton dans des circonstances graves, en particulier à étudier le comportement du béton sous haute température jusqu'a 200°C. Dans la première partie, un modèle de déshydratation a été appliqué dans le modèle thermo-hygro. Le modèle thermo-hygro a ensuite été mis en oeuvre pour simuler une maquette dont les résultats expérimentaux sont disponibles dans la littérature, sans tenir compte des comportements mécaniques. Enfin, des études paramétrique ont été réalisées pour étudier l'influence de certains paramètres. Le modèle à ensuite été appliqué à des structures sous vitesse de chauffage différente, et le modèle à ensuite été appliqué à des structure sous rythme de chauffage différents et celles avec des épaisseurs différentes pour comparer les profiles de température et de pression de gaz à travers de la mur.

Keywords: déshydratation, béton, enceinte de confinement, hautes températures, transferts
DISCIPLINE ADIMINISTRATIVE: Génie civil
INTITULE ET ADRESSE DE L'U.F.R. OU DU LABORATOIRE:
Laboratoire Matériaux et Durabilité des Constructions de Toulouse
135, Avenue de Rangueil - 31077 Toulouse Cedex 4 - France